UNIVERSITE CATHOLIQUE DE LOUVAIN
ECOLE POLYTECHNIQUE DE LOUVAIN
DEPARTEMENT SCIENCE DES MATERIAUX
ET DES PROCEDES

KATHOLIEKE UNIVERSITEIT LEUVEN
FACULTEIT INGENIEURSWETENSCHAPPEN
DEPARTEMENT METAALKUNDE EN
TOEGEPASTE MATERIAALKUNDE

Formation and Morphology of non-Metallic Inclusions in Aluminium Killed Steels

Thèse présentée par
Marie-Aline VAN ENDE
en vue de l'obtention du grade de
docteur en sciences appliquées

Composition du jury :

Prof. Christian Bailly (Président)	Université Catholique de Louvain, Belgium
Prof. Joris Proost (Promoteur)	Université Catholique de Louvain, Belgium
Prof. Bart Blanpain (Promoteur)	Katholieke Universiteit Leuven, Belgium
Prof. Francis Delannay	Université Catholique de Louvain, Belgium
Prof. Jan Fransaer	Katholieke Universiteit Leuven, Belgium
Dr. Jean Lehmann	ArcelorMittal Maizières, France
Prof. Jan Penning	Universiteit Gent, Belgium
Prof. Piotr Scheller	Technische Universität Bergakademie Freiberg, Germany
Prof. Patrick Wollants	Katholieke Universiteit Leuven, Belgium

Janvier 2010

D/2010/7515/4
ISBN 978-94-6018-165-8

Acknowledgements

Ces cinq années de doctorat ont été riches en expériences, tant sur le plan humain que scientifique. Je voudrais adresser à toutes les personnes que j'ai eu la chance de côtoyer et qui ont contribué de près ou de loin à ce travail, mes remerciements les plus chaleureux et les plus sincères.

Pour commencer, je voudrais remercier Gabriel de m'avoir convaincue d'entreprendre une thèse et de m'avoir soutenue lors de ces quelques années passées ensemble. Je voudrais également remercier Joris Proost de m'avoir présentée à Bart et Patrick lorsque je cherchais un sujet de thèse. Je le remercie également d'avoir permis d'obtenir ma bourse FRIA et d'élaborer une cotutelle entre les deux universités sœurs.

I would like to express all my gratitude to my supervisors, Bart, Joris and Patrick, for their guidance and support all along these years. I thank all of you for the interesting and constructive discussions and suggestions, and for being available at any time. I really appreciate the freedom you gave me during this research, which is for me a mark of respect and trust. I also thank you for all the opportunities you gave me to participate in international conferences.

I want to thank the jury members for accepting to evaluate this work. I am grateful for their interest, comments and corrections that helped to improve the manuscript. I gratefully acknowledge the FNRS-FRIA and ArcelorMittal for their financial support. Je remercie également Jean Lehmann et Pascal Gardin pour leurs précieux conseils durant ces quatre dernières années.

Muxing, I want to thank you for all your help and time to build up the equipment and to perform the experiments together. I really thank you for sharing your experience, for helping with writing articles and for your friendship. I will never forget our travel in China, Japan and Korea.

I would like to thank my officemates for their help and support: Veselin, Rob, Zhi, Tadej (thank you for the tea and chocolates from Slovenia!) and recently Lubica. Rob, I am grateful for sharing your knowledge on non-metallic inclusions. Zhi, many thanks for your help with the experiments. I would like to extend these acknowledgments to all the researchers at the Thermogroup for the interesting discussions, presentations and all the nice moments that makes this research group very unique. I want to thank Lieven

for his calculations on the Al dissolution in liquid Fe, Sander and Joris for their help to set up the furnace equipment, and Annelies for our climbing moments. Un grand merci à Fabienne pour son aide et son amitié.

For their excellent work and their availability, I thank all the technical personnel at the department MTM, specially Joris, Pieter, Danny, Eddy, Rudy, Luc and Louis for their precious help. Special thanks go to Joop, for his admirable work to prepare the quartz tubes, and for his advices and ideas to design the furnace flange and the CSLM addition device.

I wish to express my gratitude to the people at Corus: Sieger, Enno, Corrie, Max, Thibaut, Wouter and many others. Thank you for your warm welcome during my stay and for teaching me the AIA measurement technique.

Je tiens également à remercier toute l'équipe du laboratoire IMAP pour les analyses ainsi que les secrétaires, Viviane et Catherine, pour leur aide lors de l'organisation des défenses. Merci également à Vincent et Renaud pour la réalisation des TP HSC.

Je souhaite remercier ma famille et mes amis pour leur soutient, plus particulièrement ma mère pour m'avoir encouragée tout au long de mes études. Aussi ma chère petite sœur pour être là à tout moment, prête à aider et à partager les bons et moins bons moments.

Finally, I thank In-Ho for his support, encouragements and his fruitful comments during this last year.

Marie-Aline

December 2009

Abstract

Non-metallic inclusions are a major issue during the production of high performance steels, as they influence the microstructure and structural properties to a large extent. They are often considered as harmful to the final product quality and to the steel processing productivity, so that many industrial efforts are directed towards improving inclusion removal. Another, more positive approach is to use non-metallic inclusions to produce steels with enhanced or tailored properties. In both cases, the key issue is to control the characteristics of the inclusion population in the liquid steel, such as number, composition, morphology, size and spatial distribution.

In this doctoral research, the influence of the main inclusion-related process parameters, like the dissolved aluminium and oxygen content in liquid iron, on the formation and morphology of Al_2O_3 inclusions was studied. Deoxidation and reoxidation phenomena in liquid Fe were investigated during lab-scale experiments under rigorously controlled conditions.

First of all, a new technique was developed to enable the observation of inclusions in the initial stage of the deoxidation process, by bringing a piece of aluminium in contact at 1600 °C with liquid iron containing different dissolved oxygen levels. A significant increase in inclusion number and a change in the inclusion morphology from angular to spherical were observed with increasing dissolved oxygen content. The shape transition was explained by the evolution of the supersaturation and the oxygen availability at the reaction front.

Secondly, the inclusion formation and characteristics during reoxidation were investigated by exposing Fe-Al melts to different oxidizing atmospheres with controlled oxygen partial pressure. Dendrites, clusters, aggregates and bars were observed near the melt surface and at high oxygen partial pressure, while compact and faceted shapes were found at lower oxygen partial pressure, i.e. under lower supersaturation conditions. Finally, to assist in the interpretation of the experimental results on the inclusion characteristics, a coupled diffusion-reaction model was formulated to estimate the spatial and time dependent aluminium and oxygen concentration profiles as a function of selected process parameters.

Contents

List of abbreviations and symbols

Abbreviations

AES	Atomic Emission Spectroscopy
AIA	Automated Image Analysis
CSD	Crystal Size Distribution
CSLM	Confocal Scanning Laser Microscope
EDS	Energy Dispersive Spectrometer
ICP	Inductive Coupled Plasma
PDF	Population Density Function
SEM	Scanning Electron Microscope
SEN	Submerged Entry Nozzle

Symbols

A	Reaction area [m^2]
A_f	Frequency factor [nuclei cm^{-3} s^{-1}]
a_i	Activity of component i
$\underline{\text{Al}}$	Dissolved aluminium in liquid Fe
C_{fract}	Constant of proportionality of the fractal distribution
C_i	Concentration of component i [mol m^{-3}]
C_{Al}^0	Initial $\underline{\text{Al}}$ concentration in the Fe-Al alloy [mol m^{-3}]
$C_O^{sat.}$	$\underline{\text{O}}$ concentration at the melt surface in equilibrium with p_{O_2} [mol m^{-3}]
C_p	Heat capacity [J kg^{-1} K^{-1}]
d	Characteristic particle size [m]
D_{fract}	Fractal dimension of the fractal distribution
D_i	Diffusion coefficient of component i [m^2 s^{-1}]
dt	Time step [s]
E_A	Activation energy for growth of intermetallic layer [J mol^{-1}]
e_i^j	Interaction coefficient for effect of component j on i
$f(x)$	Statistical distribution of the variable x

f_i	Activity coefficient of component *i* in liquid Fe
g	Acceleration of gravity [m s^{-2}]
$h_{(i)}$	Heat transfer coefficient [W m^{-2} K^{-1}]
I	Nucleation rate [nuclei cm^{-3} s^{-1}]
J_D	Molar flux [mol m^{-2} s^{-1}]
k	Rate constant [μm^2 s^{-1}]
K	Equilibrium reaction constant
k_0	Frequency factor [μm^2 s^{-1}]
k_B	Boltzmann's constant [J K^{-1}]
k_{in}, k_{out}	Source and sink terms, respectively [m^3 s^{-1}]
k_m	Mass transfer coefficient [m s^{-1}]
L	Height of liquid bath [m]
m	Scale parameter of the lognormal distribution
M_i	Molecular weight of component *i* [g mol^{-1}]
N	Number of discretisation points
n	Crystal or particle population density [m^{-4}]
N_i	Rate of mass transfer of component *i* through the reaction front [mol s^{-1}]
O	Dissolved oxygen in liquid Fe
$p(u,t)$, $q(v,t)$	O concentration in domain A, Al concentration in domain B [mol m^{-3}]
p_{O_2}	Oxygen partial pressure in gas phase [atm]
ppm	Parts per million [one part in 10^6]
R	Gas constant [J mol^{-1} K^{-1}]
Ra	Rayleigh number
r_c	Critical radius of nuclei [m]
S	Supersaturation
S^*	Critical supersaturation
T	Temperature [°C, K]
t	Time [s]
T_m	Melting temperature [°C, K]
u, v	Positional variables in diffusion domain A and B, respectively ($0 < u, v < 1$)
u_p	Settling velocity of buoyant particle [m s^{-1}]
V	Volume of the melt [m^3]
V_m	Molar volume [m^3 mol^{-1}]
W_i	Weight of component *i* [kg]
wt%	Mass percentage
Z	Position relative to the melt surface [m] Or vertical axis
Z_r	Position of the reaction front [m]
β	Thermal expansion coefficient [K^{-1}]
δ	Intermetallic layer thickness [µm]
ΔG	Total Gibbs free energy change for the formation of

	nuclei [J]
ΔG_D	Activation energy for diffusion [J]
ΔG_n	Gibbs free energy change for the formation of a critical nucleus [J]
ΔG_v	Gibbs free energy change of the reaction per unit volume [J m^{-3}]
ΔG^0	Standard Gibbs free energy change for the reaction per mol [J mol^{-1}]
μ	Viscosity of the liquid [[kg m^{-1} s^{-1}]
κ	Thermal conductivity [W m^{-1} K^{-1}]
ρ_i	Density of component i [g m^{-3}]
σ	Interfacial free energy [N m^{-1}]
σ_0	Size-dependent interfacial free energy [N m^{-1}]
$\sigma_{\ln}$	Shape parameter of the lognormal distribution
τ	Average residence time [s]
φ	Crystal growth rate [m s^{-1}]
[% i]	Mass fraction of component i in percent $[100 \times W_i / W_{\text{melt}}]$

Chapter 1

Introduction

1.1. Background of the research

More than ever, the steel industry is facing an increasing demand for steels of high quality and high performance to remain competitive against newer materials. At the same time, the production costs must be reduced and the environmental issues must be tackled, creating more and more important and challenging tasks for the steel producer. To meet this demand, the steel industry is urged to improve the mechanical properties of its final products by controlling and improving the industrial practices throughout the steelmaking process and by developing new technologies to produce steels with high cleanliness and by promoting alloy design and development for existing and new applications.

Steel cleanliness is defined by a low level of detrimental non-metallic inclusions, as these inclusions may influence drastically the performance of steels. Non-metallic inclusions are generated during the deoxidation stage (secondary metallurgy), when a deoxidizing agent, such as aluminium, is added to the molten steel bath in order to decrease its oxygen content prior to cooling down and solidification. Non-metallic inclusions may also originate from unintended reactions between the deoxidized steel and its environment (atmosphere, slag, refractory, etc.), resulting in a contamination of the liquid steel.

The residual non-metallic inclusions may cause loss of product quality by generating surface defects and deteriorating the properties of the end product. In general, inclusions, such as Al_2O_3, are detrimental to the mechanical properties of the steel, reducing the ductility, fatigue strength and increasing the risk for corrosion failure of the final product during its application. Moreover, inclusions may be at the origin of significant disturbances during the continuous casting process due to the formation of a

deposit at the tundish and Submerged Entry Nozzles (also called SEN clogging). SEN clogging causes loss of product quality and productivity. It requires expensive countermeasures. However, some of these inclusions can also have beneficial effect on steel properties by promoting grain refinement during solidification. Non-metallic inclusions can serve as a mean to control the steel microstructure, which allows the development of materials with higher performance and specific properties.

The production of clean and high performance steels requires to decrease the number of non-metallic inclusions and to control their size distribution, composition and morphology. This is important as the removal of all inclusions is, in practice, difficult to reach without increasing the costs dramatically. The final inclusion size and the total inclusion number are determined by the growth conditions. The morphology and the growth of a crystal are controlled by various factors whose principal ones are [1]: the phases, the type of solvent in which the crystals grow, the temperature of growth, the degree of supersaturation and impurities. Consequently, the process conditions play a determining role on the morphology and other characteristics of inclusions. In order to be able to control the inclusion composition, size, number and morphology, a sound knowledge on the theory and practices of clean steel production and technologies is indispensable for the steel producer.

1.2. Objectives of the research

The objective of this work is to study the influence of the dissolved aluminium and oxygen contents in liquid low-alloyed aluminium-killed steel, on the formation, growth and morphology of inclusions during secondary steelmaking.

Experiments have been designed at the lab scale to study the formation of inclusions during the deoxidation stage as well as during reoxidation of the liquid melt. The experimental results provide a quantitative description of the inclusions formed under controlled and defined conditions of temperature, atmosphere and composition of the melt. The observation and the characterisation of the inclusions, in terms of number, size, size distribution and morphology, provide clues to understand the phenomena regarding their formation and their evolution during the steelmaking process. Understanding the mechanisms that determine the characteristics of inclusions will enhance clean steel production or even tailored steel products.

1.3. Outline of the text

The text is divided in nine chapters. After introducing the context and the objectives of the research in the present chapter (Chapter 1), a literature review is introduced in the two following Chapters. Chapter 2 presents the general state of the art in the formation of non-metallic inclusions in liquid steel. The steelmaking process and the concept of steel cleanliness are presented, followed by a description of the nucleation, growth and removal of Al_2O_3 inclusions. In this chapter, the concept of inclusion engineering is also introduced thereafter the various sources of inclusion formation in the steelmaking process are briefly outlined. The morphology of non-metallic inclusions is covered in Chapter 3. The first part is dedicated to the fundamentals of crystal growth and morphology. The specific case of the morphology of Al_2O_3 inclusions in liquid steel is then treated, by providing first a classification of the various Al_2O_3 inclusion shapes reported in literature. The influence of the supersaturation on the inclusion morphologies and their evolution during the steelmaking process is then explained in more detail.

Chapters 4 through 8 are dedicated to the experimental work. The description of the experimental techniques used during the present research is provided in Chapter 4. The results of the deoxidation experiments are discussed in Chapters 5 and 6. In Chapter 5, the effect of the addition of a large amount of aluminium into liquid iron on the formation and morphology of Al_2O_3 was investigated, with an emphasis on the inclusion size and morphology distributions in the samples taken after the aluminium addition. The formation and morphology of Al_2O_3 inclusions just after the deoxidation stage is discussed in Chapter 6. To achieve this goal, an innovative sampling technique was designed by forming a diffusion couple between aluminium and liquid iron with different dissolved oxygen contents. This chapter includes a description and an interpretation of the interactions between aluminium and iron, and a discussion on the influence of the dissolved oxygen content on the inclusion morphology.

As Al_2O_3 inclusions also arise from reoxidation of liquid steel, the relationship between reoxidation conditions and Al_2O_3 inclusions is studied in Chapters 7 and 8 by exposing the melt to different oxidizing atmospheres. In the former, the evolution of the local conditions during reoxidation is investigated theoretically by modelling the diffusion process of aluminium and oxygen in liquid iron. The mathematical approach is used to predict the concentration profiles and the rate of Al_2O_3 formation in the melt as a function of the initial conditions and time. The predictions are compared with experimental results in Chapter 8. The results and discussions in this

chapter emphasise the influence of changing the oxygen partial pressure in the gas phase on the inclusion morphology.

To conclude this study, a summary of the results is provided in Chapter 9. Also suggestions for future work are given.

Chapter 2
Origins of non-metallic inclusions

Non-metallic inclusions arise during the steelmaking process, as a result of many physical and chemical phenomena. In this chapter, after a short introduction on the steelmaking process, the influence of non-metallic inclusions on the steel properties and the significance of steel cleanliness as a factor of steel quality are presented. Next, the main sources of formation of non-metallic inclusions are reviewed. Finally, the concept of inclusion engineering, which aims at the control of non-metallic inclusions, is briefly described.

2.1. Steelmaking process and steel cleanliness

2.1.1. The steelmaking process

The production of steel consists in several stages, namely ironmaking, primary and secondary steelmaking, casting and hot rolling. An overview of the process is depicted in Figure 2-1.

Ironmaking [2, 3] involves the production of liquid iron, called hot metal, from iron ore. Sintered iron ore, coke and other fluxes are fed into a blast furnace, where iron oxide is reduced by carbon and CO gas, producing molten pig iron. After the blast furnace, the hot metal contains 4 to 4.5 wt% C and other impurities, such as Mn, Si, P and S, and as such is not suitable for most engineering applications.

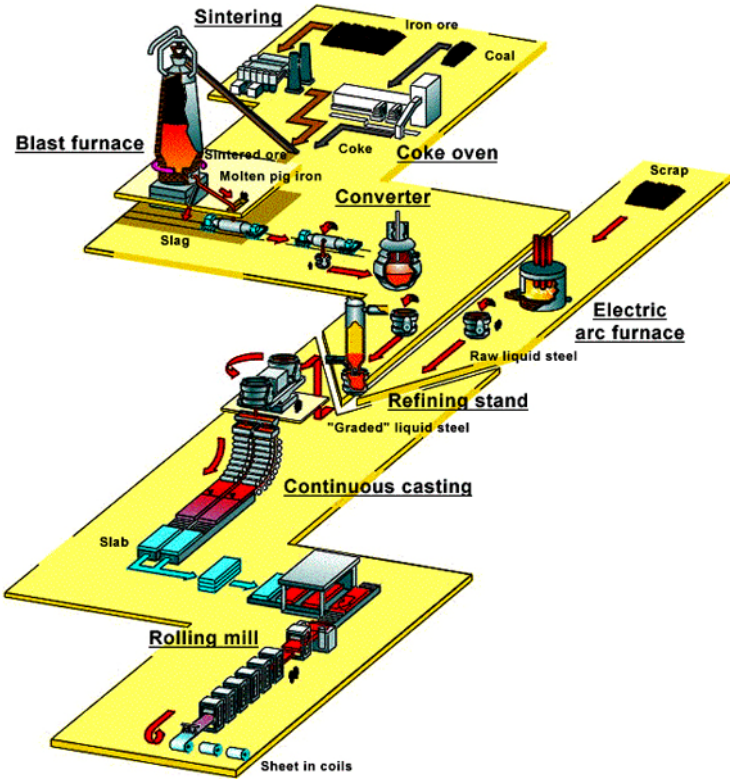

Figure 2-1: Overview of the steelmaking process [4].

The production of crude steel is achieved in the primary steelmaking process [2, 3, 5]. There are two different technologies to produce steel according to whether it is produced from iron ore (pig iron route) or from the recycling of scrap. In the first case, the carbon content is reduced in a Basic Oxygen Furnace (BOF) or converter by adding scrap metal and fluxes and blowing oxygen in the metal. This process is known as Basic Oxygen Steelmaking (BOS). The oxygen burns out the carbon into gaseous CO and CO_2 and oxidises Mn, Si and P impurities, which are collected in the slag. Alternately, scrap iron and steel originating from recycling are melted in an Electric Arc Furnace (EAF).

To achieve the required properties of steel, the steel composition, temperature and cleanliness must be adjusted. Refining treatments are carried out during the secondary steelmaking process. Crude steel is transferred in the ladle, in which some elements are added or removed in order to adjust the composition, depending on the specification of the final steel grade. The operations taking place during secondary steelmaking are summarised as follows [2, 3, 6, 7]:

- *Oxygen control:* After the BOS process, the steel has a very high dissolved oxygen content (400 to 1000 ppm). The latter must be removed before the steel is cast to prevent the formation of CO gas bubbles ("boiling" of the metal), causing disruption during the continuous casting, excessive porosity, or the precipitation of large quantities of FeO during steel solidification. This phenomenon is due to the large difference in oxygen solubility in steel with temperature. At 1600 °C, the oxygen solubility in liquid iron is 0.2284 wt% (Fe(l)-FeO equilibrium), whereas the oxygen solubility in solid iron is 54 ppm at 1390 °C and 2 ppm at 900 °C [8]. To remove dissolved oxygen, elements with high affinity towards oxygen are added to the liquid metal. The most common deoxidisers are ferromanganese, ferrosilicon, silicomanganese and aluminium. The choice and the amount of deoxidants depend on the steel grade and on the residual dissolved oxygen required. The deoxidation products consist of oxide inclusions that float out to the melt surface and are captured by the slag.
- *Alloying:* Alloying elements such as Ca, Ti, Se, Te, Nb, are added to the steel to obtain specific properties of the final product. These alloys are commonly injected in the steel. Some of the additives, especially Ca, CaSi and CaAl alloys, C, Mg, and S, are encased in a steel sheath and added to the steel in the form of cored-wires. Wire feeding can be used for deoxidation, where Al is added in the form of pure solid wire.
- *Removal of impurities:* Sulphur is one of the most detrimental impurities remaining in the crude steel from the BOS or EAF. Sulphur is removed through slag-metal reactions under reducing conditions, which requires the steel to be deoxidized prior to sulphur removal. Desulphurisation consists in the transfer of sulphur from the steel into the slag, in the presence of CaO and Al. The composition of the slag has to be carefully controlled to achieve the required desulphurisation level.
- *Stirring and homogenisation:* Ladle stirring is aimed to homogenize the bath composition and temperature, to improve slag-metal reactions and to enhance inclusion removal. Stirring is performed by bubbling Ar gas using a submerged lance or porous plugs at the ladle bottom or by using electromagnetic stirring.
- *Degassing:* Vacuum degassing is commonly performed using the RH process (Ruhrstahl-Heraeus) and the tank degasser. During the vacuum treatment, operations such as hydrogen removal, carbon deoxidation and decarburisation, vacuum alloying, and steel homogenisation are conducted. Also steel desulphurisation is

significantly improved during the vacuum treatment in the tank degasser, owing to the vigorous stirring.

- *Heating:* During alloying, flux additions and degassing, the temperature loss of the melt can be important and the steel needs to be reheated. The ladle arc furnace is used to heat the steel and to homogenise the steel composition and temperature with the assistance of Ar bubbling. Chemical reheating can be performed in the CAS-OB unit (Composition Adjustment by Sealed Argon Bubbling – Oxygen Blowing) by adding simultaneously Al and O_2 gas via a top lance. The exothermic reaction between Al and O_2 to form Al_2O_3 provides heat to the steel.

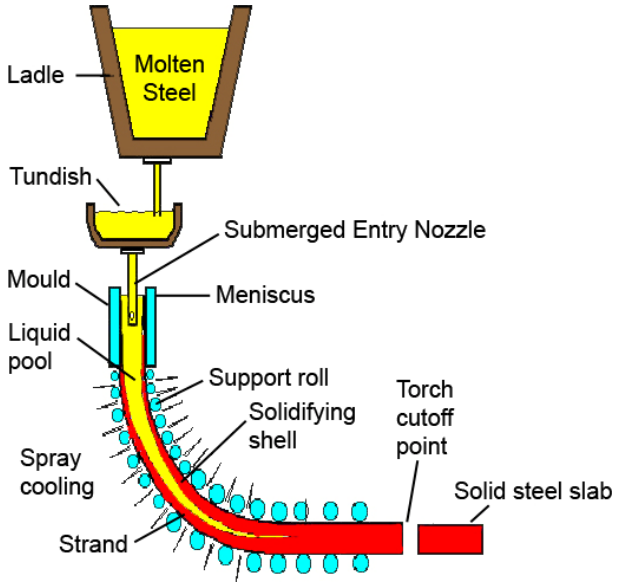

Figure 2-2: Schematic lay-out of the ladle, tundish, SEN and casting mould for curved continuous casting (adapted from [9]).

After the secondary steelmaking operations to refine and adjust the steel composition, temperature and cleanliness, the finished steel is transferred from the ladle into the tundish before being cast. Casting of steel is generally performed with continuous casting machines [2, 3], as represented in Figure 2-2. The tundish serves as a reservoir during the ladle change periods to distribute a constant flow of liquid steel to the continuous casting mould(s) [10]. The tundish is refractory-lined and is composed of an inlet section where the steel is incoming from the ladle, and an outlet section where liquid steel is supplied to the mould through a nozzle. It is equipped with stopper rods or sliding gates at the nozzle opening(s) to control the flow of the liquid steel teemed into the mould. Additional flow control devices, such as dams

and weirs, are provided along its length. Provided that reoxidation does not occur, the tundish serves as a refining station by which inclusions are removed by decantation, improving steel cleanliness.

The liquid steel enters the water-cooled copper mould where it starts to solidify, forming a strand (Figure 2-2). On leaving the mould, the strand is cooled by water sprays and is supported by rolls to prevent bulging until the strand is completely solidified. The strand is then cut into the desired dimension, depending on the final application (slabs, blooms or billets). To obtain the finished product, the ingots, slabs, blooms or billets are subjected to hot rolling. The material is reheated to 1200~1300 °C and passed repeatedly back and forth between two rolls. Hot rolling enables to shape the steel into the required size and to improve the mechanical properties.

2.1.2. Steel cleanliness

The steel industry is facing an increasing demand for high quality steels. To remain competitive, steelmakers must provide a final product with high performance, high reliability and durability, and at the same time meet the concerns on costs reductions, energy savings and environmental issues. The properties of the material are largely influenced by the microstructure. Non-metallic inclusions are particles that are embedded in the matrix of steel. They consist of oxides, sulphides, nitrides and carbides. Under normal conditions, the last three inclusion types precipitate during cooling and solidification of steel, while large oxide and some sulphides inclusions are present in liquid steel. The presence of non-metallic inclusions in the finished steel can have an extremely large effect on certain properties of the final product. For that reason, the steelmaking industry is motivated to produce cleaner steels, steel cleanliness being related to the presence of non-metallic inclusions and other impurities that influence the quality of the final product.

2.1.2.1. Classification of inclusions

Non-metallic inclusions are generally classified according to their source [11, 12]. They can be either indigenous (also named endogenous) or exogenous. Indigenous inclusions are formed during the deoxidation stage and during cooling and solidification of the liquid metal. The former are called primary inclusions and the latter secondary inclusions or precipitates. Both of them refer to inclusions formed by the reaction between oxygen dissolved in liquid Fe or liquid steel and the added deoxidant, such as Al or Si. In that case, the oxygen source for the oxide inclusions is internal to the

metal. In general, most of the indigenous inclusions consist of deoxidation products. Their formation mechanisms are summarised in sections 2.2 and 2.3.

Exogenous inclusions originate from the interactions between the deoxidized steel and its environment. While indigenous inclusions are generated on purpose, exogenous inclusions result form unintended mechanical and chemical interactions with liquid steel during processing. As a result, exogenous inclusions are generally more detrimental owing to their large size, their irregular shapes and their isolated occurrence [12]. Exogenous inclusions consist mainly of reoxidation products, refractory lining erosion and slag entrapment [13]. The latter results from mechanical interactions during turbulent mixing of slag and metal, producing liquid slag droplets suspended in liquid steel. Emulsification of slags generates slag inclusions, generally large and spherical owing to their liquid state at steelmaking temperature [12]. High molten steel velocity near refractory walls and excessive holding time in the vessel may result in the erosion of refractory and in the formation of macroinclusions. Reoxidation inclusions arise from chemical interactions between liquid steel and its surroundings. The principal mechanisms resulting in steel reoxidation are synthesised in section 2.4.

2.1.2.2. The influence of inclusions on steel properties

In general, non-metallic inclusions are considered to be detrimental to the mechanical properties of steel. Inclusions have different properties than the steel matrix, such as plasticity and thermal expansion coefficient, resulting in different behaviours upon mechanical and thermal stresses in comparison with the steel matrix [14]. Ductile fracture, toughness, fatigue and machinability are among the mechanical properties deteriorated by the presence of harmful inclusions [14, 15].

Inclusions may affect ductile fracture by providing nucleation site for the formation, growth and coalescence of voids and crack propagation [16]. The void formation forces the ductile matrix to deform more than normal, creating higher stress in the matrix near the inclusion and possibly decohesion [17]. The strain to cause ductile fracture is dependent on the volume fraction and on the shape of the inclusions [15, 16]. Elongated inclusions are potentially harmful to ductility owing to their anisotropy behaviour and their orientation relative to the working direction. As a result, the presence of “soft” inclusions, especially sulphides, such as MnS, can be detrimental to impact and fracture toughness, since they deform with the steel matrix owing to their high plasticity (types (d) and (e) in Figure 2-3).

Also, elongated inclusions decrease steel formability, resulting in premature fracture. Inclusions may reduce the fatigue strength significantly by increasing tensile stresses [18]. Most oxide inclusions, such as alumina and calcium aluminates inclusions, are stress raisers due to their lower expansion coefficient compared to that of steel. The behaviour of hard non deformable inclusions of the type globular silicate, crystalline high alumina calcium aluminate and Al_2O_3 cluster during rolling is illustrated in, respectively, Figure 2-3 (a), (b) and (c) [17]. Tensile stresses initiate cracks at the interface between the inclusion and the metal matrix. Once formed, the crack propagates into the steel matrix, eventually causing fatigue failure. Most sulphide inclusions are not detrimental to fatigue strength as they have higher thermal expansion than steel.

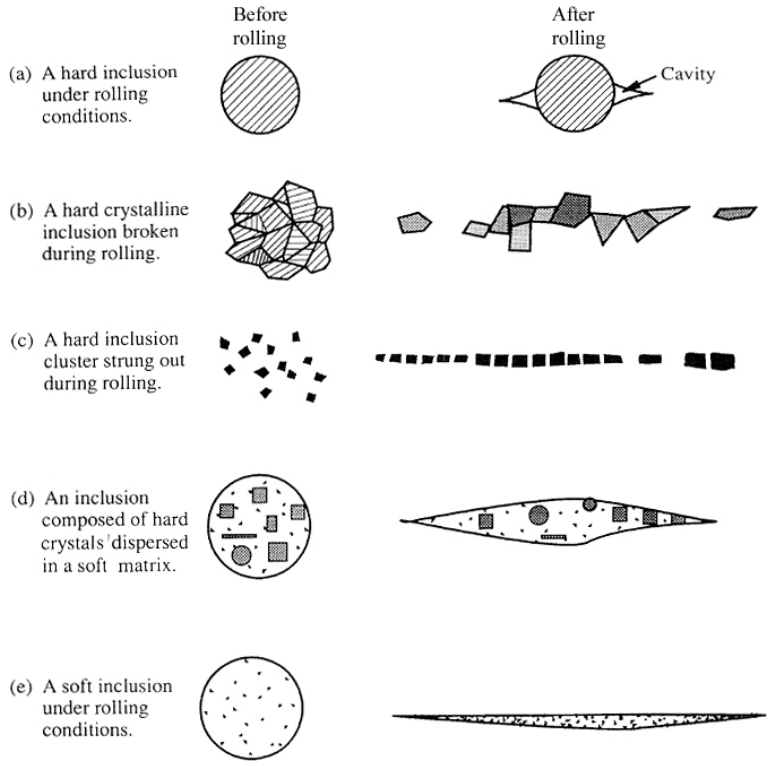

Figure 2-3: Schematic representation of inclusion shapes before and after deformation (from Engh [17]).

An increase of the detrimental effect on the properties is usually observed with an increase of the number and sizes of inclusions. In addition, inclusions can have a significant influence on surface properties, causing inferior surface appearance and poor polishability, decreased corrosion resistance (especially sulphides) and reduced coating adherence [15].

Sulphide inclusions are known to improve machinability, whereas oxide inclusions are detrimental to it [15]. Carbides and oxides, such as aluminates and silicates, are hard and abrasive, resulting in high wear of the cutting tool. Adversely, large sulphide inclusions act as lubricants and chip breakers, enhancing machinability.

The presence of harmful inclusions can lead to the premature failure of the product during its application. Since specific applications involve specific steel properties, the requirements on steel cleanliness are largely dependent on the application. Some examples of critical inclusion size and impurity contents, compiled by Emi [19] and Zhang [20], are listed in Table 2-1. In general, steel grades intended for applications with stringent mechanical properties have more restrictive requirements on maximum inclusion size. For instance, producers of shadow masks in cathode ray tube, lead frames for a large integrated circuit or plastic laminated, cold rolled thin sheet for deep-drawing and ironing cans fix the critical inclusion size at 5 μm [21].

Table 2-1: Typical steel cleanliness requirements for high performance steels [19, 20].

Application	Critical inclusion size (μm)	Critical impurity content (ppm)
Automotive and deep-drawing sheet	100	C ≤ 30; N ≤ 30
Deep drawing and ironing can sheet	20	C ≤ 30; N ≤ 30, Tot. O ≤ 20
Ball bearings	15	Tot. O ≤ 10
Tire cord	10~20	H ≤ 2; N ≤ 40, Tot. O ≤ 15
Wire	20	N ≤ 60; Tot. O ≤ 30
Sour gas* pipe	Shape control	P ≤ 50; S ≤ 10

* Sour gas: natural gas with high S and CO_2 contents, thereby extremely corrosive and dangerous.

Next to the inclusion size, inclusion shape must be controlled to reduce their harmful effect on the steel properties. The concept of inclusion modification (section 2.5.2) is to perform the addition of an alloying element during secondary steelmaking specifically to modify the inclusion population. For instance, calcium treatment is widely used to modify the composition and the shape of inclusions. In Al-killed steels, calcium treatment transforms Al_2O_3 inclusions into low melting point calcium aluminates, which are globular and less abrasive than Al_2O_3 at rolling temperatures.

Non-metallic inclusions are potentially harmful to the productivity of the steelmaking process due to the occurrence of clogging at the tundish and

Submerged Entry Nozzles (SEN). SEN clogging is the build-up of solid and semi-solid material in the flow passage between the tundish and the mould (Figure 2-2), which decreases the internal nozzle diameter, leading to a reduction in steel flow and eventually a blocking of the nozzle. Moreover, parts of the accretion layer may break free and enter the steel stream, causing important loss of quality of the final product. In addition, slag entrapments and surface defects may be generated due to disrupted flow in the mould caused by irregular or asymmetric flow patterns through the nozzle [20]. The presence of non-metallic inclusions during casting causes an early interruption of the continuous casting process, expensive repairs and rejections. Microscopic investigation of the clogs indicates that the deposit results from reoxidation of the steel rather than accumulation of inclusions exclusively [22, 23]. Sasai [24] demonstrated experimentally that adhesion and coalescence of Al_2O_3 inclusions to the continuous caster nozzle are promoted in the presence of FeO resulting from steel reoxidation. The mechanism of the deposit build-up is not fully understood. The steel composition, casting temperature, nozzle refractory material and geometry are among the parameters that influence steel castability.

Non-metallic inclusions can have beneficial effects on the properties of the final product by promoting the formation of a fine-grained structure during phase transformation. For instance, various Ti-containing oxides are known to serve as potential nucleation sites for acicular ferrite formation, thereby improving toughness [25, 26]. Ti is therefore added as an alloying element during secondary steelmaking, producing Ti stabilized Interstitial Free (IF) steels. All inclusions do not act as effective nucleation sites for acicular ferrite. Non-metallic inclusions with specific composition and size must be selected. For microstructure refinement, the inclusions, which are referred as dispersoids to distinguish them with the harmful inclusions [27], are purposely created or added in the melt. In the former concept, an alloy containing the reactive element (Ce, Zr) is added during secondary steelmaking to create the dispersoids within the system as a result of deoxidation or desulphurisation reactions. In the latter concept, a population of dispersoids is transferred to the melt via an alloy containing a high number of dispersoids. Microstructure refinement requires a strict control of the secondary steelmaking practices and an adequate design of the alloys and alloying sequence.

The performance of the finished steel is closely related to the presence of non-metallic inclusions. Highly demanding application requires a strict control of the inclusion characteristics. It is primordial to the steelmaker to understand the mechanism of inclusion formation during the steelmaking process in order to control their presence and to enhance the quality of the final product.

2.2. Deoxidation by Al addition

Deoxidation of the liquid steel is performed during the secondary metallurgy. The objective is to lower the dissolved oxygen content in liquid steel prior to cooling down and solidification. Aluminium may be charged in the ladle during tapping where it reacts with dissolved oxygen to form solid and stable Al_2O_3 inclusions. Aluminium deoxidation is a common practice owing to its high deoxidation efficiency [7]. The reactions are governed by thermodynamic and kinetics processes that are described in this section.

2.2.1. Thermodynamics of Al_2O_3 inclusion formation

The driving force of the deoxidation reaction $Al_2O_3 = 2\ \underline{Al} + 3\ \underline{O}$ is given by the Gibbs free energy change of the reaction, in J mol^{-1} [28, 29]:

$$\Delta G^0 = 1209400 - 391.2877T\ . \tag{2.1}$$

Assuming that solid Al_2O_3 is pure ($a_{Al_2O_3} = 1$), the reaction equilibrium constant K is written:

$$K = \left(a_O^3 \cdot a_{Al}^2\right)_{eq} \tag{2.2}$$

where a_i is the activity of the species i. Owing to the low concentrations of $\underline{Al}$ and $\underline{O}$ in liquid Fe, the solute activities are expressed relative to Henry's law in terms of mass percent.

$$a_i = f_i\left[\%i\right] \tag{2.3}$$

where f_i is the activity coefficient of species i in liquid Fe. The reaction equilibrium constant K becomes

$$\log K = 3\log f_O + 3\log\left[\%O\right] + 2\log f_{Al} + 2\log\left[\%Al\right]. \tag{2.4}$$

The dependence of the activity coefficient with the concentration in multi component systems is expressed using the solute interaction parameters e_i^j according to Wagner's formalism, defined as:

$$\log f_i = e_i^i\left[\%i\right] + \sum_j e_i^j\left[\%j\right]. \tag{2.5}$$

Table 2-2: Interaction parameters for liquid Fe at 1600 °C

i	j	e_i^j [28]	e_i^j [30]
O	Al	-3.9	-1.17
	O	-0.2	-0.1743
Al	Al	0.045	0.0430
	O	-6.6	-1.98

The values of the interaction parameters are chosen to reproduce the experimental data (Table 2-2). In the case of Al deoxidation, the interaction parameters between Al and O show a negative value to express the strong attractive interactions. Using the first order interaction parameters listed in Table 2-2 and rearranging, the equilibrium compositions of Al and O are given by relation (2.6).

$$\log K - \left(3e_{\mathrm{O}}^{\mathrm{O}} + 2e_{\mathrm{Al}}^{\mathrm{O}}\right)[\%\mathrm{O}] - 3\log[\%\mathrm{O}] = \left(3e_{\mathrm{O}}^{\mathrm{Al}} + 2e_{\mathrm{Al}}^{\mathrm{Al}}\right)[\%\mathrm{Al}] + 2\log[\%\mathrm{Al}] \tag{2.6}$$

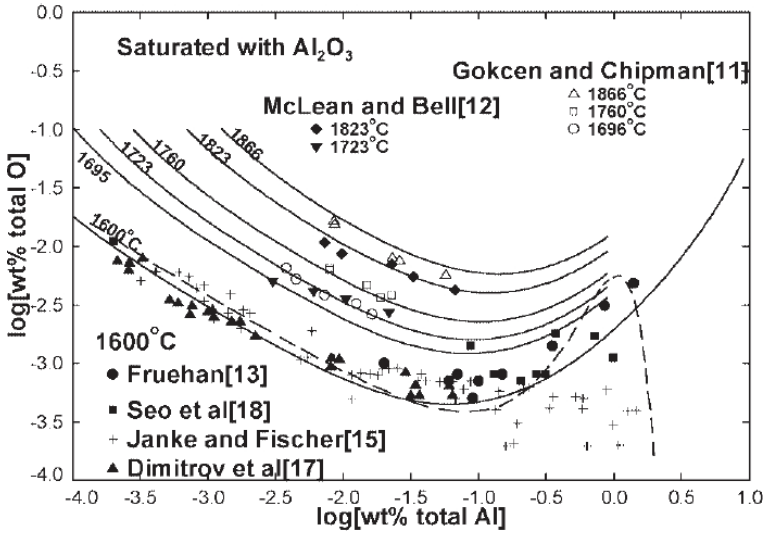

Figure 2-4: Total dissolved oxygen and total dissolved Al contents of liquid Fe in equilibrium with solid Al_2O_3. Solid lines calculated show the equilibrium deoxidation curve from the associate model. Dashed line was calculated from Wagner formalism with parameters of Sigworth and Elliott (figure and references from Jung [31]).

An alternative method to assess the thermodynamics of the deoxidation process is the associate model [31]. In contrast with Wagner's formalism, the associate model considers that Al and O atoms in liquid steel are not independent, but form dissolved Al*O and Al_2*O associates. The formation of associates is described by a Gibbs free energy change optimized to reproduce the experimental measurements. Figure 2-4 shows the equilibrium relation between total oxygen content and dissolved Al content. Experimental values and calculations using Wagner's formalism and the associate model are compared. The total oxygen concentration decreases with increasing Al content until approximately 0.1 wt% Al. After that point, the O content increases with Al content. Hence, the equilibrium deoxidation curve shows a minimum, at which the O and Al contents are, respectively, 3-4 ppm and 0.1 wt%. At the same time, O activity is decreasing with increasing Al content. According to the associate model, an increase of the Al content results in an increase of the Al*O associate concentration. The equilibrium deoxidation reaction is given by: $3\ \underline{Al*O} = Al_2O_3 + \underline{Al}$. Increasing the Al content moves the equilibrium deoxidation reaction to an increase of the O content, owing to an increase of the Al*O associate content. In that case, Al_2O_3 inclusions would dissolve in the melt as Al content increases above the minimum of the deoxidation curve.

The deoxidation diagram in Figure 2-4 reveals that a certain level of Al must be maintained in the steel to keep the dissolved oxygen content in the steel to a low value. The remaining dissolved Al content after deoxidation can be up to 0.05 wt% [7].

The supersaturation S is defined as the ratio between the activity product of Al and O at the initial state and that at equilibrium (Eq. (2.7)). The latter is given by the reaction equilibrium constant K defined above. From a thermodynamic point of view, Al_2O_3 precipitation reaction takes place when $S \geq 1$. It is a measure of the deviation from the thermodynamic equilibrium. The higher the supersaturation value, the higher the deviation and the driving force to reach the equilibrium state.

$$S = \frac{a_{Al}^2 \cdot a_O^3}{\left(a_{Al}^2 \cdot a_O^3\right)_{eq}} = \frac{a_{Al}^2 \cdot a_O^3}{K} \tag{2.7}$$

2.2.2. Kinetics of Al_2O_3 inclusion formation

The deoxidation reactions include several steps, namely the nucleation, the growth of the inclusions, and the removal from the melt bath. These steps are

not separate in time. They take place simultaneously during the deoxidation stage.

2.2.2.1. Nucleation of inclusion

In the classical homogeneous nucleation theory [32], nucleation of a new phase occurs in a solution that has become supersaturated. Following a stochastic formation mechanism, the theory assumes that molecules are added one by one and reversibly to the precritical cluster. The Gibbs free-energy change ΔG during the nucleation of a spherical nucleus with radius r is expressed by

$$\Delta G = \frac{4}{3}\pi r^3 \Delta G_v + 4\pi r^2 \sigma \,. \tag{2.8}$$

The fist term expresses the Gibbs free-energy change of the Al_2O_3 formation reaction of a nucleus, ΔG_v. The second term represents the interfacial free energy of a nucleus, where σ is the interfacial tension between nuclei and parent phase. The change of free energy per volume for the reaction ΔG_v is formulated using the degree of supersaturation S of the initial parent phase:

$$\Delta G_v = -\frac{RT}{V_m} \ln S \tag{2.9}$$

where V_m is the molar volume of Al_2O_3, R the gas constant and T the temperature.

If the parent phase is supersaturated ($S > 1$), the first term in the ΔG function is negative and the second is positive. The two terms being proportional to r^3 and r^2 respectively, the ΔG curve against r will increase to a maximum and then decrease. The position of the maximum is given by $\frac{\partial \Delta G}{\partial r} = 0$ and provide the critical radius, r_c, of the nucleus

$$r_c = -\frac{2\sigma}{\Delta G_v} \,. \tag{2.10}$$

The size of the critical nuclei is strongly dependent on the interfacial free energy and on the supersaturation of the melt. Low interfacial free energy and high supersaturation generates small size nuclei. Nuclei with $r > r_c$ will

tend to grow due to a subsequent decrease in ΔG. Substituting r_c into Eq. (2.8), the free energy change necessary for the nucleation, ΔG_n, is

$$\Delta G_n = \frac{16\pi}{3}\frac{\sigma^3}{\Delta G_v^2}. \tag{2.11}$$

Increasing the O content of the melt results in a decrease of ΔG_n, owing to the decrease of the surface tension and the increase of the supersaturation.

The rate of formation of nuclei per cm^3 of parent phase, I, is defined as:

$$I = A_f \exp\left(-\frac{\Delta G_n}{k_B T}\right) \tag{2.12}$$

where A_f is the frequency factor and k_B is the Boltzmann's constant. The frequency factor has various proposed definitions in literature. Turnbull and Fisher [33] proposed the following definition, which is proportional to the collision rate of atoms in condensed phase:

$$A_f = A_f '\exp\left(-\frac{\Delta G_D}{k_B T}\right) \tag{2.13}$$

where A_f' is another frequency factor describing atomic vibrational frequency and ΔG_D is the activation energy for diffusion at the parent phase-nucleus interface. Turnbull and Fisher [33] derived the following expression for the frequency factor A_f':

$$\begin{aligned} &A_f ' = n_m^* \sqrt{\frac{\sigma}{k_B T}} \sqrt[3]{\frac{2v}{9\pi}} n_m \frac{k_B T}{h_p}, \\ &\text{with} \quad n_m^* = \frac{4\pi r_c^2}{v^{2/3}}, \; n_m = \frac{N_{av} x_O}{3}, \; v = \frac{M}{\rho N_{av}}; \end{aligned} \tag{2.14}$$

where ρ and M are respectively the molecular weight and the density of Al_2O_3, x_O the initial molar fraction of oxygen in parent phase, h_p the Planck's constant and N_{av} Avogadro's number. n_m^* represents the number of molecules on the surface of critical nuclei and n_m is the number of molecules per mole of parent phase. Turpin and Elliott [34] evaluated the frequency factor A_f at 10^{26} nuclei cm^{-3} s^{-1} for Al_2O_3. However it is expected that the frequency factor changes with the Al and O content. In the study of Wasai

[35], ΔG_D was unknown and neglected because it is supposed to be very small compared with ΔG_n, so that $A_f = A_f'$. The frequency factor is in the range 10^{30} to 10^{34} nuclei mol^{-1} s^{-1}, depending on the Al and O contents, and increases with the interfacial free energy and the critical inclusion size.

The critical supersaturation degree S^* is defined by substituting $I = 1$ in Eq. (2.12):

$$\ln S^* = \left(\frac{16\pi\sigma^3 V_m^2}{3k_B R^2 T^3 \ln A_f} \right)^{1/2} . \tag{2.15}$$

S^* represents the supersaturation at which the nucleation rate and, consequently, the inclusion number increase. This important parameter shows that, even if the condition for the reaction to take place is satisfied ($S > 1$), the energy barrier for nucleation might require that the supersaturation of the melt is larger than 1. Li and Suito [36] experimentally measured the critical supersaturation ratio with respect to Al_2O_3 formation. They used solid electrolyte galvanic cell to measure the evolution of oxygen activity (EMF signal) during reoxidation of Fe-Al-O melt by CO_2 gas. They reported that the $\log(S^*)$ curve versus time reaches a maximum value of 3.5 due to an increase in Al and O activities after starting to blow CO_2, and then decreases rapidly.

The interfacial free energy between liquid Fe and solid Al_2O_3 has a significant influence on the nucleation process and is strongly dependent on the oxygen content in liquid Fe. The latter decreases with an increase in O content, modifying significantly the physical properties of the surface. As highlighted by many investigators [37-44], interfacial reaction rates are lowered by the presence of surface active elements, such as oxygen and sulphur. Using the data listed in literature [35, 45-47], the dependence of the oxygen content on σ is expressed using Eq. (2.16) (in N m^{-1}) for a plane interface between Al_2O_3 and liquid Fe at 1600 °C:

$$\sigma = 519.85[\%O]^2 - 69.97[\%O] + 2.39 . \tag{2.16}$$

This estimation is reasonably valid until approximately 500 ppm O. Above this value, σ was assumed constant at approximately 0.2 N m^{-1}. Equation (2.16) is defined for a plane interface and is acceptable for a curved boundary if the curvature radius is larger than the width of the transition zone [32]. The latter is the interface layer surrounding the pure vapour or solid region of the nucleus, in which the density varies from the density of the central region to the density of the bulk liquid phase. In the case of

nucleation, the curvature of small nuclei is large and the expression for σ may have to be changed to take into account this effect. With an increase in the interface curvature, the interfacial energy decreases, as reported by Christian [32]. Wasai [35] formulated the dependency with nuclei size r of the surface free energy between liquid Fe and Al_2O_3 nucleus, σ_0, using that between gas and liquid phases:

$$\sigma_0 = \frac{r}{WV_m + r}\sigma \tag{2.17}$$

where $W = \frac{2}{N_{av}^{1/3} V_m^{2/3}}$. σ is replaced by σ_0 in the classical nucleation theory. After insertion of the expression for σ_0 in Eq. (2.8), the free energy change of the system becomes:

$$\Delta G = \frac{4}{3}\pi r^3 \frac{\Delta G_m}{V_m} + 4\pi r^2 \sigma_0 = \frac{4}{3}\pi r^3 \left(\frac{\Delta G_m}{V_m} + \frac{3\sigma}{WV_m + r} \right) \tag{2.18}$$

where ΔG_m is the free energy change of the reaction in J mol^{-1} ($\Delta G_m = V_m \Delta G_v$). The critical nucleus size r_c is determined by the maximum of the ΔG function ($\frac{\partial \Delta G}{\partial r} = 0$) and is equal to:

$$r_c = \frac{V_m}{\Delta G_m}\left(-W\Delta G_m - \sigma \pm \sqrt{\sigma\left(\sigma - W\Delta G_m\right)} \right) \tag{2.19}$$

Wasai [35] compared the results of the nucleation theory using σ and σ_0. Both of them give an adequate explanation for the nucleation tendency, although quantitative results are significantly different. Without experimental data to compare with calculations, the actual value of σ to be used in the case of small particles or nuclei remains a difficult question and more exact formulation of the problem is necessary.

Jiang [48] derived general equations for the size-dependence of the solid-liquid interface energy considering a compressible spherical particle with diameter d_s immersed in a bulk liquid. The model uses the Laplace-Young equation to describe the pressure difference between inside and outside the particle and expresses the corresponding surface stress f using d_0, the diameter of the crystal when almost all atoms are on the surface (diffuse solid-liquid interface). This assumption implies that when $d_s \rightarrow d_0$, $\sigma_{SL} \rightarrow 0$. The following expression for $\sigma_{SL}(d_s)$ is then derived:

$$\frac{\sigma_{SL}\left(d_s\right)}{\sigma_{SL0}} = \frac{1 - d_0 / d_s}{1 - \sigma_{SL0} d_0 / \left(f d_s\right)}, \tag{2.20}$$

$$\text{with } f = \pm\sqrt{\frac{3\sigma_{SL0} d_0}{8\kappa}} \tag{2.21}$$

and where σ_{SL0} is the corresponding bulk value of $\sigma_{SL}(d_s)$ and κ is the particle compressibility. As seen in Eq. (2.20), a decrease in d_s results in a decrease of $\sigma_{SL}(d_s)$. The value of d_0 was approximated by the possible smallest value for d_s considering particles with curved surfaces. The latter is taken as $3d_{at}$, where d_{at} is the atomic diameter. The predictions of Jiang's model agreed well with other theoretical and experimental results. Equations for $\sigma_{SV}(d_s)$ and $\sigma_{SS}(d_s)$ were also derived and compared with $\sigma_{SL}(d_s)$. The same trend with the particle size was observed, but the magnitude was different. The decrease in the surface tension with a decrease in particle size is more significant with, in an decreasing order, $\sigma_{SV}(d_s)$, $\sigma_{SL}(d_s)$ and $\sigma_{SS}(d_s)$. In that respect, the formula used by Wasai to evaluate the size dependency using the gas-liquid interfacial equations might give a too low corrected value of the surface tension between solid and liquid phase.

These considerations show that, in order to build a nucleation model, it is crucial to have good estimates of the interfacial energies, the density of nucleation sites and the free energy of critical nucleus formation.

2.2.2.2. Growth and removal of inclusions

Critical nuclei are in unstable equilibrium with the parent phase (ΔG is maximum). Depending on the time evolution of the supersaturation S, they either grow ($r > r_c$) or resorb ($r < r_c$). This growth mechanism is governed by the minimisation of the free energy change of the system and, therefore, acts on two fronts (Eq. (2.8)): the suppression of the supersaturation through reaction and the minimisation of the surface energy. Since both nucleation and growth are affected by the supersaturation of the melt, they occur simultaneously and cannot be separated. Figure 2-5 represents the time evolution of the supersaturation degree after the addition of the deoxidiser according to Suito and Ohta [49]. After the addition of the deoxidant, the supersaturation of the melt increases fast. Once the critical value S^* is reached, nucleation takes place and the new nuclei grow by diffusion of oxygen and deoxidant to the surface of the inclusion and Ostwald ripening. The supersaturation passes through a maximum and decreases with time as a result of the consumption of the oxygen and deoxidant through nucleation

and growth. Nucleation ceases when the supersaturation is driven down to S^*.

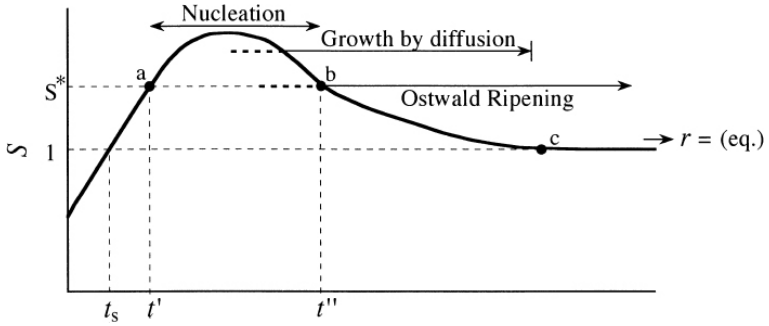

Figure 2-5: Variation of supersaturation degree with time after deoxidant addition, showing the co-existence of nucleation and growth (from Suito and Ohta [49]).

Without collisions between the inclusions, the contribution to inclusion growth is limited to growth by diffusion of oxygen and deoxidant to the surface of the inclusion and Ostwald ripening or coarsening. Growth by diffusion of deoxidant and oxygen to the inclusion acts as long as supersaturation is available ($S > 1$) and is controlled by the transport of oxygen and deoxidant to the inclusion. Diffusion-controlled growth of a spherical particle is approached using Wert and Zener's formula [50], assuming that growth is controlled by the diffusion of <u>O</u> to the inclusion [49, 51-53]:

$$\frac{dr}{dt} = \frac{D_O}{r}\frac{\left(C_\mathrm{O} - C_\mathrm{eq}\right)}{\left(C_\mathrm{p} - C_\mathrm{eq}\right)} \tag{2.22}$$

where r is the radius of the inclusion at time t, D_O the diffusion of <u>O</u> in liquid Fe, C_O, C_eq and C_p are the oxygen content (kg m^{-3}) in, respectively, the bulk Fe, at equilibrium and in the oxide inclusion. Wert and Zener [50] derived t_{90}, the time for the inclusion to attain 90% of its final volume:

$$t_{90} = \frac{1}{D_\mathrm{O}}\frac{\left(C_\mathrm{p} - C_\mathrm{eq}\right)}{\left(C_\mathrm{O,i} - C_\mathrm{eq}\right)}\bar{r}_\mathrm{f}^{\,2} \tag{2.23}$$

where $C_\mathrm{O,i}$ is the initial O content (kg m^{-3}) in bulk Fe before deoxidation and $\bar{r}_\mathrm{f}$ is the mean inclusion radius after growth by diffusion. In the case of Al deoxidation of liquid Fe containing initially 500 ppm <u>O</u> ($C_\mathrm{O,i}$ = 3.5 kg m^{-3})

with a resulting equilibrium O content of 4 ppm (C_{eq} = 28 10^{-3} kg m^{-3}), t_{90} is plotted as a function of $\bar{r}_f$ in Figure 2-6 (with D_O = 10^{-8} m^2 s^{-1} and C_p = 1880 kg m^{-3}). As seen in Figure 2-6, growth of the inclusions by diffusion is achieved very rapidly. Growth by diffusion of oxygen and deoxidant to the surface of the inclusion is limited to a very short period after nucleation as supersaturation decreases rapidly after nucleation.

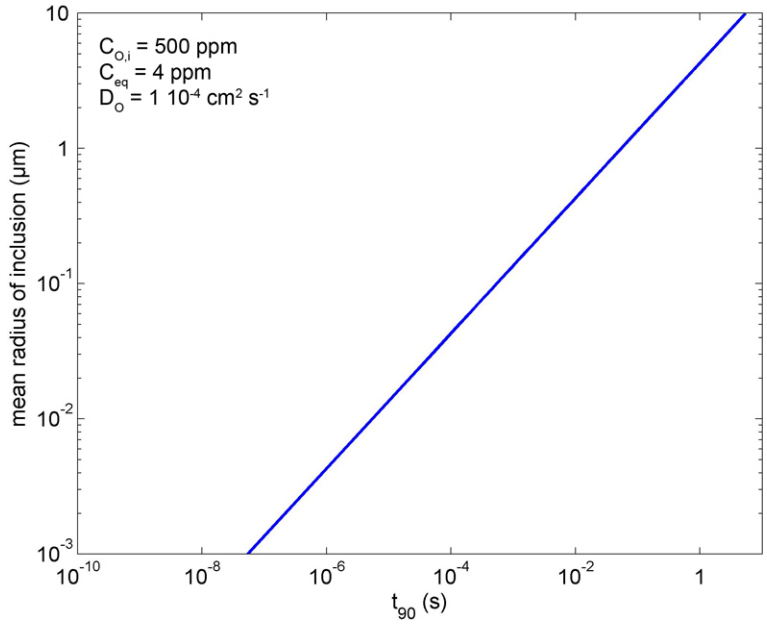

Figure 2-6: Relation between t_{90} and the mean radius of inclusion for inclusion growth by diffusion of oxygen and aluminium to the surface of the inclusion (Eq. (2.23)).

The principle of coarsening is to reduce the interfacial energy contribution to ΔG through the spontaneous growth of large particles (thermodynamically favoured) and the shrinkage of those of smaller size. Ostwald ripening involves a mass transfer from smaller particles to larger ones, resulting in an increase of the average particle size and a decrease in the number of particles with time, while the total volume fraction of particles remains constant. The equation describing the evolution of the particle size with time resulting from Ostwald ripening is derived from the Lifshitz-Slyozov-Wagner theory [51, 53]:

$$\bar{r}^{-3} = \bar{r}_0^{-3} + \frac{4}{9}\frac{2\sigma V_m C_O D_O}{RT\left(C_P - C_O\right)}t \qquad (2.24)$$

where $\bar{r}$ and $\bar{r}_0$ are, respectively, the mean radius of inclusions at time t and before the start of Ostwald ripening, V_m the molar volume of oxide per mol of oxygen, R is the gas constant and T the temperature. With 4 ppm O in liquid Fe, σ equal to 2.3 J m^{-2} and a temperature of 1600 °C, the growth rate is estimated at 0.0002 μm^3 s^{-1}. With the initial conditions (500 ppm O) and σ reduced to 1 J m^{-2}, the growth rate increases barely to 0.009 μm^3 s^{-1}. The contribution of Ostwald ripening to inclusion growth is very limited at the beginning of the deoxidation process and contributes to growth after a long period of time.

When two or more Al_2O_3 inclusions collide, they tend to coalescence or agglomerate if the interfacial tension between the particle and the melt is high [51]. The coagulation-agglomeration process between inclusions contributes to the growth of inclusions. Several collision growth mechanisms are considered: Brownian collisions, Stokes collision, gradient collisions and turbulent collisions. The rate of particle collisions is mainly governed by the presence of turbulences in the melt, giving rise to turbulent and gradient collisions, and by the sizes of the inclusions, generating Brownian and Stokes collisions.

The buoyancy forces leading to the settling velocity u_p are driven by the particle size (diameter d) and the difference between the particle density (ρ_P) and the liquid density (ρ_L), as represented by relation (2.25), also known as the Stokes equation.

$$u_p = \frac{d^2}{18\mu} g\left(\rho_L - \rho_P\right) \tag{2.25}$$

where μ is the absolute viscosity of the liquid (taken as 3.5 10^{-3} Pa s) and g the gravitational acceleration (9.81 m s^{-2}). The velocity, u_p, of a 2 μm Al_2O_3 inclusion is estimated at 1.93 10^{-6} m s^{-1} using Eq. (2.25). In liquid steel, oxide inclusions move towards the melt surface with a velocity proportional to their size squared, since they have a lower density compared to the melt. Larger inclusions, with a higher settling velocity, collide with smaller ones during their ascension to the melt surface.

Brownian motion describes the random motion of very small particles suspended in a fluid. According to Einstein-Stokes theory on Brownian motion [54], the diffusivity D of spherical particles suspended in a liquid is given by relation (2.26).

$$D = \frac{k_B T}{3\pi\mu d} \tag{2.26}$$

where k_B is the Boltzmann constant and T the temperature. The Brownian motion is, therefore, more active the smaller the particles, the higher the temperature and the less viscous the fluid. The particles move independently and their composition or density have no effect on particle trajectory. The mean value of the displacement λ of the particle in time t is calculated by relation (2.27).

$$\lambda = \sqrt{2Dt} = \sqrt{\frac{2k_B Tt}{3\pi\mu d}} \tag{2.27}$$

For a 0.1 and 1 μm diameter particle at 1600 °C, the mean value of displacement in 1 s is, respectively, about 3.96 and 1.25 μm. The contribution of Brownian motion is therefore limited to the first stage of deoxidation.

Turbulent and gradient collisions originate from the nature of the fluid flow (turbulent or laminar due to convection and stirring). Inclusions follow the liquid steel stream. The formation of eddies in a turbulent flow generates local rapid variations of inclusion velocity and direction relative to others. The collision frequency is proportional to the turbulent energy dissipation ε and the kinematic viscosity of the steel. It increases with the size of the inclusion and ε. Gradient collision arises from the transport of inclusion along different streamlines under laminar flow conditions. The collision rate is proportional to the inclusion size and the velocity gradient perpendicular to the laminar flow.

After substantial growth, inclusions are removed from the metal bath. Inclusion separation is mainly governed by interfacial reactions, in which interfacial tension plays a crucial role [12, 55]. Some of the inclusions are removed to the top slag by buoyancy forces. As expressed in Eq. (2.25), the removal of larger inclusions is more quickly achieved compared to smaller inclusions. The turbulent liquid steel flow may bring the inclusion near the refractory walls where they adhere and remain attached [56]. Also inclusions might attach to a gas bubble during gas stirring [56, 57]. Inclusions attached to the gas bubble are transported to the top slag through bubble flotation. This removal mechanism is enhanced by the non-wetting behaviour of Al_2O_3 inclusions towards liquid steel. As a result, Al_2O_3 inclusions have a larger probability to attach to a gas bubble. Also, they show a tendency to form aggregates through a sequence of inclusion attraction and coagulation at the solid/liquid/gas interface, as highlighted by several in-situ studies using a Confocal Scanning Laser Microscope (CSLM) [58-60]. In addition to the

homogenisation of liquid steel, gas stirring in the vessel can be an efficient way to enhance inclusion removal.

2.2.3. From nucleation and growth to inclusion size distributions

Crucial inclusion features, such as size, size distribution and morphology, are determined by the conditions during the earliest stages of precipitation and growth. These processes depend on many chemical and physical parameters that control and strongly affect the formation of the nuclei, the growth of the inclusion and the collision-coagulation behaviour. During the deoxidation process, depending on the conditions, one of the growth mechanisms can be more important than the others and influence the size distribution of the inclusion population, as well as their morphology.

The formation of a new phase (or a new inclusion) begins by the nucleation stage, during which new nuclei of given size are formed. The nucleus becomes thermodynamically a new phase when the growing nucleus has distinct properties relative to the bulk mother phase, such as well-defined structure, composition or density. The conditions prevailing during the nucleation stage will determine the size of the nucleus. As a result, the size distribution develops during nucleation, once particles with sizes equal to or larger than that of critical nucleus appear and grow [61].

At constant supersaturation, the critical size of nuclei is constant (Eqs. (2.9) and (2.10)). Under these conditions, the number density of nuclei decreases with the nuclei size and no maximum appears in the size distribution. In a closed system, the mother phase becomes depleted as the nucleation progresses, which results in a decrease of the supersaturation with time (Figure 2-5). The decrease in supersaturation was reported to proceed faster with an increase of the initial supersaturation [62]. As a result of the decrease in supersaturation, the critical size of nuclei increases (Eqs. (2.9) and (2.10)). The size distribution of nuclei will therefore evolve with time and initial supersaturation, showing different features compared to the standard model using constant supersaturation. After a short time (~3 μs), the mathematical model of Kozisek [62] reveals that the decrease in supersaturation influences the formation and growth of the nuclei. A maximum in the number density of nuclei appears due to an increase of the critical nuclei size as the mother phase becomes depleted. The kinetics of nuclei formation are rendered more complicated owing to the depletion of the mother phase. With an increase of the critical nuclei size, Kozisek [62] shows that the nucleation process is slowed down whereas the growth process is accelerated.

The contribution of the different mechanisms to inclusion growth is illustrated in Figure 2-7 from the study of Lindborg [51], which was dedicated to Si deoxidation and the collision between SiO_2 inclusions. The time evolution of the growth mechanism contribution in case of Al deoxidation is similar.

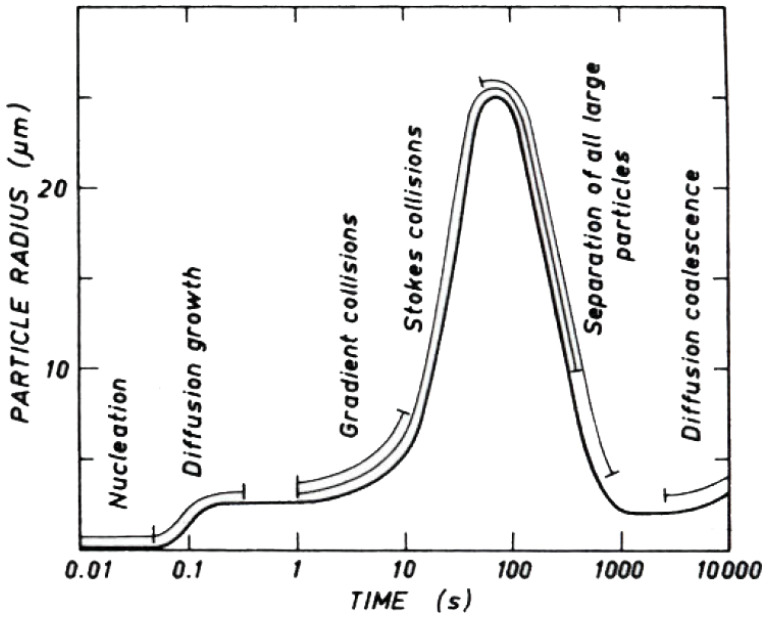

Figure 2-7: Schematic diagram over the typical size of silica particles during the deoxidation period (from Lindborg and Torsell [51]).

Precipitation and the reduction of supersaturation are achieved within 1 to 10 μs after the deoxidation [51, 63, 64]. Few studies were dedicated to the observation of the early stage of deoxidation. Numerical approaches [51, 63, 64] give insight to predict the size distribution of inclusions from the nucleation stage. The predictions reveal that, at the initial stage, the growth of inclusions is mainly determined by O and deoxidizer diffusion and Ostwald ripening. Models of size distribution predictions reveals that, after 1 μs, Brownian collision contribution is dominant when the particle size attains $1\sim3\ 10^{-3}$ μm.

Deoxidation is a fast and complex process, demanding experimental challenges to be able to observe the inclusions soon after nucleation. By measuring the inclusion size distribution from 60 s after the nucleation stage, Suito [49] identified the interfacial energy between oxide and liquid Fe as a critical parameter in predicting the inclusion size, enabling to modify the spread of the size distribution by selecting appropriate deoxidant and

supersaturation conditions. Due to the high interfacial energy between Al_2O_3 inclusion and liquid Fe, the size distribution is broader with Al deoxidation compared to Si/Mn deoxidation. Ohta and Suito [53, 65] investigated the growth and the characteristics of the size distribution of Al_2O_3 inclusions, among others, below 1 μm under no fluid flow. They concluded that growth by Ostwald ripening was the dominant mechanism and was largely influenced by the dissolved O content. The coarsening rate of Al_2O_3 inclusions is high owing to the large spread of the Al_2O_3 inclusion size distribution. Beskow [66] studied experimentally the homogeneous nucleation and agglomeration of Al_2O_3 inclusions in a melt quenched at 5, 15, 30 and 120 s after Al deoxidation. Homogeneous nucleation of Al_2O_3 took place in the areas supersaturated with Al, resulting in the formation of small Al_2O_3 inclusions 5 s after deoxidation, followed by agglomeration with longer time. The effect of the amount of Al addition on the formation of the small spot-like inclusions was more pronounced compared to the initial O content. It was explained by the slow mass transfer process of Al under limited convection, causing a much higher local supersaturation. Wakoh and Sano [67] measured the initial size distribution of Al_2O_3 inclusions by sampling the deoxidized steel 1 s after the reaction. They observed larger inclusion size with increased O content and concluded that inclusion growth under these conditions was controlled by O diffusion.

The contribution of turbulent collision to inclusion growth becomes significant from 1 to 2 s, once the inclusion size reaches about 0.3 to 0.5 μm. This collision mechanism results in a fast increase of the average inclusion size and of the number of large inclusions. The frequency of turbulent collisions becomes significant as the number of large inclusions increases. Growth due to turbulent collisions is often considered as the dominant mechanism [51, 56, 68] after the deoxidation process. Experimentally, Karasev [69] and Braun [70] showed that mixing and turbulences have a significant impact on the size distribution thanks to the formation of aggregates or clusters of Al_2O_3 inclusions. Compared to turbulent collisions, the contribution of gradient collisions was found to be limited [56, 71], as this mechanism applies only next to walls.

Also Stokes collision mechanism is reported to contribute significantly to inclusion growth. However, this mechanism occurs when the difference in inclusion size is large, implying that the inclusion size distribution must have reached a significant width before this mechanism can contribute noticeably. The inclusion removal process acts mainly on the right hand side of the inclusion size distribution by removing large inclusions. They have a higher settling velocity and higher probabilities to be caught by a gas bubble, to collide with other inclusions and to adhere to refractory walls. By promoting turbulences and collisions between inclusions, stirring is a very efficient way to enhance inclusion removal [70].

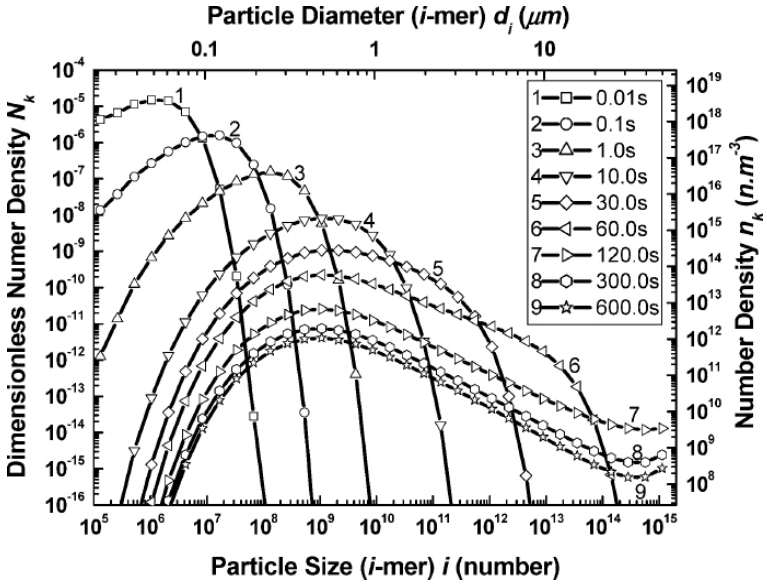

Figure 2-8: Time evolution of particle size distribution based on the static model of Zhang [63]. The model includes nucleation, Ostwald ripening and collisions growth (Brownian, Stokes, gradient and turbulent collisions).

The size distribution of the inclusion population after deoxidation is the result of a combination of processes of nucleation, growth and removal. Each size distribution is unique and represents the history of the inclusion population. Figure 2-8 shows the predictions, according to the static model of Zhang [63], of the size distribution of Al_2O_3 inclusions after deoxidation of steel containing initially 300 ppm O. By considering the theories of homogeneous nucleation, growth by diffusion and the mechanisms of collision and coalescence, it demonstrates that one or more of these growth processes dominate the growth of inclusions at various stages of the process, involving significant changes in the inclusion size distribution.

It is interesting to note that these calculated size distribution curves (Figure 2-8) follow the same general tendency as those obtained experimentally [49, 65, 67, 72, 73]. The combination of all processes yields size distributions that can be satisfyingly modelled by lognormal functions [16, 49]. The size distribution is initially narrow, with a maximum of the number density located at small inclusion size. With time, the size distribution become broader and is shifted to larger inclusion sizes. The position of the maximum number density is also shifted to the right, while its value decreases. Recently, the static model of Zhang [63] was extended to a dynamic model [74], which considers inclusion removal, time and space dependence of

temperature, concentration and fluid patterns in the ladle produced by a Computational Fluid Dynamics (CFD) model. The calculated inclusion size distribution was consistent with experimental size distributions sampled at a specific location in the ladle.

2.2.4. Interpretation of the size distribution

The size distribution is an important tool as it provides a snapshot of the system in time and is shaped by nucleation and growth mechanisms. It is commonly used in the interpretation in nature and in crystallisation experiments to estimate important parameters, such as thermal history, growth and nucleation rates, when these phenomena cannot be observed in-situ and good estimates of the interfacial energies, density of nucleation sites and the free energy of critical nucleus formation are not available. The crystal size distribution (CSD) analysis uses population balance modelling, in which the population density of crystals is the fundamental variable. This technique was developed in the chemical engineering industry in 1971 by Randolf and Larson [75] and applied to geologic systems by Marsh [76]. In this approach, the distribution of observed crystal sizes in a sample is combined with conservation differential equations describing the balance of crystal numbers growing into and out of a size class in a time Δt. The general form of the population balance equation of numbers of crystal in a volume V is given in Eq. (2.28):

$$\frac{\partial(Vn)}{\partial t} = \frac{\partial(\varphi Vn)}{\partial d} + (k_{\text{in}} - k_{\text{out}})n \tag{2.28}$$

where n is the crystal population density (number of crystals per given size class per unit of volume), φ the growth rate, d the characteristic crystal size, k_{in} and k_{out} are, respectively, the source terms (gain of crystals from segment of the size distribution) and sink terms (loss of crystals to the segment) involving nucleation, breakage and agglomeration events. By imposing various restrictions on the system, various solutions can be obtained from Eq. (2.28).

Marsh [76, 77] established theoretical basis for CSD for both batch and open systems under various kinetic scenarios and showed that the shape of the CSD can reveal the operation of several different processes during crystallisation. The analytical results were used to study and interpret observed CSDs of natural igneous systems. CSDs of natural rocks often show remarkably smooth log-linear trends with negative slopes. According to Marsh's investigations, the downward slopping log-linear form of the CSD is due to either an exponential increase of the nucleation rate with time

with a constant growth rate, or a constant nucleation rate with an effective growth rate increasing exponentially with crystal size. The former is the most important and yet debatable assumption of Marsh's model. Under the particular circumstances of steady state nucleation and size independent growth rates [76, 78], simplification and integration of Eq. (2.28) produces an exponential distribution $n(d)$ of the crystal population density:

$$n = n_0 \exp\left(\frac{-d}{\varphi\tau}\right) \tag{2.29}$$

where n_0 is the population density of nucleus-size crystals and τ the average crystal residence time in the system, i.e. time scale available for growth. Using Marsh's assumptions, a plot of $\ln(n)$ against crystal size d is linear with slope $1/\varphi\tau$, from which φ may be evaluated provided that τ is known, and the intercept provides $\ln(n_0)$, as illustrated by the straight line in Figure 2-9. Under this specific circumstance, the slope gives a direct access to the nucleation history.

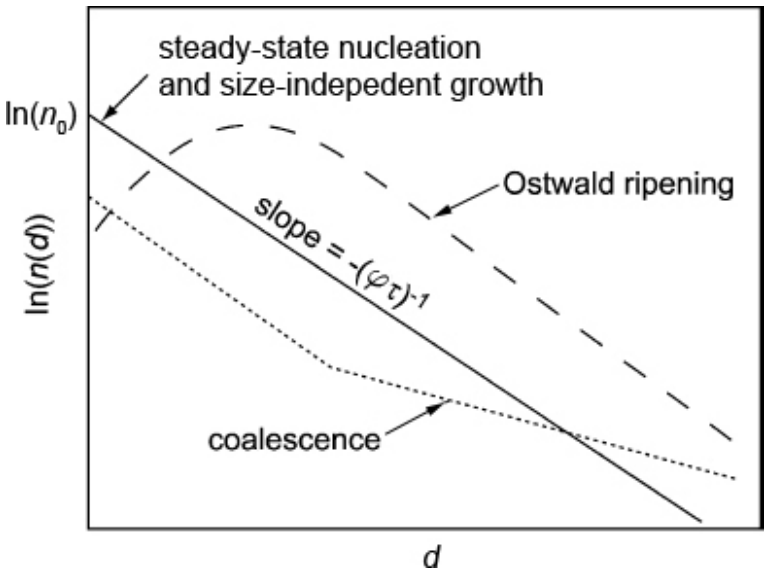

Figure 2-9: Representation of the crystal size distribution in a $\ln(n(d))$ versus d following the model of Marsh. The solid line represents steady state nucleation and constant growth rates, while dotted lines and dashed lines show, respectively, coalescence and Ostwald ripening processes causing deviation from the straight line (adapted from Blower *et al.* [79]).

Variations in growth rate or nucleation with time will affect the shape of the CSD. Following Marsh's interpretations [76, 77], kinked CSDs, as represented by the dotted line in Figure 2-9, may result from sudden changes in exponential nucleation rate, which are reflected by changes in slope, or from other growth processes, such as aggregation of small crystals to form larger ones.

CSDs describing numerous other physical systems do not show a straight line (log-linear) when plotted as ln(n) versus d, but often exhibit concave down (lognormal) curves (dashed line in Figure 2-9). Several processes were proposed to be capable of producing lognormal CSDs. The most common is Ostwald ripening [76, 77, 80], which consists in the growth of larger crystals at the expense of smaller ones. Size-dependent growth was suggested to yield lognormal CSDs [61, 81-83] and was experimentally demonstrated [83]. As outlined by Eberl [82], lognormal shaped size distributions cannot be generated by a constant growth rate, unless the nucleation rate varies through time, e.g. exponential nucleation rate followed by Ostwald ripening at the end of the process [77]. The latter is in contradiction with general observations that nucleation ceases after a relatively short time as supersaturation disappears. Also Ostwald ripening process may follow different kinetics depending on the mineral species and mostly affects smaller crystals [84]. Eberl *et al.* [82] showed that size-dependent growth according to the Law of Proportionate Effect can generate and maintain the log-normal shape of the CSDs, giving more robust description and consistent interpretation of experimental and natural CSDs. Crystal fragmentation and dissolution-reprecipitation events may lead to lognormal-shaped CSDs [85, 86].

The interpretation of CSDs, the deduction of quantitative information on nucleation and growth rates, and the evaluation of the relative importance of chemical reactions from the shapes of CSDs are complex tasks. Many processes that shape the CSD curve are proportionate and selective, and may affect a limited range of crystal sizes, creating distortions and curvatures in the CSDs. Growth and nucleation histories are not simple, and, in most cases, cannot simply be described by Eq. (2.29). Simulations of CSDs using various crystal growth mechanisms can reveal their effects on the CSD shape [61]. The simulation results can be used to provide valuable information on the growth and nucleation histories and growth mechanisms from measured CSDs. This method of interpreting size distributions has not been applied to inclusions in steel, though inclusion nucleation theories and inclusion growth mechanisms are used to simulate inclusion size distributions (see previous section). In section 4.2.3 in Chapter 4, the method to draw a size distribution plot of an inclusion population from a measured sample is described in detail.

2.3. Inclusion formation during solidification

The supersaturation condition related to inclusion formation can be obtained by changing the temperature [34]. During cooling of liquid Fe or steel, the values of the reaction equilibrium constant K in Eq. (2.2) are modified. As oxidation reactions are exothermic, a decrease in temperature causes the decrease of K, favouring the formation of oxide inclusions. The evolution of the oxide phase stability domains must consider the temperature dependence of all thermodynamic parameters, such as the interaction parameters. As seen in Figure 2-4 for the $\underline{Al}$-$\underline{O}$-Al_2O_3 equilibrium, the equilibrium line is shifted to lower $\underline{O}$ and $\underline{Al}$ contents with decreasing temperature from 1823 °C to 1600 °C, providing a larger Al_2O_3 stability domain.

During solidification of steel, the difference in solute solubility between the solid and liquid phases may initiate the formation and growth of inclusions. The remaining liquid phase during solidification becomes supersaturated owing to the enrichment of solute elements, such as O, N and S. New inclusions precipitate and grow once both the equilibrium value and favourable kinetic conditions are obtained. Typically, Al_2O_3, SiO_2, TiO_x, MnO, TiN, AlN and sulphide inclusions, such as MnS, may precipitate during cooling. The size of these inclusions is in general less than 10 μm [12, 87-89].

Experimental [45, 88-95] and mathematical [96-101] studies were initiated to control the precipitation during solidification in order to obtain cleaner steels and to effectively utilise fine particles in steel. The latter, which is called “oxide metallurgy” (see section 2.5.2), uses methods of deoxidation with Mn, Si, Ti, Mg, or combination of several deoxidisers in order to precipitate fine oxides during solidification.

Modelling of precipitation and growth of non-metallic inclusions is intensively used to study the solidification of steel. Mathematical models [96-103] are dedicated to the prediction of inclusion size and composition during solidification processes. Most of them are based on thermodynamic and kinetic analyses and consider micro-segregation during solidification. The results of the studies generally agree upon the fact that growth of the inclusion is controlled by diffusion and by interfacial reactions. In the experimental studies of Suzuki [88] and Ohta [92], it was concluded that Ostwald ripening was the dominating growth mechanism of deoxidation particles.

During the solidification, the inclusions interact with the solid metal phases and show different behaviour depending on the inclusion and steel compositions, and on the cooling rate. Al_2O_3 particles are pushed to the

region of final solidification, while MgO and ZrO_2 particles are engulfed [92]. Since these processes are driven by interfacial energy and wetting behaviour, the oxygen and sulphur content in steel have a significant effect on engulfment and pushing of the particles [45]. Because primary deoxidation products can serve as nucleation site for the precipitation of sulphide inclusions, a uniform dispersion of these particles during cooling is an important aim.

2.4. Reoxidation of liquid steel

Steel reoxidation is one of the major causes for the formation of exogenous inclusions after the refining stage. It is a complex process that can occur at different places at the same time after the deoxidation stage. Although the sources of reoxidation are numerous, the process is driven by the difference of oxygen potential between deoxidized liquid steel and its environment. Deoxidizing elements present in liquid steel, such as Al, are preferentially oxidized, generating unintended inclusions. These exogenous inclusions are released in liquid steel, deteriorating the internal steel cleanliness drastically. The reoxidation mechanisms are mainly investigated in the ladle and in the tundish. As regards to the ladle (Figure 2-10), the oxygen sources considered relevant in the reoxidation process of liquid steel are the air atmosphere, ladle slag, ladle glaze, alloying purity, and refractory lining materials [12, 15, 20, 104]. In the tundish, the following factors are responsible for steel reoxidation [105]: air ingression due to leaks, at joints or breaches made in the tundish and/or through the refractory brick, exposure with air at tundish inlet and bath surface; ladle well packing material; tundish cover powder; tundish residual slag and ladle slag; and tundish refractories.

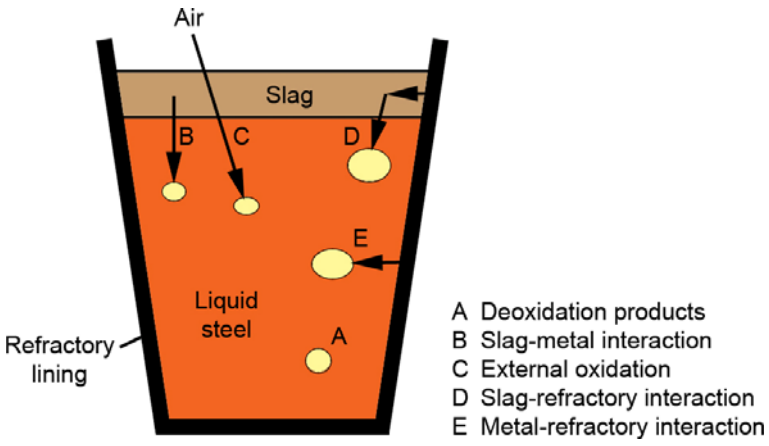

Figure 2-10: Sources of inclusions in the ladle (adapted from Dyson *et al.* [104]).

2.4.1. Reoxidation by exposure to air

Exposure of molten steel to air leads to the formation of oxides at the surface of the liquid metal (Figure 2-10, arrow C). Studies dedicated to steel reoxidation through gas-steel reactions [106-110] reported mainly on the estimation of the oxidation rates of the steel. Observations on inclusion formed under reoxidation are less numerous, although differences in kinetics and thermodynamic driving forces can lead to important changes. Sasai and Mizukami [109] studied the oxidation rate of Al-killed molten steel in still state and under stirred conditions. They showed that the oxidation rate is not controlled by an interfacial chemical reaction process at the gas-oxide or at the oxide-metal interface, but by diffusion processes. Depending on the presence of a continuous and uniform oxide film on the liquid steel, the oxidation rate is controlled by the diffusion of oxygen in the oxide film (still state) or by the diffusion of O_2 gas in the gas phase (stirred melt). In case of a pure Fe melt in contact with pure O_2 gas and O_2-bearing gases, Emi [106, 107] and Sasai [109] reported that the oxidation rate is dependent on the p_{O_2} and controlled by the diffusion of O_2 in the gas phase. The gaseous oxidation of more than one element in liquid Fe involves thermodynamic relations that influence the reaction rates. When the content of the elements in the alloy phase are relatively low, diffusion of these elements can become the rate limiting step [111, 112]. Wang and Beckermann [113] developed a mathematical model to predict the composition of reoxidation inclusions arising from liquid steel being exposed to air during the transfer from ladle to mould. With the oxygen absorption and steel reoxidation, the steel and subsequently the inclusion composition change. In the case of high Al and low Al carbon steels, the inclusions consist only of Al_2O_3 at low absorbed oxygen. SiO_2, then MnO and FeO are predicted to be present in the inclusions with increasing absorbed oxygen from the gas phase. Their predictions were in good agreement with experimental measurements of inclusion compositions for various steel grades.

A number of recommendations are given in order to limit reoxidation of the steel by exposure to air in the ladle and tundish [13, 20]. The steel can be protected by shrouding the nozzles with Ar gas for the transfer from ladle to tundish and tundish to mould, purging the tundish with Ar gas prior to ladle opening, using a protective cover for the tundish, guarantee tightness of refractory pieces and assemblages, carefully sealing joints in the shrouds, performing Ar injection to pressurize the shrouds, injecting Ar at the stopper rod or sliding gate, controlling the stirring intensity to avoid the formation of a slag eye (covering slag is pushed to the side due to the gas bubbling, forming an open-eye of molten metal exposed to atmosphere), using tight air

covering flux, employing high viscosity and surface tension slags for ladle and tundish, etc.

2.4.2. Reoxidation caused by slag

Interactions between steel and slag can lead to the formation of exogenous inclusions in liquid steel (Figure 2-10, arrow B). The reoxidation mechanism involves the presence of oxide compounds in the slag phase that are less stable than Al_2O_3. These oxides, such as FeO, MnO and SiO_2, can be reduced by Al or another strong deoxidant dissolved in liquid steel (Eq. (2.30) [12]).

$$1.5\ SiO_2\ /\ 3\ FeO\ /\ 3\ MnO + 2\ \underline{Al} = 1.5\ \underline{Si}\ /\ 3\ \underline{Fe}\ /\ 3\ \underline{Mn} + Al_2O_3. \quad (2.30)$$

The formation of inclusions by reoxidation was investigated for ladle slag [114-119] and tundish slags [118, 120, 121]. According to Eq. (2.30), steel reoxidation and inclusion formation would take place at the metal/slag interface. During the reoxidation process, the composition of the steel and the slags can be significantly altered. The steel is gradually depleted in Al and becomes enriched in Si and/or Mn. Conversely, the slag is progressively enriched in Al_2O_3 and depleted in SiO_2, Fe_tO and/or MnO.

Sun [118] and Park [120] explained the reoxidation process by considering that reoxidation may occur in the bulk metal owing to the phenomenon of oxygen supersaturation in the metal. The oxygen potential in Al-killed steels is very low according to the equilibrium relations (Figure 2-4). In the initial stage of the reoxidation process, the reactions take place at the slag/metal interface, as described by Eq. (2.30). As the reoxidation progresses, a reduction or dissociation of SiO_2, FeO and/or MnO can take place at the slag/metal interface due to the lower oxygen potential at the metal side compared to the slag. Oxygen is thereby provided to the metal and transported from the metal/slag interface into the bulk, where it can further react with Al in the bulk metal. This mechanism was proposed to explain the formation of Al_2O_3 inclusions in the bulk metal [118] and, in the case of reoxidation of Ti-bearing Al-killed steels [120], the formation, in the bulk metal, of two-layer structure inclusions, consisting of an Al_2O_3 core surrounded by complex Al-Ti-O oxide.

A sound slag practice is therefore necessary in order to limit the contribution of the slag to steel reoxidation. It is recommended to lower the MnO, Fe_tO and SiO_2 contents in ladle, tundish and mould slags to less than 1 wt%.

Moreover, an increase of the CaO/SiO_2 ratio results in a decrease of the number of Al_2O_3 inclusions. The latter is explained by an enhanced assimilation of Al_2O_3 in the slag, as a result of high dissolution rate and good wetting behaviour, combined with a decrease of the activity coefficients of MnO, Fe_tO and SiO_2 in the slag [119].

2.4.3. Reoxidation caused by refractory materials

Refractory lining materials may contribute to inclusion formation both by mechanical and chemical erosion (Figure 2-10, arrows D and E). Mechanical erosion is observed in areas with turbulent flow and high shear velocity, causing the detachment of refractory macro-inclusions into liquid steel. Depending on the melt chemistry and on the refractory type and quality, liquid steel can be contaminated by a direct reaction between the steel and the refractory (Figure 2-10, arrow E) or by indirect reactions via the slag phase [122] (Figure 2-10, arrow D). In contact with Al-killed low alloyed steel, residual water in tundish refractory material, SiO_2, MnO and Fe_tO present in dolomite and MgO-based refractories can be directly reduced by Al in liquid steel. Moreover, the low activities of dissolved O, Si and Mg in liquid steel may initiate the dissociation of these components and the transfer of O, Si and Mg from the refractory to the liquid steel [13, 122, 123]. Oxide inclusion consisting of spinel ($MgO \cdot Al_2O_3$), $CaO \cdot Al_2O_3 \cdot MgO$ and silicate are formed at the steel/refractory interface.

In the case of oxide-graphite refractories, refractory oxides, such as MgO and SiO_2 can be directly reduced by the refractory C phase into gaseous products (Mg(g) and SiO(g)) that diffuse out of the refractory and form liquid or solid oxides at the steel/refractory interface [122, 124]. In addition, the decarburisation of the refractory hot face leads to a weakened brick structure, which facilitates erosion, and to an increase of the refractory permeability [122].

The interaction between the refractory and the slag can contribute to the formation of inclusions in liquid steel (Figure 2-10, arrow D). The mechanism consists in the penetration and the attack of the refractory by the slag and the fluxing of the refractory hot zone, causing the breakdown of the refractory structure [104]. The interaction between infiltrated slag and refractory components results usually in the formation of low melting point phases that initiate erosion of the refractory grains into the slag. The elements constituting the brick, including O, are leached out and may promote oxide formation through reoxidation of the liquid steel.

To avoid reoxidation of the liquid steel, it is therefore crucial to choose non-reactive refractory linings with a high resistance to wear. The chemical stability of the refractory should be investigated both with the slag systems and with the steel grade. Ladle wall for clean steel production is made of high quality refractories, such as high Al_2O_3 bricks with low SiO_2 contents [13]. To reduce reoxidation, the refractories should be fired at 1200 °C to remove water [123].

2.4.4. Reoxidation by ladle glaze

When draining the ladle, a film of slag adheres to the ladle wall and penetrates into the ladle refractory pores (Figure 2-11 (a)). This slag film, known as ladle glaze [125-133], solidifies on the ladle wall during cooling. During the next heat, the ladle glaze melts, penetrates further in the refractory and reacts with the lining components, as the glaze is generally liquid at steelmaking temperature (Figure 2-11 (b)). The outer layer of the glaze is partially removed in the liquid steel after filling of the ladle, resulting in the formation of inclusions. In addition, the glaze was found to react with the liquid steel [131, 132] (Figure 2-11 (c)). SiO_2, Fe_tO and/or MnO contained in the glaze are reduced by Al in the liquid steel, with the formation of inclusions (Eq. (2.30)). The reaction with the refractory components causes a modification in inclusion chemistry compared to the glaze composition. As the refractory lining is subjected to fluxing by the ladle glaze, the refractory structure is broken down, causing the detachment and the release of refractory grains into liquid steel under strong stirring conditions [128, 129] (Figure 2-11 (d)). The contribution of the glaze to the number of inclusions is increasing with the ladle treatment duration [128] and the ladle age [128, 130], as the infiltrated layer grows thicker and becomes more porous, enhancing its detachment. This mechanism was confirmed as a source of inclusions in liquid steel by using BaO tracers in ladle slag [134]. Inclusions containing BaO were found in heats processed with the same ladle where the BaO-doped slag had been previously added.

Tripathi [130] concluded from the investigation of industrial samples taken at various stages of the ladle treatment that the ladle glaze was the most important source of inclusions in tool steel. In order to control the glaze layer, Thunman [133] indicated that the composition of the ladle slag and the cooling rate of the glaze can significantly influence the composition and the structure of the ladle glaze. Also, the studies of Beskow [128, 129] emphasized the importance of optimized stirring conditions, and degassing and flotation time on the number of inclusions supplied by ladle glaze.

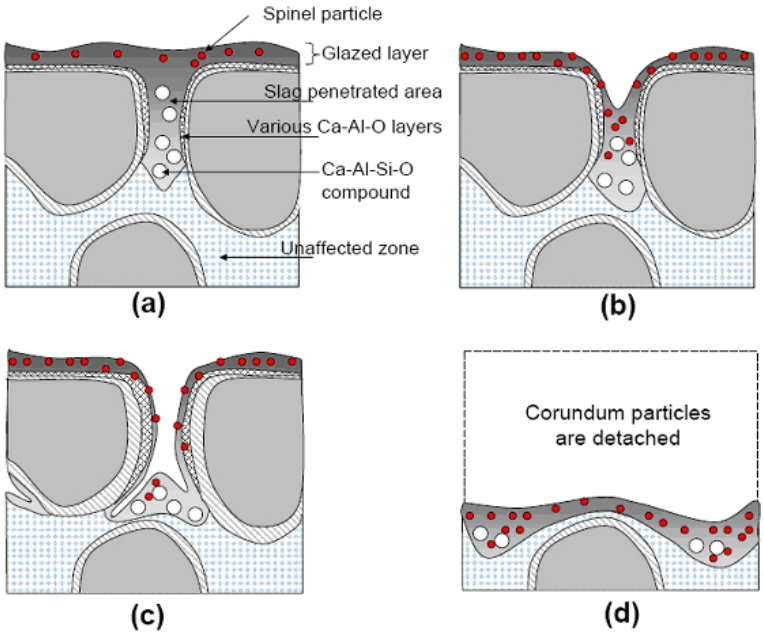

Figure 2-11: Erosion process of the glazed refractory of a high alumina refractory lining during the secondary steelmaking process. (a) Formation of glazed refractory, (b) pitting of glazed refractory, (c) severe erosion at the interface of corundum particle and spinel matrix, and (d) detachment of corundum particle barrier layer [135].

The identification of the origins of exogenous inclusions is often a difficult task, requiring sound knowledge of the composition of the different materials in contact with liquid steel as well as of the thermochemistry of the possible reactions taking place during steel processing.

2.5. Inclusion engineering

The occurrence of non-metallic inclusions is inevitable during the steelmaking process. The deoxidation of liquid steel is an important and inevitable step, leading to the formation of inclusions. As described in section 2.1.2.2, two main factors are responsible for the deterioration of the steel quality and productivity caused by non-metallic inclusions [14]:

- Geometrical factors: size, shape, size distribution and volume fraction of inclusions;
- Property factors: deformability, elasticity modulus at various temperatures, coefficient of thermal expansion.

It is therefore of primary importance to control both factors in order to minimize the damage to the steel properties. Inclusion control is classified into two categories: the minimisation of macroinclusion number and inclusion modification.

2.5.1. Minimization of macroinclusion number

Large inclusions, called macroinclusions, are the main responsible for the problems during casting and for the damages to the steel properties and should be eliminated. The design and operations in the ladle and tundish should be improved to minimize macroinclusion formation and to remove effectively inclusions.

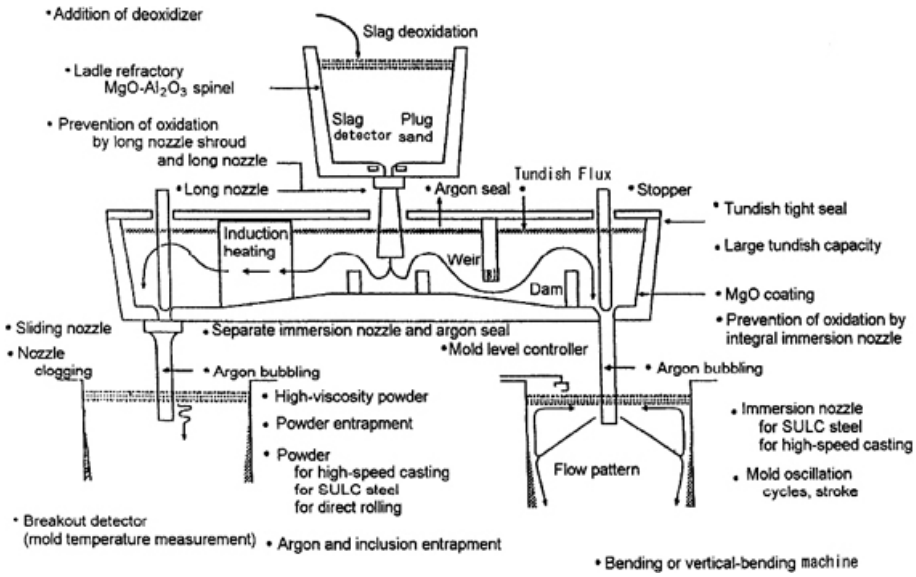

Figure 2-12: Continuous casting system (ladle, tundish and moulds) with all devices and precautions for casting clean steel (SULC = Super Ultra Low Carbon steel) [10].

As seen in Figure 2-12, Clean Steel technologies are developed and introduced during the ladle and tundish operations to limit steel reoxidation and to enhance inclusion removal before the steel is teemed in the mould. As discussed earlier, these include appropriate choice of the slags, improvement of the ladle, tundish and nozzle refractories, use of long nozzle, inert gas shrouding, melt flow control devices, temperature control, etc. [10]. Steel deoxidation is generally performed in two stages [14]. Deoxidizers are first added during taping in the ladle, where efficient stirring promotes inclusion

growth and removal and quickly homogenise the melt bath. The second addition is performed in the ladle furnace, in the CAS-OB or in the vacuum degasser where gentle stirring is sufficient to achieve a good deoxidation. At the end of the process, gentle purging should be conducted to avoid slag entrapment, exposure to air and refractory erosion prior to steel teeming.

In practice, the removal of all macroinclusions is difficult to achieve without excessive costs. Transient period in the continuous casting process, such as ladle opening, ladle change between two heats, or ladle emptying creates disrupted conditions of the steel flow, promoting macroinclusion formation through steel reoxidation and slag entrapment. Also the size distributions after deoxidation stage (Figure 2-8) show that a large number of fine inclusions remain in the liquid steel after deoxidation. These inclusions are transported with the steel flow, collide and coalesce to form large aggregates. Upon late formation, these aggregates have no time to float out of the melt, causing casting problems and loss of final product quality. The key is to determine how to reduce the harmful effects of the residual inclusions on the steel product.

2.5.2. Inclusion modification

To be able to produce high performance steels, inclusions engineering was developed. The latter is based on two alternative approaches to inclusion removal. The first approach consists in the minimisation of the harmful effect of the residual inclusions on the steel product by modifying, in the liquid steel, their chemical composition towards harmless compounds. The latter requires good knowledge of how non-metallic inclusions influence steel properties in order to select the appropriate inclusions to achieve the desirable properties. The last step involves the adjustment of the process parameters to obtain these inclusions.

Several examples of effective inclusion modification can be found. Sulphide inclusions are not detrimental to fatigue since their coefficient of thermal expansion is larger than of the steel matrix. Encapsulating Al_2O_3 inclusions with a layer of MnS reduces the detrimental effect of Al_2O_3. It requires the control of the sulphur content to reach a minimum S/O ratio of the duplex oxide-sulphide inclusions [6]. The composition of non deformable inclusions can be modified towards low melting point compounds. Owing to their higher deformability, the modified inclusions become elongated during hot rolling, forming long stringers. During cold rolling, the modified inclusions are brittle, resulting in the breaking of the thin stringers into small pieces that are not detrimental to steel properties [10]. As a third example, Si/Mn deoxidation can be performed as an alternative to Al deoxidation for the

production of ultra clean steels [136]. With an adequate steel chemistry, Si/Mn deoxidation results in the formation of low melting point manganese silicate glass. Owing to their non-crystalline (glassy) structure, these inclusions have a glass transition temperature, T_g, at which their behaviour changes from brittle to ductile as temperature increases. By selecting the glass composition so that T_g is below the working temperature, the glassy manganese silicate inclusions are deformable during hot working.

Another example of inclusion modification, which is widely used in secondary steelmaking, is the calcium treatment [6]. In addition to the decrease of the oxygen content in the steel and the improvement of steel desulphurisation, calcium treatment is used to transform solid and harmful Al_2O_3 inclusions into liquid $CaO{\cdot}Al_2O_3(\text{-}SiO_2)$ inclusions. The modification from solid to liquid inclusions at steelmaking temperature provides globular-shaped inclusions, which are less harmful to steel properties and increase steel castability by reducing SEN clogging events. Inclusion modification can be achieved by the addition of rare earth elements, such as Ce. They are strong deoxidizers and desulphurisers like Ca, and can replace deformable MnS into nondeformable rare earth sulphide and oxysulphide inclusions [14, 15, 91]. The inclusion modification results in the improvement of impact toughness owing to the isotropy after hot rolling treatment.

The other approach is to beneficially utilize inclusion to enhance mechanical properties. In contrast with macroinclusions which are detrimental to steel properties, microinclusions or dispersoid, which are in the 1 μm range, can enhance mechanical properties of the steel. This approach, known as Oxide Metallurgy [137, 138], utilises non-metallic inclusions in steel as nucleation sites of acicular ferrite during the austenite to ferrite transformation, leading to a significant increase of the strength of structural steels and the development of tailored microstructures to obtain the desired properties. Oxides such as FeO, MnO, TiO_x, $MnO{\cdot}SiO_2$, $Fe(Mn)O{\cdot}Al_2O_3$, etc. act as nucleation sites for a variety of precipitates such as sulphides, nitrides and carbides [138]. These precipitates inhibit grain growth during hot rolling and thermo-mechanical treatments. The grain refining can be achieved through a strict control of the nature and the size distribution of the nucleating particles [27]. A very fine, narrow size distribution of the nucleating particles should be the aim. Inclusions smaller than 1 μm are inefficient to serve as nucleation sites, whereas larger inclusions are detrimental to steel properties [27]. The influence of non-metallic inclusions on the nucleation of acicular ferrite was reviewed recently by Sarma [139].

Effective inclusion engineering requires accurate knowledge and understanding of the relations between steel chemistry, processing variables and inclusion chemical composition. Thermodynamics and kinetics of the

high temperature chemical reactions occurring between liquid steel, slag, inclusions, refractory and gas phase must be accurately known in order to control the inclusion characteristics and to produce steels with enhanced properties.

2.6. Conclusions

The formation of non-metallic inclusions is inherently part of the steelmaking process. They originate from various sources depending on the physical and chemical interactions between steel, slag, refractory, inclusion and gas phases. Next to the deoxidation process, many investigations indicated that steel reoxidation can contribute significantly to inclusion formation. The presence of non-metallic inclusions can be the source of loss of steel quality and productivity. As a result, steel cleanliness requires the strict control of the amount, composition, size distribution and morphology of non-metallic inclusions. In order to understand how inclusions evolved during the secondary steelmaking and casting processes, the thermodynamics and kinetics of inclusion formation, growth and removal were discussed.

In order to improve steel performance and meet the increasing demand of steel cleanliness, inclusion engineering was developed. By controlling and improving operating practices throughout the steelmaking process, it is possible to reduce the amount of harmful inclusions, to render them inoffensive towards steel properties or even to beneficially utilise them to produce steels with enhanced mechanical properties.

In the next chapter, the various morphologies of non-metallic inclusions will be presented. Also it will be shown how the process variables during the formation and growth of non-metallic inclusions can influence their morphology.

Chapter 3
Morphology of Al_2O_3 inclusions in steel

In Chapter 2, it was highlighted that non-metallic inclusions can strongly influence the performance of steels. The demand for high performance clean steels requires the strict control of inclusion size distribution, composition and morphology. Morphology control is of fundamental importance as it influences, during deformation, the inclusion behaviour relative to the steel matrix. The purpose of this second part of the literature review is to report the present knowledge on how various Al_2O_3 inclusion morphologies appear and how morphological variations and growth conditions in liquid steel are related.

Before examining Al_2O_3 inclusion morphologies in steel, the current understanding of morphological aspects of crystals will be briefly summarised. Then the particular case of Al_2O_3 inclusions in steel will be treated in more detail. The classification of the various Al_2O_3 inclusion shapes reported in literature is first presented, followed by a review on the relation between the inclusion shape and supersaturation conditions obtained after deoxidation, reoxidation and solidification of steel. Finally, the morphological evolution of Al_2O_3 inclusions during the steelmaking process from ladle metallurgy to casting is discussed.

3.1. Fundamental aspects of crystal morphology

The external form of crystals results directly from the way they grow. The information on the growth mechanisms is retained in the various forms that the crystal takes. The same crystal species may show different crystal forms (polyhedral, skeletal, dendritic or spherical) depending on the growth conditions. Therefore, the crystal shape is determined by its structure but also by factors involved during the growth process. The interconnection between the crystal structure (internal factor), the growth condition and the

process of that growth (external factors) will determine the shape of the crystal [140]. The investigation and interpretation of crystal morphologies may indicate the growth and environmental conditions.

The equilibrium form of a crystal is unambiguously determined from a consideration of the surface free energies of the various crystallographic faces (Wulff construction) and the facet corresponding to a minimum surface energy determine the final form of the grown crystal [141]. However, crystals can neither nucleate nor grow under equilibrium condition. Both nucleation and growth of crystals require driving forces, which are created by conditions deviating from the equilibrium state. In practice, the shape of the crystal is determined by the relative growth rates of its various faces. The various external forms of a crystal result from anisotropic growth rates of the faces. The face with the slowest normal growth rate is the largest and determines the crystal habit, while the face with the highest normal growth rate disappears from the crystal [140]. The growth rates are determined principally by the binding energies of the atoms or molecules at the crystal surface, which are function of the internal crystal structure and of the interatomic and intermolecular interactions [142].

3.1.1. Growth mechanisms

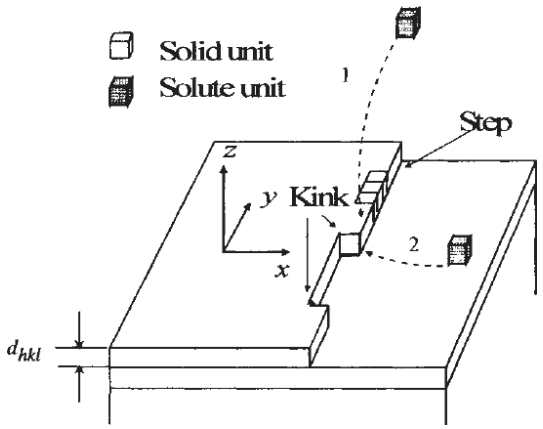

Figure 3-1: Surface model showing steps and kinks, and the incorporation of a growth unit into the crystal structure at kink sites (from Liu [141]).

Crystal growth involves the transport of the growth units (molecules or ions) from the bulk to the surface of the crystal, adsorption of the growth units, surface diffusion to the growth sites and incorporation into the crystal lattice. As depicted in Figure 3-1, the atomic crystal surface consists of steps, with

terraces and kinks, adatoms and vacancies. Kinks are preferred growth sites since they offer more bonds to the adatom [143]. Growth and dissolution processes take place on the surface of the crystal, at the interface between the solid crystal and the liquid solvent. The structure of the interface, which is defined by its roughness at the atomic scale, will therefore play an important role on the growth mechanism. The interface roughness is dependent on crystallographic directions, which are related to crystal structure (bond strength, dislocations, etc.) [144].

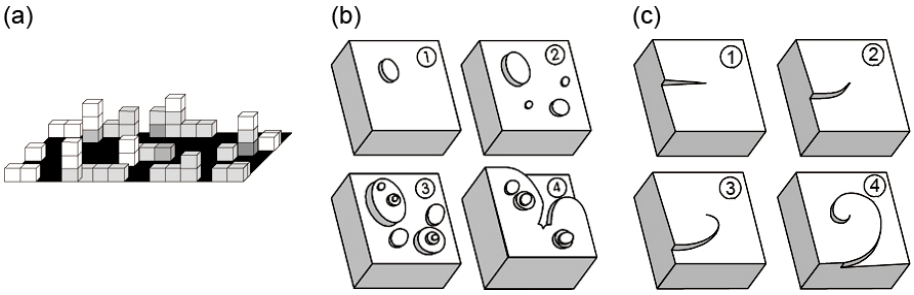

Figure 3-2: Schematic representation of the different growth mechanisms: (a) adhesive-type growth, (b) two-dimensional nucleation growth and (c) spiral growth (adapted from [145]).

In the case of an atomically rough interface, the crystal growth follows an adhesive-growth mechanism [143-145]. Growth units are incorporated directly and randomly on the crystal surface (terraces, steps or kinks), as seen in Figure 3-2 (a). The growth rate is high and simply proportional to the flow of atoms from the parent phase, i.e. the growth is controlled by diffusion. Rounded morphologies are usually obtained with this growth mechanism. The crystal takes on a dendritic form when morphological instabilities occur on the rough interface [144].

When a solid-liquid interface is atomically smooth, two growth mechanisms are reported, depending upon the growth conditions and the nature of screw dislocations on the crystal surface [146]: two-dimensional nucleation growth, called Kossel-Stranski-Volmer (KSV) mechanism [147, 148], and spiral growth, known as the Burton-Cabrera-Frank (BCF) mechanism [149]. In the case of an atomically smooth interface without surface defects, the new steps are created by two-dimensional nucleation on the crystal surface, according to the KSV theory. This mechanism involves an energy barrier to the formation of each new crystal layer. After the nucleation stage, the step advances laterally by deposition and incorporation of the growth units from the bulk to the step [143-145], until the crystal face is completely covered (Figure 3-2 (b)). The growth rate of such face will be controlled by the frequency of the formation of two-dimensional critical nuclei.

The presence of defects on the crystal surface, such as screw dislocations, facilitates crystal growth, providing a source of steps to which the growth units attach [149]. The steps advance along the surface perpendicular to the step. Growth proceeds layer by layer upon the defect, forming a self propagating spiral shown in Figure 3-2 (c) [141, 143-146]. In general, growth spirals are elevated spirals, having their centres at the highest level [146]. The growth rate is determined by the rate of lateral movement of the steps [141].

With an atomically smooth interface, growth proceeds parallel to the interface, resulting in a polyhedral or hopper morphology bounded by crystallographic flat faces [144] (i.e. well-developed crystal faces, Figure 3-4). External factors, such as temperature, supersaturation, solvent and impurities, may cause an alteration in the deposition rate at any surface of the crystal habit [142]. The effects of these factors will be briefly described in sections 3.1.2 and 3.1.3.

3.1.2. Thermodynamic and kinetic roughening transitions

The structure of the interface transforms from smooth to rough with increasing temperature, known as thermodynamic roughening transition [144, 150], and driving force, called kinetic roughening transition [144].

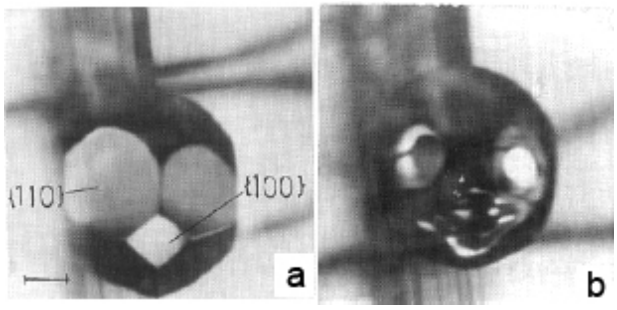

Figure 3-3: Thermal evolution of α-Ag_2S crystal (a) equilibrated at 350 °C and (b) at 565 °C [150].

At low temperature, the equilibrium shape is a polygonal limited by well defined crystallographic faces (Figure 3-3 (a)). Sharp edges of the crystal observed at low temperatures arise from the pronounced cusps of the surface free energy. Upon an increase of temperature, the edges and faces in the equilibrium form change to continuously curved faces and round areas [150], as seen in Figure 3-3 (b). At elevated temperatures, the equilibrium shape

will be nearly spherical cut off by facet faces. The temperature at which the faces transform from smooth to rough is called the roughening transition temperature T_r. As temperature increases, the free energy of the steps for a given facet decreases and vanishes at T_r [151]. The corresponding cusp of the surface energy plot (Wulff construction) disappears and the planar facet is replaced by a curved surface [150, 151]. With a decrease of the free energy of the steps, the growth rate of the facet increases. The facets with low T_r disappear. Only the faces with a high T_r remains, delimiting the shape of the crystal [151].

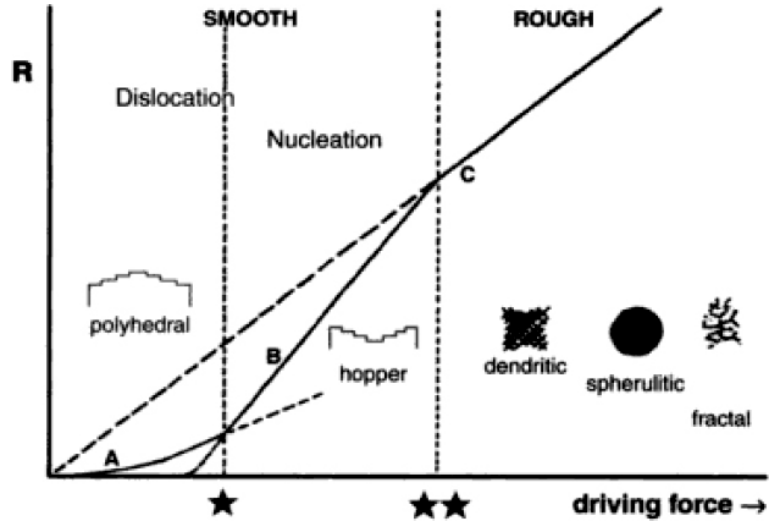

Figure 3-4: Morphologies of single crystals (polyhedral, hopper, dendritic) and polycrystalline aggregates (spherulitic and fractal) in relation to growth rate R, driving force, interface roughness and growth mechanisms. Curve A represents the spiral growth, curve B the two-dimensional nucleation growth, and curve C adhesive-type growth mechanisms. The critical points indicated by * and ** are the points where the predominant growth mechanism changes (from [1, 144])

The evolution of the crystal morphologies with an increase of the driving force has been qualitatively discussed by Sunagawa [1] using growth rate versus supersaturation relation depicted in Figure 3-4. As mentioned in the previous section, the two-dimensional nucleation growth or KSV mechanism requires a certain supersaturation degree to initiate the nucleation of the new crystal layer (curve B in Figure 3-4). Below this critical driving force indicated by * in Figure 3-4, the growth mechanism is determined by spiral growth or BCF mechanism. The presence of screw dislocations on the crystal surface provides a source of steps for growth. Under spiral growth conditions, the facet shows a polyhedral shape and the crystal is bounded by

convex faces. The growth rate of the facet under spiral growth conditions increases moderately with the driving force (curve A in Figure 3-4), until the curve intersects that of the two-dimensional nucleation growth. The intersection point defines the transition between these two growth mechanisms. Above this point, a hopper face appears and the crystal is bounded by concave faces. The reason is that nucleation occurs principally along the edges where supersaturation is higher compared to the centre of the face. If the driving force increases further, multiple two-dimensional nucleation sites appear, giving rise to a multilayer mechanism. As long as the rate of lateral growth of the face is high in comparison to the nucleation rate, the surface is smooth.

With increasing supersaturation, the size of the two-dimensional critical nucleus decreases and nucleation is progressively facilitated. Above a certain supersaturation, the density of critical nuclei becomes so large that the coming growth units can be incorporated at any site on the surface. This point, indicated by ** in Figure 3-4, corresponds to the transition from a smooth to a rough surface, where the layer growth mechanisms change to the adhesive growth mechanism. The roughening of the crystal surface occurring at high supersaturation below T_r is called kinetic roughening. The crystal is bounded by rounded non crystallographic interfaces. The dendritic shape appears on the rough interface under morphological instability conditions. Spherulitic and fractal shapes appear with increasing driving force, through aggregation of polycrystals. The growth rate increases linearly with the supersaturation (curve C in Figure 3-4), owing to the diffusion controlled growth mechanism of atomically rough surfaces.

In practice, the growth conditions can vary significantly with time, providing complex systems in which the crystals nucleate and grow. Growth parameters may change gently or abruptly during the growth process, modifying accordingly the external form of the crystals. In a closed system, the supersaturation decreases as growth proceeds, affecting the growth conditions of the crystals. For example, a dendritic morphology of the crystals appears at the beginning of the process under high driving force conditions, and subsequently changes to a polyhedral shape as the driving force diminishes. Traces of the dendritic growth are recorded in the polyhedral crystal.

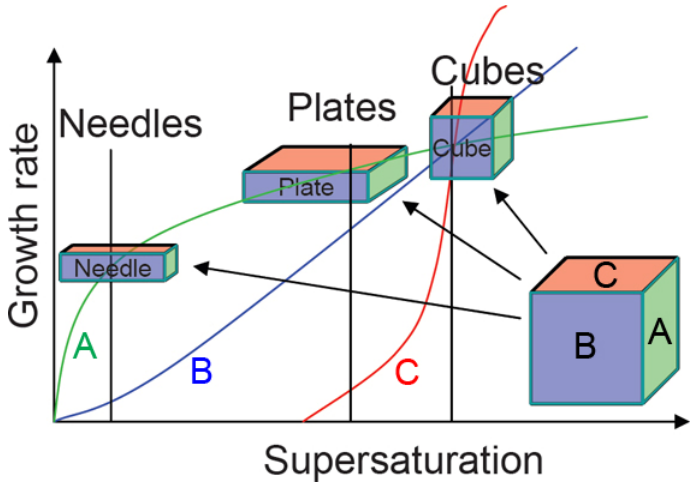

Figure 3-5: Evolution of the crystal shape according to the relative growth rate of the different faces. The line colour and the letter (A, B or C) next to the curve indicate that of the face of the initial cubic crystal (adapted from [152, 153]).

Interface roughness and growth kinetics are different in different crystallographic directions. The overall shape of the crystal will depend on the relative growth rates of all faces. The latter is illustrated in Figure 3-5 [152, 153]. Starting from a cubic crystal, the growth rate curves in relation to the supersaturation can turn the crystal habit into a needle-like, plate-like or block-like habit. A needle shape is obtained when the growth rate of one of the faces is significantly larger than the others (Figure 3-5, green A curve). As mentioned before, this face is almost disappearing from the crystal owing to its high growth rate. With increasing supersaturation, the growth rate of another face increases (Figure 3-5, blue B curve). As the growth rates of two of the three faces are significantly larger than the third one, the shape of the crystal habit becomes plate-like. With similar growth rate of the faces, the crystal habit is block-like.

The prediction of the shape of growing crystals is important for many applications in crystallization. Several approaches were developed in order to predict growth shapes of crystals. The Bravais-Friedel-Donnay-Harker (BFDH) theory is based on crystal lattice geometries [154-156]. It is simple and commonly used to estimate the morphological importance of crystal faces. According to the BFDH theory, the crystal form is dominated by the faces with the largest interplanar distance. The main limitation of this theory lies in the lack of sound physical foundation, as it does not incorporate environmental factors (chemical bonding, interfacial energies, crystal growth mechanisms, etc.).

The model developed by Hartman and Perdok (HP) considered the bonding within the crystal structure and introduced the concept of Periodic Bond Chains (PBCs) within the crystal structure [154-157]. The PBC is defined as an uninterrupted chain of first nearest neighbour bonds with a periodicity of the lattice. Three types of faces are distinguished in the HP theory: flat (F) faces characterised by low growth rate due to a layer growth mechanism, kinked (K) faces characterised by high growth rates (no nucleation required), and stepped (S) faces with intermediate growth rates (one-dimensional nucleation). Due to their low growth rates, F faces will determine the crystal habit. The HP theory assumes that the relative growth rate of a face is proportional to the attachment energy: the larger the attachment energy, the faster the growth rate. The weakest bond within the PBCs governs the growth rate along the direction of the chain. In general, the results of the HP theory show a good agreement with experimental observations. Liu *et al.* [141] presented another approach, which integrates the HP theory, spiral growth and roughening transition theories and molecular dynamics simulations at the solid-fluid interface to predict the crystal growth morphology. They consider the energy required to create a step at the crystal surface and the free-energy barrier for an adsorbed solute molecule to be incorporated in the crystal. They related these energies to the mole fraction of adsorbed solute molecules in dynamic equilibrium with those in the crystal surface. When applying their theory to urea crystals growing from an aqueous solution, they predict a growth shape substantially different from that according to the HP theory. Their prediction is in agreement with the experimental observations.

3.1.3. Effect of solvent and impurities

The attachment energies of a molecule or ions to the crystal surface are controlled by the internal crystal structure and vary for different crystal surfaces. Since crystal growth is a surface-specific process, solvent and impurities may influence the attachment energies of specific faces, causing a significant change in the crystal habit.

The effect of an impurity on the crystal habit involves two processes [142]. First, the impurity is absorbed at growth sites on a specific face, depending on the binding affinity of the impurity to a specific lattice plane. Once the impurity is adsorbed on the crystal surfaces, the deposition of additional layers is inhibited, due to the increase in the attachment energy of the host molecule or ion onto a surface with adsorbed impurity. The impurity blocks a growth site and alters the intermolecular bonding, reducing thereby the growth rate of one specific face relative to the others. These processes result in a modification of the morphology, the faces on which the additive is

absorbed becoming more pronounced. The impurity is called a habit modifier.

Similar to the influence of impurities, the interactions between the solvent and the crystal surfaces, which depend on the chemical nature of the solvent and on the surface atoms of the crystal faces, can lead to dramatic morphology modifications. Two approaches are used to explain the role of the solvent [142]. The first approach involves the preferential adsorption of solvent molecules on specific crystal faces. The growth rate of these faces is decreased as the solvation layer must be removed before the next layer is deposited, inducing a change in crystal habit [158]. The second approach suggests that interfacial tension can be significantly reduced through favourable interactions between the solute and the solvent at specific faces, causing a transition from a smooth to a rough interface. The increased growth rate of these faces results in their disappearance from the crystal. For example, the polarity of the solvent influences crystal growth: polar solvents are preferentially absorbed by polar faces and the non-polar solvents by non-polar faces [158, 159].

The addition of impurities during the crystallization can be used to engineer crystal habit, by identifying the additive or solvent that can modify the growing crystal into a desirable morphology. By using "tailor-made" additives, specific physical properties, such as optical properties, ease of handling and compression, filtration, drying or dissolution characteristics, can be obtained by modifying crystal morphology [160].

3.2. Morphology of Al_2O_3 inclusions

Various inclusion morphologies have been reported in steel: clusters and dendrites, aggregates, faceted inclusions, platelets and spherical inclusions [70, 110, 161-174]. The different inclusion morphologies have been explained qualitatively. The morphology of the inclusions is controlled by the growth conditions of the inclusions, i.e. the supersaturation degree of the steel with respect to dissolved Al and O content, the holding time, and the liquid flow conditions [70]. Since in-situ observation of inclusion formation at high temperature is difficult (unless using the CSLM), the formation mechanism of various morphologies is sometimes uncertain. Assessment of inclusion morphologies are mainly performed on solidified samples, where primary and secondary inclusions co-exist in such a way that their distinction is rendered complicated.

3.2.1. Classification of inclusion morphologies

The classification used in the present work follows that given by Braun [70] and Dekkers [171-173]. The five morphology types, i.e. clustered and dendritic, faceted, plate-like, spherical and aggregated, are not exclusive. The characteristics of more than one type can be found in an inclusion. They co-exist in the liquid steel from the ladle to the mould. Their relative frequency can change significantly between the different treatments after the deoxidation stage. In this section, the principal morphologies of Al_2O_3 inclusions are briefly described. The description focuses mainly on studies reporting inclusion morphologies after extraction of the inclusions from the metal matrix, as this method is believed to provide the most appropriate way to observe inclusion morphologies compared to the traditional examination of polished cross sections.

3.2.1.1. Spherical inclusion

Spherical inclusions are singular and in the shape of sphere (Figure 3-6 (a)). They are usually abundant in industrial steel samples and have a size less than 1 µm [172, 173]. Larger spherical inclusions, 2 to 5 µm diameter, are occasionally found. The way spherical inclusions are formed is yet subject of discussion as several formation mechanisms are proposed.

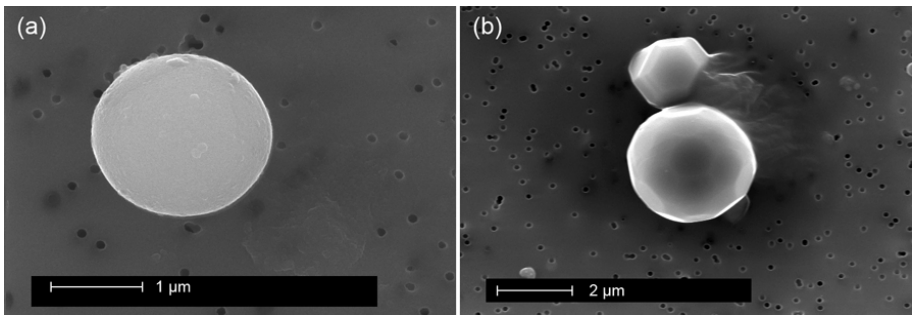

Figure 3-6: Spherical Al_2O_3 inclusions.

Owing to their spherical shape, some authors [11, 175] suggest that spherical Al_2O_3 inclusions were liquid or partly liquid at steelmaking temperature. This hypothesis would require the local temperature in the steel bath to exceed the melting point of Al_2O_3 at 2072 °C [176]. The necessary heat would be provided by the exothermic reaction between Al and O [11, 175] during the deoxidation stage.

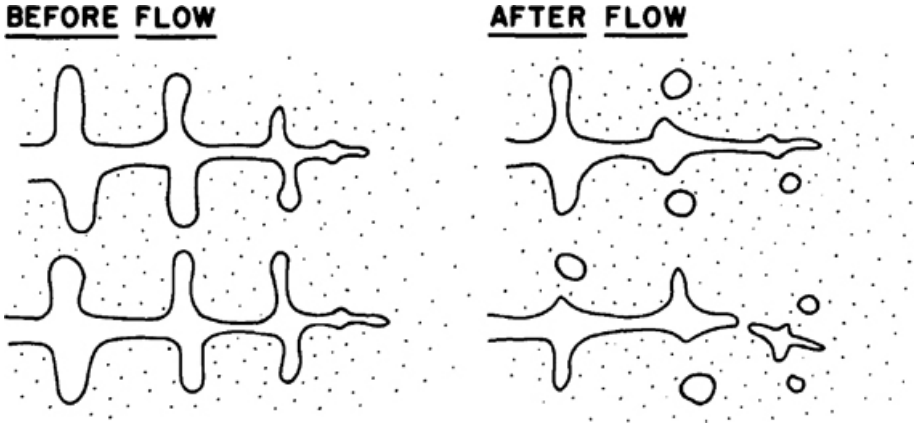

Figure 3-7: "Dendrite multiplication" resulting from convection and associated thermal pulses (from Flemings [177]).

Flemings [177, 178] and Robinson [166] suggested that spherical inclusions are the result of coarsening and breaking of dendrites arm. Due to their high surface to volume ratio, dendrites and other high surface area inclusions are unstable. Coarsening takes place in order to reduce the surface area. As a result, dendrites arms can melt or dissolve off completely and be carried away in the melt, forming new inclusions. This process, represented in Figure 3-7, is referred to as dendrite multiplication and is enhanced with melt stirring [177].

As shown in section 3.1.2, the crystal can have a spherical habit under an adhesive-type growth mechanism (rough interface). Spherical crystals can grow under combined conditions of large driving force (i.e. high supersaturation) and uniform supply of growth units to the crystal. Dekkers [171, 172] observed that the size and number of the small spherical inclusions did not evolve significantly between samples taken from liquid steel between the ladle and tundish. He concluded that they were formed during the steel sampling. Rapid cooling of liquid steel could provide high supersaturation with respect to Al and O and uniform growth conditions. Similarly, Wasai [179] reported a change in size of the small spherical inclusions with the sample cooling rate and concluded that these are secondary inclusions. However, they both noted that larger spherical inclusions are most probably primary inclusions. The development of facets of spherical inclusions, as depicted in Figure 3-6 (b), was attributed to a decrease in supersaturation [171, 173].

In addition, Al_2O_3 is known to form many polymorphs. α-Al_2O_3 or corundum is the stable crystal phase at steelmaking temperature. However, the presence of γ, δ, θ and κ phases of Al_2O_3 has been observed in Al-killed

steels by X-ray diffraction analysis [179]. Wasai observed δ- and γ-Al_2O_3 as secondary inclusions formed during cooling. Among them, the small spherical inclusions were identified mainly as γ-Al_2O_3, possibly mixed with δ-Al_2O_3. To explain the presence of metastable phases, he based his argument on the Ostwald Step Rule [180] stating that the first phase to form is not necessarily the thermodynamically most stable. Instead, the phase with the lowest free-energy barrier of formation will nucleate rather than the phase that is globally stable under the prevailing conditions [181]. These metastable phases would therefore be formed during the solidification of a supercooled liquid phase. Furthermore, on the basis of the Ostwald rule and homogeneous nucleation theories, Wasai [182] concluded that the nucleation of liquid and metastable δ- and γ-Al_2O_3 from liquid Fe at 1600 °C was possible above a critical value of supersaturation. The critical supersaturated state could be obtained upon cooling of Fe owing to the lower O solubility in solid Fe pushing the O at the solidification front.

Up to now, there is no evidence for the presence of liquid Al_2O_3 after the deoxidation process. In Wasai's study [182], the possibility of liquid Al_2O_3 formation was supported by the observation of amorphous spherical SiO_2 inclusions in Al-deoxidised Fe, which would form from liquid SiO_2. Other ways of obtaining amorphous solid phases without first being liquid, such as condensation of a vapour phase to an amorphous solid, were not considered.

3.2.1.2. Faceted inclusions

Inclusion with well developed facet planes and a three-dimensional character are classified as faceted inclusions (Figure 3-8). They are also numerously found in industrial samples. Their size ranges from a few μm to few tens μm [161, 172, 179]. In the work of Dekkers [171, 173], faceted inclusions are further classified as octahedral (Figure 3-8 (a)) or non-octahedral (Figure 3-8 (b)). The reason is the belief that corundum, which cannot develop an octahedral habit, is not the only Al_2O_3 phase present in liquid steel. Other Al_2O_3 polymorphs could explain the presence of octahedral inclusions.

The facets appear in the crystal habit as a result of slower growth rate, and the subsequent ability of the crystal to arrange the incoming growth units in the configuration that minimises the surface energy. As seen in section 3.1.2, such growth conditions are obtained at lower supersaturation degree. From that point of view, faceted inclusions cannot be formed during cooling [171, 173]. Also, the size of the polygonal inclusions was found to be independent on the cooling rate of the Fe [179]. As a result of different supersaturation degrees during the growth of the polyhedral crystal, flat, concave or hopper

faces (Figure 3-8 (c)) on the octahedral inclusions were observed [171, 173, 174].

Large faceted inclusions can also result from the sintering and densification processes of aggregates (see section 3.2.1.5). Overgrowth of plate-like inclusions or dendrites was occasionally observed on small octahedral inclusions [171, 173].

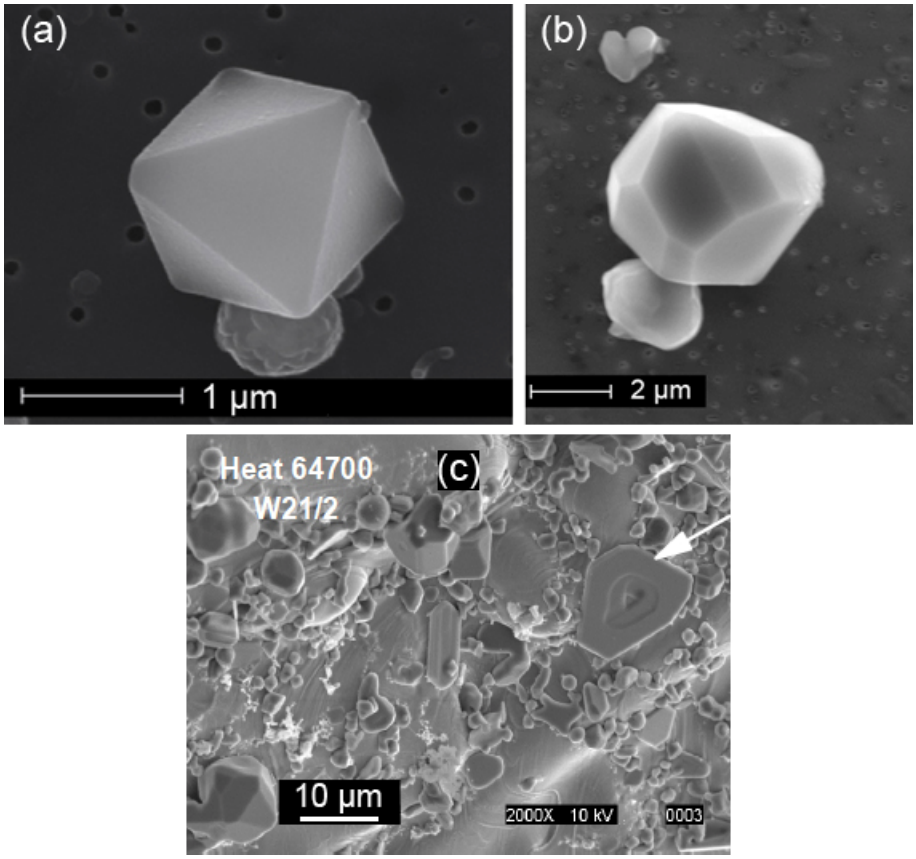

Figure 3-8: Examples of faceted Al_2O_3 inclusion: (a) octahedral (from [173]); (b) non-octahedral; (c) hopper morphologies (indicated by the arrow, from [174]).

3.2.1.3. Plate-like inclusions

Plate-like inclusions are characterised by a large surface to volume ratio and appear as two-dimensional, flat plates. Like faceted type, they have well-developed facet planes.

Plate-like inclusions may grow as singular platelets (Figure 3-9 (a)) or dendritically. They can have various shapes, but they mostly exhibit a trigonal or hexagonal habit, which gives them the name flower, star or maple-like inclusions (Figure 3-9 (b) and (c)). Elongated plate-like inclusions can also be found (Figure 3-9 (d)). They are assumed to be the result of layer growth following convection streams and governed by one-directional supply of components at one side of the crystal [173].

The origin of plate-like inclusions is not fully understood. Dekkers [173] suggested that the <111> face of corundum can be preferentially affected by supersaturation or the presence of impurities compared to the other faces, giving this typical plate-like habit to corundum [183].

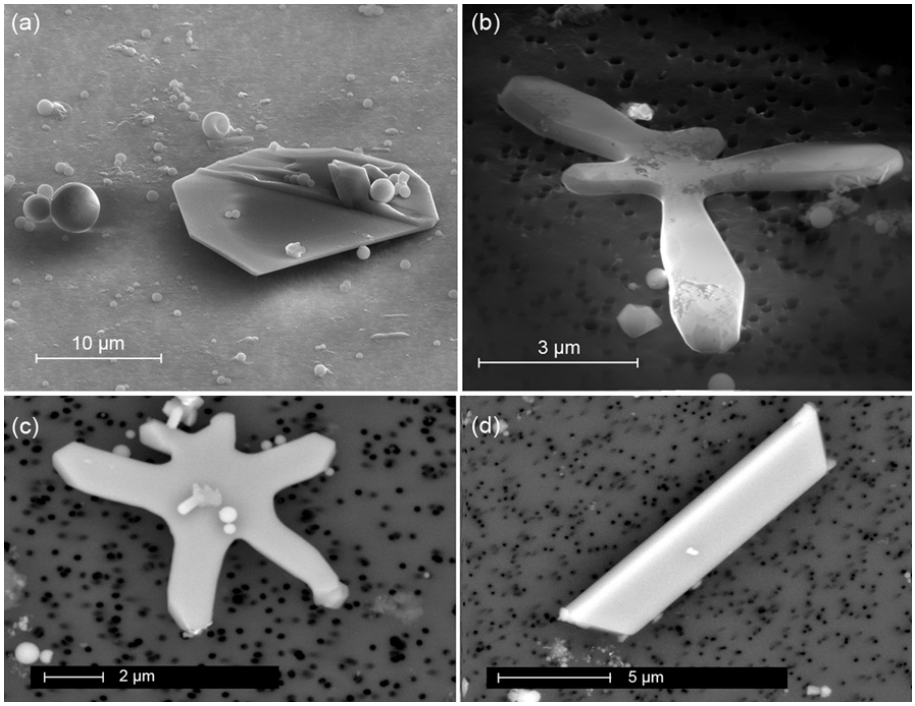

Figure 3-9: (a) Singular plate-like inclusions; (b) and (c) plate-like inclusions growing dendritically; (d) elongated platelet (bar-like).

3.2.1.4. Dendrites and clusters

Dendrite inclusions are those developing a symmetrically branching and multi-branching form, as shown in Figure 3-10. Dendritic particles are the result of growth along the supersaturation gradient. High supersaturation

leads to unstable growth since the rate of component supply to the crystal exceeds the rate at which the crystal accommodates the coming growth units. The high supply rates is located and maintained at the corners of the Al_2O_3 particles, resulting in dendritic growth, forming needles and dendrites [177, 184, 185]. At large growth velocities, instabilities develop near the tip, generating the dendritic side-branches (Figure 3-11 (a)).

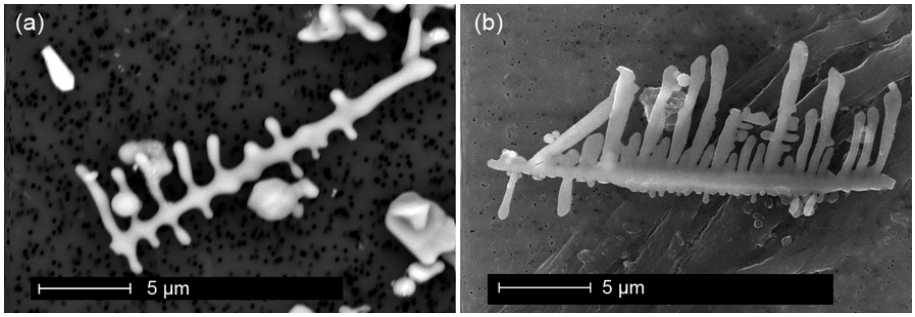

Figure 3-10: Dendritic Al_2O_3 inclusion, showing the primary arm and side branching. Coarsening of dendrites causes neck formation at the base of the dendrite arms, possibly leading to the dismembering of the arm.

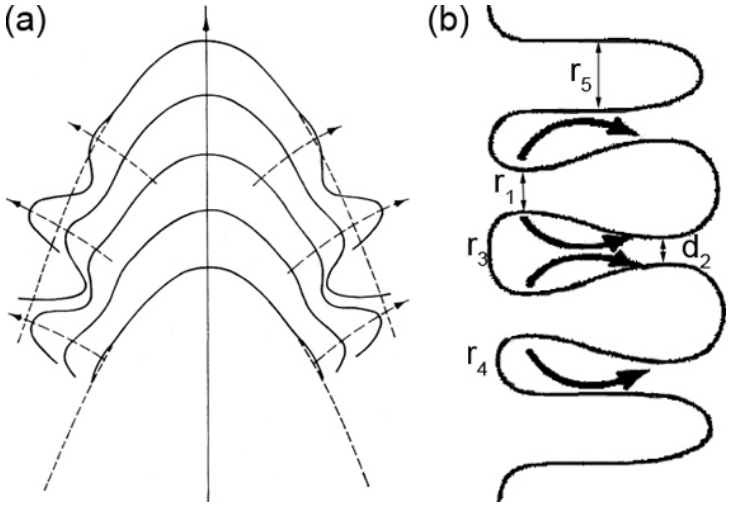

Figure 3-11: (a) Mechanism of side branching formation. The dendrite tip is shown in five successive positions as the dendrite moves up. The dashed lines indication approximate growth paths for the secondary tips (from [185]). (b) Material transport for tear-shaped arms of the dendrite as a result of coarsening, leading to the separation of dendrite arms [184].

In more turbulent conditions, clusters appear as the result of dendritic growth while the directions of the supersaturation gradient are changing. Their shape is therefore irregular, forming an open network of Al_2O_3. The presence or absence of turbulences gives rise to dendrites or clusters. Like dendrites [166], clusters results from growth of one single Al_2O_3 crystal. Steinmetz [164, 165] showed that the clusters are monocrystalline α-Al_2O_3, which demonstrates that they originate from growth of one single crystal. Clusters may be coral-like, dendritic or plate-like shaped.

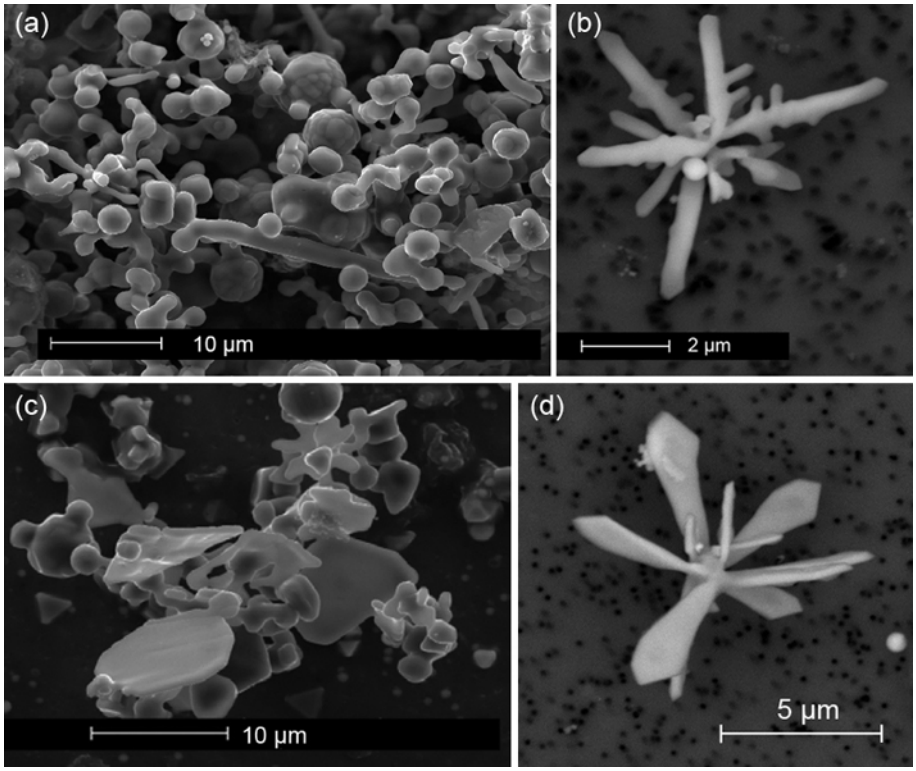

Figure 3-12: Clusters may occur with (a) coral-like, (b) dendritic, or (c) and (d) plate-like structure ((a) is taken from [22] and (c) from [173]).

The tip of dendrites and clusters can exhibit a different shape than the rest of the crystal body. Facets can form on dendrites tip as a result of lower growth rates as supersaturation decreases. In some cases, agglomerates of rounded particles were observed at the end of dendrite or cluster tips (Figure 3-12 (a)), resulting from the densification of the cluster or the dendrite [173]. Due to the large size and the subsequent larger effective collision volume, dendrites and clusters can undergo agglomeration and coagulation with other inclusions in the melt [70].

Dendrites and clusters are unstable growth shapes owing to their large surface to volume ratio, which makes them energetically unstable. They are prone to spontaneous surface rearrangements to lower their surface area. This phenomenon can lead to the dismembering of dendrites through coarsening, during which the material is transported from the base where the curvature radius is small to the tip, where the radius is large. The dendrite arms are tear-shaped, with the formation of a neck at the basis (Figure 3-11 (b) and Figure 3-10 (a)). Eventually, the arm detaches and separates from the main body (Figure 3-7). Sintering is also a direct consequence of surface reordering, resulting in densification of the cluster and the appearance of facets with minimum surface energy.

3.2.1.5. Aggregates

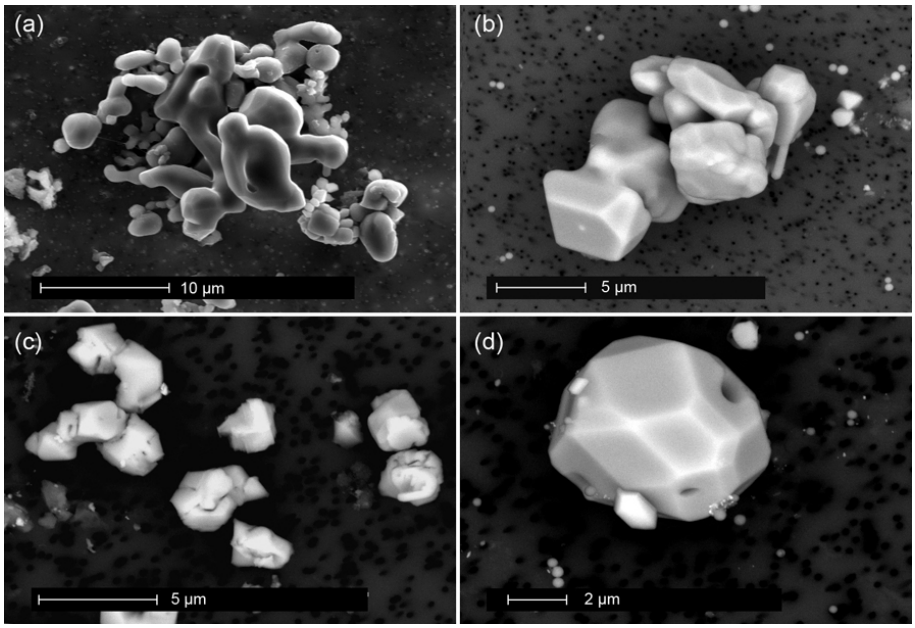

Figure 3-13: Aggregates of Al_2O_3 inclusions, originating from collisions and coagulation of two or more inclusions. Sintering induces the densification of the aggregate, forming polyhedral inclusions.

Aggregates are the result of collision and agglomeration of several inclusions. In many studies, aggregates are also referred to as clusters. However, the growth mechanism of aggregates and clusters are believed to be distinctive. The former results from collisions between several inclusions and is polycrystalline by nature [161], while the latter forms by growth of a

single Al_2O_3 crystal, creating monocrystalline Al_2O_3 with an open structure [161].

Owing to the high surface tension between Al_2O_3 and liquid iron, the liquid iron film formed in between two approaching Al_2O_3 inclusions will disappear immediately. The surfaces forces tend to maintain the particles together and sintering proceeds between the colliding inclusions through the formation of a neck or bridge between the particles [70]. In the early stage of attachment, inclusions forming an aggregate are individually distinguishable (Figure 3-13 (a) through (c)). For that reason, aggregates can show different morphology types depending on that of the single particles forming the aggregate. However, with longer holding time, sintering occurs, leading to the densification of the aggregate and the formation of large polyhedral inclusions. Sintering is driven by the minimization of surface energy. In some cases, entrapment of liquid metal was observed between the sintering crystals, forming holes or cavities [166, 171, 173], as depicted in Figure 3-13 (d).

3.2.2. Influence of supersaturation on inclusion morphologies

As shown in section 3.1.2 of the present chapter, the degree of supersaturation has a significant influence on the crystal morphology, as a result of a modification in the driving force and subsequently in the growth rates of specific facets. Supersaturation is defined by the Al and O activities in the melt (Eq. (2.7) in Chapter 2) and can arise from deoxidation, reoxidation and solidification processes of the melt.

3.2.2.1. Inclusion morphology and deoxidation conditions

In 1974, Okohira [161] examined the evolution of the shape of Al_2O_3 inclusion in industrial samples taken from liquid steel in ladle and tundish and found that the inclusion shapes vary with time, oxidizing potential of slag and Al concentration in liquid steel. With high Al content (400 to 600 ppm), inclusions with dendritic shape were dominant among the morphologies. Dendritic growth was attributed to conditions under which diffusion and high supersaturation remain for a long period of time (~100 s). In contrast, smaller spherical and faceted inclusions were formed due to shorter diffusion and growth, associated with the disappearance of supersaturated conditions before the formation of dendrites. Under reoxidation condition provided by slag (by changing the FeO content), a transition from faceted to spherical type was attributed to an increase of the oxidizing slag potential.

Few years later, Steinmetz [162, 163] investigated the influence of the Al and O activities in liquid steel on the inclusion morphologies. The evolution of the shapes of oxide inclusions as a function of the local mass transport and activities is summarised in Figure 3-14. He observed that, at high O activities and as long as the O supply was maintained compared to the deoxidizer, spherical iron oxide-rich inclusions were formed. With increasing activity of the deoxidizer, oxides formed through reactions with the deoxidizer became more stable compared to iron oxide. Instabilities and subsequently ramifications appeared on the spherical shapes as a result of accelerated growth rates, forming dendrites. At high initial O contents, deoxidation by Al addition causes the formation of dendrites and coarse-spherical hercynite ($FeAl_2O_4$) [164, 165]. With further increasing the activity of the deoxidizer and decreasing the O activity, the branched growth shapes changed to compact shapes and finally octahedrons.

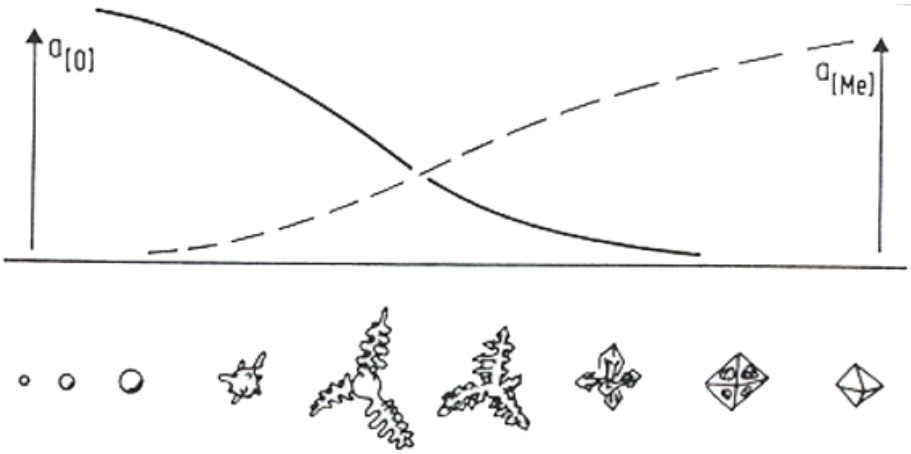

Figure 3-14: Evolution of the growth shapes of oxide inclusions as a function of the local O activity (solid line) and deoxidizer activity (dashed line) according to Steinmetz [163].

Robinson *et al.* [166] studied the formation of Al_2O_3 inclusions in laboratory experiments where Al deoxidation was performed with high O steel (1600 ppm) and low O steel (300 ppm). They found the same morphological evolution with varying O and Al activities as described in Figure 3-14 by Steinmetz [162, 163]. Also deoxidation of the melt containing high O resulted in the formation of highly dendritic Al_2O_3 inclusion and aggregates. The turbulent mixing created high supersaturated conditions at the interface between Al-rich deoxidized melt and O-rich non-deoxidized melt. Depending on the local Al and O concentrations, the degree of dendritic Al_2O_3 was modified. With high O and high Al concentrations, dendrites were highly ramified and well developed with hexagonal section and high

surface to volume ratio. Upon a decrease in O concentration, the dendrite arms tend to spheroidize, forming coral-like inclusions. The dendrite arms began to sinter as they touched each other, leading to the collapse of the dendrite and the formation of large polycrystalline aggregates. According to Robinson [166], this process is driven by the decrease of surface to volume ratio to minimize the surface energy. No dendrites were observed after the deoxidation of the melt containing low O. In contrast, highly spheroidized Al_2O_3 inclusions and polycrystalline aggregates originating from collision and sintering processes were observed.

Braun *et al.* [70] performed deoxidation experiments to investigate the influence of stirring conditions and initial O content ranging from 100 to 500 ppm on the formation and clustering of Al_2O_3 inclusions. They showed that melt stirring promoted the formation and growth of Al_2O_3 clusters. The O content had little or no influence on cluster formation, whereas it influenced significantly the inclusion morphologies. With increasing O content, the inclusions in the clusters changed from dendritic and plate-like shapes to spherical inclusions. In non-clustered regions of the samples, individual inclusions consisted of numerous small dendrites with 100 ppm initial O. Submicron size spherical inclusions, large dendrites and large globular inclusions appeared among the inclusion shapes with increasing O content above, respectively, 350, 450 and 500 ppm. Meanwhile, the number of faceted inclusions decreased with increasing initial O content.

3.2.2.2. Supersaturation provided by steel reoxidation

The influence of reoxidation conditions was also studied qualitatively by Steinmetz and co-workers [167, 168]. They classified the Al_2O_3 inclusion morphologies as a function of the local Al and O content. The evolution of the Al_2O_3 inclusion shapes during reoxidation is depicted in Figure 3-15 in relation with the measured Al and O content. Above 800 ppm O (thus below 200 ppm Al), oval and rounded shaped were observed and attributed to primary liquid inclusions. Between 0.002 and 0.02 % Al, needle-like and bar-like inclusions were dominant and transformed into dendritic shape with increasing Al content and decreasing O content. With further increasing the Al content above 0.2 % Al and decreasing O content below 0.002 % O, compact shapes and eventually strips appeared.

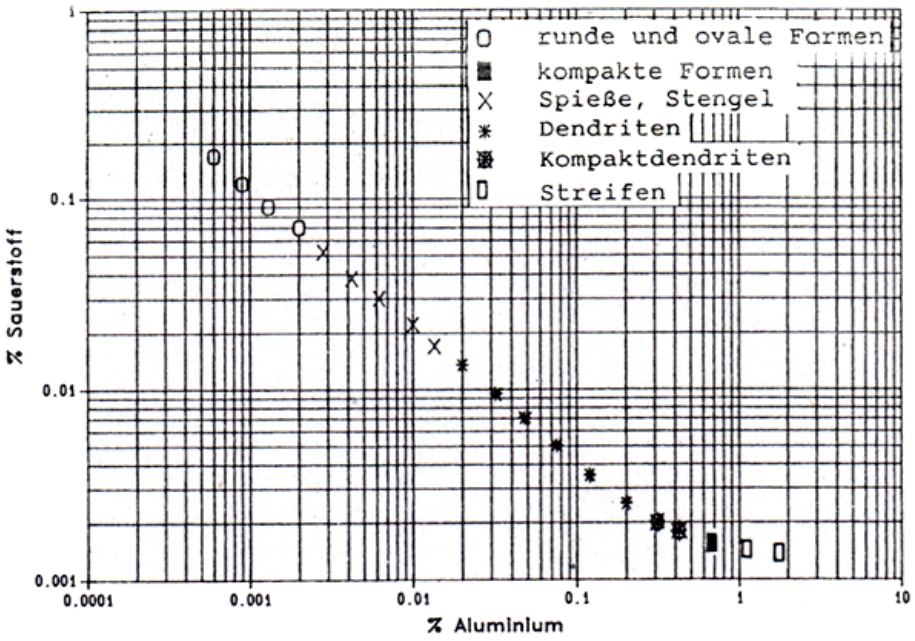

Figure 3-15: Evolution of the Al_2O_3 inclusion shapes during reoxidation as a function of the local oxygen and aluminium content, according to Steinmetz [168] (Sauerstoff = oxygen, legend: ○ round and oval shapes, ■ compact shapes, × needle-like and bar-like, ✳ dendrites, ❋ compact dendrites, ▯ strips).

Recently, Wang and Sridhar [110, 186] studied the *in-situ* formation of Al_2O_3 inclusions by reoxidation of the surface of liquid Al-killed low carbon steel by using a high temperature Confocal Scanning Laser Microscope (CSLM). The influence of various gas flow rates and temperatures ranging from 1580 to 1630 °C were investigated. Growth of inclusions on the melt surface took place after a certain time, which was attributed to the time required to dissolve enough O near the melt surface to reach the necessary supersaturation degree for inclusion formation. This time period to observe reoxidation increased with increasing temperature and decreasing flow rate. With increasing gas flow rate, the inclusion morphology changed from dendritic to aggregates. Octahedral inclusions were observed among the aggregates, as a result of simultaneous growth and sintering processes. Under these conditions, the rate of nucleation and growth of oxide was controlled by the mass transfer of oxygen in the gas phase to the melt surface. A change in temperature was found to influence the inclusion growth rate on the melt surface. They observed that the growth rate increased with decreasing temperature from 1630 to 1580 °C, as a consequence of the increase in driving force (more stable oxide phases at lower temperatures). They concluded that the temperature has a stronger

impact on the driving force than on the transport properties of O_2 in the gas phase. However, the morphology of the inclusions was not altered by a change in temperature.

3.2.2.3. Influence of cooling on inclusion morphologies

Steinmetz [164, 165] studied the influence of the solidification conditions on Al_2O_3 inclusion growth. Upon cooling and solidification of the melt, the remaining Al and O content initiates supersaturated conditions in comparison with the equilibrium at solidification temperature. In that case, the growth conditions of the precipitated inclusions depend on the segregation concentrations of Al and O at the solidification front, mass transport and solidification conditions. They observed a transition from spherical to coral-like with increasing O content. Above 190 ppm O, dendritic shape inclusions form. Coral-like inclusions result from slower growth with irregular mass transport of Al and O, producing the branched irregular shape of coral-like crystals. Dendrites can form as a result of extreme quenching condition and higher oxygen contents. Similar conclusions were obtained by Wasai [179], who observed that the size of the small spherical inclusions and the trunk thickness of the coral-like inclusions increase with decreasing cooling rate, concluding therefore that these shapes were obtained during solidification.

3.2.3. Morphology evolution during steelmaking process

3.2.3.1. Inclusion morphology at the onset of deoxidation

Very few studies [49, 66, 67, 175] were dedicated to the observation of the early stage of deoxidation. The attention was mainly given on the inclusion size distribution [49]. Beskow *et al.* [66] observed the formation of small Al_2O_3 inclusions 5 s after deoxidation resulting form homogeneous nucleation in the areas supersaturated with Al, followed by agglomeration with longer time. By sampling the deoxidized steel 1 s after the reaction, Wakoh and Sano [67] measured the initial size distribution of Al_2O_3 inclusions and reported four morphologies, i.e. sphere, octahedron, hexagonal and a minority of coagulated inclusions.

By adding rimming steel[1] to Al in an ingot, Tiekink [175] observed a repetitive sequence of several Al_2O_3 morphologies and explained it by a mechanism of local reaction and diffusion of Al and O. When Al comes into contact with rimming steel having approximately 700 ppm O, small Al_2O_3 inclusions were formed at the reaction plane by homogeneous nucleation under high O conditions (Figure 3-16, 1). The heat generated by the reaction would have decreased the reaction speed. The reaction consumed O near the reaction plane, allowing Al to dissolve into the deoxidized zone (Figure 3-16, 2). Further away from the reaction plane, Al encountered new O diffusing from the melt. Under the conditions of counter diffusion of O and Al maintained for some time, growth of needle-like and dendritic inclusions took place (Figure 3-16, 3). As Al and O continued to diffuse to the reaction site, conditions of homogeneous nucleation were met again, with the formation of small inclusions (Figure 3-16, 4). This pattern of inclusion morphologies (small inclusions followed by needle-like and dendritic inclusions) recurred several times, separated by a distance of about 100 µm.

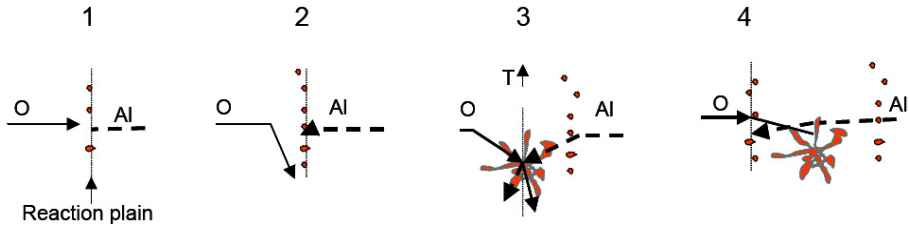

Figure 3-16: Schematic of suggested reaction mechanism of aluminium with rimming steel [175].

3.2.3.2. Morphology evolution in steel melts

The evolution of inclusion morphologies during the secondary steel refining treatments is important to assess as it will influence the quality of the final product and the risk of clogging during continuous casting. Variations in the local degree of supersaturation of Al and O, stirring conditions and temperature through the process can lead to significant changes in inclusion formation and growth mechanisms, and thereby on inclusion morphologies.

[1] Rimming steel is steel which is not deoxidized prior to ingot casting. During cooling, carbon in steel reacts with the excess oxygen to produce gaseous CO ("boiling") in the cooler parts near the mould surface, creating a rim. The outer surface of the ingot is almost pure Fe, while the center part is porous with impurities concentrated along the axis.

By performing deoxidation experiments under an inert atmosphere, Braun [70] reported that with long stirring time or vigorous stirring, almost all inclusions can be gathered in clusters, which move rapidly to the melt surface due to their large size (Eq. (2.25) in Chapter 2).

Several authors [169, 170, 173, 174] showed that the inclusion morphologies depend on the growth conditions and on the residence time in the liquid melt., The evolution of the Al_2O_3 morphology during deoxidation and ladle treatments according to Tiekink [169] is summarised in Figure 3-17.

Large clusters are formed upon deoxidation in the RH-OB degasser, among which two types of clusters were distinguished: needle-shaped dendritic alumina clusters and spheroidised Al_2O_3 clusters, having a dendritic structures with sphere at the tips of the dendrite arms. Dendritic growth is attributed to the large local supersaturations of Al and O created in the RH-OB degasser, where Al is added in a short time (~1 min) to a rather small amount of steel in which excess O compared to the C-O equilibrium is present. Once the nuclei are formed, large supersaturation lead to high reaction rates and dendritic growth. With the decrease of the supersaturation, the reaction speed decreased, causing the appearance of spheres at the dendrite tips.

During deoxidation at the stirring station, high supersaturation conditions are provided soon after the Al addition in the areas where the Al is dissolving. Dendritic growth took place in these zones. In contrast with the RH-OB degasser, the supersaturation is lower at the stirring station since the Al is added by wire during 3 to 4 min and no excess O is present (C-O equilibrium). The lack of high local supersaturation caused the reaction to slow down and the formation of spheres at most of the dendrite tips (coral-like clusters).

Faceted inclusions were observed next to the large clusters. Their facets indicate that the reaction at the interface is slow compared to the Al and O diffusion. Large clusters formed in the RH-OB degasser and the stirring station will float out in a short period of time, decreasing substantially the amount of inclusions. At the end of the treatment, sintering process initiated a change in morphology from spherical to irregular, angular and more compact clusters. A second Al addition in the RH-OB brought about the formation of finger-like inclusions, which were hardly removed due to the lower available time before casting. It was concluded that deoxidation should be performed in one time at high O excess, in order to create large clusters that are removed rapidly from the melt.

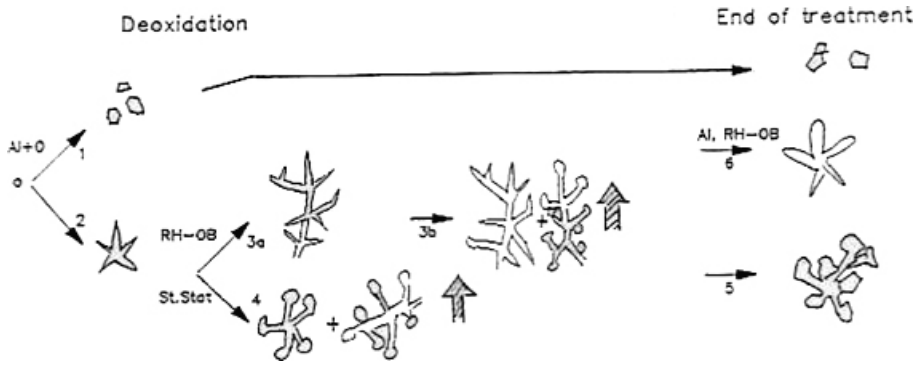

Figure 3-17: Schematic representation of the morphology of Al_2O_3 during deoxidation and ladle treatment, according to Tiekink [169]. 1. Nuclei form small particles. 2. Nuclei grow to dendrites. 3a. Dendritic growth continues in RH-OB because of high reaction speed by large supersaturations of Al and O. 3b. Agglomeration of dendrites gives clusters, at some dendrites spheres have been formed. Big clusters float out of the steel. 4. At the stirring station spheres form on dendrite tips because of a lower reaction speed by low supersaturation of Al or O. Agglomerates form and float out of the steel. 5. The remaining small clusters become compact and the particles become irregular. 6. Small finger-like dendrites form in RH-OB when adding aluminium in already aluminium killed steel.

Pielet *et al.* [174] analysed samples taken from the RH-OB treatment and from the tundish, mould and tundish well nozzle plugs during the production of Ti Stabilized Ultra Low Carbon (TiSULC) steels. Although the steel grade was different, similar evolution of the inclusion morphology was reported compared to the studies of Tiekink [169, 170]. Several minutes after deoxidation, the frequency of dendrites, flower-like, and coral-like agglomerates first increased in the ladle and then decreased. These high surface-area inclusions formed during deoxidation as a result of high supersaturation, underwent agglomeration by stirring and were quickly removed from the melt. The number of spherical inclusions increased in the ladle. They were also found in the tundish. The frequency of small faceted inclusions (< 2 μm) first increased in the ladle then started to decrease. Larger ones (> 5 μm) were absent in the ladle and became more frequent in the tundish. By comparing the size distribution of the large faceted inclusions in the tundish at different stages of ladle pouring, they showed that the size of the faceted inclusions increased as the ladle is emptied and their frequency increased with decreasing superheat, suggesting that these inclusions grew in the ladle as the steel cooled.

The evolution of the inclusion types during the production of medium carbon aluminium killed (MCAK), low carbon silicon-aluminium killed (LCSAK) and low carbon aluminium killed (LCAK) steels were investigated by total oxygen measurements and morphology assessments on samples taken at small time interval until the end of the secondary metallurgy treatment [171, 172]. Submicron spherical inclusions were the most abundant inclusions shape throughout the secondary metallurgy process, but clusters and aggregates contributed to most of the oxygen present in the steel. While clusters were typical for the deoxidation stage and are removed within about 15 minutes after aluminium addition, aggregates and large polyhedra appeared a few minutes after deoxidation and increased in size with holding time. It was suggested that growth of agglomerated inclusions occurred by coagulation of single inclusions. Evidence of inclusion growth during the treatment was highlighted. As a result of temperature decrease with time, dendrite tips formed on existing particles and the frequency of polyhedral inclusions increased with time at the expense of octahedral inclusions, suggesting that the former arose from overgrowth on octahedral inclusions. Also the rounded surfaces of clusters were attributed to severe cooling or reoxidation. The study concluded besides that, though increasing the holding time improves inclusion removal by flotation, steel cleanliness might be deteriorated by too long holding times, as aggregates and large polyhedra increased in size during the treatment.

3.2.3.3. Morphology of clog deposits

Tundish nozzle clogging is an important issue during continuous casting of steel due to the influence on the quality of the finished products and on the production costs. Clogging is affected by numerous factors related to casting operations but also to the secondary metallurgy practices. Kaushik [187] emphasized that the build-up of the clog is progressive, which requires the investigation of all heats cast. The origins of clogging are difficult to assess as many factors can contribute simultaneously, rendering the clogging mechanism complex. The formation of the clog can result from metal temperature drop during casting (thermal clogging), chemical reactions and deposition of inclusions on the nozzle wall [13, 188]. The plugging usually consists of a white dense material and a network-like layer of inclusions embedded in the steel matrix [13, 23, 187, 188], as shown in Figure 3-18.

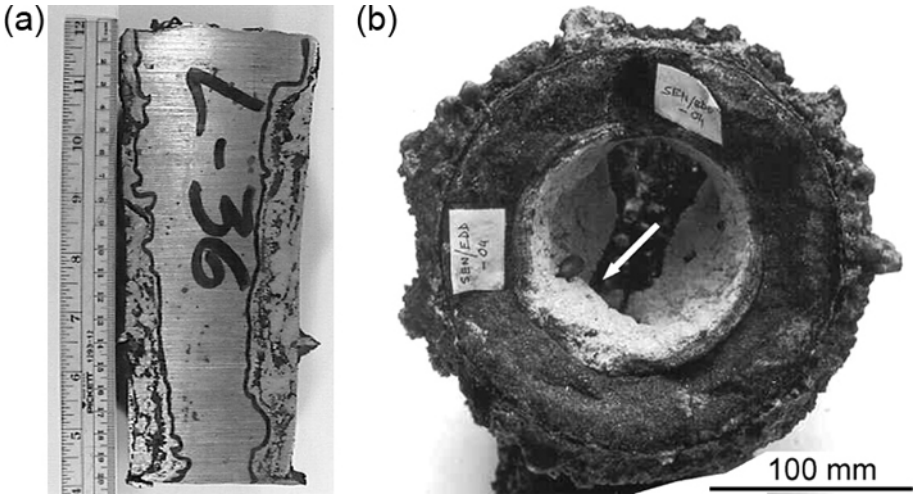

Figure 3-18: (a) Longitudinal section of the tundish nozzle plug (from Pielet *et al.* [174]), where the continuous black line delimits the deposit build-up along the nozzle wall from the solidified steel; (b) transverse section of the SEN, where the white inclusion deposits are indicated by the arrow (from Basu *et al.* [23]).

Several authors [22, 23, 170, 174] suggested that the origin of the inclusions in the clog is steel reoxidation, resulting from local supersaturation. In particular, Dekkers [22] reported that the clogging deposit consisted mainly of coral-shaped clusters, dendritic clusters and irregular plates, which are similar to the clusters typically formed in liquid steel shortly after deoxidation in the ladle under high supersaturation conditions. Clusters originate from diffusion growth and not accretion growth. Moreover, they are not present in the liquid steel at the end of the ladle metallurgy, indicating that they are formed in the tundish or in the SEN. For these reasons, it was concluded that the clogging mechanism was controlled by the degree of reoxidation during casting.

Another proposed mechanism of clogging is the deposition on refractory pieces of non-metallic inclusions originating from the liquid melt. The latter was demonstrated by correlations between inclusions in liquid steel and those in the deposits, combined with rare earth oxide tracing of deoxidation inclusions [188]. Based on total oxygen measurements and on the presence of identical inclusion morphologies in the tundish plugs as in the steel in the tundish and mould, Pielet [174] identified that tundish nozzle clogging was due to transport and adherence of Al_2O_3 inclusions formed in the melt through reoxidation caused by reactions with ladle sand.

Multiple factors contribute to clogging, requiring systematic investigations of the different process stages from refining to casting practices in order to identify the causes of clogging. Studying the inclusion morphologies in the deposit and in the steel throughout the steelmaking and casting processes is an important step, as the inclusions serve as indicator of growth and environmental conditions, provided that the mechanisms leading to the various inclusion morphologies is fully understood.

3.3. Conclusions

The crystal morphology is determined by the growth conditions, i.e. the degree of supersaturation, the flow conditions, the residence time and the presence of impurities. As a result, Al_2O_3 inclusions observed in steel samples exhibit various morphologies, which are strongly dependent on the local supersaturation of Al and O. Dendritic, cluster and spherical inclusions appear under high supersaturation conditions, whereas faceted inclusions and the development of facets on existing inclusions arise from low supersaturation conditions.

As a consequence of various conditions prevailing during the steelmaking process, the morphology of Al_2O_3 inclusions evolve from clusters and dendrites shortly after deoxidation to faceted and aggregates at the end of the secondary metallurgy. However, the different inclusion morphologies and the relation between inclusion shape and supersaturated conditions have been explained qualitatively. Also, the mechanisms leading to Al_2O_3 inclusion morphologies, such as spherical or plate-like, are still unclear.

Steel cleanliness is controlled by a large number of important operating conditions throughout the steelmaking and casting processes. The control of inclusion morphology requires the comprehension of the processes leading to the formation of specific particle shapes and the quantification of the relationship between oxide inclusion morphology and the main process parameters during their nucleation and growth. Such quantitative data are rare.

Chapter 4
Experimental techniques

As seen in the two previous chapters, the influence of the process parameters on the inclusions during deoxidation and reoxidation processes is significant. To obtain accurate and quantitative data on the formation and characteristics of Al_2O_3 inclusions, it is primordial to control the conditions of the melt (purity, temperature) and the gas phase during the experiments. In addition, samples of the melt must be taken in an appropriate way to ensure that the inclusions characteristics are preserved and the conditions are not significantly altered. Methods and procedures were developed accordingly and are described in the first part of the chapter. The second part is dedicated to the analysis of the samples, including the chemical composition of the metal and the acquisition of the characteristics of the inclusion population in a given sample.

4.1. Raw materials

Table 4-1: Chemical analysis of electrolytic iron (Mairon SHP, Toho Zinc Co. Ltd.)

Element	Concentration (ppm)	
	Max. guaranteed	Typical
C	20	5~15
P	5	1
S	5	1~3
Si	5	< 5
Mn	5	1
Cu	5	1
Cl	-	< 20
O	50	20~50
N	10	5
H	5	1~3

Electrolytic iron was used as starting material to perform deoxidation and reoxidation experiments. A high purity grade electrolytic iron, the Mairon SHP with a purity of 99.99% Fe, was chosen to ensure low level of impurities, especially a low level of total oxygen, and no particles. The chemical analysis, provided by Toho Zinc Co. Ltd., is given in Table 4-1. The material consists of square flakes 25 x 25 mm, about 2 to 3 mm thick.

The deoxidation of liquid iron and the preparation of the Fe-Al alloys for the reoxidation experiments were performed with aluminium granules supplied by Chempur, with a size ranging from 2 to 5 mm and minimum 99 % purity. The major impurities are Fe (~0.65 wt%), Mn (~0.20 wt%) and Si (~0.15 wt%).

4.2. Materials preparation

Electrolytic iron flakes were cut in small pieces, ground, followed by washing in running water, ultrasonic cleaning in acetone, rinsing in acetone and drying. The Al granules were pickled in 5% NaOH solution for 1 min, followed by washing in running water, rinsing in acetone and drying. No further preparation was needed for the deoxidation experiments.

Fe-Al alloys aimed at the reoxidation experiments were produced in a vacuum arc melting furnace (Model ABJ-338 from Materials Research Furnaces Inc.). The 4 x 15 g charge made of electrolytic Fe pieces and Al granules were melted in a copper hearth with 4 half spherical cavities, clamped to a water-cooled base. The amount of Fe and Al was weighed to obtain a final Fe-Al alloy with the desired composition. The Al charge was increased to about 50% to counterbalance the material loss during the melting. The use of a water-cooled copper crucible prevents the incorporation of impurities in the liquid metal. Before melting the charge, the furnace chamber was evacuated by a vacuum pump and back-filled with purified Ar gas for five times. A continuous flow of 0.2 l/min purified Ar was used during the melting. The tungsten electrode provides a high energy plasma arc, able to heat the charge above 2000 °C. Once the arc is started, the stinger is moved over the four samples to melt them. The intensity of the arc can be controlled during melting. Once the samples were melted, the arc was stopped. After that the charge was allowed to cool down, the latter is reversed in the cavities and melted a second time to improve homogeneity.

After the melting, the surface of the alloys was cleaned to remove contaminations. The procedure consists in grinding the surface of the material, washing in running water, ultrasonic cleaning in acetone, rinsing in acetone and drying.

4.3. Experimental method

Reoxidation and deoxidation experiments were conducted in a high temperature vertical tube furnace illustrated in Figure 4-1 (GERO HTRV 100-250/18 with $MoSi_2$ heating elements). The furnace tube is made of sintered Al_2O_3, with dimension 80 mm inside diameter (ID), 90 mm outside diameter (OD), and 1000 mm height (H).

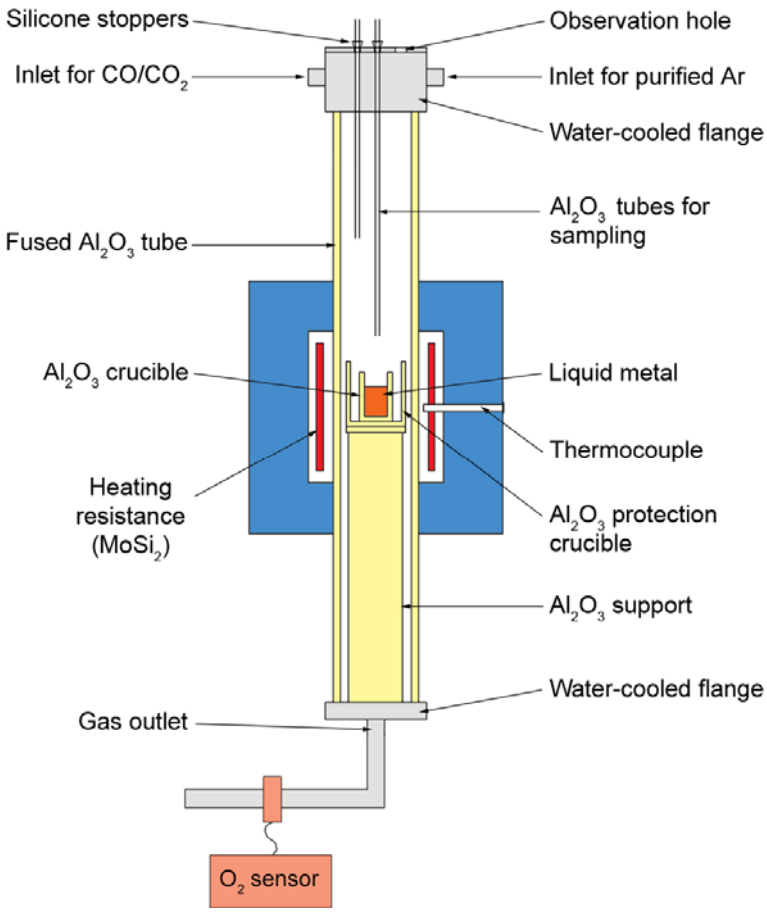

Figure 4-1: Setup for reoxidation experiments

The temperature is controlled by a PID temperature and process controller from Eurotherm (3504 series). The type B thermocouple (Pt-6% Rh vs. Pt-30% Rh) of the controller is located next to the heating elements, outside the furnace tube. The inside temperature of the furnace tube is measured with

the experimental setup, by an additional type B thermocouple after each replacement of the furnace tube. The vertical temperature profile in the furnace ensures a hot zone, approximately 4 cm in length, in which the temperature varies by less than ± 1 K.

In the experimental setup, a high density, high purity Al_2O_3 crucible (ALSINT 99.7 % Al_2O_3, 30 mm ID, 35 mm OD, 50 mm H) in which the material is melted, is placed in a protective Al_2O_3 crucible, which is positioned on an Al_2O_3 support. A Mo handle is made to the crucible to lift it out for quenching. The distance between the crucible bottom and the top of the furnace is approximately 80 cm.

4.3.1. Sampling – addition – observation

The Al_2O_3 furnace tube is sealed at both ends by water-cooled flanges. The lid of the upper flange was specially designed for the observation, sampling and addition at high temperature without breaking the atmosphere. A schematic drawing of the functionality of the flange is provided in Figure 4-2. Four large holes are made to the flange, of which one is dedicated to the observation (borosilicate glass + welding glass shade no. 10). A smaller central hole is foreseen for moving the crucible upwards and downwards, or for performing additional measurements (sensor, thermocouple, etc.).

The sampling of the liquid metal during the experiments was performed with Al_2O_3 tubes (5 mm ID, 8 mm OD, 900 to 1500 mm H). Silicone stoppers with holes drilled along their vertical axes to fit the sampling tubes are employed to seal the furnace and to allow the tubes to move in all directions (Figure 4-2, arrows 5). Before the start of the experiments, the sampling tubes are positioned on the flange lid on top of the furnace, the end of the tube being halfway between the flange and the crucible (Figure 4-1). The other end of the sampling tube was closed by a 5 ml syringe, connected to the sampling tube by a thin silicone tube (Figure 4-2, arrows 6, 11 and 12). To perform the sampling, the sampling tube was quickly lowered and maintained above the crucible where it was preheated and flushed several times with hot furnace gas by using the syringe. The sampling tube was then immersed into the liquid metal and a small volume (1.5~2 ml) of liquid was sucked into the bottom part of the tube by using the syringe. For convenience and reproducibility, the choice of the sampling location in the melt was the bottom of the crucible. Due to the large distance between the observer and the liquid metal (80~90 cm) and the heat radiation at the furnace hot zone, the exact position of the tube end was difficult to estimate. After suction of a small volume of liquid metal, the Al_2O_3 sampling tube was

quickly lifted to the top part of the furnace where the liquid metal sample solidified.

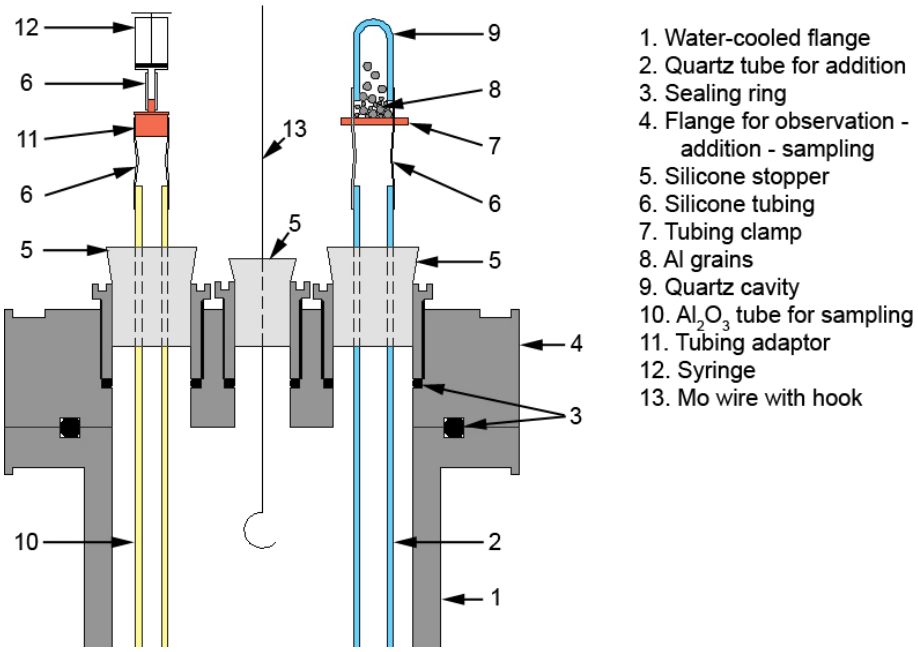

Figure 4-2: Schematic drawing of the flange lid, showing the sampling, addition and sample insertion/removal procedures at high temperature.

The addition of Al to deoxidise liquid iron was perform by storing the specific amount of Al in a quartz cavity, at the upper end of a quartz tube, as indicated by arrows 2, 6-9 in Figure 4-2 . The quartz cavity was closed by a tubing clamp fixed on the silicone tubing connecting the quartz tube to the cavity. The quartz tube was also positioned on the flange lid through a silicone stopper before the start of the experiments. To perform the addition, the quartz tube was lowered in the furnace and positioned above the crucible. After opening the tubing clamp, the aluminium grains were then released from the cavity and fell, from a height of approximately 80 cm, inside the melt, guided by the quartz tube. After the addition, the quartz tube is lifted to the top of the furnace.

This procedure to perform the sampling and the addition ensures that the atmosphere of the furnace is maintained during the whole experiment. For the first trial of the new flange lid and whenever leaks were suspected, the sealing of the furnace was checked with helium gas and a helium detector. Also, the gas at the furnace outlet is bubbled in a dibuthyl phthalate solution. The furnace atmosphere being in a slight overpressure, the presence and the

intensity of gas bubbles in the solution is a good indicator that the furnace has no major leak.

4.3.2. Atmosphere control

During the deoxidation and reoxidation experiments, the control of the furnace atmosphere is of primary importance. The purity of the argon gas is 99.998 % and contains less than 5 ppm O_2 and less than 5 ppm H_2O, according to the specifications provided by the company Praxair. In case liquid iron is held at 1600 °C in this Ar grade atmosphere, it cannot provide a protective atmosphere for liquid iron, leading to its oxidation. Therefore, a gas cleaning system (Figure 4-3) was designed to remove water vapour and oxygen in argon gas before being blown in the tube furnace. The gas cleaning system consists of a H_2SO_4 concentrated solution in which argon gas is bubbled to remove water. The argon gas enters a horizontal tube furnace heated at 500 °C, in which magnesium turnings are stored. At that temperature, gaseous oxygen reacts with magnesium to form magnesium oxide according to the reaction Eq. (4.1):

$$2\,\mathrm{Mg(s)} + \mathrm{O_2(g)} = 2\,\mathrm{MgO(s)}. \tag{4.1}$$

Deoxidation of gas by means of heated magnesium is a very efficient process. The oxygen content in the gas can be decreased to a very low value, typically less than 10^{-14} ppm O_2. The deoxidized argon was used as a protective atmosphere during heating and stabilizing of the temperature, during which no reaction should take place.

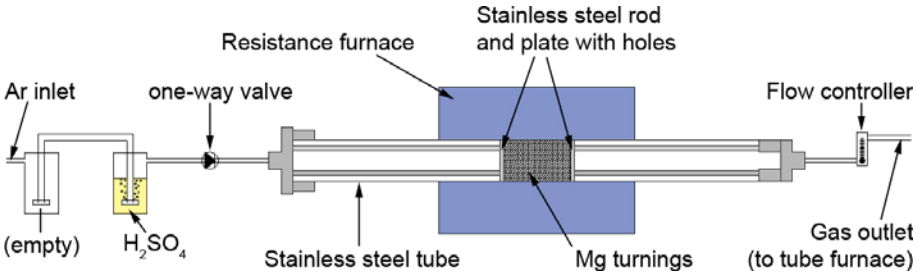

Figure 4-3: Schematic overview of the gas cleaning system.

The reoxidation experiments were performed, once the temperature is reached and stabilized, by exposing the Al-containing iron alloy to an oxidative atmosphere. The oxygen partial pressure in the gas phase, p_{O2}, was changed by using a CO/CO_2 gas mixture with a fixed ratio. From that

moment, equilibrium between CO(g), CO_2(g) and O_2(g) is established in the gas phase according to reaction Eq. (4.2):

$$2\,\mathrm{CO(g)} + \mathrm{O_2(g)} = 2\,\mathrm{CO_2(g)}. \tag{4.2}$$

The standard Gibbs free energy change ΔG^0 (J mol^{-1}) and the equilibrium constant K_1 of the reaction are, respectively [189]:

$$\Delta G_1^0 = -562288 + 170.57T = -RT \ln K_1, \tag{4.3}$$

$$K_1 = \frac{p_{CO_2}^2}{p_{CO}^2 p_{O_2}}. \tag{4.4}$$

Combining Eqs. (4.3) and (4.4), the oxygen partial pressure at equilibrium can be calculated by specifying the CO/CO_2 ratio and temperature (in K):

$$p_{O_2} = \exp\left(-67627.4\frac{1}{T} + 20.515\right)\left(\frac{p_{CO_2}}{p_{CO}}\right)^2. \tag{4.5}$$

The relation between the p_{O2} and the temperature in the range 1550 °C to 1650 °C is shown in Figure 4-4, for CO/CO_2 ratios of 10 and 20. The sensitivity of the p_{O2} value with temperature can be evaluated from the slope of the curves in the semi-logarithmic representation. If the CO/CO_2 equilibrium is assessed at 1600 °C, a decrease or an increase of 5 degrees in the temperature will generate an error of about 10% of the p_{O2} value at 1600 °C.

The CO and CO_2 gas flows were controlled by mass flow controllers and a Brooks microprocessor Control and Read Out Unit (Model 0152). The maximum flow of CO and CO_2 is, respectively, 0.5 and 0.1 l/min. The accuracy is 0.1% of maximum input/output range per channel. The set point of the CO mass flow was fixed at its maximum value of 0.5 l/min. The CO_2 mass flow was adjusted considering the desired CO/CO_2 ratio and set as slaved to the master CO channel.

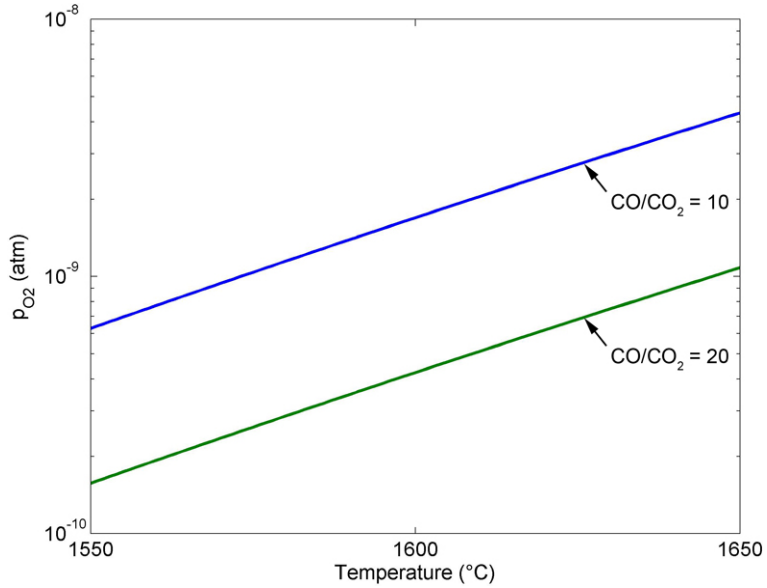

Figure 4-4: Relation of the equilibrium p_{O2} with temperature for CO/CO_2 ratios of 10 and 20.

The oxygen content in the furnace off-gas (Figure 4-1) was monitored with a solid state ceramic oxygen sensor (Rapidox 2100, Cambridge Sensotec Ltd). The sensor is heated at 650 °C, which means that CO-CO_2-O_2 equilibrium will be changed compared that in the furnace at 1600 °C and must be recalculated using Eq. (4.5). The range of measurement goes from 10^{-20} ppm to 100% O_2. The O_2 analysis is performed continuously and has a typical response time of less than 4 s. The accuracy is ± 1% of the actual measured value with a precision of ± 0.5%. The calibration requires two gas mixtures. To obtain a decent calibration in the low concentration ranges, air and a CO/CO_2 gas mixture with a ratio of 25 was employed.

4.4. Analysis techniques

After the experiments, two types of samples were obtained: pin samples from the Al_2O_3 sampling tubes and the remaining material in the crucible after quenching. The middle part of the pin samples were subjected to different analysis techniques to extract information on the inclusion number, size, composition, morphology and the metal composition. Four types of analysis are conducted on the samples:

- The measurement of the total oxygen content of the metal, which consists of oxygen dissolved in steel and oxygen present as oxides.

- Investigations with a Scanning Electron Microscope (SEM) equipped with an Automated Image Analysis software (AIA) provides information on the inclusion composition, number, size and spatial distribution from two-dimensional cross-sections.
- Wet chemical analysis gives the soluble and insoluble Al fraction in the steel sample. The soluble fraction corresponds to the dissolved Al content in the metal. The insoluble fraction represents the fraction of Al-containing inclusions in the sample.
- Inclusion extraction of the steel matrix is an appropriate way to assess the inclusion morphology as they are removed from the steel matrix.

4.4.1. Sample preparation

SEM-AIA measurements were performed on polished samples. The preparation included cutting perpendicular to the vertical axis of the pin or crucible sample, mounting in epoxy resin, grinding and polishing, and carbon coating to improve conductivity.

Steel samples intended for total oxygen measurement, wet chemical analysis and inclusion extraction were prepared with the following procedure. A small piece of the pin or crucible sample was cut at about 0.2 to 0.5 g, followed by grinding the surface of the material, washing in running water, ultrasonic cleaning in acetone, rinsing in acetone and drying. The samples were carefully weighed and stored in a desiccator.

4.4.2. Total oxygen measurement

The determination of the total oxygen in steel is an indirect method which is widely used to evaluate steel cleanliness. Because the dissolved oxygen content in Al-killed steel is low and approximately constant (< 10 ppm according to the equilibrium between Al and O during deoxidation), the total oxygen content is considered as a reasonable value of the total amount of oxide inclusions [20].

The total oxygen and nitrogen contents of the sample were determined with a LECO combustion analyszer using the inert gas fusion method. The principle is based on fusion of the 0.5 to 1 g sample in a high purity graphite crucible at temperatures up to 3000 °C in an inert gas (argon). The oxygen in the sample, in all forms present, reacts with the carbon of the crucible to form gaseous CO and CO_2. Nitrogen is released as gaseous molecular

nitrogen. Oxygen is detected as CO and/or CO_2 using infrared absorption, whereas nitrogen is measured by thermal conductivity. The calibration of the instrument is performed with standard steel samples of known oxygen and nitrogen concentrations, which are selected to be within the expected range of concentration of the unknown sample. The total oxygen measurement performed from a pin or crucible samples was repeated 2 to 3 times to obtain an average value. Abnormally high total oxygen results were disregarded due to possible surface oxidation.

4.4.3. SEM-AIA analysis

The SEM-AIA analysis combines the advantages of Energy Dispersive X-ray Spectrometry (EDX) with those of digital image analysis of Backscattered Electron (BSE) micrographs. This technique, also known as Computer Controlled Scanning Electron Microscopy (CCSEM), was developed in the 1980's for coal minerals [190], dust particles and fibres [191], aerosols, sediments in earth science [192], and so on. Application to imaging of fine inclusions was reported in 1988 by Schwoeble [193] from the RJ Lee Group. This technique provides accuracy, precision and fast measurements of composition, size and morphology for hundreds of particles and bulk materials. Nowadays, this technique is widely used for inclusion analysis in steelmaking owing to its numerous advantages.

4.4.3.1. Data collection

The SEM-AIA analysis was undertaken using a Jeol JSM-5900 LV SEM and a Philips XL-40 SEM equipped with Noran Energy Dispersive systems (EDS). The X-ray microanalysis system is a NORAN System Six system by Thermo Scientific (version 2), including the feature sizing package with chemical typing, which is used to automatically collect X-ray spectra, size and morphology of all objects.

Table 4-2: Fixed parameters for the AIA acquisition

SEM JEOL 5900 LV		SEM XL40	
Acceleration voltage	15 kV	Acceleration voltage	15 kV
Filament current	0.8 nA	Spotsize	5~6 nm*
Working distance	10 mm	Working distance	10 mm
Contrast	3300	Contrast	90 %

*The spotsize value is adjusted to have a detector dead time of about 30%

The samples were studied in the BSE contrast mode where the individual objects with a compositional contrast appear with different grey levels. Objects with a low average atomic weight, such as oxide, sulphide, or nitride inclusions, appear darker in the bright iron matrix (higher average atomic weight). To obtain reproducible images, the SEM parameters are fixed at specific constant values, which are summarised in Table 4-2 as a function of the SEM.

The settings of the BSE image must be adjusted to ensure that the inclusions with different compositions (Al_2O_3, CaO, MgO, MnS, …) and, thereby, different grey intensities on the BSE image are appropriately detected by the software. A binary image of the BSE micrograph is created by the image analysis function integrated in the software, which gives the grey level intensities of each pixel on the image (in arbitrary units from 0 to 65 535). The optimal condition to obtain a good segmentation between the matrix and the inclusions is to fix the grey level of the iron background at 60 000 grey scale units by adjusting the brightness. The grey-level intensity threshold between inclusions and the metal matrix is set at 50 000 grey level units, in such a way that the software will consider as an object any group of pixels that has a grey-level intensity between 0 and 50 000 units. An example of a grey-level segmentation is provided in Figure 4-5.

A grid of image frames covering a 25 mm^2 area was defined by entering the coordinates of the two opposite corners of the analysed area and by setting the required magnification at 250×. The image resolution is 2048 x 1576 pixels and the acquisition time is 40 s (response time 10 s). A guard region between each frame can be used to ensure that double measurements of large particles in the sample was avoided and that only particles that lay completely within the image frame were taken into account in the analysis. Objects with an area less than 0.75 μm^2 were excluded from the analysis to avoid the measurement of particles that are only a few pixels in size.

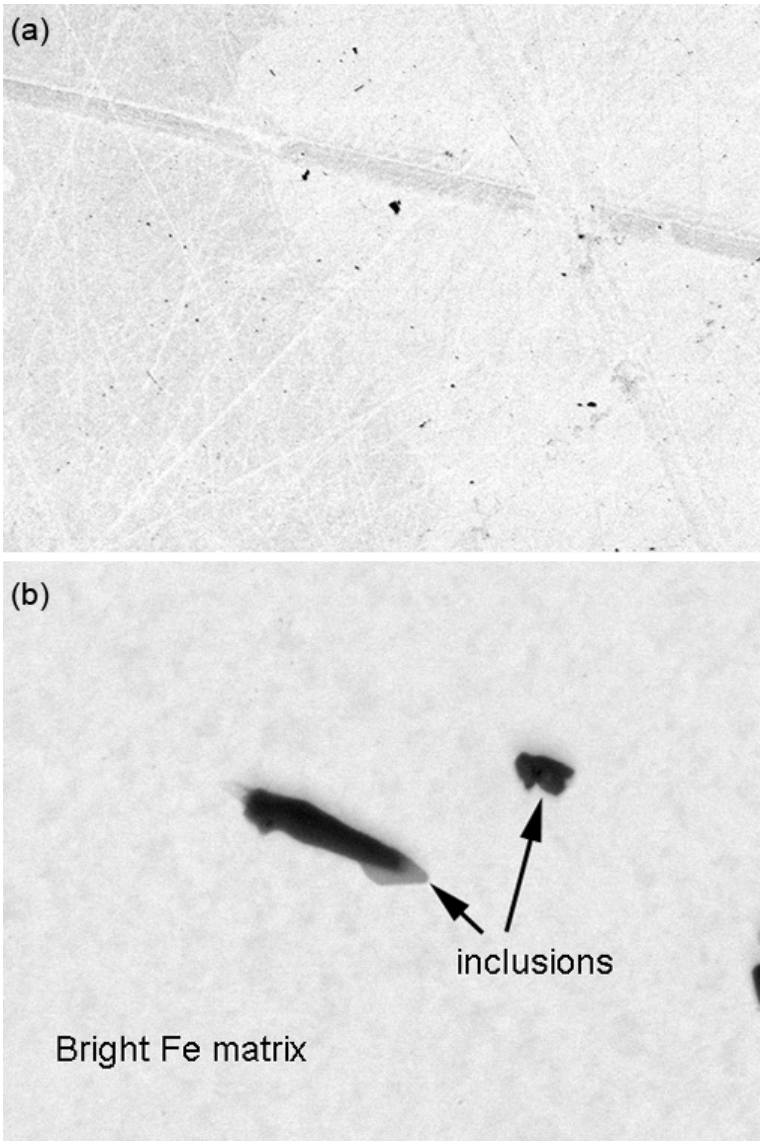

Figure 4-5: (a) BSE micrograph of a frame to be measured by AIA. The contrast and brightness have been adjusted for a good segmentation between the Fe matrix (bright) and the inclusions (black). (b) Enlarged view of the inclusions.

The created binary image formed the basis for the measurements of the object chemistry. The software commands the microscope to scan within the perimeter of each detected object to obtain the X-ray spectrum of the object. The EDS spectrum is acquired during 5 s by scanning the entire surface of the object (raster mode), providing an average spectrum of the feature. The

software calculates the contents, normalised to 100 %, of the usual elements found in steel, such as Mg, Al, Si, Mn, Ti, Ca, V, Cr, Nb, F, Na, P, S, Cl, K, which are predefined by the user. Fe and O are not quantified. In addition to these common elements, heavy metal elements, such as Cu, are also quantified from the spectrum. Spectra with a very low number of counts can be removed to ensure good measurement statistics. The software also enables to subtract the substrate spectrum. An EDS spectrum of the matrix is taken prior to the automated analysis. During the subtraction step, the software normalises the Fe peak of the background spectrum with that of the object spectrum. The remaining peaks after subtraction of both spectra are entirely attributed to the object chemistry. It should be noted that this subtraction has a major drawback when Fe-containing inclusions are present in the sample. In that case, the composition would be overestimated due to the removal of the Fe contribution. Also, pure iron oxide inclusions would be classified as non-inclusions, since the Fe peak in the spectrum is subtracted and the O peak is not quantified.

Commonly, 2000 objects were measured within 5 h. For each detected object, the software generates a result table listing the key morphological data based on pixel outline (area, perimeter, circularity, length, width, aspect ratio, orientation), the location on the sample (x-y coordinates) and the quantification after matrix subtraction (chemical classification, EDS max peak counts, total concentration and elemental concentration, in wt%). Also the full spectrum and images of each individual analysed frames and individual objects are saved. Spectrum files can be reprocessed without the need to physically reanalyse the sample.

4.4.3.2. Data reduction

The raw data are then processed to eliminate non- inclusion objects (holes, scratches, dust, etc.) using the following procedure. Objects with insufficient data in the spectrum after background subtraction are rejected (low spectrum intensity). After converting the weight to molar fractions, the sum of molar fractions, sum_{Elements}, of the typical elements found in inclusions in steel (= Mg + Al + Si + S + Ca + Ti + Mn + P + Cl + Na) is calculated for each object. The objects are sorted based on sum_{Elements} in a decreasing order and plotted against the object ordering number. The plot is used to determine the threshold of sum_{Elements} to accept objects as inclusions or to reject them. Typically, the curves show a high and approximately constant value of sum_{Elements}, usually above 0.8, over a large number of objects. The threshold is determined when sum_{Elements} starts to decrease abruptly, ensuring that the separation between inclusion and non-inclusion is sharp. All objects having a sum_{Elements} below this limit are rejected. These inclusions are mostly holes

and scratches, of which the spectrum is identical to the background, the Fe matrix. After the subtraction step, the spectrum does not contain any elemental peaks. Only fluctuations (noise) remain in the spectrum. The software attempts to quantify this spectrum based on the noise and gives a composition looking arbitrary. The quantification of heavy elements in the spectrum, such as Cu, allows the identification of these artefacts, as the Cu content will be arbitrarily high and sum_{Elements} will decrease. The objects containing a significant P, Cl and /or Na contents, typical of contamination, are also rejected.

In case of doubt, the spectrum and the image of the object can be examined manually and the classification of the object is judged according to the operator experience. The remaining objects are accepted as inclusions and are further classified in different categories as a function of their composition.

4.4.3.3. Data processing

Once the inclusion database has been processed to remove non-inclusion objects, the size distribution of the inclusions can be derived from the AIA measurements on the particle cross sectional area. The inclusions were classified and counted according to their size. The characteristic parameter chosen to describe the inclusion size is the equivalent diameter d. It is defined as the diameter of a circle with the same area as the particle (Eq. (4.6)).

$$d = 2\sqrt{\frac{\text{area}}{\pi}} \tag{4.6}$$

To draw the size distribution, the frequency of inclusions in a given bin (particle number per volume) is divided by the bin width. The latter is the definition of the Population Density Function (PDF) [194] and has length^{-4} units. Compared to classic (and popular) histograms, this representation of the size distributions eliminates the arbitrariness caused by the choice of the number and the size of the bins defined by the user. The PDF is unique for a given distribution and summarises the properties of the population. The use of the PDFs is therefore very functional to compare size distributions between different samples or studies. To illustrate this, Figure 4-6 (a), (b) and (c) show histograms of the same data set when different definitions of the bins are employed. The respective PDF curve calculated from the histogram is plotted on the diagram. It is clear that the three histograms are completely different and can yield different conclusions on the particle size

distribution, depending on the choice of the bins. On the other hand, the three PDF curves, which are gathered together in Figure 4-6 (d), are identical, providing a better way to display the size distribution.

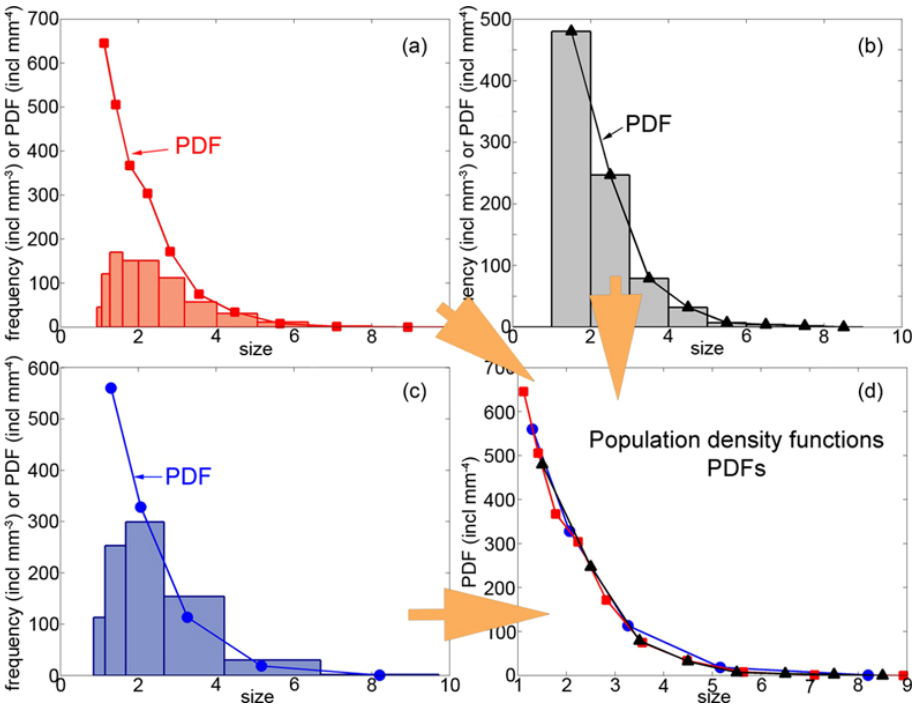

Figure 4-6: (a) to (c): Histogram and PDF representations of the size distribution of an identical data set using three different bin definitions. The three PDFs curves are superimposed in (d).

The AIA software gives access to two dimensional data, resulting from the intersection of the three dimensional inclusions with a plane. The estimate of the parameters in three dimensions calls upon stereology methods. It is essentially based on two aspects [78, 194]. The "cut-section" effect results from the fact that the intersection plane rarely cuts exactly through each particle centre. Figure 4-7 illustrates the results of the intersection of a cube and a prism by one hundred randomly oriented planes. The frequency of intersection length can be estimated for specific shapes, yielding specific size distributions of a monodisperse population. The second effect is called the "intersection-probability" effect and states that the probability of small particles to be intersected by a plane is less than for larger particles. In case of objects of complex shape, such as cluster, aggregate, dendrite, etc, the estimate of information on the number or volume of the objects based on cuts of the sample is difficult due to the complexity to identify them. Under these conditions, the solution obtained is not unique [194].

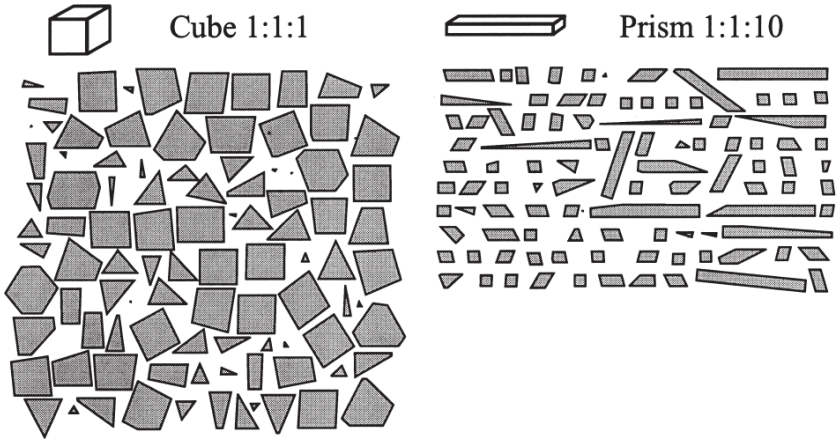

Figure 4-7: Intersections of one hundred randomly oriented planes with a cube and a prism elongated in one direction.

The conversion of two-dimensional to three-dimensional data was done using the program *CSDCorrections* that includes this correction method [194, 195]. A detailed description of the calculation method is provided by Higgins [194]. The raw data set of the equivalent diameters and the measured area are given as input to the software. The overall shape of the particles must be estimated using four parameters, namely the three aspect ratios (short, intermediate and long dimensions) and the degree of roundness. These parameters can be estimated from the examination of the particles shapes in the sample. Based on the two-dimensional raw data and the overall shape parameters, the software calculates the PDF curve, the total number and the total volume percentage of particles, and the goodness of the fit. In principle, the total volume percentage of particle is equal to the area percentage in the section [196], which is provided by the two-dimensional measurements and defined as the total area of the intersected inclusions divided by the analysed area. Therefore, the size distribution obtained by the software can be verified by comparing the calculated total volume fraction with the measured area fraction.

The divergence between the calculated total volume fraction and the measured area fraction usually arises from incorrect input shape parameters. The necessity to give the shape parameters as input to the software originates from the fact that the intersection of three-dimensional particles by a random plane will yield different sectioned shapes depending on the aspect ratios and the roundness of the true particle, as illustrated in Figure 4-7. For example, the frequency distribution functions for random intersection of a sphere, a cube or an elongated solid are different. As a result, the size distributions, calculated from the same two-dimensional data set, for a population of

spheres, cubes or elongated solids will be different. Also, the total volume fraction, which is derived from the calculated size distribution, will depend on the input shape parameters. In that case, the shape parameters can be adjusted so that the calculated volume fraction corresponds to the measured area fraction.

The shape of the size distribution is remarkably linear or quadratic in a logarithmic representation. Consequently, the most relevant statistical distributions to describe size-frequency distributions are respectively fractal (or power law) and lognormal distributions [85]. These distributions are entirely defined by two adjustable parameters. Moreover, the statistical properties of the distribution, such as the mode, the median, the standard deviation, etc. are easily accessible and facilitate the comparison of size distributions.

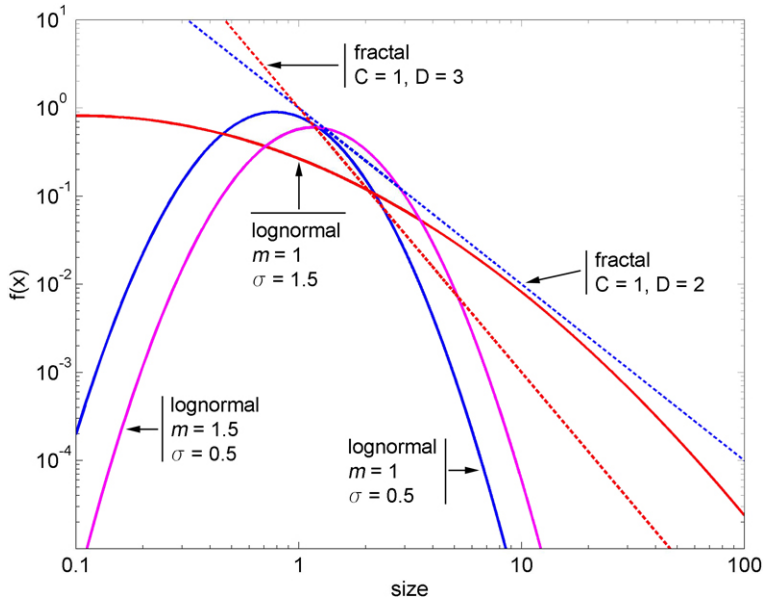

Figure 4-8: Comparison of size distributions on a log-log frequency *f(x)* versus size diagram. Lognormal and fractal distributions are represented, respectively, with solid and dashed lines. The parameters describing the distribution are indicated next to the curve.

A variable X has a lognormal distribution if $f(x) = ln(x)$ is normally distributed. The general formula for the probability density function of the 2-parameter lognormal distribution is given in Eq. (4.7), where σ_{ln} is the shape parameter and m the scale parameter (Figure 4-8, solid lines). A change in the scale parameter m affects the scaling in horizontal and vertical directions,

leaving the shape of the curve unchanged. The latter is specified by the value of the shape parameter $\sigma_{\ln}$, which is a measure of the skewness of the lognormal distribution compared with a normal distribution with the same median. The estimation of the parameters can be obtained by fitting a second degree polynomial curve to the empirical data points in a log-log frequency size diagram. The coefficients of the polynomial equation give access to the values of $\sigma_{\ln}$ and m according to Eq. (4.8).

$$f(x) = \frac{1}{x\sigma_{\ln}\sqrt{2\pi}} \exp\left(-\frac{\left(\ln(x) - \ln(m)\right)^2}{2\sigma_{\ln}^2} \right) \qquad m, \sigma_{\ln} > 0 \tag{4.7}$$

$$\begin{aligned} \ln\left(f(x)\right) = & -\frac{1}{2\sigma_{\ln}^2}\left(\ln(x)\right)^2 + \left(\frac{\ln(m)}{\sigma_{\ln}^2} - 1\right)\ln(x) \\ & - \left(\ln\left(\sigma_{\ln}\sqrt{2\pi}\right) + \frac{\left(\ln(m)\right)^2}{2\sigma_{\ln}^2} \right) \end{aligned} \tag{4.8}$$

The fractal or power law distribution is described by two parameters, a constant of proportionality C_{fract} and the fractal dimension D_{fract} (Eqs. (4.9) and (4.10)). In a log-log frequency size diagram, this distribution is a straight line, with a slope given by the fractal dimension D_{fract} (Figure 4-8, dashed lines). The main property of this distribution is the scale invariance.

$$f(x) = \frac{C_{fract}}{x^{D_{fract}}} \tag{4.9}$$

$$\ln\left(f(x)\right) = \ln\left(C_{fract}\right) - D_{fract}\ln(x) \tag{4.10}$$

The shape and location parameters of the power law distribution are accessed by plotting the probability distribution versus the size in a log-log diagram. After normalization, the fractal dimension D_{fract} in unchanged. Only the constant C_{fract} is modified to C'_{fract}. The definition of the probability density function of the power law distribution is given in Eq. (4.11).

$$PDF = \frac{km^k}{x^{k+1}} \tag{4.11}$$

where $k > 1$ is the shape parameter and $m > 0$ the location parameter. The values for k and m can be easily extracted from the linear fit of the data points after normalisation (i.e. $\ln\left(C'_{fract}\right)$ and D_{fract}):

$$k = D_{fract} - 1, \tag{4.12}$$

$$m = \left(\frac{C'_{fract}}{k}\right)^{1/k}. \tag{4.13}$$

Table 4-3: Definition of the statistical properties of the lognormal and power law distributions.

	Lognormal distribution [197-199]	Power law distribution [199]
Mean	$\exp\left(\ln(m) + \frac{\sigma_{\ln}^2}{2}\right)$	$\frac{km}{k-1}$
Median	m	$m(2)^{1/k}$
Mode	$\exp\left(\ln(m) - \sigma_{\ln}^2\right)$	m
Standard deviation	$\sqrt{\exp\left(2\ln(m) + \sigma_{\ln}^2\right)\left(\exp\left(\sigma_{\ln}^2\right) - 1\right)}$	$\frac{m}{k-1}\sqrt{\frac{k}{k-2}}$, $k > 2$

The important statistical properties of the lognormal and power law distributions derived from the scale and shape parameters, such as median, mode and standard deviation, are listed in Table 4-3.

In chemical engineering and earth sciences, the method of the size distributions is widely used to perform a quantitative study of the active processes in various physical systems. The main advantage of this method compared to traditional particle size analyses lies in the physical comprehension of the data. Writing the conservation of the crystal numbers in each segment of the size distribution leads to the conservation equation, which takes into account physical processes such as nucleation, growth, breakage, agglomeration, sintering and removal of crystals. It appears that the PDF is the fundamental variable in the population balance equation. Having access to the PDF provides thus a deeper and more quantitative comprehension of the physical processes described by these data [76].

4.4.4. Wet chemical analysis

The determination of acid soluble and acid insoluble Al was performed by acid dissolution and fusing in sodium carbonate, following the experimental method provided in [91, 200, 201] and described in the standard method for Inductively Coupled Plasma Atomic Emission Spectrometry (ICP-AES) analysis of iron and steel from the Japan Iron and Steel Federation (JIS G 1258-3).

About half a gram of metal sample was dissolved in 10 ml HCl (1 : 1) and 1 ml HNO_3 (1 : 1) and heated to 80~100 °C. Ultra pure grades of water and acids were used. After complete dissolution of the metal, the solution was vacuum filtered on a 0.2 µm polycarbonate membrane to separate the acid soluble and the insoluble fractions. The solution was analysed with ICP-AES (Varian Liberty series II instrument with an axial plasma configuration) to obtain the acid soluble Al fraction, which corresponds to the dissolved Al content in the metal. The residue on the filter containing the acid insoluble fraction was fused with 1 g reagent grade Na_2CO_3 in a Pt crucible and dissolved in 10 ml HCl (1 : 1) under heating (80~100 °C). The solution was analysed with ICP-AES to obtain the acid insoluble Al fraction, which corresponds to Al-containing inclusions. The standard solutions and blanks were prepared with the same acid concentrations as those of the sample solutions. Also the same amount of Fe and Na_2CO_3 as the sample solutions were added to the standards and blanks aimed at, respectively, the quantification of the acid soluble and insoluble Al fractions.

4.4.5. Inclusion extraction for morphology assessment

The method of extraction of the inclusions from the iron matrix was based on that developed by Dekkers [171, 172]. Inclusion extraction is one of the most appropriate method for the investigation of inclusion size, composition and morphology [16, 171, 202, 203] and is, therefore, widely used in literature.

The 0.2 g metal sample was dissolved in 10 ml HCl (1 : 1) and heated to 80~100 °C. Elemental iron is dissolved, while the Al_2O_3 inclusions remain mostly undissolved. Once the steel is completely dissolved, the iron solution is vacuum filtered and the inclusions are collected on a Nuclepore Polycarbonate membrane (PC MB, 25 mm diameter, Nuclepore Track Etch Membrane, Whatman) with 0.2 µm pore size. After the iron solution, the membrane is washed alternatively with hot water and hot diluted HCl (100 : 2), at least 5 times. The membrane is resistant to acid and appropriate for SEM investigation. Since the membrane and the oxide inclusions are non

conductive, the membrane was coated with carbon before microscopy investigation. Assessment of the inclusion morphology was performed with a high resolution SEM (XL30 FEG from Philips), equipped with an EDS spectrometer from EDAX. Inclusion size, morphology and composition are assessed with BSE and Secondary Electron (SE) detectors.

4.5. Conclusions

This chapter presented in detail the experimental procedures and techniques that were used in this study. The attention was given on the purity of the initial materials and on the control of the gas phase to study the formation of Al_2O_3 inclusions during reoxidation and deoxidation. The experimental procedure includes performing addition and samplings of the metal during the process without breaking the atmosphere.

The samples resulting from the deoxidation and reoxidation experiments were subjected to total oxygen determination, wet chemical analysis to obtain the acid soluble and the insoluble Al fractions, inclusion extraction to assess inclusion morphology, and SEM-AIA measurements to collect two-dimensional information on inclusion size, position, composition and morphology. The procedure to process the two-dimensional data and to obtain inclusion size distributions was discussed.

Chapter 5
Evolution of inclusion size distribution and morphology during deoxidation of liquid iron

The process parameters during the nucleation and growth of the inclusions will greatly influence the characteristics of the inclusion population, such as the size and the morphology. Controlling inclusion morphology, which is of fundamental importance for the production of cleaner steels or even tailored steel products, requires the comprehension of the processes leading to the formation of specific inclusion shapes, as well as the quantification of the relationship between oxide inclusion morphology and the main process parameters during their nucleation and growth.

The general strategy of the experiments presented in this chapter is to perform the deoxidation of liquid Fe by the addition of a large amount of Al (3 wt% Al), aiming to create high supersaturation conditions for the formation of inclusions. Although such high Al contents are not common for steels, the mixing process of Al in liquid steel shortly after the Al addition in the ladle can yield locally high Al concentrations and conditions where Al-rich melt encounters O-rich melt. By taking samples at specific time after Al deoxidation of Fe, this work examines the evolution of the inclusion population in terms of size and morphology distributions with holding time and soluble Al content in Fe.

5.1. Experimental procedure

Details on the experimental method can be found in Chapter 4. Deoxidation experiments were carried out with 80 g of electrolytic iron melted in a high purity Al_2O_3 crucible under purified argon, in which the typical value of the oxygen content before the deoxidation step was about 10^{-20} atm. According to the supplier specifications, electrolytic iron contains about 50 ppm total O.

After melting, the total O content varies between 100 and 150 ppm. After 30 minutes of stabilisation of the melt at 1600 °C, deoxidation was performed by adding pure Al into the melt following the procedure described in section 4.3.1 of Chapter 4. The amount of Al was weighed to obtain a final Fe-Al alloy containing 3 wt% Al. After the deoxidation of the melt, samples were taken at the crucible bottom and at specific time intervals using sampling tubes. Three tests were performed following the same procedure.

After the experiment, the samples were collected from the sampling tubes and cut in several pieces, of which each one is aimed at a specific analysis described in detail in section 4.4 of Chapter 4. The analyses included:

- Wet chemical analysis to obtain the soluble and insoluble Al content;
- SEM-AIA on the polished cross sectional area to obtain the number, size distribution and volume percentage of inclusions;
- SEM investigation of inclusions after their extraction from the metal matrix to assess their morphology.

5.2. Results and discussion

5.2.1. Aluminium dissolution in liquid iron

The evolution of the dissolved Al content in liquid Fe as a function of the holding time after the Al addition is shown in Figure 5-1. The results of three tests performed with the same procedure are shown. There is a significant discrepancy between the tests. The dissolution of the solid Al grains added in the melt was not immediate. More than 40 minutes was necessary to reach the final targeted Al concentration. Several facts are at the origin of this slow dissolution.

- Before the addition of Al, the motion of the liquid metal in the crucible is insignificant due to the very small temperature differences in the vertical direction (± 2 K) and radial direction (max 2 K).
- Given the small value of the Al diffusivity in liquid Fe [204] at 1600 °C (D_{Al} = 5.3 10^{-9} m^2 s^{-1}), transport of <u>Al</u> by diffusion is limited. According to our estimations, the diffusion length 1h is 4.4 mm, which is small compared to the height of the metal bath (approximately 1.5 cm).

- Liquid Al, three times lighter than liquid Fe, tends to remain at the surface.

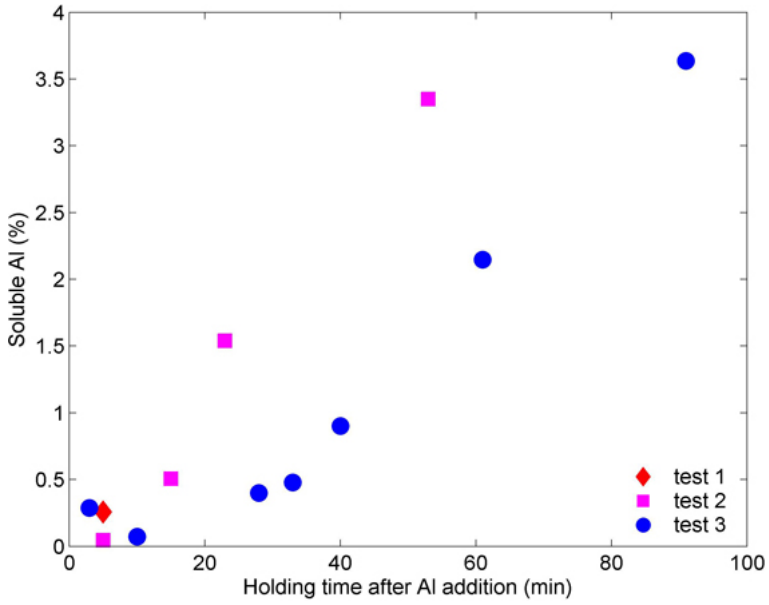

Figure 5-1: Evolution of the soluble Al content (in wt%) as a function of the holding time after the Al addition for three tests performed with identical conditions.

The overall mass transfer coefficient of Al in the liquid iron, k_m, can be estimated from the equation of molar flux J_D [mol m^{-2} s^{-1}] (Eq. (5.1)).

$$J_D = k_m \left(C^b_{\mathrm{Fe}} - C^i_{\mathrm{Fe}} \right) \tag{5.1}$$

where C^b_{Fe} and C^i_{Fe} are the bulk and interfacial molar concentrations of Al in the liquid iron phase, respectively. Assuming that the mass transfer of Al in the liquid iron is rate limiting, that all the Al is located on top of the liquid iron at the time t = 0, and that the temperature is constant, the relation between the Al concentration in the bath and time was found (Eq. (5.2)) [205].

$$-\ln\left(\frac{S_e - S(t)}{S_e}\right) = \frac{100 \cdot A \cdot k_m}{\left(100 - \frac{W_{\mathrm{Fe}}}{W_{\mathrm{Al}}} S_e\right) V} \cdot t \tag{5.2}$$

where $S(t)$ and S_e are, respectively, the concentration of Al in liquid iron at time t and at equilibrium (wt%), A is the interfacial area (m^2), W_{Fe} and W_{Al} are, respectively the weight of Fe and Al (kg), and V the volume of iron (m^3). The value of k_m can be estimated as $4\ 10^{-7}$ m s^{-1} from the slope of the straight line in the plot of $(-\ln((S_e - S(t))/S_e))$ versus time. In comparison with the typical value of $5\ 10^{-4}$ m s^{-1} found in gas-stirred systems [205, 206], the present system is indeed characterised by a lower mass transfer of Al through the liquid iron bath.

However, according to the above considerations, the evolution of the Al content as a function of the holding time after the Al addition does not correspond to the experimental results. Other factors have promoted the dissolution and mixing of Al in liquid Fe. When the Al grains, initially at room temperature, enter inside the liquid Fe, a shell around the Al is formed due to the temperature difference between the liquid Fe and the Al [207]. From a first approximation, if no heating was applied to the crucible, the temperature of the melt would drop from 1600 °C to 1518 °C when 2.5 g of Al at 25 °C is added to 80 g of liquid Fe held at 1600 °C. Due to the high thermal conductivity of metals, the Al would melt very fast, but a part of the liquid Fe would be solidified. The subsequent radial and vertical temperature gradient drives free (or natural) convection in the melt, providing some active stirring of the liquid. The nature of the flow (laminar or turbulent) can be evaluated from the Rayleigh number Ra. Its definition is given in Eq. (5.3), using the inner radius of the crucible as the length scale x. The temperature difference ΔT is taken as the difference between the crucible wall temperature (1602 °C) and the melting point of Fe (1538 °C).

$$Ra = \frac{g\beta\Delta T x^3 \rho_{Fe}^2 C_p}{\mu\kappa} \tag{5.3}$$

where g is gravitational acceleration (9.81 m s^{-2}), β the thermal expansion coefficient ($1.2\ 10^{-4}$ K^{-1}), ρ_{Fe} is the density of liquid iron (7000 kg m^{-3}), C_p the heat capacity (824 J kg^{-1} K^{-1}), μ the viscosity (0.005 kg m^{-1} s^{-1}) and κ the thermal conductivity (34.6 W m^{-1} K^{-1}). The Ra number is equal to $6\ 10^4$, which is in the laminar flow range [208] ($10^3 < Ra < 10^9$). In addition, the strongly exothermic deoxidation reaction will generate significant local temperature gradients and rather turbulent convection. However, the amount of oxygen in the melt is not sufficient to balance the temperature drop caused by the addition of the large amount of Al. Simultaneously, the furnace will reheat the charge within a few minutes and stabilize at 1600 °C. The time necessary for the iron to reach its initial temperature (1600 °C) can be roughly estimated from the temperature profile for unsteady-state heat conduction in an infinite cylinder [209, 210]. Imagining that the melt is the cylinder and assuming that its surface is maintained at T_1 = 1602 °C, it

would take about 40 seconds for the liquid Fe to reach 1600 °C at the axis of the cylinder initially at T_0 = 1518 °C. Taking into account that (1) the temperature of the crucible wall is affected by the temperature drop of the iron, (2) the material is not infinite, and (3) the iron will remelt once its melting point is passed, it would take a few minutes before the melt is stabilized at 1600 °C.

In addition to the temperature gradient and the Al concentration gradient (due to transport), the dissolved oxygen content may vary according to time and temperature. The precipitation of Al_2O_3 inclusions in regions with an existing supersaturation degree drastically decreases the local dissolved O content. Moreover, once the temperature drops, the precipitation of oxide particles will take place, due to decrease of the oxygen solubility in liquid Fe.

The presence of an Al gradient through the sample height was confirmed by two additional tests conducted with the same deoxidation procedure as previous tests, except that the entire crucible sample was removed from the furnace (with the help of a Mo hook) after a specific holding time of 2 and 10 min after the Al addition, and subsequently quenched in water. The Al content was measured throughout the cross section of the crucible samples by SEM-EDS analysis. The contour plots of the Al content are given in Figure 5-2 (a) and (b) for, respectively, a holding time of 2 min and 10 min after the Al addition.

Without external stirring, the Al remains in the upper half of the sample even after 10 min. The Al content is high near the melt surface and decreases rapidly with sample depth. The maximum Al content measured at the melt surface attained 20.4 wt% and 22.1 wt% in sample with a holding time of, respectively, 2 min and 10 min after the Al addition. The lower maximum Al content after 2 min compared to that after 10 min is most likely due to the presence of large holes at the melt surface of the sample with 2 min holding time (Figure 5-2 (a)). As the melt surface is irregular, the location with maximum Al concentration is more difficult to find.

The measurements of the soluble Al concentration are in agreement with those obtained from samplings performed at the bottom of the crucible, as shown in Figure 5-1. Less than 1 wt% Al was detected in the samples within a holding time of 10 min. It is expected that the Al dissolves and mixes with the iron with increasing holding time, as suggested by the time evolution of the soluble Al content in Figure 5-1.

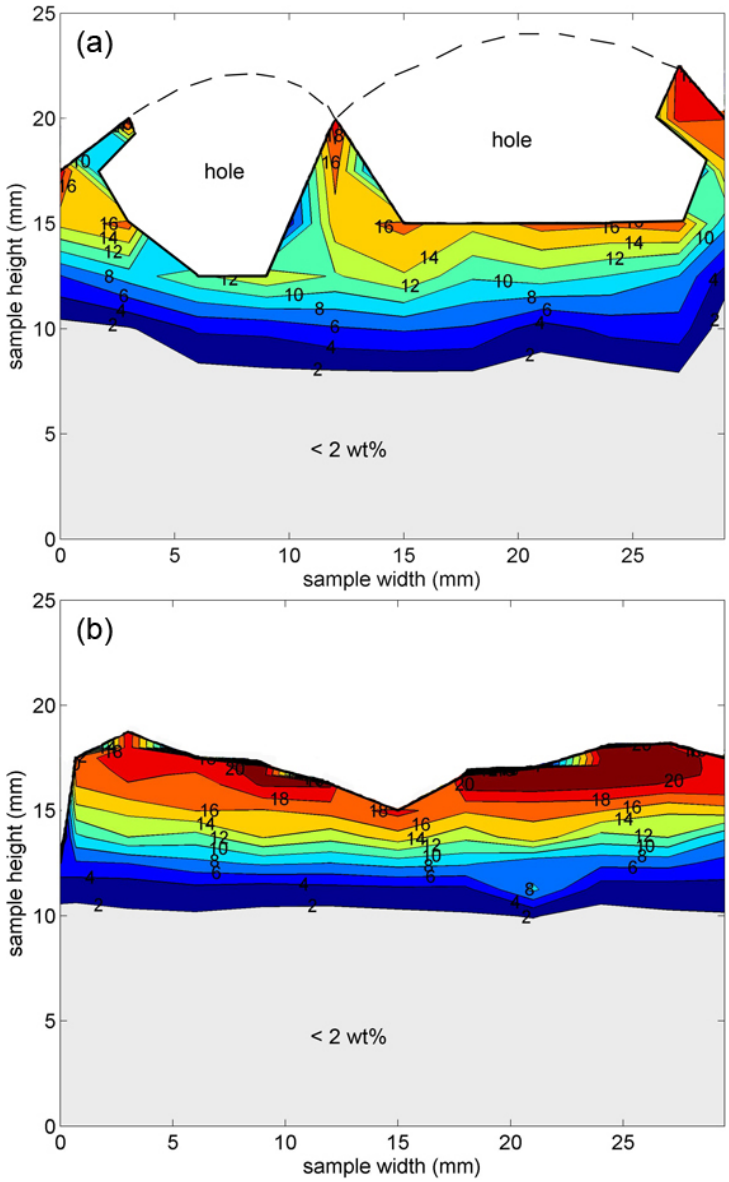

Figure 5-2: Contour plots of the Al concentration (in wt%) throughout the sample cross section after a holding time of (a) 2 min and (b) 10 min after the Al addition.

5.2.2. Inclusion number and size distribution

5.2.2.1. Inclusion number

The evolution of the inclusion number is described by the volume fraction of inclusion as a function of the holding time after Al addition (Figure 5-3). The inclusion volume fraction derived from the insoluble Al fraction (chemical analysis) is compared to the AIA measurements.

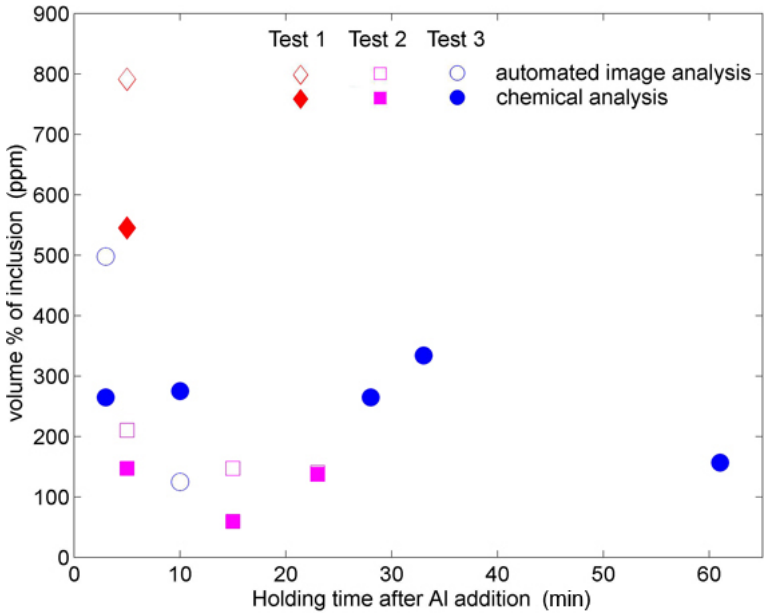

Figure 5-3: Evolution of the inclusion volume fraction derived from AIA measurements and chemical analysis (insoluble Al fraction) as a function of the holding time after Al addition.

In the first 15 minutes, the difference between the volume fraction obtained by chemical analysis and by image analysis is significant. The volume fraction obtained by AIA shows a high value followed by a fast decrease with holding time, which may be attributed to inclusion growth and removal to the surface (flotation). In contrast, the value given by the chemical analysis remains almost constant with time and is in general lower than that derived from the AIA measurements. This difference may be the result of acid dissolution of a part of the inclusions. Small size inclusions which are found in great quantity shortly after deoxidation are likely to be dissolved during the acid treatment. Filtration, aimed to separate the non-acid-dissoluble inclusions from the acid solution, cannot be the main cause for the

loss of small inclusions, since those that are small enough to pass through the pores of the filtering membrane (0.2 µm pore size) would not be included in the AIA analysis (sieve on particle area set at 0.75 μm^2). Furthermore, strong variations of the inclusion distribution in the sample volume may have an influence.

An important aspect in the treatment of the AIA measurements to be underlined is the surface to volume conversion. While chemical analysis gives the true volume fraction in a given mass of material, the volume fraction derived from the AIA measurements is drawn from the area of the two-dimensional inclusion cross sections. The estimation of the parameters in three-dimension calls upon stereology, a method based on statistical en geometrical principles. In the presence of objects with complex shapes (cluster, aggregate, dendrite, etc.), the information on objects based on two-dimensional sample cuts is hard to estimate because of the difficulty to identify them. In these cases, the solution obtained is not unique [194].

5.2.2.2. Size distribution

The size distribution of the inclusion population was derived from the AIA measurements on the inclusion cross sectional area. The conversion of two-dimensional to three-dimensional data was carried out using the program *CSDCorrections* that includes a correction method based on stereological analysis (section 4.4.3.3 in Chapter 4). The inclusions were classified and counted according to their size. The characteristic parameter chosen to describe the inclusion size is the equivalent diameter *d*. It is defined as the diameter of a circle with the same area as the inclusion. The PDF method was applied to the data obtained from the deoxidation experiments. The empirical data and the polynomial fit of the size distributions for the first samples of tests 1, 2 and 3 are plotted in Figure 5-4. The adjustable parameters and statistical properties of the distributions are summarised in Table 5-1. The comparison of the shape and the characteristics of the curves highlighted several interesting observations.

Most of the curves represented in these logarithmic diagrams are approximately quadratic, symmetrical concave downwards. The PDF curve passes through a maximum and tends to zero with increasing inclusion size. The log-normal probability density function can be used to represent this inclusion size distribution. The first sample of test 3 (holding time of 3 minutes and Al content of 0.29 wt%) provides an exception to these observations. The amount of small inclusions having an equivalent diameter below 1.5 µm is much larger than in the other distributions. The shape of the

PDF curve changes to a straight line in the logarithm representation, providing a fractal (or power law) distribution.

Table 5-1: Statistical distribution, adjustable parameters and statistical properties estimated from the empirical probability density function as represented in Figure 5-4 and Figure 5-5.

test	holding time (min)	Al content (wt%)	statistical distribution, adjustable parameters and estimated statistical properties (µm)					
			Log-normal		mean	median	mode	standard deviation
			σ_{ln}	m				
1	5	0.26	0.5	2.4	2.6	2.4	1.9	1.3
2	5	0.04	0.5	1.7	1.9	1.7	1.3	1.0
	15	0.50	0.6	1.5	1.7	1.5	1.1	1.0
	23	1.54	0.5	1.6	1.7	1.6	1.2	0.9
3	10	0.07	0.6	1.7	2.0	1.7	1.3	1.2
	3	0.29	fractal $C_{fract} = 3.3$, $D_{fract} = 3.9$		1.6	1.3	1.1	1.0

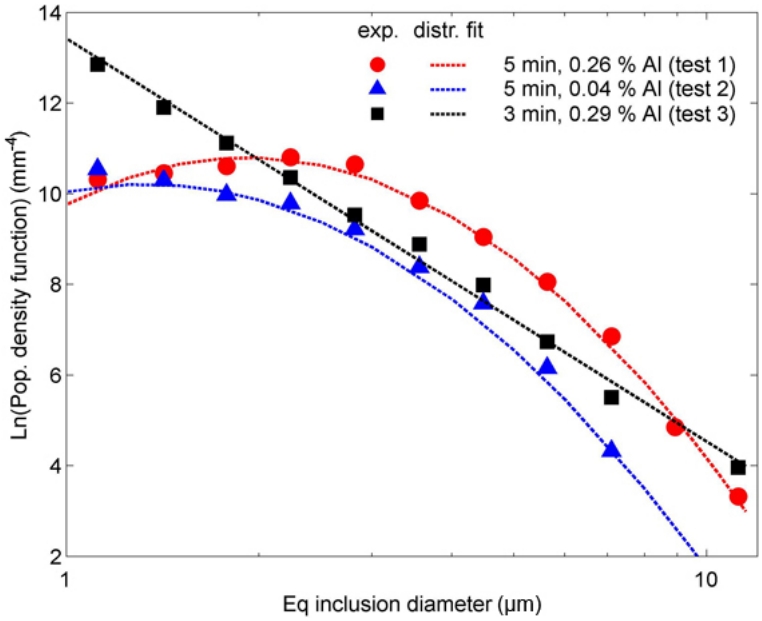

Figure 5-4: Inclusion size distribution determined by AIA measurements. Each curve represents a sample with a holding time of 3 or 5 min and a soluble Al content of 0.04 or 0.3 wt%. The full markers represent the experimental distribution, while the dotted lines indicate the statistical distribution estimated from the experimental data.

The comparison of the size distributions in Figure 5-4 points out that the main differences appears with the samples taken within 5 min after the Al addition. Short holding time and high Al concentration lead to the emergence of numerous small inclusions in the sample of test 3. With comparable dissolved Al concentration (0.26 wt%) but longer holding time (5 min), the amount of small inclusions having an equivalent diameter lower than 2 µm is less on the sample surface of test 1, while the frequency of inclusions whose equivalent diameter is included in the interval 2 µm – 10 µm is larger. With similar distribution shape and holding time but a lower Al content (0.04 wt%), the most frequent value of the population density function in test 2 is reached at a smaller inclusion size (1.3 µm). The values of the mean and median, respectively 1.9 and 1.7 µm, are also comparatively lower.

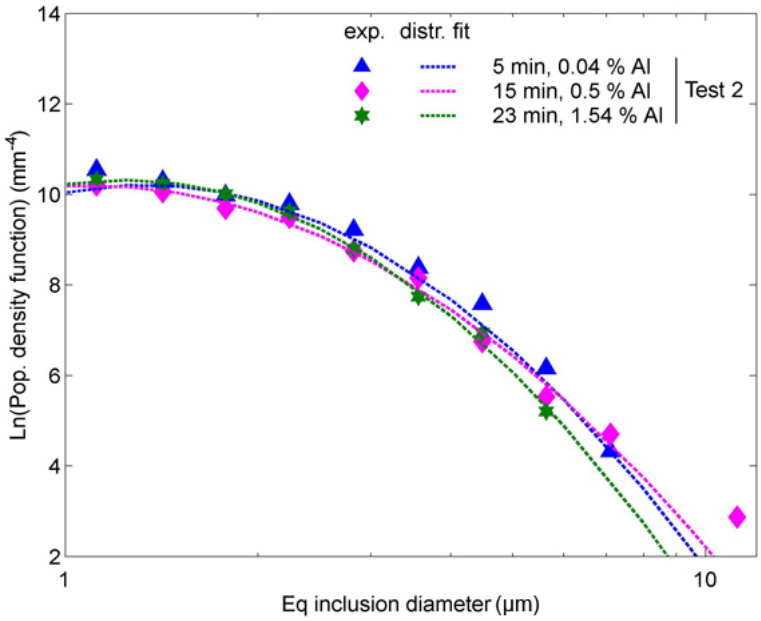

Figure 5-5: Inclusion size distribution determined by AIA measurements. Each curve represents a sample of test 2 with increasing holding time and soluble Al content. The full markers represent the experimental distribution, while the dotted lines indicate the statistical distribution estimated from the experimental data.

The evolution of the size distributions of three samples taken during test 2 depicted in Figure 5-5 reveals no particular changes between the samples, even if the holding time and the Al content change significantly. This would indicate that the precipitation and the growth processes are over or significantly slowed down, leaving the size distributions almost unchanged

with holding time. Indeed, the remaining small inclusions have a low settling velocity and a low collision frequency, which doesn't promote their growth and removal from the liquid bath.

5.2.2.3. Inclusion morphology

Several inclusion morphologies were recognised during the SEM investigation of the inclusions after their extraction from the metal samples. The distribution of the morphologies observed amongst the inclusions is depicted in Figure 5-6.

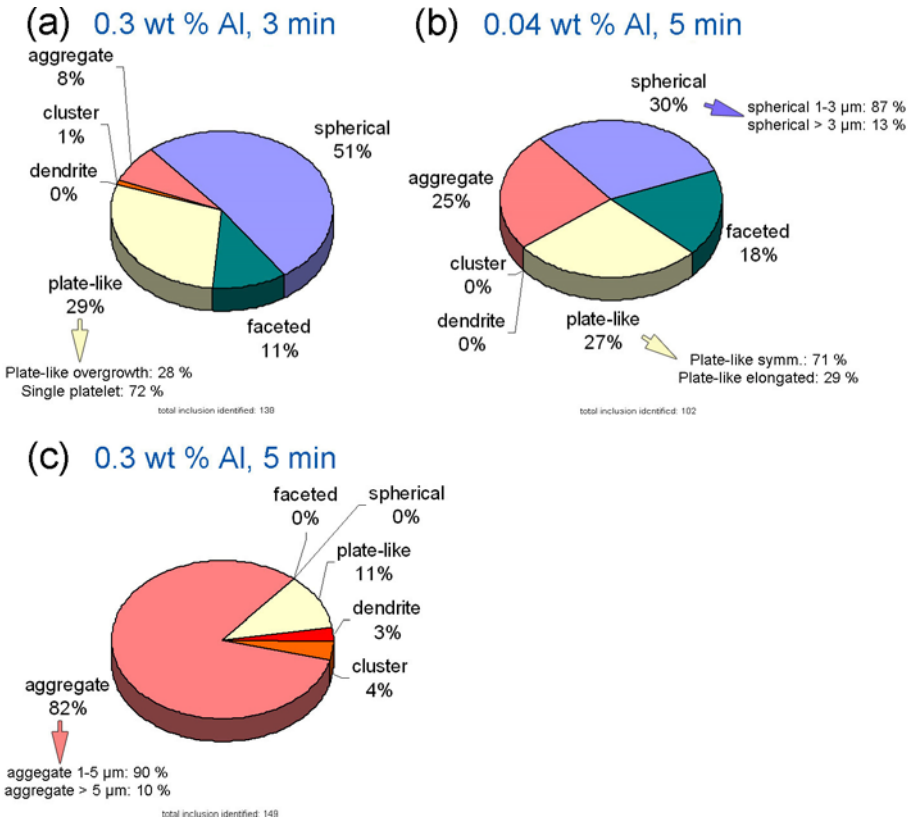

Figure 5-6: Distribution of the inclusions according to their morphology in the first samples resulting from (a) test 3 (3 min, 0.29 wt% Al), (b) test 2 (5 min, 0.04 wt% Al) and (c) test 1 (5 min, 0.26 wt% Al).

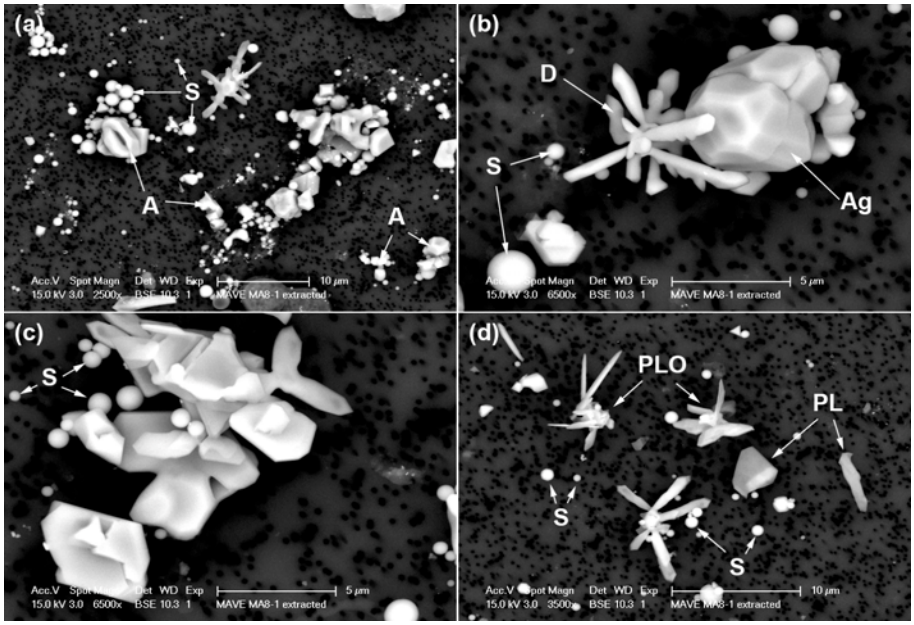

Figure 5-7: Overview of the inclusion morphologies after acid extraction of the sample with 0.3 wt% dissolved Al and a holding time of 3 minutes after the Al addition (test 3). (a) spherical inclusions [S] are abundant and less than 2 µm sized, angular inclusions [A] are larger. (b) dendritic cluster [D] and large agglomerate [Ag] of faceted inclusion, leading to the formation of a large polyhedral inclusion. (c) occurrence of a cluster of plate-like inclusions. (d) occurrence of plate-type overgrowth on an inclusion at the centre [PLO], and individual plate-like inclusions [PL].

In the sample with a holding time of 3 minutes and 0.3 wt% dissolved Al (test 3), spherical, plate-like, faceted and aggregated inclusions were identified among the dominant morphologies (Figure 5-7). Spherical inclusions dominate largely the morphologies (Figure 5-6 (a)) and are typically less than 2 µm size, while faceted shapes are observed for inclusions with a diameter above 2 µm (Figure 5-7 (a) and (b)). The fact that the morphology distribution is dominated by small inclusions is in agreement with the size distribution of the inclusion population (Figure 5-4). The latter shows that the inclusion frequency in the size range 1-2 µm is considerably larger than in the other size distributions. Large clusters (> 15 µm) of plate-like inclusions were noticed (Figure 5-7 (c)). Indications of agglomeration and sintering processes were found amongst the angular inclusions (Figure 5-7 (b)). The observation of plate-type overgrowth on existing small inclusion was also numerous (Figure 5-7 (d)). The latter may be the result of a second growth stage from the inclusion located at the centre, while the growth conditions have changed.

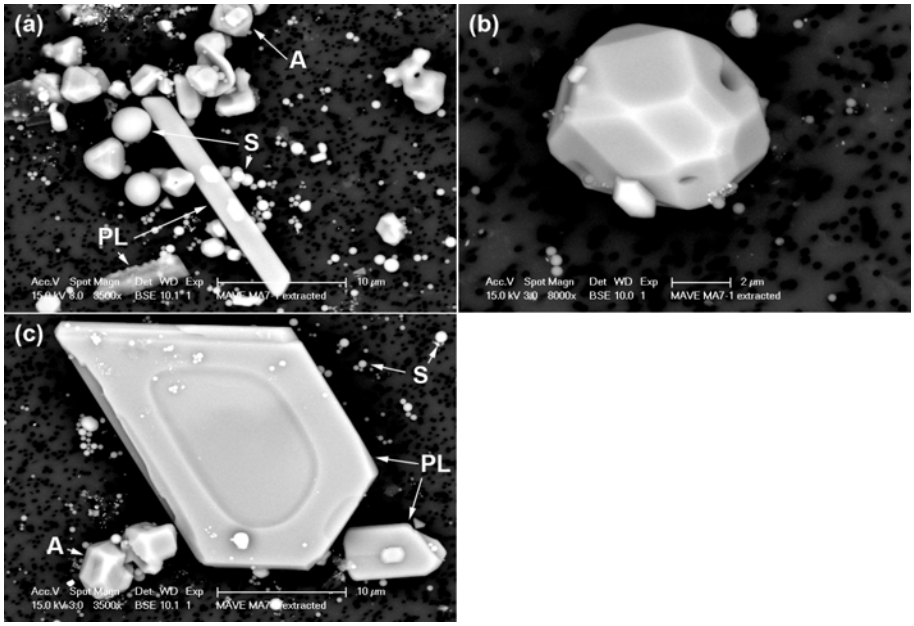

Figure 5-8: Overview of the morphology of the inclusions observed in the sample containing 0.04 wt% dissolved Al with a holding time of 5 minutes (test 2, after acid extraction). (a) many sub-micrometer spherical inclusions [*S*] were observed. Singular larger spherical inclusions of 1.5 to 3 µm were also found. Faceted inclusions [*A*] and aggregates of angular inclusions are the main morphology for the 2 to 10 µm range. Plate-like inclusion [*PL*] may have different shapes. (b) large faceted inclusion. (c) large plate-like inclusions.

In the sample with a holding time of 5 minutes and a lower Al concentration (0.04 wt% Al, test 2), the morphologies distribution is almost equally divided between spherical, plate-like, aggregated and faceted shapes Figure 5-6 (b)). The sub-micrometer inclusions are spherical, but singular larger spherical inclusions (up to 2 to 3 µm diameter) were found as well (Figure 5-8 (a)). Faceted inclusions are observed in a vast range of sizes (Figure 5-8 (a) and (b)), overlapping with the spherical series. Holes were observed in some of the large angular inclusions (Figure 5-8 (b)), probably resulting from sintering and densification of an aggregate. Next to aggregates of angular and of plate-like inclusions, large individual plate-like inclusions (> 10 µm) are frequent (Figure 5-8 (c)).

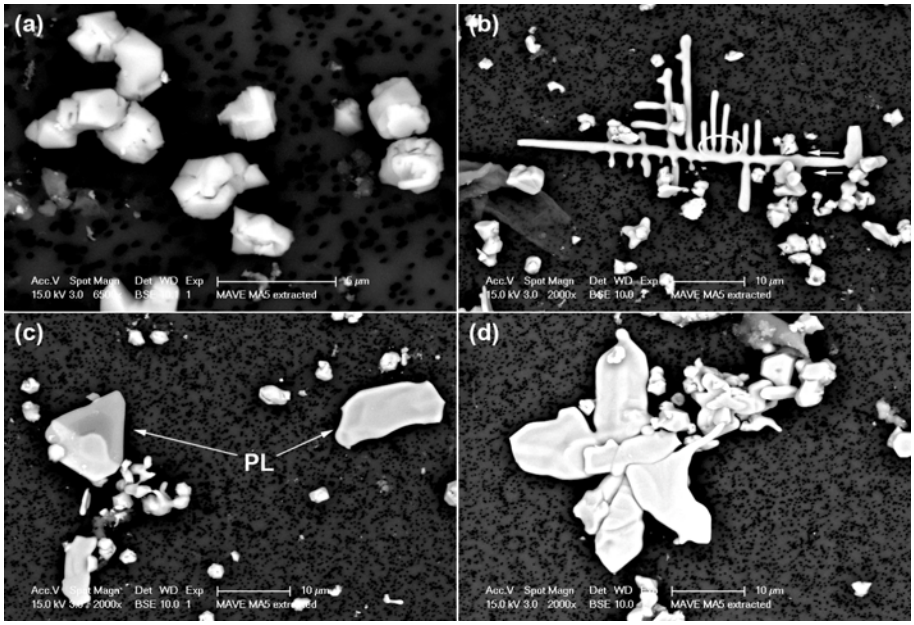

Figure 5-9: Overview of the morphology of the inclusions observed in the sample containing 0.3 wt% dissolved Al with a holding time of 5 minutes (test 1, after acid extraction). (a) aggregates of small angular inclusions, forming larger polyhedrons after sintering. (b) large dendrite likely to have started to grow from an inclusion located on the right (arrows indicate the growth direction). Note the necking of the dendrite arms (encircle). (c) example of individual plate-like inclusions [*PL*]. (d) plate-like cluster.

In the sample with a holding time of 5 minutes and 0.3 wt% Al (test 1), aggregates belonging to the 1 to 5 µm size range are by far the dominant morphology (Figure 5-6 (c)). They seem to be the result of accretion and densification of smaller angular inclusions (Figure 5-9 (a)). The large frequency of these inclusions is reported in the corresponding inclusion size distribution (Figure 5-4) where the PDF curve shows a maximum for an equivalent diameter of 1.9 µm. The major difference with the previous samples is the absence of spherical inclusions amongst the investigated inclusions, while larger inclusions occur as dendrites and dendritic clusters (Figure 5-9 (b)). The dendrite arms show neck formation at their base, possibly leading to the dismembering of the dendrite arm from the primary dendrite. Some individual 10 µm sized platelets (Figure 5-9 (c)) and plate-like shaped clusters (Figure 5-9 (d)) were found as well. There may be evidence of some transition between dendritic shaped and faceted morphology.

The samples are characterized by a large variety of different inclusion shapes. Similar particularities in inclusion shapes were observed in investigated industrial samples [173]. The comparison between the size and the morphology distributions charts indicates that the increasing frequency of aggregates among the inclusion shapes is associated with a downward concave curvature of the PDF. Due to the complexity of the phenomena leading to the morphology distribution of the inclusions, further studies are required to investigate in detail the correlation between inclusion morphology, Al content in Fe and holding time.

5.3. Summary and conclusions

Deoxidation of liquid Fe was performed by the addition of a large amount of Al at 1600 °C. Samples were taken at specific moment to investigate the evolution of the inclusion size and morphology as a function of time and Al content. The characterisation of the inclusion population in terms of size distribution and morphology highlighted the following aspects:

- The dissolution of Al in the liquid Fe was found to be slow under the present experimental conditions. After the Al addition to the melt, a temperature gradient, along with Al and O concentration gradients are created through the melt, generating complex conditions for inclusion growth.
- The inclusion size distribution was described using PDFs. This representation provides a highly practical form of summarizing the properties of a specific inclusion population. It is easy to compare and independent of the user. Combined with a curve-fitting method, a graphical estimation of the adjustable parameters and properties of the statistical distribution are easily accessible.
- The curves of the PDF exhibited different shapes, which were approximated by two distinct statistical distributions. Significant differences were reported in the parameters and main properties of the distributions describing the inclusion populations shortly after deoxidation. These differences in the shape of the PDF curves originate from various growth mechanisms.
- The diversity in inclusion shapes observed in the samples, especially the presence or absence of specific morphologies, indicate the occurrence of different growth mechanisms. Similar particularities in inclusion shapes were observed in investigated industrial samples.

With the present experimental approach, it is difficult to estimate the conditions at which the inclusions were formed and grew from those

prevailing during sampling. Clearly, the melt inhomogeneity resulting from the deoxidation stage created different local conditions, which are reflected in the inclusion characteristics. As the Al mixing was found to be slow, whereas the formation of Al_2O_3 is believed to occur very fast, it would be ideal to evaluate inclusion characteristics shortly after their formation. In the next Chapter, a novel experimental approach will be presented, enabling the observation of inclusions in the initial stage of deoxidation.

Chapter 6
Formation and morphology of Al_2O_3 inclusions at the early stage of deoxidation

In the previous chapter, deoxidation of liquid Fe was performed by the addition of Al at 1600 °C. Addition of a large amount of Al created a time-dependent temperature as well as Al and O gradients in the melt. These complex conditions for inclusion growth were reflected in the inclusion size distributions and morphologies. The relation between the conditions during the nucleation and growth of the inclusions and their characteristics was difficult to obtain owing to the inhomogeneous and time-dependent melt conditions. Therefore, another experimental approach was developed in order to enable the investigation of inclusion formation and morphology shortly after the interactions between liquid Fe and Al. The experimental method, in a way similar to the diffusion couple technique, consisted in bringing a piece of Al in contact for a very short time with liquid Fe containing different oxygen levels at 1600 °C.

In the first part of the present chapter, the microstructures of the reaction zone are examined and interpreted in order to study the interactions between Fe and Al and to identify the nature of the phases during the experiments. The second part of the chapter is dedicated to the formation and morphology of Al_2O_3 inclusions, resulting from the reaction between Al and dissolved oxygen in liquid Fe. The influence of the dissolved oxygen content and the interaction time on their growth and morphology is discussed.

6.1. Experimental procedure

The details of the experimental procedure were given in Chapter 4. 100 g of electrolytic Fe, put in an alumina crucible was melted at 1600 °C under purified argon atmosphere. The oxygen content in the melt was adjusted by

the addition of reagent grade iron oxide powder (Fe_2O_3), followed by stirring with an Al_2O_3 rod. The impurity level of the electrolytic Fe being low, the dissolved oxygen, (O) is assumed equal to the total oxygen content. The latter was determined by combustion analysis on the bulk Fe of the samples.

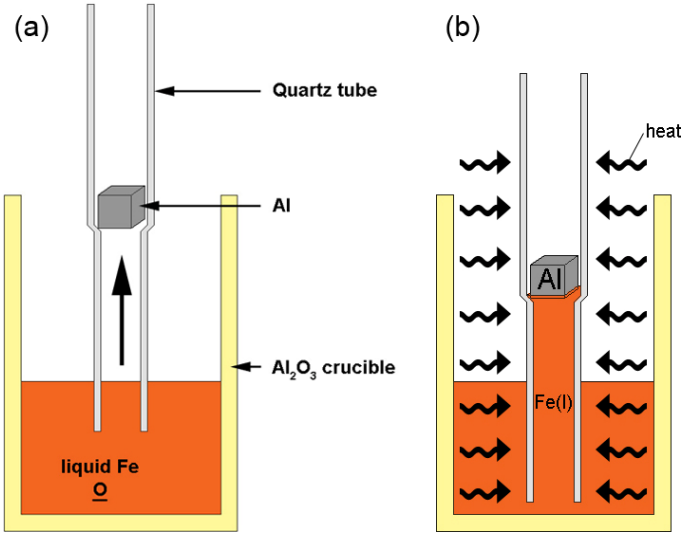

Figure 6-1: Experimental setup: schematic representation of (a) Fe suction inside the quartz tube and (b) the material being subjected to heating during the interaction.

A piece of Al (99 % Al) was cut in a cubic shape (~5 mm side), ground, pickled in 5% NaOH solution for 1 min, followed by washing in demineralised water, rinsing in acetone and drying. The Al piece was placed inside a quartz tube (8 mm inside diameter, 10 mm outside diameter). The last 3 cm of the quartz tube was narrower in order to fix the Al piece (6 mm inside diameter, 8 mm outside diameter). After 30 min at 1600 °C to stabilize the temperature of the melt, the quartz tube containing the Al piece was quickly introduced inside the liquid Fe. The Al piece was not preheated to avoid melting before the interaction. A small volume of molten iron was sucked in the tube and brought into contact with Al (Figure 6-1 (a)). Except for sample 4, the contact between Fe and Al took place at the lower facet of the cubic piece of Al. In case of sample 4, the contact was made at a corner of the Al piece. During the interaction between Fe and Al, the quartz tube was maintained at that position in the liquid Fe, so that the material inside the tube was subjected to the furnace heat (Figure 6-1 (b)). After the desired reaction time, the quartz tube was rapidly withdrawn from the metal bath, removed from the furnace and quenched in water. Maximum 4 s elapsed during the sample removal procedure. The contact time between liquid Fe and Al in the furnace hot zone varied from 1 s to 60 s. The detailed

conditions for each test are listed in Table 6-1. After the experiments, the upper part of the samples were cut along the longitudinal axis and prepared for SEM investigations following the analysis procedures described in Chapter 4.

Table 6-1: Details of the experimental procedure.

Sample	Initial O content (ppm)	Contact time (s)
1	160	30
2	450	1
3	780	1
4	1800	1
5	1800	5
6	1800	60

Calculations of the shell period and the temperature profile as a function of interaction time and position relative to the cold end of Al were performed using Pandelaers' model [211-213]. The authors empirically and theoretically investigated the microstructural development of the reaction zone between Ti and a solid Fe shell, using a one-dimensional sharp interface model which considers mass and heat transport in all phases. In the present work, the description of the problem was simplified to a one-dimensional heat and mass transfer along the vertical direction *Z*. Al was initially held at 25 °C and bounded between $Z = 0$ (cold end of Al) and $Z = 5$ mm (initial interface), forming a plate of 5 mm thickness with infinite width and thickness. Liquid Fe at 1600 °C entered into contact with cold Al at $Z = 5$ mm. The heating provided to the side wall (Figure 6-1 (b)) by the furnace was not considered. The details on the formulation of the model are provided in reference [212]. Essentially, it is assumed that thermodynamic equilibrium is valid at each interface, where the temperature-concentration relation is given by the phase diagram. The intermetallic phases thermodynamically stable were initialized with 1 μm thickness. Diffusion in the solid phases was not considered due to the lack of information on the diffusion coefficients in the Fe-Al intermetallic compounds. This simplification should not be too far from reality since diffusion in a solid phase is far slower than in a liquid phase. The information on the diffusion in the liquid phase was taken from the DICTRA database. It was found that the diffusion data are not optimised since the diffusion coefficient was constant at $1\ 10^{-9}$ $m^2\ s^{-1}$. For these reasons, the concentration profiles are not discussed. Also no convective transport has been considered in the reaction zone.

6.2. Interactions between Fe and Al

6.2.1. Introduction

Due to the large temperature difference and the heat transfer between Fe and Al, Al in contact with Fe will heat up and partly melt, whereas Fe will solidify at the interface, forming a shell. The solid shell grows to a maximum thickness determined by heat transfer balance [207, 214]. As the melting point of Al is much lower than that of steel, Al normally melts completely inside the shell. Once the solid shell melts back, the content of the encasing steel shell is then released in the melt. During the shell period, interactions between solid Fe and liquid Al may give rise to the formation of Fe-Al intermetallic compounds with a melting point intermediate between steel and Al. Their lower melting point and the heat generated during their formation may contribute to the shell melting.

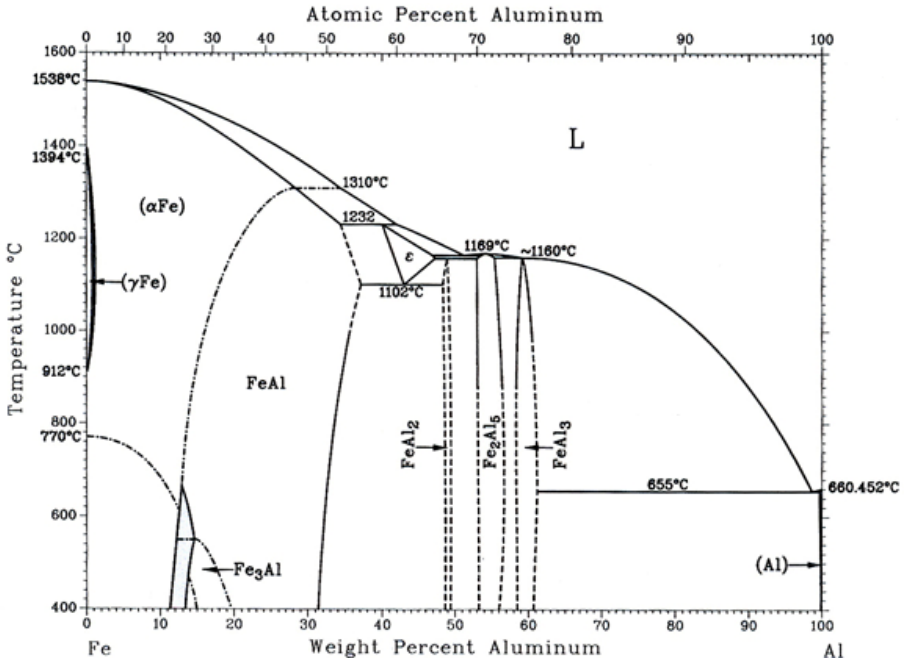

Figure 6-2: Binary phase diagram of Fe-Al system [215].

The phase diagram of the binary Fe-Al system is shown in Figure 6-2 [215-217]. On the left hand side of the diagram, it can be seen that the solubility of Al in f.c.c. γ-Fe is limited to a few percents. In disordered b.c.c. α-Fe, up to 28 wt% Al can be dissolved depending on temperature. The Fe solid

solution dissolving some Al is noted αFe(Al) in the text. Intermetallic phase formation can occur from 12 wt% Al. Six non-stoichiometric intermetallic compounds are listed in the Fe-Al binary system. Depending on the Al content, Fe_3Al ($D0_3$-ordered), FeAl (ordered B2), $FeAl_2$, Fe_2Al_3 (ε), Fe_2Al_5 and $FeAl_3$ are formed, respectively. Information on the physical, thermodynamic properties and phase reactions in the Fe-Al system are provided by Shahverdi [218]. The Fe-Al phase diagram according to Kubaschewski [219] includes different variants of the ordered-B2 FeAl phase, which is relevant for changes in mechanical properties. On the right hand side of the phase diagram, the solubility of Fe in Al is close to zero, resulting in a very early phase formation when Fe is dissolved in Al.

The microstructural analysis of interface layers when molten Al comes into contact with solid Fe or steel is mainly documented at temperatures ranging between 700 to 900 °C [218, 220-223]. The interfacial reaction in this binary system has implications in many processes including aluminizing, mould casting, bimetals fabrication, joining and welding, etc. The types of interfacial phases formed, their morphology as well as their kinetics of growth were examined. The major intermetallic phase identified is an Al-rich intermetallic compound Fe_2Al_5 close to the steel substrate. Minor phases were also reported, principally the formation of $FeAl_3$ close to the solidified Al. These studies highlighted that the interfacial phases observed are not those given by the equilibrium phase diagram of the system. Some phases predicted by thermodynamic equilibrium are not found, indicating that the formation mechanisms and the diffusion conditions in the phases greatly influence the growth process and the overall interfacial structure at a given temperature. Higher temperatures and longer diffusion time would be necessary to form Fe-rich intermetallic compounds [224]. Recently, the formation of a Fe-rich alloy layer consisting of FeAl and αFe(Al) with Al content less than 30 wt% was obtained by high temperature aluminising [224-229], where hot dipped aluminised steel was subjected to diffusion treatment at temperatures above 900 °C. Toughness, workability, wear and corrosion resistance are significantly improved by the preferential formation of Fe-rich intermetallic compounds on the steel surface by heating the Fe_2Al_5/steel diffusion couple. During the diffusion treatment, $FeAl_2$ and FeAl were formed inside the Fe_2Al_5 layer, whereas the αFe(Al) layer grew inside of the steel substrate [228].

In regard to the Fe-Al-O ternary system, phase relations were investigated in a wide temperature range (500~1750 °C) to identify the oxide phase stabilities and to construct equilibrium oxygen pressure diagrams (for example [230]). Investigations on the Al-O equilibrium in liquid Fe are abundant for the typical range of Al content in Al-killed steels (0.04-0.05 wt% Al) owing to its importance for Al deoxidation of liquid steel; however, large discrepancies occur between the results of these investigations [231].

For higher Al content, data on Al-O equilibrium are rare [231-233]. Based on several experimental data at high Al content, Itoh *et al.* [231] derived equations for the Al-O equilibria in liquid Fe at 1600 °C. According to their assessment, the O solubility in liquid Fe containing 1 wt% Al is about 10 ppm and exceeds 100 ppm for Al contents above 3.5 wt%. Very recently, Kang *et al.* [233] performed Al-O equilibrium experiments at 1600 °C involving Fe-Al alloy with Al content from 0.01 to 10 wt%. In the range 1-10 wt% Al, the O content is less than 10 ppm, which is much lower than previous studies.

To the author's knowledge, the diffusion couple technique was not used to investigate this ternary system at steelmaking temperatures.

6.2.2. Results

6.2.2.1. General overview

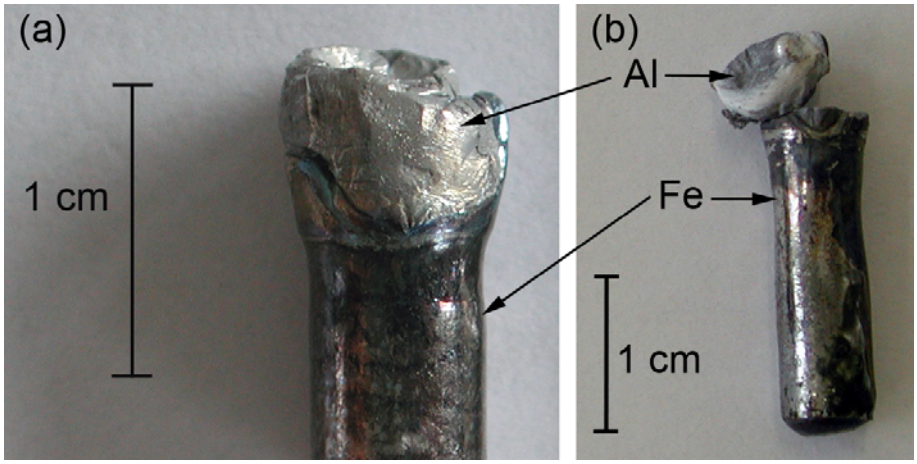

Figure 6-3: Picture of the sample after (a) 1 s and (b) 60 s interaction with liquid Fe at 1600 °C. The Al piece is located on top (appearing silvery) and Fe lies beneath (appearing dark).

Macroscopic examination of the samples after the interaction clearly shows that the mixing between Fe and Al was not complete, even after an interaction time of 1 min. The Al piece is easily recognisable from the Fe (Figure 6-3) and has partially changed shape from the initial cube to a more rounded shape. After 1 s interaction, the change in height of the remaining Al piece above Fe is very small compared to the initial one (Figure 6-3 (a)).

As a result of Al dissolution in Fe, it has considerably decreased after 60 s interaction (Figure 6-3 (b)).

6.2.2.2. Evolution of the reaction zone microstructure

During the experiments, a diffusion couple is initiated between Fe and Al, which is illustrated in Figure 6-4. Interdiffusion of Fe and Al results in the formation of a reaction zone, which is characterised by a composition intermediate between pure Fe and pure Al. The reaction zone (noted Fe-Al) is bounded by two diffusion fronts, namely diffusion fronts 1 and 2 indicated by dashed lines in Figure 6-4. Diffusion front 1 is located at the interface between the reaction zone and Fe, while diffusion front 2 is located at the reaction zone/Al interface. Since our main interest lies in the interactions occurring at the lower part of the diffusion couple, the term diffusion front will be used to designate the Fe/Fe-Al interface (i.e. diffusion front 1 in Figure 6-4).

The diffusion couple involves a third component, O, which is present in liquid Fe at a given concentration. Due to their high affinity, Al and O will react to form solid Al_2O_3 inclusions at the reaction front, which is indicated by the dotted line in Figure 6-4. Since both Al and O must be available for the reaction to take place, the reaction front is located in the reaction zone. To simplify the microstructure description and the discussion, it is assumed that the Al_2O_3 formation reaction is instantaneous, that equilibrium is reached and that Al and O equilibrium compositions are negligibly small. With these assumptions, the position of the reaction front corresponds to that of the diffusion front, as it will be shown during the investigation of the sample reaction zone.

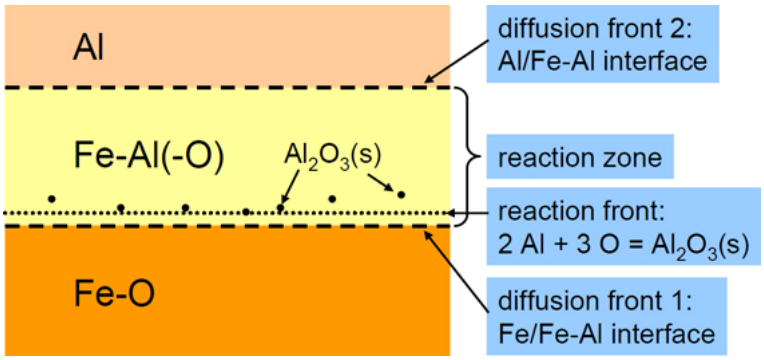

Figure 6-4: Schematic view of the reaction zone development in the diffusion couple Fe-Al(-O).

The reaction zone consists of several product layers composed of intermetallic compounds in a specific sequence dictated by the phase diagram [234]. The various product layers between the Al-rich region and the bulk Fe were identified by SEM observations and EDS analysis, showing different composition, intermediate from pure Fe to pure Al. Based on the occurrence, the morphology and the composition of the product layers, some differences were noticed between samples 1 to 3 with low initial O content and samples 4 to 6 with high initial O content.

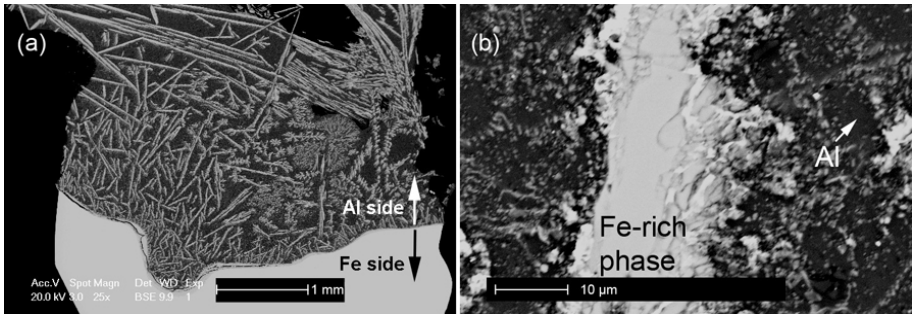

Figure 6-5: (a) Overview of the Al and Fe side of the sample cross section after contacting Fe with a piece of Al (sample 2: 450 ppm O and 1 s interaction time); (b) enlarged view of the Fe-rich phase in the Al.

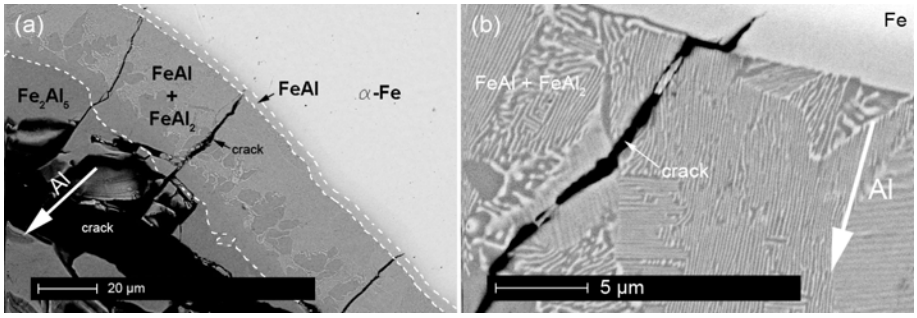

Figure 6-6: BSE micrograph of the reaction zone between Al and Fe in sample 3 after 1 s interaction time and 780 ppm O: (a) occurrence of intermetallic layers between Fe and Al-rich area, the dotted lines indicating the boundary of the intermetallic layers; (b) the fine quenched eutectoid structure of the two-phase layer FeAl+$FeAl_2$. The white arrows indicate the direction of the Al.

An overview of the cross section of sample 2 (450 ppm O and 1 s interaction time) is provided in Figure 6-5 (a). The Al-rich side contains an Fe-rich phase, presenting needle shapes. The composition of this Fe-containing phase ranged between 16 and 38 wt% Fe depending on the location. Less

than 2 wt% Fe was measured in the dark region of the Fe-Al region (Figure 6-5 (b)).

Table 6-2: Thickness of the intermetallic layers and of the reaction zone for each sample. The layers are delimited by the stability range of the phases: αFe(Al): 0-26 wt% Al; FeAl: 26-33 wt% Al; FeAl+$FeAl_2$: 33-48 wt% Al, Al-rich eutectic: 58 wt% Al.

sample	time (s)	O content (ppm)	layer thickness (μm)				
			αFe(Al)	FeAl	FeAl +$FeAl_2$	Al-rich eutectic	reaction zone
1	30	160	220	270	200*	-	> 1000
2	1	450	2-5	2-5	10-30*	-	50-100
3	1	780	2-5	2-5	10-30*	-	50-100
4	1	1800	20-25	17	500-1000	mixed	600-3000
5	5	1800	5	1-5	10-15	130	320
6	60	1800	500	250	460	400	> 2000

* with quenched eutectoid structure

The sequence and morphology of the product layers were identical for samples 2 and 3 with low O content and 1 s interaction time. The reaction zone of sample 3 is shown in Figure 6-6 (a). Close to the Al side, a 40 to 70 μm thick phase containing 54 wt% Al and 46 wt% Fe was found in samples 2 and 3 (Figure 6-6 (a)), which corresponds to Fe_2Al_5. In sample 1 with low O content and longer holding time, successive layers of $FeAl_2$, Fe_2Al_5 and $FeAl_3$, mostly dendritic shaped, as well as quenched liquid were identified. In samples 1 to 3, a composite layer was observed towards the Fe-rich side, as shown in Figure 6-6 (a) and Figure 6-7 (b), for, respectively, sample 3 and sample 1. This phase has an average composition of 42.6 wt% Al, corresponding to Fe_2Al_3 (ε phase). Below 1100 °C, this compound transforms into the compounds FeAl and $FeAl_2$ (eutectoid reaction). The thickness of this layer is variable from sample location, but remains in the 10-30 μm width range in samples 2 and 3 (1 s) and attains about 200 μm in sample 1 (30 s). Higher resolution images of this intermetallic layer show that a fine eutectoid structure has formed (Figure 6-6 (b)), presumably during quenching at the end of the experiment. Next to the two-phase FeAl+$FeAl_2$ layer towards the Fe-rich side, the product layer was identified as the ordered-B2 FeAl phase, based on its composition ranging between 26 and 35 wt% Al. This layer is 2 to 5 μm thick in samples 2 and 3 (Figure 6-6 (a)), and about 270 μm in sample 1 (Table 6-2). In direction of the Al-rich area, the BSE contrast reveals that the FeAl grains in sample 1 are surrounded by a brighter phase (Figure 6-7 (b)), presumably richer in Fe. This secondary phase would have a higher melting point than the FeAl phase due to the higher Fe content and would solidify at last, indicating that this

structure is formed during quenching of the liquid. Finally, αFe(Al) with a composition ranging from 0 to 26 wt% Al and thickness listed in Table 6-2 was identified between the Fe rich diffusion front and the FeAl product layer (Figure 6-6 (a) and Figure 6-7 (a)). Large cracks are found in between the as-quenched intermetallic layers, parallel to the Fe/Fe-Al diffusion interface, as well as through the FeAl and the two-phase FeAl+$FeAl_2$ layers, perpendicular to the interface (Figure 6-5 (a), Figure 6-6 and Figure 6-7).

The Al-rich intermetallic layers sequence (above 60 wt% Al) in the samples with high initial O content (samples 4 to 6) are similar to that observed in samples 1 to 3 (Figure 6-8 (a), Figure 6-9 (c) and Figure 6-10 (a), and Table 6-2). The main difference compared to the samples 1 to 3 is the presence of, towards the Fe-rich areas, a two-phase layer consisting of an Al-rich eutectic ($FeAl_3$-Fe_2Al_5 at approximately 58 wt% Al, 1160 °C), about 130 µm and 400 µm thick in, respectively samples 5 and 6, with a very fine eutectic structure formed during quenching (Figure 6-8 and Figure 6-9 (b) and (c)). Between the αFe(Al) and the two-phase layer (Figure 6-8 (b)), two layers can be identified thanks to the BSE contrast. From the Al content, the lower layer consists of FeAl and the upper layer has a composition lying in the domains FeAl+$FeAl_2$ and $FeAl_2$. The thickness of the layers in samples 4 to 6 is provided in Table 6-2. Neither microsegregation nor a eutectic structure was detected in this layer (Figure 6-8 (b), Figure 6-9 (a) and (b)). Based on the composition provided in the phase diagram (Figure 6-2), αFe(Al), which can dissolve up to 26 wt% Al, is about 20 to 25 µm, 5 µm and 500 µm thick for, respectively, samples 4, 5 and 6. As regards sample 4, the contact between Fe and the Al piece was made at one corner of the Al piece instead of a face, resulting in Fe penetrating deeper in the Al, as seen in Figure 6-10 (a). Though the sequence and the morphology of the solidified intermetallic layers are identical to those in samples 5 and 6, the layers are much thicker compared to the other samples with similar holding time, as seen in Table 6-2. A network of cracks was also found between the main intermetallic layers as well as through them. Owing to the high O content initially in the Fe, numerous Al_2O_3 inclusions are found distributed through the solidified intermetallic layers (Figure 6-9 and Figure 6-10 (b)). Near the diffusion front, the inclusions are mostly individual (Figure 6-9 (a) and Figure 6-10 (b)). In sample 5, nm sized Al_2O_3 inclusions were found (see section 6.2.2.3, Figure 6-12 (a)), whereas those in samples 4 and 6 attain, respectively, 0.7 and 2 µm (Figure 6-12 (b) and (c)). Towards the Al-rich area, they form aggregates, which are increasing in size as the number of inclusions forming the aggregates increases (Figure 6-9 (b) and (c), and Figure 6-10 (b)).

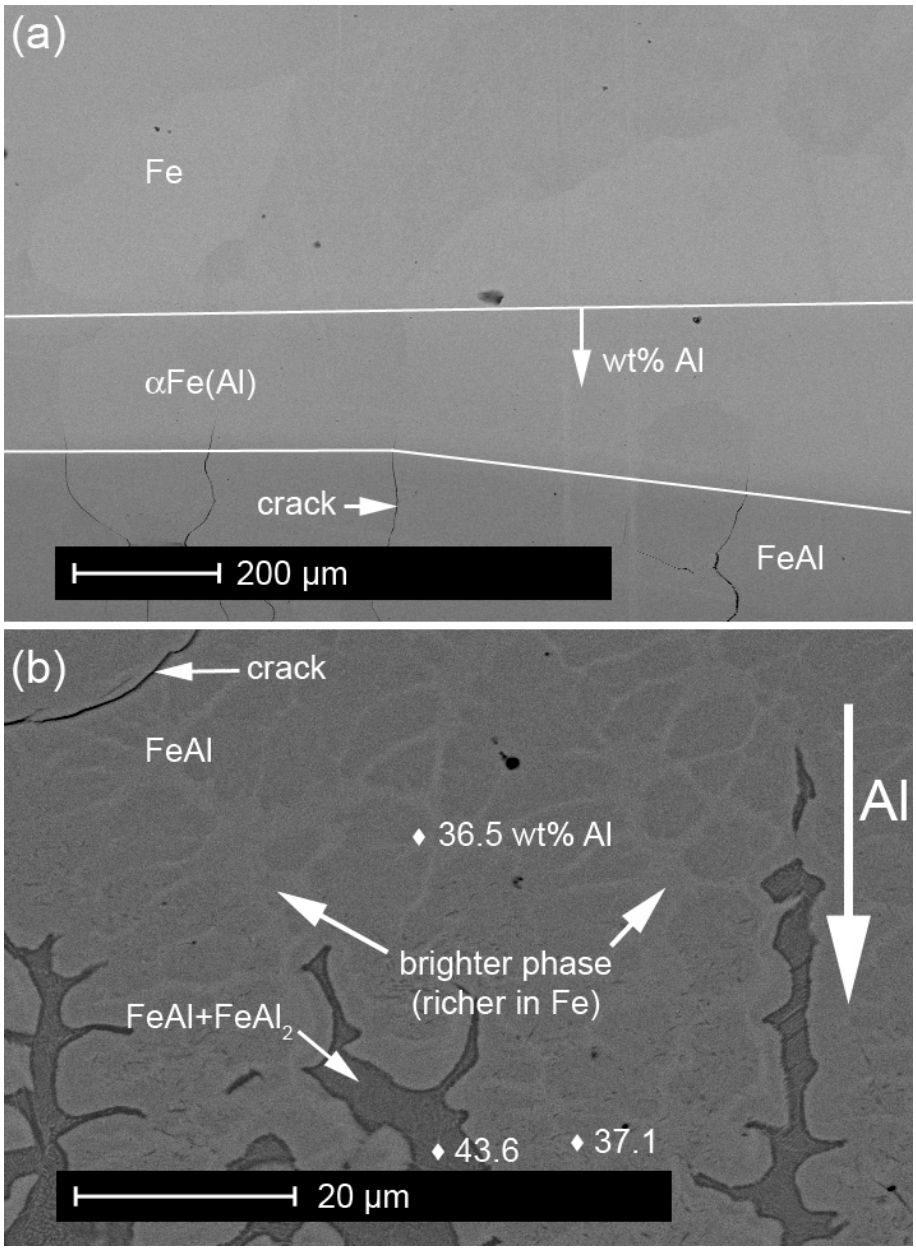

Figure 6-7: BSE micrographs of the reaction zone between Al and Fe after 30 s interaction time (sample 1, 160 ppm O): (a) overview of the diffusion front and (b) interface between FeAl phase and the eutectoid FeAl+$FeAl_2$ phase. The thick white arrow indicates the direction of the Al.

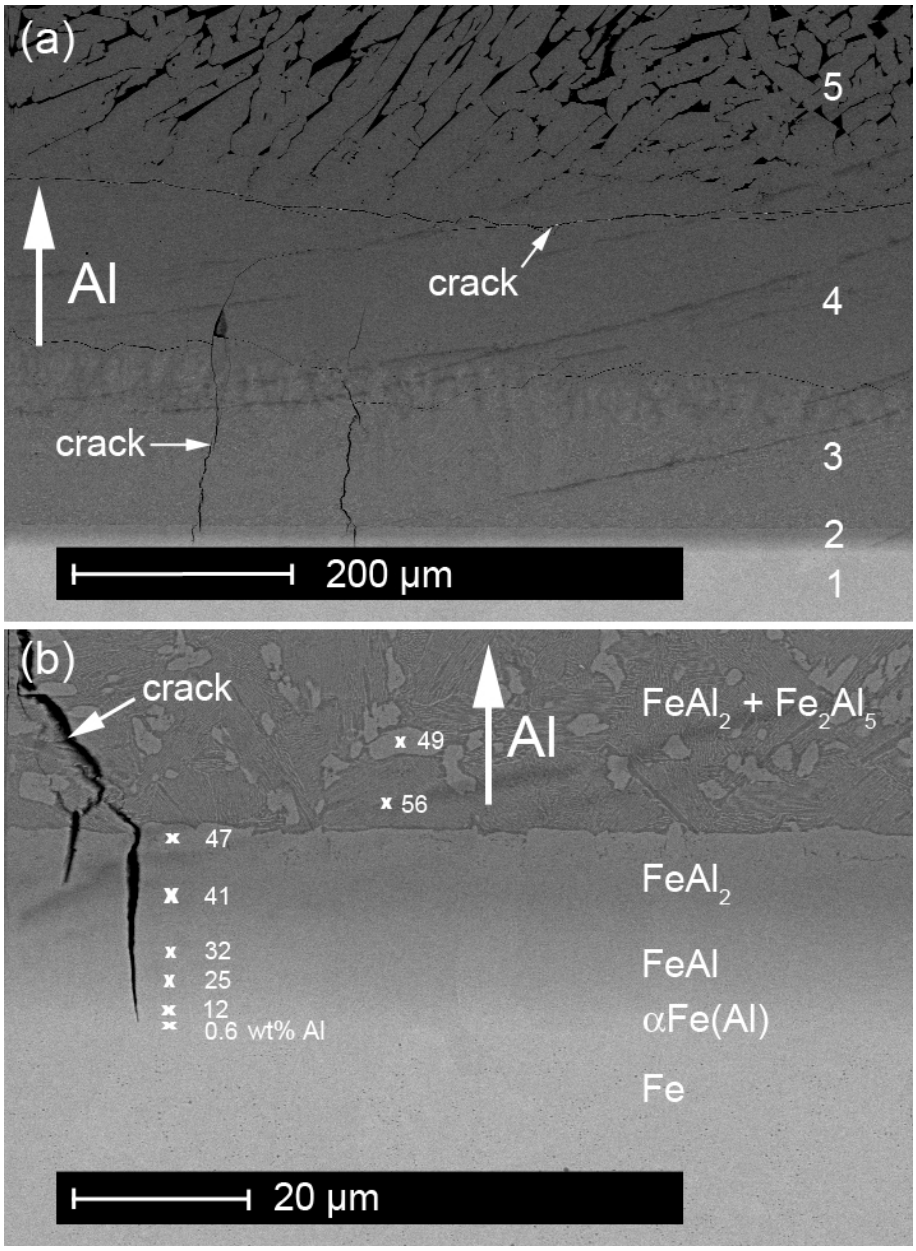

Figure 6-8: BSE micrographs of the reaction zone between Al and Fe after 5 s interaction time (sample 5, 1800 ppm O). (a) 1: Fe; 2: thin layers of FeAl and $FeAl_2$; 3: Al-rich eutectic (Fe_2Al_5-$FeAl_3$); 4: $FeAl_3$; 5: $FeAl_3$ + Al; (b) enlarged view of the diffusion front between Fe and Al-containing area. The thick white arrow indicates the direction of the Al.

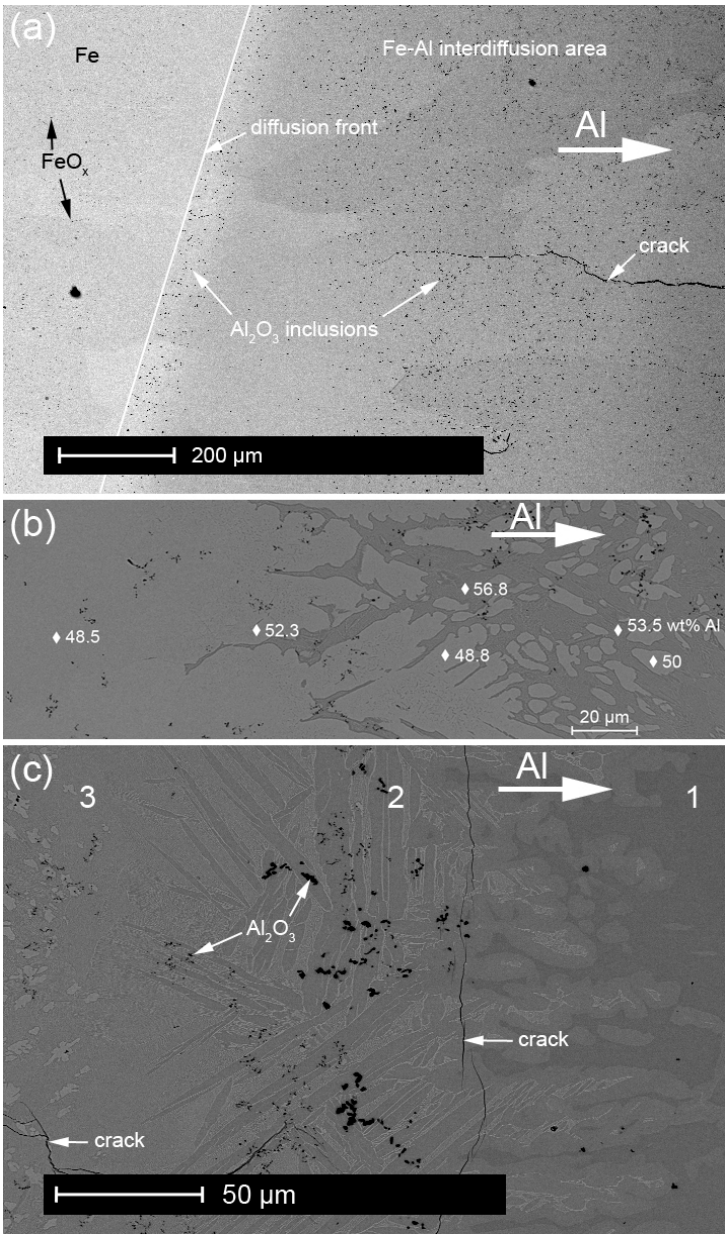

Figure 6-9: BSE micrograph of the reaction zone in sample 6 (60 s interaction time, 1800 ppm O). The Al rich side is on the right side: (a) overview of the reaction zone near the diffusion front. Black spots in the reaction zone are Al_2O_3 inclusions; (b) enlarged view of the interface between quenched liquid and the Al-rich eutectic on the right hand side; (c) reaction zone showing the Al-rich eutectic (3), the dendritic $FeAl_3$ phase (2) and the quenched liquid phase (1). The thick white arrow indicates the direction of the Al.

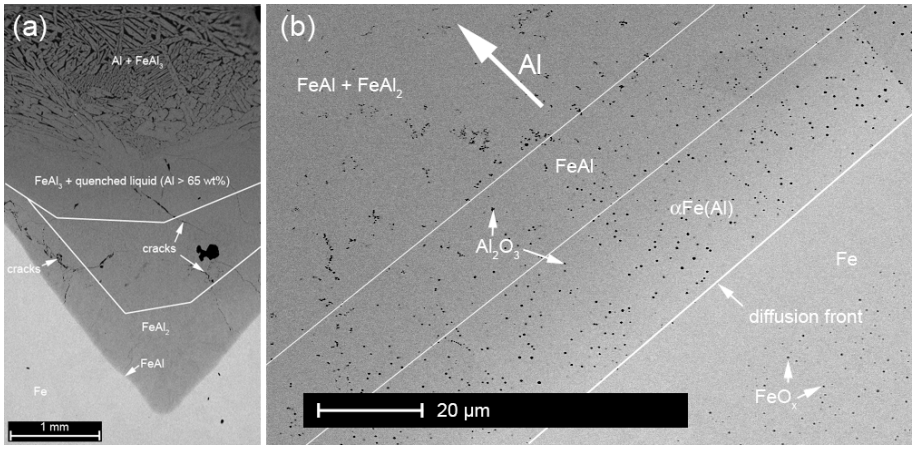

Figure 6-10: BSE micrograph of the reaction zone in sample 4 (1 s interaction time, 1800 ppm O): (a) overview of the interaction area, from the bulk Fe (bottom) to the Al-rich region (top); (b) enlarged view of the reaction zone, showing the diffusion front and the solidified intermetallic layers. The white lines delimit the different intermetallic layers. The thick white arrow indicates the direction of the Al.

6.2.2.3. Concentration gradient

Figure 6-11 shows the Al concentration profile measured on the samples with various interaction time and initial O contents as a function of the distance from the diffusion front. The concentration profile was measured perpendicular to the diffusion front. With a contact time of 1 or 5 s (Figure 6-11 (a)), the Al profiles, which are shown only for the first hundred µm, are very steep until the first 20 µm and have a half-arc shape. The concentration is then slowly increasing. The effect of the initial O content is hardly noticeable. The less steep Al concentration profile near the diffusion front measured in sample 4 is due to a different position of the Al inside the quartz tube, as shown in Figure 6-10 (a), creating a two-dimensional and thereby faster diffusion process compared to the other samples.

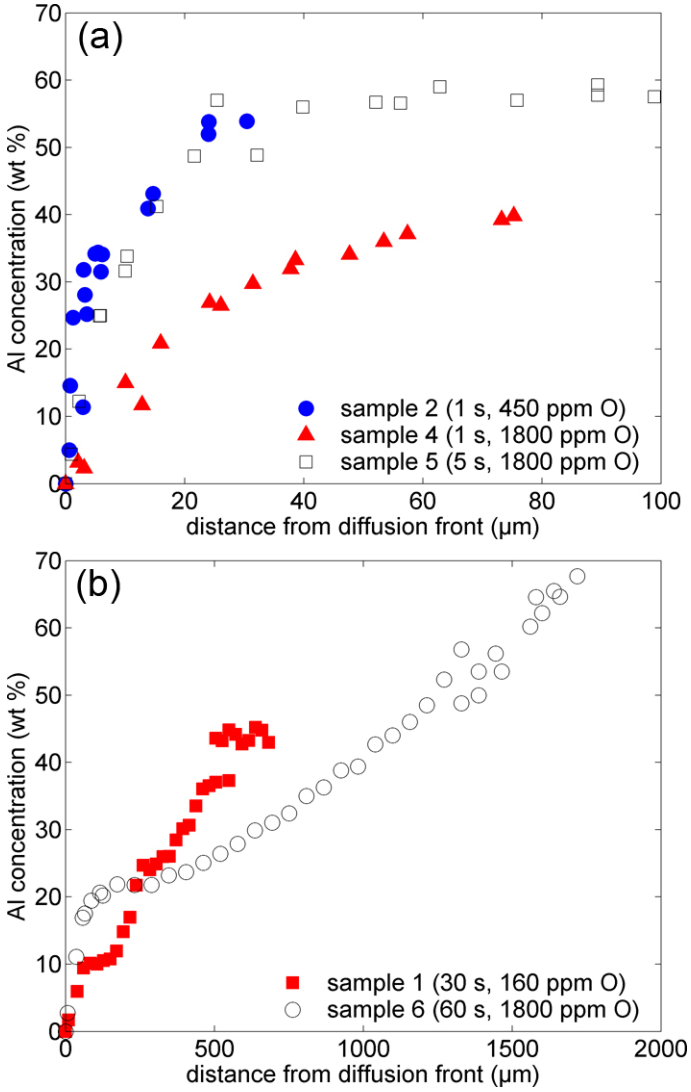

Figure 6-11: Al concentration profile in the reaction zone next to the diffusion front, measured with SEM-EDS for samples (a) with interaction time of 1 and 5 s (samples 2, 4 and 5) and (b) with interaction time of 30 s (sample 1) and 60 s (sample 6).

Figure 6-11 (b) shows part of the Al concentration profiles in samples 1 and 6, with a longer interaction time. The Al profile extended over a larger area due to a longer diffusion time compared to samples 2 to 5. The concentration profile for sample 1 (30 s, 160 ppm O) is steep and exhibits also the half-arc shape over approximately 100 µm near the diffusion front, though less steep compared to samples 2 to 5. Within a range of 70 µm, it remains almost constant at 10 wt% Al. Beyond that point, the Al concentration increases significantly again. The fluctuations in the concentration profiles are due to local inhomogeneities, especially with the presence of two-phase layers. Some steps are also found further in the profile, usually corresponding to a change of intermetallic phase. The shape of the Al profile of sample 6 (60 s, 1800 ppm) is similar to that of sample 1, yet different in magnitude. The Al profile is steep within approximately 120 µm, remains nearly constant at approximately 21 wt% Al for another 10 µm and increases again, almost linearly. Comparing the magnitude of the profile near the interface, that of sample 6, with longer interaction time, is steeper than sample 1, with shorter holding time. With an identical diffusion process, the profile at the interface is expected to become less steep with holding time. It is believed that the difference comes from the O content in the bulk Fe which is significantly higher in sample 6.

Because the O level in the Fe matrix was below the detection limit of the EDS system, the O concentration profile near the interface could not be quantified. However, for samples 4, 5 and 6 in which the initial oxygen content was high, the presence of an O gradient near the interface is suggested by the formation of a "precipitate-free" zone separating the Fe-O from the Fe-Al domain (Figure 6-12). In the Fe-O domain, FeO_x inclusions are found numerously, due to high O content in liquid Fe and the decreasing O solubility in Fe with temperature. The absence of precipitates means therefore a lower O content at high temperature so that the FeO_x supersaturation has not become critical for nucleation of FeO_x. The size of the 'precipitate-free' zone indicates the extent of liquid Fe with low O content. As most of the mass transport under the experimental conditions is assumed to be driven by diffusion processes, it follows that the O concentration profile in case of a thin 'precipitate-free' zone is relatively steeper compared to a larger one. In the αFe(Al) layer next to the interface, only Al_2O_3 inclusions are found, resulting from the diffusion of Fe, Al and O and the deoxidation reaction at the diffusion front when Al and O meet.

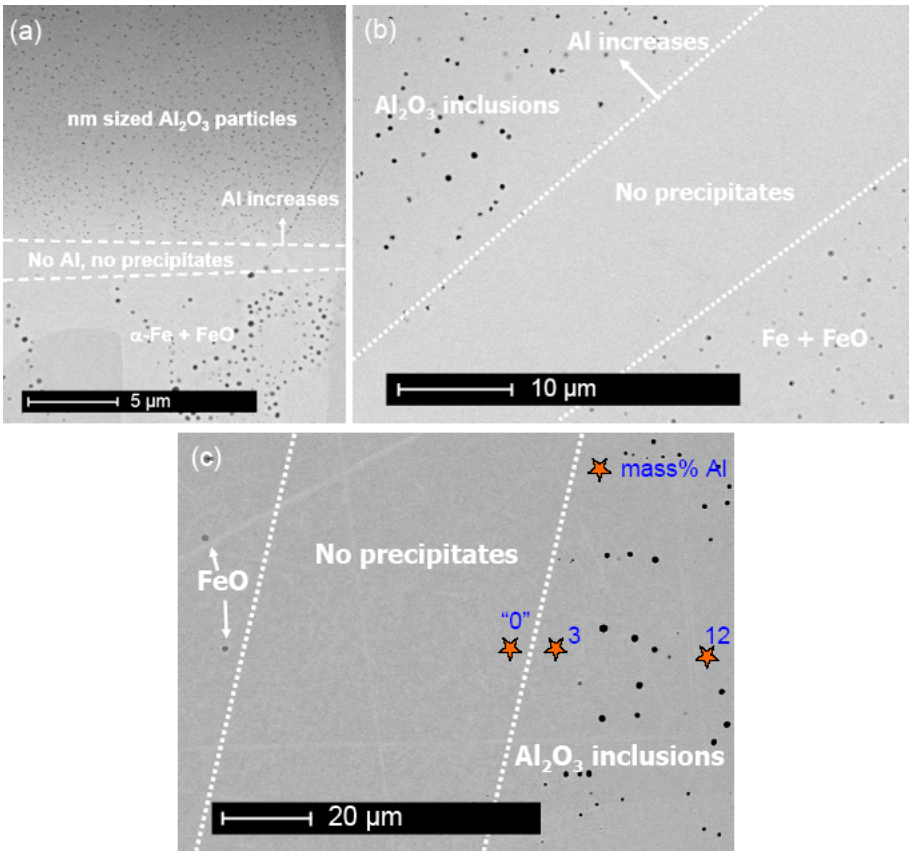

Figure 6-12: Overview of the Fe/Fe-Al diffusion front showing the 'precipitate-free' free zone (delimited by the dotted lines) separating the pure Fe region containing FeO_x precipitates from the Fe-Al region containing Al_2O_3 inclusions for samples (a) 5, (b) 4 and (c) 6.

From Figure 6-12, the thickness of the precipitate-free zone is clearly varying between the samples. For sample 5, this zone is 1.5 to 2.5 µm thick (Figure 6-12 (a)), whereas it reached approximately 17 µm for sample 4 (Figure 6-12 (b)) and 63 µm for sample 6 (Figure 6-12 (c)). From the comparison between these values and the Al concentration profiles given in Figure 6-11 (b), the precipitate-free areas tend to be thinner when the Al gradient is steeper near the interface. Since the Al and O equilibrium concentration values after reaction are negligible, O cannot theoretically be transported through the diffusion front. O is consumed at the diffusion front through the Al_2O_3 formation reaction. This implies that, at the diffusion front Z_r, the slope of the O concentration profile $\frac{\partial C_O}{\partial Z}$ is linked to that of Al

$\frac{\partial C_{Al}}{\partial Z}$ by relation (6.1) in order to satisfy the mass balance at the diffusion front and the reaction stoichiometry:

$$-\frac{1}{3} D_O \left.\frac{\partial C_O}{\partial Z}\right|_{Z=Z_r} = \frac{1}{2} D_{Al} \left.\frac{\partial C_{Al}}{\partial Z}\right|_{Z=Z_r} \quad (6.1)$$

where C_i and D_i are, respectively, the concentration and the diffusion coefficient of species i (Al or O). With appropriate estimates of D_{Al} and D_O, the O concentration profile can be derived from that of Al. With this condition to be fulfilled at the reaction interface, the correlation between the precipitate-free zone thickness and the Al gradient at the interface can be understood. According to relation (6.1), a steep Al gradient at the Fe-Al side of the interface implies a steep O gradient at the other side of the interface (proportional to 3/2 D_{Al}/D_O), which then forms a thin precipitate-free zone where the FeO_x supersaturation has not become critical for nucleation of FeO_x (sample 5). When the Al gradient become less sharp (samples 4 and 6), the O concentration profile should follow, resulting in larger precipitate-free zone at the interface, which is in agreement with the SEM observations.

6.2.2.4. Predictions of the solid shell period and temperature profile

Predictions of the solid shell period and temperature profiles through the reaction zone were compared with the experimental observations in order to help in the comprehension of the interactions between Fe and Al. The temperature difference between the edge of the solid shell (1537 °C) and the mass of liquid Fe enclosed inside the lower part of the quartz tube (1600 °C) initiated natural convection in the liquid. The Rayleigh number, using the height of liquid Fe contained in the sampling tube below the piece of Al as the length scale, is approximately 4.6 10^5 (see Eq. (5.3)), which is in the laminar flow range [208]. The heat transfer coefficient, h, associated with the natural convection must be provided as an input to the calculations. A numerical simulation of natural convection was not found in literature for the present geometry and boundary conditions. Instead, the value of h was evaluated using the correlation for a rectangular enclosure, heated from the bottom, cooled from the top surface and insulated at the vertical wall [235]. Using the adequate physical data of Fe at the average temperature, h_1 was found equal to 5.25 kW m^{-2} K^{-1}, which seems rather low. Another estimation of h, h_2, was calculated at 20 kW m^{-2} K^{-1}, using the numerical correlation from Lemembre [236] for a laterally heated and upper cooled vertical cylindrical enclosure with an aspect ratio of 2, which is the largest aspect

ratio considered by the authors. Using the inner diameter of the sampling tube as the length scale, the *Ra* number is decreased to 3700. To a first approximation, the resulting heat transfer coefficient would be higher, assuming that the empirical correlations to estimate h_1 and h_2 are still valid. Both values h_1 and h_2 were used to calculate the evolution of the shell thickness (Figure 6-13 (a)) and the temperature profiles in the solid Al, in the liquid and in the shell (Figure 6-13 (b)) as a function of time.

From Figure 6-13 (a), the first liquid phase nucleated after 0.9 s and the Al was completely molten after 3 s. These values were not significantly influenced by *h*, as the solid and dashed lines separating the FCC-Al and the liquid phases are superimposed. Immediately after the interaction, the shell formed and grew to a maximum thickness which strongly depends on the value of *h*. With h_1, the maximum shell thickness was about 18.3 mm reached in 31.3 s. After that, it decreased and finally disappeared after 154 s. As seen in Figure 6-13 (a), a higher value of *h* resulted in a decrease of the maximum shell thickness and of the shell melting time. In the case of h_2, the shell grew to a maximum of 11.5 mm in 12 s and disappeared after 39 s. Except for FeAl, the intermetallic layers appeared immediately after the contact and completely disappeared after 13 and 16 s for, respectively, h_2 and h_1. Their thickness was limited to a couple of μm since diffusion was not considered in these phases.

The calculated temperature profiles through the solid Al, the liquid phase and the solid shell are plotted in Figure 6-13 (b) for interaction time of 1, 5 and 30 s using h_1 and h_2. For interaction time of 60 s, only the temperature profile calculated with h_1 is represented as the solid shell has already disappeared when using h_2. Different markers are used on the temperature profiles to distinguish between the solid Al, the liquid and the solid shell. The position of the different interfaces is indicated by thin vertical lines on the curves. Due to the high thermal conductivity of Al, the temperature gradient was small throughout the Al area. On the other hand, the temperature gradient inside the Fe shell was large, especially at short interaction time. With time, the temperature of the Al was increasing fast and the temperature gradient through the shell became gradually smaller. The latter is due to the decrease of the temperature difference between both sides of the shell, combined with an increase of the shell thickness. The influence of the heat transfer coefficient on the temperature profile was not significant for interaction times of 1 and 5 s. For 30 s, a higher heat transfer coefficient resulted in a faster increase of the Al and the shell temperatures. After 60 s, the temperature through the Al and the shell obtained with h_1 is almost constant, whereas the shell has already disappeared with h_2.

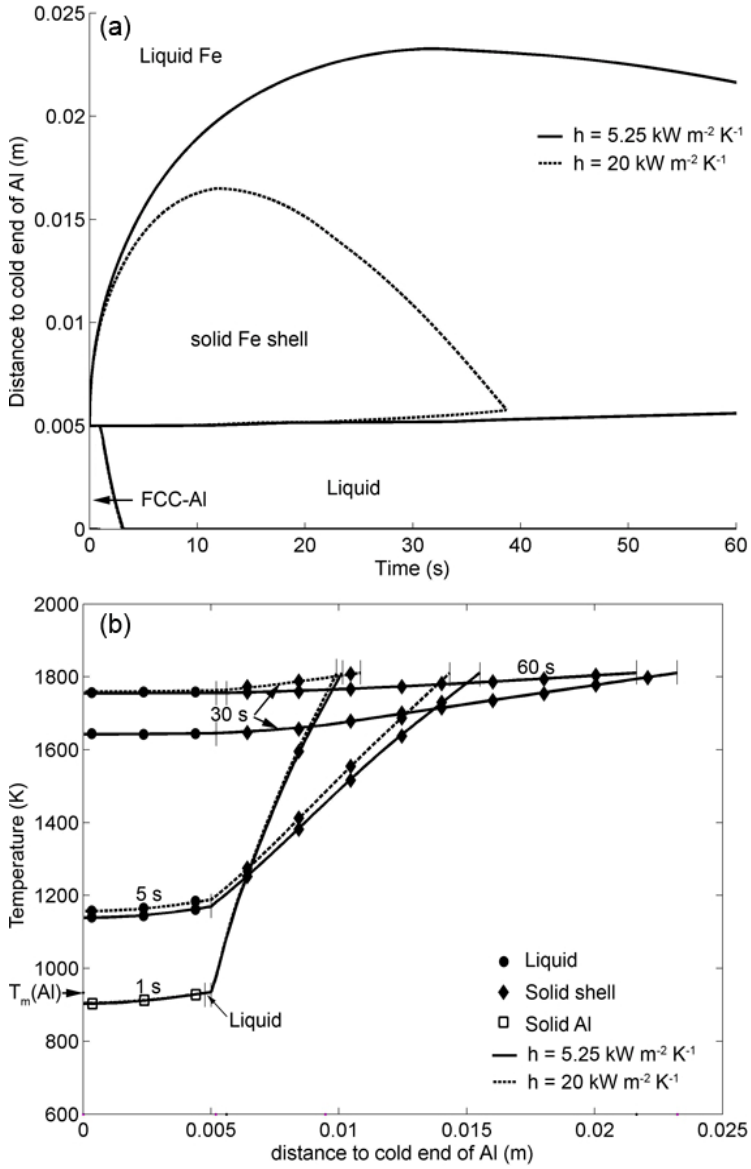

Figure 6-13: (a) Position of the solid and liquid interfaces relative to the top end of the Al piece as a function of time for h_1 = 5.25 kW m^{-2} K^{-1} (solid lines) and h_2 = 20 kW m^{-2} K^{-1} (dashed lines). (b) Temperature profiles in the solid Al, in the liquid and in the solid shell for interaction time of 1, 5 and 30 s using both values of h and that for interaction time of 60 s using h_1. The markers indicate in which phase the temperature is given and the thin vertical lines on the curves correspond to the position of the interface between the solid Al and the liquid phase or that between the liquid phase and the solid shell.

6.2.3. Discussion

6.2.3.1. Fe transport in the Al-rich region

Bouché [221] also observed thin needle-shaped $FeAl_3$ phase uniformly dispersed in the Al matrix. The formation of these crystals is attributed to a eutectic reaction during solidification of liquid Al containing some dissolved Fe. According to Stefanescu [237], rapid solidification conditions in hypereutectic Al alloys containing Fe can lead to the formation of Al solid solution as primary phase to solidify, with intermetallics forming in the intercellular region. This transition is due to kinetic effects.

The presence of Fe in the Al solid solution is an indication that the diffusion of Fe in Al occurred even if the immersion time was very short. The diffusion of Fe atoms in the Al-rich area seems to be much faster than the conventional diffusion process. According to Shahverdi *et al.* [218], Fe is brought to the Al-rich area through the breakage, flotation, re-melting and dissolution of $FeAl_3$ into molten Al. To support this idea, they measured that the $FeAl_3$ phase is harder and more brittle than Fe_2Al_5, thus easier to be cracked and spalled during intermetallic formation. Under the present conditions, the flotation of Al-rich intermetallics in liquid Al seems not possible owing to their higher densities compared to liquid Al. According to Plevachuk's density measurements in liquid Fe-Al alloys [238], the richest intermetallic they measured, $FeAl_4$, has a density ranging between 3.15 g cm^{-3} at the liquidus temperature of 1157 °C and 2.69 g cm^{-3} at 1550 °C, whereas that of liquid Al varies between 2.39 g cm^{-3} at the melting temperature of 660 °C and 1.94 g cm^{-3} at 1550 °C. Most of the Fe-Al intermetallic compounds are heavier than liquid Al. In the present case, the mechanism mentioned by Shahverdi [222] cannot be responsible for the enhanced Fe transport.

Instead, turbulent flow might be initiated owing to the large temperature difference between liquid Fe, initially at 1600 °C, and solid Al, initially at 25 °C, combined with the furnace heat surrounding the quartz tube and reheating the charge. In the case of turbulent flow, the mixing is significantly accelerated and Fe can be transported faster in the liquid phase. This mechanism is likely responsible for the Fe transport to the Al-rich region, indicating that the latter was in liquid state during the interaction.

Moreover, liquid Al, which forms at the bottom of the remaining solid Al, tends to be on top of it due to its lower density compared to solid Al. As

liquid Al moves away, solid Al moves downwards in the higher temperature zone where it can heat up and melt. This phenomenon may have contributed to mass transport and promoted melting of the solid Al.

6.2.3.2. Influence of O on the diffusion and microstructure

By comparing the concentration profiles of sample 1 and sample 6 in Figure 6-11 (b), it was shown that the presence of a high O content in the Fe has influenced the Al profile near the diffusion front. The profile at 30 s with low O content is less steep than that at 60 s with significantly higher O content. It seems that an increase in the O content has slowed down the Al diffusion. This can be explained by the inclusion formation reaction taking place more significantly at the diffusion front of sample 6 (Figure 6-9 (a)) compared to that of sample 1 (Figure 6-7 (a)). Part of the diffusing Al is consumed by the reaction and not available for transport. O has a diffusion coefficient which is 1 to 2 orders of magnitude larger than Al. In addition, O tends to concentrate at interfaces (surface active element). Under these conditions, O would be transported to the diffusion front faster than Al. Since Al cannot diffuse in oxidized Fe, O, which is transported towards the interface by concentration gradient and surface tension effects, must be consumed by the reaction before Al can diffuse further. With higher O content in Fe, the Al penetration is slowed down and the Al concentration profile remains steep compared to the case with low O. Owing to the low rate of this process, the influence of O on the Al profile is only noticeable for longer holding time.

A difference in the microstructure was noticed with the samples containing high O (1800 ppm O, samples 4 to 6) compared to those with low oxygen (samples 1 to 3). The two-phase layer FeAl + $FeAl_2$ with a eutectoid structure in samples 1 to 3 (Figure 6-6 (b)) was not observed in samples 4 to 6. Instead, a single homogeneous phase was found in that composition range and an Al-rich eutectic formed the Al-richer area. The reasons for this are not clear. The main difference between these samples is the O content and the numerous Al_2O_3 inclusions distributed in most of the solidified layers. The presence of Al_2O_3 inclusions brings an additional element in the system, oxygen. The ternary systems Fe-Al-O should be considered instead of the binary system Fe-Al. In some alloys, such as Al-Ti alloys [239], oxygen influences the solidification behaviour by shifting phase transitions and extending stability domains compared to binary systems. Further work would be needed to clarify the influence of oxygen on the solidification behaviour in Fe-Al alloys.

6.2.3.3. Identification of the solid and liquid phases at experiment temperature

a) Reaction zone

- *Fine solidified structure and limited growth rate of intermetallic compounds*

It was shown in section 6.2.3.1 that the upper Al-rich part of the sample should be in the liquid state to enable the fast transport of Fe in liquid Al. The observation of the microstructures revealed a typical quenched structure in all samples, especially in the eutectic and eutectoid composition range. Considering that all the material from the quenched eutectoid layer must have been heated above the eutectoid transformation temperature, the local temperature during experiment should be at least 1102 °C, according to the Fe-Al phase diagram (Figure 6-2). Moreover, if we assume that the region of the sample with a composition lying in the $FeAl_3$ domain is liquid, the temperature in that area should be above 1160 °C according to the Fe-Al phase diagram in Figure 6-2. The minimal temperature beneath the two-phase layer is difficult to estimate directly from the description of the microstructure. No evidence of a liquid, solid or mushy zone was found for the αFe(Al) and FeAl layers.

The growth rate of intermetallic layers during interaction between solid Fe and liquid Al are documented in the temperature range of 700 °C to 1050 °C [218, 220-222, 224-229]. After 1 min hot-dipped aluminising treatment at 800 °C, the maximum reported layer thickness consisting of Fe_2Al_5 is about 200 µm [221] and attains about 700 µm after 45 min at 800 °C [220]. After a diffusion treatment of the aluminised specimen during 15 min at 1000 °C, αFe(Al) and FeAl layers were formed and attained a thickness of, respectively, 32 and 16 µm [224, 228]. The growth kinetics of the intermetallic layers is reported to be diffusion-controlled, following a general parabolic equation [220-222, 226, 228]:

$$\delta^2 = kt \tag{6.2}$$

where δ is the layer thickness (µm) at time t (s) and k the rate constant (µm^2 s^{-1}). Since the latter is a function of the diffusion coefficient, the temperature dependence is given by an Arrhenius law:

$$k = k_0 \exp\left(\frac{-E_A}{RT}\right) \tag{6.3}$$

where k_0 is a frequency factor ($\mu m^2\ s^{-1}$), E_A the activation energy for the growth of the layer ($J\ mol^{-1}$) and R the gas constant ($J\ mol^{-1}\ K^{-1}$). The activation energy for the growth of Fe_2Al_5, FeAl and αFe(Al) were evaluated at, respectively, 109 kJ mol^{-1} in the temperature range from 700 to 900 °C [222], 180~200 kJ mol^{-1} at 750-1050 °C [226, 228] and 180 kJ mol^{-1} at 950-1000 °C [228]. The parabolic growth law for αFe(Al) and FeAl is given by Eqs. (6.4) and (6.5), respectively [228].

$$\delta_{\alpha Fe(Al)} = \sqrt{43.3 \cdot 10^6 t \exp\left(\frac{-180 \cdot 10^3}{RT}\right)} \tag{6.4}$$

$$\delta_{FeAl} = \sqrt{63.46 \cdot 10^6 t \exp\left(\frac{-200 \cdot 10^3}{RT}\right)} \tag{6.5}$$

Using these relations, the calculated thickness of αFe(Al) and FeAl heated at, respectively, 1811 K and 1583 K, which are the respective melting point of these compounds, are provided in Table 6-3 for diffusion times of 35 and 65 s (samples 1 and 6). These temperatures are employed in the calculations to obtain an estimate of the maximum possible layer thickness. As listed in Table 6-3, the calculated thickness is much smaller than the observed values, indicating that the reaction zone could not possibly be formed entirely by growth of solid intermetallic compounds. Most of the reaction zone results from the solidification of a liquid phase, which corroborates the microstructure observations.

Table 6-3: Comparison of the calculated and measured thickness of αFe(Al) and FeAl for samples 1 and 6. The calculations are performed using Eq. (6.4) at T = 1811 K for αFe(Al) and Eq. (6.5) at T = 1583 K for FeAl.

	time (s)	αFe(Al) thickness (μm)		FeAl thickness (μm)	
		calculated	measured	calculated	measured
sample 1	35	99	~220	23.6	~270
sample 6	65	135	~500	32.2	~250

Numerous cracks were observed throughout the solidified intermetallic layers. Dybkov [240] proposed two main causes for the apparition of layer cracking. Brittle intermetallic layers may crack due to the difference in thermal expansion coefficient creating significant mechanical stresses during cooling. The second reason is the volume changes associated with intermetallic compound formation, implying that the cracks are formed during the growth of the layer. In the present case, the intermetallic layers

are too thick to possibly have grown in the solid state in such limited time. The crack formation observed in this study occurred during cooling of the sample from the experiment temperature to room temperature.

- *Comparison with simulations*

The calculations revealed that the Al melting time is relatively fast compared to the shell melting time and the temperature gradient within the Al-rich area is small. The microstructure observations indicated that most of the Al-rich area was in the liquid state already after 1 s. Also the eutectoid and eutectic transformations observed in the sample microstructures suggested that the temperature reached at least 1373 K near the diffusion front. Compared with the experimental observations, the heating and melting time calculated with the model seems too long. The temperature in the Al side is underestimated and the shell thickness seems enormous, especially with the predictions using h_1. The difference between the model and experiment results might originate from several simplifications. Al might have been preheated during the introduction of the quartz tube in the furnace, so that the initial temperature of the cold Al prior to contact with Fe was higher than 25 °C. The heat transfer coefficient in liquid Fe might be underestimated, although the influence of h on the shell thickness and on the temperature profiles is limited for short holding times, as illustrated in Figure 6-13 (b). Probably the most important reason is that the model did not consider the finite dimensions of the system nor the heat provided by the furnace to the lateral side walls of the quartz tube containing Al and Fe, as depicted in Figure 6-1 (b). The latter induces a rise in temperature of the material inside the tube and might initiate natural or even turbulent convection in the reaction zone. For these reasons, it is believed that the Al and the shell melting time, and the shell thickness should be substantially reduced compared to the calculation results shown in Figure 6-13.

The thickness of the intermetallic layers calculated by the model remained extremely small, owing to limited growth rate under non isothermal conditions. The limited layer growth is due to the large difference in mass transport between the liquid and solid phases. In general, the value of the diffusion coefficient in the solid is at least 1 or 2 orders of magnitude lower than that in the liquid. Although the diffusion coefficients were fixed at zero for the present system, similar conclusions were drawn from calculated layer thickness of FeTi intermetallic compounds [212], for which the values of the diffusion coefficient were provided. With these considerations, solid intermetallic layers, if present at experiment temperature, should be very thin and even broken up.

- *The presence of Fe-rich intermetallic compounds and the Al concentration profile*

The occurrence of layers of the intermetallic compound FeAl and αFe(Al) near the diffusion front, even in samples with very short holding time, is also a sign that the reaction zone was liquid. At 900 °C, the FeAl and $FeAl_2$ phases are absent from the intermetallic layers identified between solid Fe and liquid Al, which is attributed to low diffusivities and low growth rate compared to $FeAl_3$ and Fe_2Al_5 [221]. If solid Fe would have been in contact with an Al-containing liquid at a temperature allowing the formation of solid intermetallics, Al-rich intermetallic compounds would appear at first, followed by Fe-rich intermetallic layers later in the process owing to the limited diffusion of Al in solid Fe. Also, the presence of solid intermetallic layers would have limited the diffusion of Fe to the liquid phase, which is in disagreement with the large mass transport of Fe observed in the samples. The most plausible explanation for the formation of the Fe-rich intermetallic layers is that the reaction zone was fully liquid with an Al gradient. The latter implies that the temperature near the diffusion front was higher than 1310 °C so that no intermetallic compounds could form (Figure 6-2). Under these conditions, a high Fe content could have been attained in the liquid phase near the diffusion front in order to form the Fe-rich intermetallic compounds on cooling.

In binary systems, only single-phase intermetallic layers, which are separated by straight interfaces, can occur in the reaction zone under isothermal conditions [234]. In the present observations, some areas in the reaction zone consisted of more than one single-phase. Also the Al concentration profile across the reaction zone is very gradual, which is not the case for a binary diffusion couple. Both arguments suggest that the reactions consisted of a liquid phase.

- *The formation and behaviour of Al_2O_3 inclusions*

Numerous Al_2O_3 inclusions were observed in the samples with high initial O content. They were formed immediately after the diffusion front. In the first tens of μm from the diffusion front, mainly individual inclusions were found (Figure 6-9, Figure 6-10 (b) and Figure 6-12). Beyond that point, they tend to form aggregates through a collision-coagulation mechanism (Figure 6-9 and Figure 6-10 (b)). An increase of the size of the aggregates was observed in the direction of the Al-rich areas. A collision-coagulation mechanism implies that the inclusions had some freedom to move, which indicate that the metal matrix was in liquid state. At the position where the collision-coagulation of inclusions was observed, the Al content reached 33 wt% for sample 4 and 20 wt% for sample 1. According to the phase diagram in

Figure 6-2, the local temperature was therefore not less than 1300 °C and 1420 °C, respectively.

Concerning the individual inclusions found near the interface, the question is whether they have precipitated in an Al-containing solid phase or in a liquid phase. Precipitation of oxides in a crystalline solid occurs mainly at grain boundaries due to the decrease in the free energy for nucleation compared to that for homogeneous nucleation [241]. The growth of the oxides is controlled by the diffusion of O in the solid, which is a very slow process, and by Ostwald ripening in a final stage. For these reasons, oxide precipitates at grain boundaries are usually in the nm size range [242]. Except for sample 5, some of the Al_2O_3 inclusions observed at the interface of samples 4 and 6 have a size of, respectively, 0.7 and 2 μm (Figure 6-12 (b) and (c)). This size appears to be difficult to obtain through solid state precipitation and growth. This corroborates that this area is most likely liquid. Concerning the nm sized Al_2O_3 particles found at the interface of sample 5 (Figure 6-12 (a)), the hypothesis of precipitation in the solid is possible. However, assuming precipitation at the grain boundaries, it would imply that the grain size in the Al-containing solid phase was less than 1 μm before or during precipitation to obtain the spatial distribution of Al_2O_3 inclusions shown in Figure 6-12 (a). In the case of sample 5, it is difficult to conclude, based solely on the inclusion characteristics, on the solid or liquid nature of the Al-containing phase neighbouring the diffusion front.

To summarise the discussion on the reaction zone, it was shown that most of it was in liquid state during experiment. In the case of samples 1 and 6 with longer holding times and of sample 4, it was concluded that the reaction zone was completely liquid before quenching. In case of samples 2, 3 and 5, it is unsure whether the thin layers of FeAl and αFe(Al) next to the shell interface were liquid or solid.

b) Solid Fe shell

- *The Al concentration profile*

The main consequence of the presence of a solid shell at the interface is the appearance of a significant discontinuity in the Al profile, owing to the large difference in mass transport between the liquid and the solid phase. The shell provides a barrier for the transport of Al, creating a step in the concentration profile. The height of the step will gradually decrease as the Fe dissolution progresses, yet the discontinuity remains as long as the shell exists. A steep Al concentration profile was measured at the interface with samples 2, 3 and 5 (Figure 6-11 (a)), which may be interpreted as a step, indicating the presence of the solid shell at the other side of the interface. The measured Al concentration profiles showed a different behaviour for samples 1, 4 and 6.

The step was not present and the profiles exhibited a gradual increase in Al concentration. Al seemed to have diffused and penetrated in Fe. This suggests that the solid Fe shell was not present anymore in samples 1 and 6. Under the present conditions, the shell melting time was less than 30 s. The calculation results shown in Figure 6-13 (a) predicted that the shell disappeared after 39 s using h_2. It was previously highlighted that the calculated heating and melting time seemed too long compared with the microstructural observations. The actual shell melting time should be less than the predicted value of 39 s, which is in agreement with the experimental observation on the concentration profile.

- *The precipitate-free zone*

In section 6.2.2.3, it was shown that the presence of a precipitate-free zone suggests the formation of an O gradient at the Fe side of the interface. The development of the O concentration gradient in pure Fe implies that the O should be able to be transported to some extent. The range of the diffusivity of O in solid Fe [243] is in general comprised between $7\ 10^{-5}$ to $7\ 10^{-7}$ $cm^2\ s^{-1}$ in the temperature interval 1538-600 °C. In liquid Fe, the O diffusivity is higher ($1.4\ 10^{-4}$ $cm^2\ s^{-1}$ at 1600 °C [244]). The O content is very low in the cold Fe matrix (low solubility of O in solid Fe, most of the O is present as FeO_x inclusions) and its diffusion in the solid phase is very limited. For that reason, one would expect the absence of the precipitate-free zone and the occurrence of FeO_x inclusions at the diffusion front if Fe was in solid state next to the Fe/Fe-Al diffusion front. From the experimental observations on the samples with high initial O content (samples 4 to 6), it is clear that this precipitate-free zone exists and that O diffusion took place from the O rich area to the Fe/Fe-Al diffusion front. Considering the short interaction time, Fe in the precipitate free zone at the Fe/Fe-Al diffusion front was most likely in liquid state to allow O to be transported at a sufficiently high rate.

6.2.4. Summary

The first part of this chapter examined the quenched microstructures of the diffusion couple to identify the interactions and the nature of the phases at the experimental temperature. The reaction zone consisted of several layers of Al-rich and Fe-rich intermetallic compounds of the Fe-Al system. Based on the microstructure, the concentration profiles, diffusion processes in solid and liquid phases, and on the behaviour of Al_2O_3 inclusions in the reaction zone, it was shown that the reaction zone was completely liquid and that the solid Fe shell melted for the samples with holding time of 30 and 60 s. For holding times of 1 and 5 s, the liquid or solid nature of the thin layers of

FeAl and αFe(Al), which are adjacent to the shell/reaction zone interface, could not be determined with certainty.

6.3. Formation and morphology of Al_2O_3 inclusions at the onset of deoxidation

Next to alloying and interdiffusion between Fe and Al, non-metallic inclusions were observed in the deoxidized area. Variations in size, type, morphology and relative occurrence of the inclusions were observed between the samples containing different O levels. Three different types of inclusions were identified in the samples depending on the location and/or the experimental conditions (time and O concentration).

- FeO_x inclusions were found in bulk Fe in samples 4 to 6 containing high initial O contents (Figure 6-8 (b), Figure 6-9 (a), Figure 6-10 (b) and Figure 6-12).
- Al_2O_3 inclusions were observed in the region between the position of the initial Fe/Al interface and the position of the diffusion front (Figure 6-6 through Figure 6-10).
- Large Al_2O_3 inclusions containing traces of Si and Fe were found near the $FeAl_2/Fe_2Al_5$ interface (Figure 6-8 (a), Figure 6-9 (c), Figure 6-10 (a)). They are located the furthest away from the diffusion front, in the vicinity of the initial Fe/Al interface.

6.3.1. Sequence of inclusion formation

Due to the significant temperature difference between liquid Fe held at 1600 °C and solid Al initially at 25 °C (Figure 6-14 (a), $t = 0$), a solid Fe shell forms at the interface with colder Al, while Al in contact with Fe will heat up and partly melt (Figure 6-14 (a), $t = t_1$). Note that the configuration between solid and liquid Al depicted in Figure 6-14 (a) is not stable. Liquid Al, which is less dense than solid Al, will tend to move away to be on top of solid Al. For convenience and simplicity, this tendency is not represented in Figure 6-14 (a).

During solidification of the Fe in the shell, the oxygen solubility in Fe will decrease, causing the formation of iron oxide inclusions. With pure liquid Fe, mainly FeO_x will be generated when liquid Fe cools down in contact with colder Al. Also some SiO_2 crystals arising from devitrification of the fused quartz above 1000 °C may be carried away with the liquid Fe flow during sampling. These solid oxide inclusions may provide preferential sites

for heterogeneous nucleation of Al_2O_3, generating large inclusions in the vicinity of the initial Fe/Al interface (e.g. Figure 6-9 (c)). With the diffusion of Fe and Al and the subsequent formation of FeAl intermetallic compounds in this area (Figure 6-14 (a), $t = t_2$), the FeO_x precipitates and SiO_2 crystals initially contained in the shell would undergo a reduction by Al provided by the nearby liquid Al, forming solid Al_2O_3 inclusions with a SiO_2 or FeO_x core. Because these precipitates represent an important O source in a limited volume, the Al_2O_3 inclusion formed by reduction of the precipitates might be larger than those formed later through Al and O diffusion to the diffusion front. Remaining traces of Si and Fe were detected in such large crystals. Those tend to decrease with time, confirming the ongoing reduction by Al.

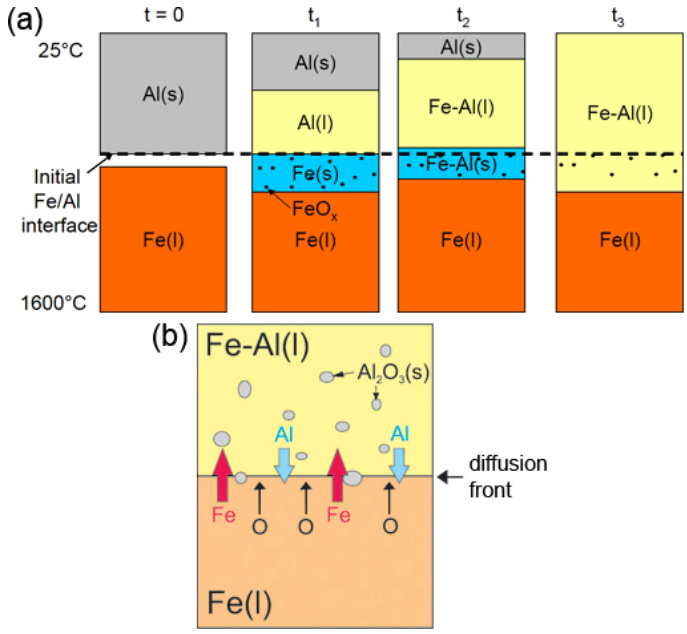

Figure 6-14: (a) schematic illustration of the interactions between Fe and Al during the shell period. $t = 0$: initial conditions; $t = t_1$: Al melting and formation of the solid shell upon contact between cold Al and liquid Fe. FeO_x precipitates and SiO_2 are present in the solid shell; $t = t_2$: formation of Fe-Al liquid and Fe-Al solid phases due to interdiffusion of Fe and Al. FeO_x precipitates and SiO_2 inclusions are reduced by Al to form large Al_2O_3 inclusions; $t = t_3$: melting of the shell. (b) Schematic illustration of the mass transport of Fe, O and Al between the Fe and the reaction zone after melting of the shell (directions of diffusion are indicated by arrows). Al_2O_3 inclusions are formed at the diffusion front, where O and Al meet.

With the melting of the shell (Figure 6-14 (a), $t = t_3$), the interactions between the two liquid regions are intensified. Al_2O_3 inclusions are formed

at the diffusion front, where O from liquid Fe meets Al from a liquid Fe-Al alloy (Figure 6-14 (b)). The deoxidation of liquid Fe and subsequent O consumption cause the diffusion front to move downwards with time and to coincide with the diffusion front. Once the front moves further, Al_2O_3 inclusions are surrounded by liquid Fe-Al containing (almost) no oxygen. Those located next to the diffusion front are therefore the most recent ones. As diffusion proceeds, the O and Al gradients are modified with time, which may affect the inclusion nucleation and growth conditions.

6.3.2. Inclusion growth mechanisms

The deoxidation reaction (implying the formation of new inclusions) mainly takes place at the diffusion front, where Al and O meet, creating the required high supersaturation conditions for the nucleation and growth of inclusions. As nucleation occurs at the diffusion front, supersaturation decreases very fast, substantially decreasing the Al and O contents at the diffusion front. Once Fe is locally deoxidised (O level is such that nucleation and growth are no longer possible), Al can diffuse further, resulting in the displacement of the diffusion front further away. The latter causes the newly formed inclusions to be surrounded by the Al-rich melt. O transport from the bulk Fe to the Al-rich melt is halted at the diffusion front due to the low Al and O equilibrium concentrations. Diffusion growth is significantly influenced by the velocity of the diffusion front, which is controlling the O availability to the growing crystal. Owing to the lower O available near the inclusions, growth by diffusion, which is reported as the main growth mechanism shortly after nucleation, is significantly slowed down. Other growth mechanisms, such as collision-coagulation growth, might become more important. These mechanisms are governed by inclusion motion, which determines the probability that several inclusions collide and form a single inclusion.

In a still melt, the inclusion velocity is determined by considering buoyancy forces and Brownian motion. As described in section 2.2.2.2 in Chapter 2, the buoyancy forces creating a settling velocity are governed by the inclusion size and the density difference between the inclusion and the surrounding liquid. Given the small size of the inclusions, the short contact time before solidification and the decreasing density of the Fe-Al melt in direction of the surface, the inclusion settling velocity is virtually insignificant under the present conditions. Brownian motion describes the random motion of very small inclusions suspended in a fluid. For a 0.1 and 1 μm diameter inclusion at 1600 °C, the mean value of inclusion displacement in 1 s is, respectively, about 3.96 and 1.25 μm (see Eq. (2.27) in Chapter 2). Also the moving distance of the inclusions is very limited.

The reaction zone is characterised by temperature and composition inhomogeneities. The temperature gradient may generate convection in the reaction zone with formation of local turbulences contributing to inclusion growth through collision-coagulation mechanism. In addition, an interfacial energy gradient might be created at a liquid surface or interface as a result of temperature and/or solute concentration gradients [245, 246]. The interfacial energy gradient can induce the motion of the liquid from zones of lower surface tension, i.e. higher temperature and higher surface active element concentration, to zones of higher surface tension. This convection along the interface, called Marangoni convection, can strongly affect the transport phenomena near the interface. It was found to play an important role in various processes in steelmaking [245], such as the motion and interactions of inclusions at the melt surface and at the solidification front [247, 248] and local refractory corrosion at the slag/metal interface [249]. In general, the contribution of Marangoni flow to the bulk flow is weak, except under microgravity and under high temperature or concentration gradients [248]. Under the present conditions, both temperature gradient and concentration gradient might have driven locally Marangoni convection in the reaction zone and at the diffusion front, contributing to inclusion growth through collision-coagulation mechanism.

The contribution of collision-coagulation mechanism to inclusion growth is small under such conditions, unless the distance separating the inclusions is less than their moving distance. It results that inclusion growth is principally controlled by the availability of O and Al at the diffusion front and by the vicinity of other inclusions.

6.3.3. Inclusion size and number

With increasing initial O content in liquid Fe, an increase in the number of precipitated inclusions was observed. The inclusion number was low in samples 1 and 2 with, respectively, 160 and 450 ppm initial O content, as inclusions are relatively difficult to find in the reaction zone shown in Figure 6-15 (a) and (b). The inclusion number increased drastically with sample 3 (780 ppm O) as evidenced by the high number of inclusions collected on the filtration membrane after acid extraction of the metal matrix (Figure 6-15 (c)). For samples 4 to 6, the very high initial O content (1800 ppm O) gave rise to very high inclusion number density all along the area covered by the motion of the diffusion front with time (Figure 6-8, Figure 6-9 and Figure 6-10).

For interaction times of 1 and 5 s, the inclusion size tends to decrease with increasing O content in liquid Fe. The average inclusion size was about 2.1 µm at 160 and 450 ppm O (samples 1 and 2), and decreased to below 1 µm with increasing O content to 780 ppm (sample 3). Al and O diffusion and deoxidation reaction cause the concentration profiles to become flatter with the interaction time.

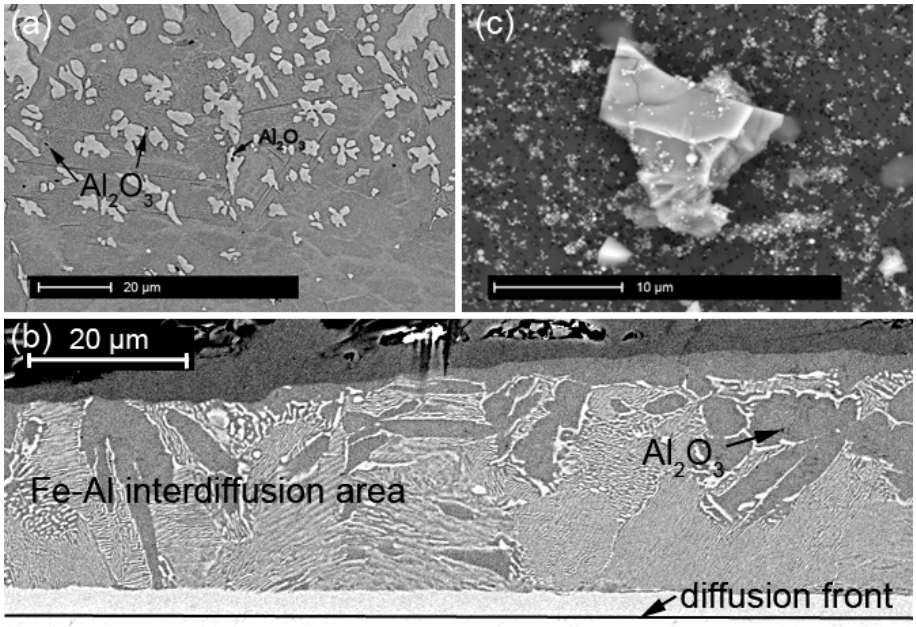

Figure 6-15: Comparison of the relative amount of inclusions as a function of the initial O content: (a) and (b) are SEM images of polished cross sections of the reaction zone with Al_2O_3 inclusions appearing black for (a) sample 1 (160 ppm O); (b) sample 2 (450 ppm O). (c) is a SEM image of Al_2O_3 inclusions (appearing white) on the filtration membrane after extraction of sample 3 (780 ppm O).

The cross section of samples 4 to 6 was distinctive owing to the very high initial O content (1800 ppm). Inclusions show specific features as a function of their location, delimiting several areas depicted in Figure 6-16. Two zones are found in Fe (lower part of Figure 6-16 and Figure 6-17 (a)): one containing FeO_x, resulting from the excess O upon cooling, and a "precipitate-free" region located between the bulk Fe and the diffusion front (zone 0). The absence of precipitates in this specific area suggests a lower O content compared to the bulk Fe. As shown in Table 6-4, a thinner "precipitate-free" zone (i.e. high O source closer to the diffusion front) seems correlated with a larger Al gradient near the diffusion front. This aspect was discussed in section 6.2.2.3.

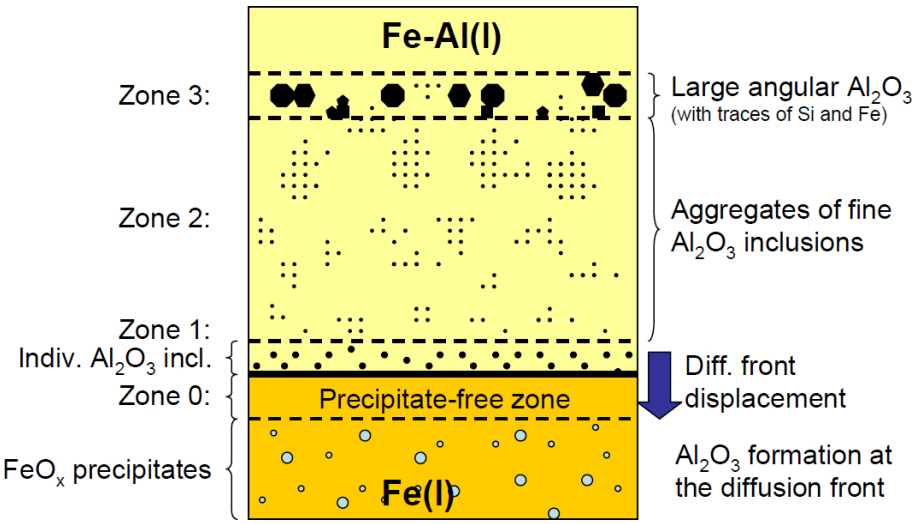

Figure 6-16: Simplified representation of the Fe and reaction zone in the case of high initial O content (samples 4 to 6), showing the different zones according to inclusion characteristics (delimited by dashed lines). Black markers represent Al_2O_3 inclusions and grey-filled markers FeO_x inclusions.

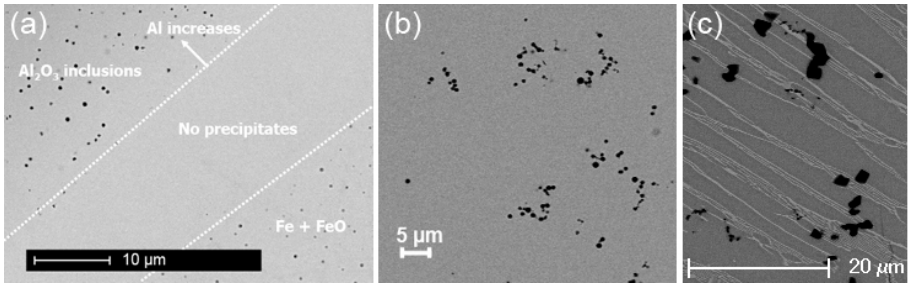

Figure 6-17: (a) BSE micrograph of diffusion front in sample 4 (1800 ppm O, 1 s), showing the "precipitate-free" free zone (zone 0, delimited by the dotted lines) separating α-Fe containing FeO_x from Fe-Al containing Al_2O_3 inclusions (zone 1); (b) Aggregates of fine Al_2O_3 inclusions observed in zone 2 of sample 6 (1800 ppm O, 60 s); (c) large angular Al_2O_3 inclusions with traces of Si, located in zone 3 of sample 6 (1800 ppm O, 60 s).

In the reaction zone, three regions containing inclusions were identified, as illustrated in Figure 6-16. The first one (zone 1) is located just above the diffusion front and comprises individual Al_2O_3 inclusions (Figure 6-17 (a)). Table 6-4 gathers the thickness and inclusion characteristics measured in this area. Also the layer thickness and the inclusion size in this area seem

correlated with the Al profile. The steeper the Al concentration profile at the diffusion front, the smaller the inclusions and the thinner the layer (Figure 6-12). At the beginning of the diffusion process, high nucleation rate and high diffusion front velocities are obtained because of steep concentration profiles at the diffusion front. Due to high O and Al contents at the diffusion front, the formation of numerous small inclusions is kinetically favoured, but their growth rate is limited by the high diffusion front velocity. As diffusion progresses, the concentration profiles at the front become less sharp and, consequently, the diffusion front velocity decreases. As shown in Table 6-4, the latter results in larger inclusions, indicating an increase of the inclusion growth rate.

Table 6-4: Extent of zones 0 and 1, inclusion characteristics in zone 1 and Al gradient at the diffusion front in samples 4 to 6 with high initial O content. Zone 0 corresponds to the "precipitate-free" area and zone 1 contains individual Al_2O_3 inclusions, as depicted in Figure 6-16 (a = angular; s = spherical; +++ = high; ++ = medium; + = low).

sample	thickness zone 0 (µm)	thickness (µm)	zone 1 average inclusion diameter (µm)	inclusion shape	Al gradient
5	1.5 - 2.5	~20	< 0.1	a	+++
4	~15	~35	0.3	a + s	++
6	~60	~70	1.0	s	+

In the adjacent zone 2 (Figure 6-16), aggregates of fine Al_2O_3 inclusions are found (Figure 6-17 (b)), as a result of inclusion collision and coagulation. Owing to the high inclusion number density, collisions are much more likely compared to the samples with lower initial O contents. As seen in Figure 6-18, when moving away from the diffusion front, the size of the aggregates increases as the number of collisions increases with time. On the other hand, the size of the inclusions forming the aggregates decreases. This is consistent with the evolution of the inclusion size with the profile steepness reported above.

Finally, zone 3 (Figure 6-16) comprises large Al_2O_3 inclusions with traces of Si and Fe (Figure 6-17 (c)). Oxide inclusions are hardly found above area 3, suggesting that O was not transported beyond this point.

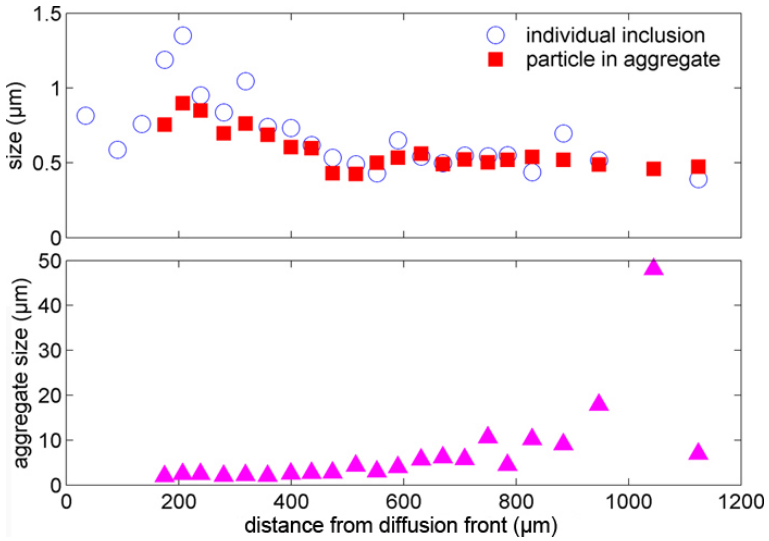

Figure 6-18: Evolution of (a) the size of the individual inclusions and that of the particles forming the aggregates and (b) the aggregate size as a function of the distance from the diffusion front for sample 6 (1800 ppm O, 60 s).

6.3.4. Inclusion morphology

The O content available at the diffusion front was found to influence the inclusion number by acting on the inclusion formation process. The growth process is also greatly influenced by supersaturation degree nearby the crystal. Therefore, a modification in the initial O content is expected to influence growth and morphology of the inclusions.

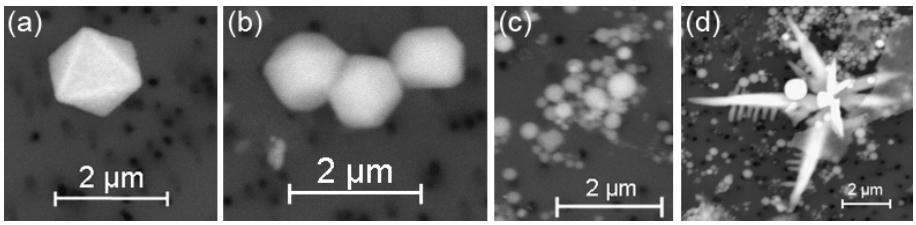

Figure 6-19: Evolution of the Al_2O_3 morphologies after extraction: (a) and (b) angular inclusions are dominant at low initial O content (sample 2: 450 ppm O, 1 s), (c) small spherical inclusions increase in number (d) and dendritic shaped inclusions are found with increasing initial O content (sample 3: 780 ppm O, 1 s).

Angular inclusions with a mean size of 2.1 µm were dominant in samples 1 and 2, often as individual particles (Figure 6-19 (a)), while spherical inclusions were hardly found. Small and sparse agglomerated angular inclusions were found as well (Figure 6-19 (b)). With increasing O content to 780 ppm (sample 3), numerous small spherical inclusions, mainly pure Al_2O_3 with a size less than 1 µm, were found (Figure 6-19 (c)), together with larger Al-Fe-O inclusions (Fe ~10 at%) with an average size of 3.9 µm. Small clusters were occasionally found.

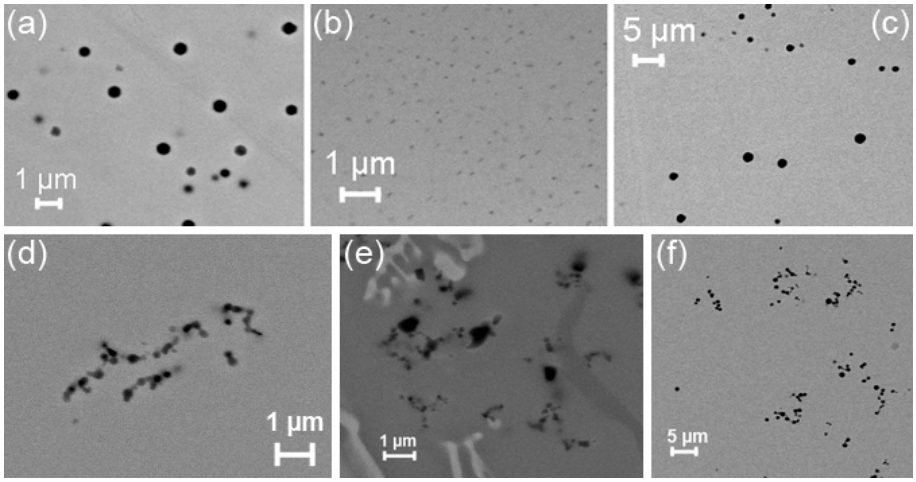

Figure 6-20: (a)-(c): Morphology of individual Al_2O_3 inclusions in zone 1 (Figure 6-16) for samples (a) 4 (1 s), (b) 5 (5 s) and (c) 6 (60 s) with 1800 ppm initial O content. (d)-(f): aggregates of fine Al_2O_3 inclusions found in zone 2 (Figure 6-16) of samples (d) 4 (1 s), (e) 5 (5 s) and (f) 6 (60 s) with 1800 ppm initial O content.

Figure 6-20 and Figure 6-21 show an overview of the inclusion morphologies observed in samples 4 to 6 with 1800 ppm initial O content based on the polished cross sections (Figure 6-20) and on extracted inclusions (Figure 6-21). The individual inclusions (originating from zone 1) in sample 6 have a spherical shape (Figure 6-20 (c) and Figure 6-21 (g)). Those in sample 4 have a shape intermediate between spherical and angular (Figure 6-20 (a) and Figure 6-21 (a) and (b)). Facets are appearing but are not well defined. As seen in Figure 6-20 (b), those in sample 5 were too small to obtain an average size and evaluate easily their shape.

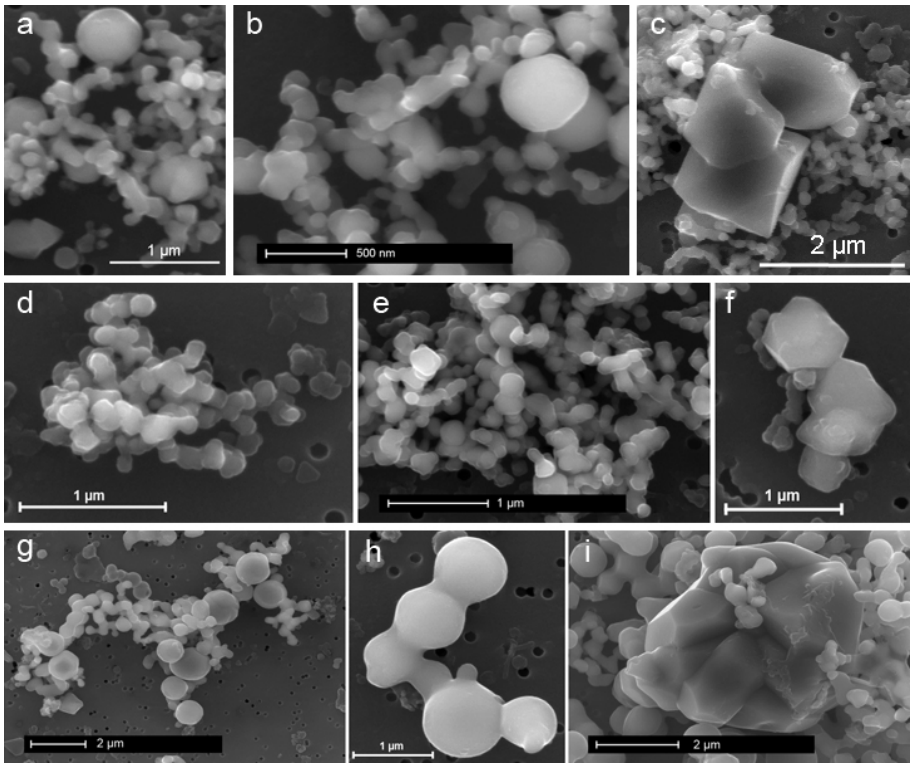

Figure 6-21: Overview of Al_2O_3 inclusion morphologies after extraction from (a) to (c): sample 4 (1 s, 1800 ppm O); (d) to (f): sample 5 (5 s, 1800 ppm O) and (g) to (i): sample 6 (60 s, 1800 ppm O).

As mentioned after the observation on the polished cross sections, a collision-coagulation mechanism is suggested for the formation of aggregates in zone 2. The fine Al_2O_3 inclusions forming the aggregate have a size far less than 1 µm and exhibit spherical and angular shapes. Even if the holding time is changing between samples 4 to 6, the aggregates are very similar in shape (Figure 6-20 (d) to (f)). However, the size of the particles forming the aggregates tends to be larger in sample 6 compare to samples 4 and 5. After extraction from the metal matrix, the individual inclusions forming the aggregates are easily distinguishable. In samples 4 and 5, the latter are mainly angular shaped (Figure 6-21 (a) and (b); (d) and (e)). In sample 6, both angular and spherical morphologies are found numerously (Figure 6-21 (g) and (h)).

The third distinct morphology that was identified in every sample concerns the large, compact angular inclusions (Figure 6-21 (c), (f) and (i)). Contrasting with the other inclusions, they show well defined and smooth facets and tend to be larger and more compact with time (Figure 6-21 (i)).

The absence of intermediate morphologies between aggregates (network structure) to such compact shapes corroborates that these large angular inclusions are formed by a distinct mechanism.

Inclusion shape depends on the conditions during their formation and growth. One of the most important contributors is the melt supersaturation, which increases with the O and Al content. Clusters and dendrites, bars and globular inclusions are typically found at high supersaturation, whereas angular and compact shapes are observed at low supersaturation [70, 162, 164-168, 170, 173]. The inclusion shape evolution from faceted prevailing at low initial O content (samples 1 and 2) to globular appearing at higher initial O content (samples 3) can be explained by higher supersaturation conditions.

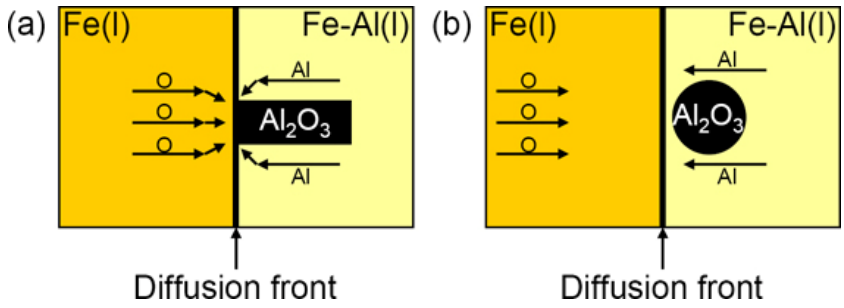

Figure 6-22: Proposed mechanism for the formation of Al_2O_3 inclusions at the diffusion front in case of (a) high mass transport rate of Al and O to the diffusion front, generating bar-like inclusions, and (b) slow mass transport of Al and O to the diffusion front, giving rise to compact-shaped inclusions.

Although four distinct inclusion morphologies are reported in literature under high supersaturation conditions, i.e. clusters, dendrites, bars and spheres, only the last one was observed in the present study. As explained in Chapter 3, to obtain bars, dendrites or clusters, continuous and non uniform conditions of supersaturation must be applied, where Al and O are supplied along one or several directions. In most of the studies reporting on inclusion morphologies, well-stirred and turbulent liquid steel flow is usually attained, providing high supersaturation conditions and relatively high mass transport rates. Under the present conditions, turbulences are limited and Al and O are transported by a unidirectional counter-current diffusion process. Local growth conditions are controlled by O and Al diffusion rates to the diffusion front. In order to grow bar-like or dendritic inclusions, O and Al must be continuously transported to the diffusion front to maintain enough supersaturation. This implies that O and Al diffusivities in Fe and Fe-Al phases must be high enough to ensure mass transport to the diffusion front

without cessation. Figure 6-22 (a) illustrates the growth process of such elongated inclusions.

In the present study, small and short-shaped inclusions were observed, suggesting that mass transport rate was too slow to obtain bar-like shapes. To explain this, the following mechanism is proposed, as depicted in Figure 6-22 (b). Once nucleation took place, the local O and Al concentrations decreased drastically. Due to low diffusivities of O and Al, the O or Al content remains too low to enable nucleation and/or growth at the diffusion front. The inclusion size is therefore limited. Diffusion of Fe towards Fe-Al (or reciprocally Al into deoxidized Fe) proceeds, causing the displacement of the diffusion front. Once enough supersaturation is provided at the front, nucleation and growth of a new inclusion takes place. Under these conditions, the determining factor for inclusion size and morphology would be, therefore, O transport to the diffusion front.

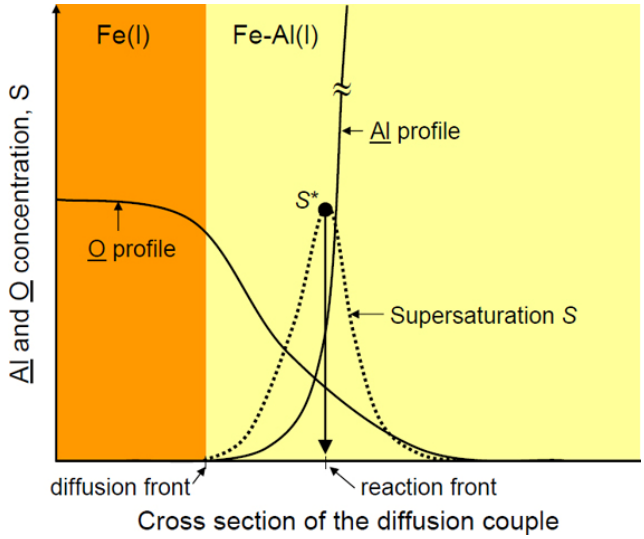

Figure 6-23: Schematic view of the reaction zone during high temperature interaction, representing the overlap between the Al and O concentration profiles and the buildup of the supersaturation curve in the reaction zone (Fe-Al(l)) near the diffusion front, and the distinct position of the reaction and diffusion fronts. The reaction front appears when *S* reaches *S**.

The proposed mechanism in Figure 6-22 requires that the reaction front, where the formation of Al_2O_3 inclusions takes place, corresponds exactly with the diffusion front during the experiments. Another approach would consider that, during the high temperature interaction, the reaction front is located behind the diffusion front, in the reaction zone. This situation, which

is depicted schematically in Figure 6-23, occurs if the reaction is delayed or requires a certain level of supersaturation S^* to initiate nucleation. As a result, diffusion of O in the reaction zone proceeds, creating an overlap between the O and the Al profiles in the reaction zone near the diffusion front. The local supersaturation S increases gradually in the reaction zone near the diffusion front, as diffusion of both Al and O progresses (dashed line in Figure 6-23). Once the local S value reaches S^* at a specific location, nucleation takes place in that area, defining the reaction front position (Figure 6-23). As the Al availability is high in the reaction zone, the O availability at the reaction front, which is controlled by the initial O content in liquid Fe and by O transport to the reaction zone, will determine the inclusion nucleation and growth conditions at the reaction front. Nucleation and growth occurs in a confined supersaturated zone where the amount and the transport of O is limited, providing conditions for the formation of short-shaped inclusions. Once nucleation is initiated, the growth process is limited owing to the limited transport of O to the reaction front, as demonstrated by the small inclusion size in the reaction zone.

Since S increases with decreasing temperature, the supersaturation of the Fe-Al-O melt comprised between the diffusion front and the reaction front increases during cooling of the sample to room temperature. Formation of Al_2O_3 inclusions, which was not possible in that area at the experiment temperature, can take place upon cooling. Quenching significantly slows down the diffusion process and activates inclusion formation and precipitation, causing the reaction front to catch up with the diffusion front during cooling, as observed during the sample investigations. These inclusions would have different characteristics, such as size and morphology, compared to the inclusions formed during high temperature interaction. In view of these aspects, some of the individual inclusions found in zone 1 of the samples 4 to 6 (confer Figure 6-16) might have formed during quenching as their characteristics, such as size and morphology (Table 6-4 and Figure 6-20), differ from those in zone 2.

6.4. Conclusions

Inside a quartz tube, a piece of Al was brought in contact for a very short time with liquid Fe containing different oxygen levels at 1600 °C. The purpose was to investigate the interactions between Fe and Al and to examine the formation and the morphology of Al_2O_3 inclusions at the interface shortly after the deoxidation stage.

In the first part, it was shown that the reaction zone, where the interactions between Fe and Al took place, was composed of successive layers of Fe-Al

intermetallic compounds dictated by the phase diagram of the system. Microstructural features, the gradual Al concentration profile across the reaction zone, the presence of a precipitate-free zone near the diffusion front, estimations of the diffusion processes in solid and liquid phases, and the behaviour of Al_2O_3 inclusions in the reaction zone indicated that the latter was completely liquid and that, for the samples with holding time of 30 and 60 s, the solid Fe shell melted. The layers of intermetallic compounds observed in the solidified reaction zone are therefore formed during cooling of the liquid phase containing Fe and Al concentration gradients.

Al_2O_3 inclusions were formed as a result of the reaction between Al and O in the liquid Fe. Variations in size and morphology of the inclusions with the initial O content and the reaction time were reported. The following aspects were highlighted:

- The Al_2O_3 inclusions were located in the reaction zone, between the initial Fe-Al boundary and the final diffusion front.
- Large angular inclusions with traces of Si and Fe were observed near the initial Fe/Al interface, likely resulting from heterogeneous nucleation of Al_2O_3 on FeO_x and/or SiO_2 inclusions.
- In the samples with high O content, small spherical and angular inclusions were found near the diffusion front, while clusters and aggregates of small inclusions, resulting from collisions, are numerous further away from the diffusion front.
- With lower O content, the amount of inclusion decreases and faceted inclusions are dominant among the morphologies, owing to lower supersaturation conditions.

The evolution of the supersaturation in the reaction zone near the diffusion front was examined when a critical value of supersaturation is required for the formation of inclusions. In that case, the reaction front is located in the reaction zone and its position differs from that of the diffusion front. Inclusion nucleation and growth, which determine inclusion size and morphology, seem to be controlled by the availability and the mass transport rate of O to the reaction front.

Chapter 7
Diffusion-controlled model for the prediction of Fe-Al melt reoxidation

---

After the deoxidation stage, reoxidation of liquid steel is one of the major causes for the formation of inclusions. Numerous sources of steel reoxidation have been presented in Chapter 2. Since they may deteriorate the internal steel cleanliness drastically, sound knowledge of the formation mechanism and the characteristics of the newly formed inclusion population are necessary.

The formation and morphology of Al_2O_3 inclusions during reoxidation of Fe-Al alloys were experimentally investigated by modifying the oxygen partial pressure in the gas phase. The experimental results are shown in Chapter 8. In parallel, a diffusion model for Al and O in liquid Fe was developed to estimate the evolution of the local conditions during the formation and growth of inclusions which can be linked to the inclusion characteristics observed with the reoxidation experiments. Modelling of the diffusion and formation of Al_2O_3 inclusions is the subject of the present Chapter. First, the reoxidation process will be formulated mathematically by considering the equilibrium between the melt surface and the gas phase. The diffusion equations of Al and O in the melt, which include the reaction of Al_2O_3 formation, are then solved analytically for a semi-infinite geometry and numerically for a finite geometry, using two different approaches. The results obtained by the three models are compared. Finally, the influence of the diffusion time and the initial conditions on the motion of the reaction front, the concentration profiles through the melt, the inclusion formation and on the accumulated supersaturation is discussed.

7.1. Problem description and formulation

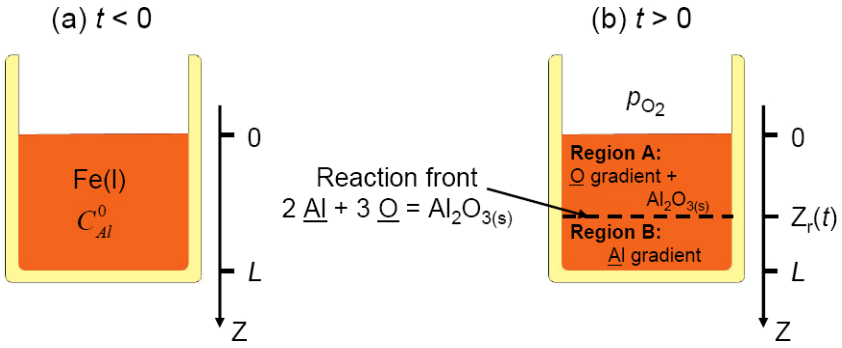

Figure 7-1: Schematic diagram illustrating the system (a) at the initial condition (deoxidized Ar, t < 0) and (b) during reoxidation of the Fe-Al alloy, at time $t > 0$.

Prior to the reoxidation, a cylindrical Al_2O_3 crucible (inside diameter 30 mm) containing a given amount of liquid Fe-Al alloy of known composition C^0_{Al} and height L is held at a temperature of 1600 °C under a deoxidised Ar atmosphere ($p_{O_2} < 10^{-20}$ atm). The initial conditions are illustrated in Figure 7-1 (a).

7.1.1. Equilibrium in the gas phase

At time $t \geq 0$, the oxygen partial pressure, p_{O_2}, in the furnace is changed by applying a CO/CO_2 gas mixture with fixed ratio. From that moment, equilibrium between CO, CO_2 and O_2 is established in the gas phase:

$$2\,CO(g) + O_2(g) = 2\,CO_2(g). \tag{7.1}$$

The standard Gibbs free energy ΔG^0 (J mol^{-1}) and the equilibrium constant K_1 of the reaction are, respectively [189]:

$$\Delta G_1^0 = -562288 + 170.57T = -RT \ln K_1, \tag{7.2}$$

$$K_1 = \frac{p_{CO_2}^2}{p_{CO}^2 p_{O_2}}. \tag{7.3}$$

Combining Eqs. (7.2) and (7.3), the oxygen partial pressure at equilibrium can be calculated by specifying the CO/CO_2 ratio and temperature:

$$p_{O_2} = \exp\left(-67627.4\frac{1}{T} + 20.515\right)\left(\frac{p_{CO_2}}{p_{CO}}\right)^2 . \tag{7.4}$$

Owing to the presence of oxygen in the gas phase, oxidation of the Fe-Al melt will start from the liquid surface ($Z = 0$). The O equilibrium between the melt and the atmosphere can be represented by Eq. (7.5).

$$O_2(g) = 2\,\underline{O} \tag{7.5}$$

with standard Gibbs free energy ΔG^0 (J mol^{-1}) and equilibrium constant K_2 [250]:

$$\Delta G_2^0 = -234300 - 5.78T = -RT\ln K_2 , \tag{7.6}$$

$$K_2 = \frac{[\text{wt\% }\underline{O}]^2}{p_{O_2}} . \tag{7.7}$$

From Eqs. (7.6) and (7.7), the dissolved oxygen concentration is determined by the value of the p_{O_2} at a given temperature. The latter is written:

$$[\text{wt\% }\underline{O}] = \exp\left(14089.8\frac{1}{T} + 0.3476\right)\sqrt{p_{O_2}} \tag{7.8}$$

where p_{O_2} is expressed in atm. To simplify the problem, the reoxidation reactions of liquid steel by CO(g) and CO_2(g) are not considered.

7.1.2. Gas-liquid metal equilibrium

The solubility of oxygen in liquid Fe is determined by the equilibrium with liquid FeO:

$$FeO(l) = Fe(l) + \underline{O} . \tag{7.9}$$

The standard free energy change ΔG^0 (J mol^{-1}) and the equilibrium constant K_3 of the reaction are [251]:

$$\Delta G_3^0 = 121000 - 52.35T = -RT \ln K_3, \tag{7.10}$$

$$K_3 = \frac{[\text{wt\% } \underline{\text{O}}]}{a_{\text{FeO}}}. \tag{7.11}$$

The value of the saturation is found by imposing that the activity of FeO, a_{FeO}, is unity. The oxygen saturation in liquid Fe is, therefore, a function of temperature only:

$$[\text{wt\% } \underline{\text{O}}]_{\text{sat.}} = \exp\left(-14552.89\frac{1}{T} + 6.296\right). \tag{7.12}$$

At 1600 °C, the oxygen solubility in liquid Fe is 0.2291 wt% (Eq. (7.12)). Inserting this value in Eq. (7.8) gives an oxygen partial pressure of 7.66 10^{-9} atm. Above this value, liquid Fe would be oversaturated with oxygen, causing the formation of FeO. $\underline{\text{O}}$ concentration is then fixed at 0.2291 wt%, even if the p_{O_2} is increased. On the other hand, liquid Fe is not saturated with $\underline{\text{O}}$ if the p_{O_2} lies below 7.66 10^{-9} atm. The $\underline{\text{O}}$ concentration is determined by equilibrium reaction (7.5) and can be calculated with Eq. (7.8).

7.1.3. Reoxidation process of Fe-Al alloy

Dissolved oxygen in liquid iron ($\underline{\text{O}}$) reacts with dissolved aluminium ($\underline{\text{Al}}$) in an instantaneous irreversible reaction 2 $\underline{\text{Al}}$ + 3 $\underline{\text{O}}$ = Al_2O_3(s). The latter implies that a reaction front is created parallel to the melt surface at a distance Z_r from it. This front separates the region A containing no $\underline{\text{Al}}$ ($0 < Z < Z_r$) from the region B containing no $\underline{\text{O}}$ ($Z_r < Z < L$). The position of the reaction front evolves with time because region A grows over region B as $\underline{\text{Al}}$ is used in the chemical reaction. At the reaction front, where $\underline{\text{O}}$ and $\underline{\text{Al}}$ meet and react to form solid Al_2O_3, we assume that equilibrium is reached and that the equilibrium contents of $\underline{\text{Al}}$ and $\underline{\text{O}}$ are negligibly small. Because Al_2O_3 inclusions are created at the reaction front and they move upwards owing to the buoyancy forces, inclusions are all located in region A. A scheme of the system at time t is given in Figure 7-1 (b).

The geometry of the system is planar and species diffuse along the vertical direction (Z axis). Given the small $\underline{\text{O}}$ and $\underline{\text{Al}}$ concentrations in the melt,

Fick's second law adequately describes the diffusion processes of O and Al in, respectively, regions A and B. Moreover, the diffusion coefficients of Al and O, D_{Al} and D_O, are assumed independent of the concentration. The governing equations for C_O and C_{Al}, i.e. the concentrations of O and Al in the liquid melt, are therefore:

$$\frac{\partial C_O}{\partial t} = D_O \frac{\partial^2 C_O}{\partial Z^2} \qquad 0 \le Z \le Z_r(t) \tag{7.13}$$

$$\frac{\partial C_{Al}}{\partial t} = D_{Al} \frac{\partial^2 C_{Al}}{\partial Z^2} \qquad Z_r(t) \le Z \le \infty \tag{7.14}$$

With appropriate initial and boundary conditions:
Initial conditions: $t = 0$, $Z > 0$:

$$\begin{cases} C_{Al}(Z,0) = C_{Al}^0 \\ C_O(Z,0) = 0 \\ Z_r(0) = 0 \end{cases} \tag{7.15}$$

Boundary conditions: $t > 0$:

$$Z = 0 : C_O(0,t) = C_O^{sat.} \tag{7.16}$$

$$Z = Z_r(t) : C_O = C_{Al} = 0 \tag{7.17}$$

$$Z = Z_r(t) : -\frac{1}{3} D_O \frac{\partial C_O}{\partial Z} = \frac{1}{2} D_{Al} \frac{\partial C_{Al}}{\partial Z} \tag{7.18}$$

Equation (7.18) describes the motion of the reaction front and is derived by requiring the reaction stoichiometry (the formation of 1 mole Al_2O_3 requires 2 moles Al and 3 moles O). Equations (7.13) to (7.18) form a coupled system of non-linear differential equations with moving boundaries (also known as Stefan problems).

7.2. Solutions of the counter-current diffusion model

7.2.1. Analytical solution (semi-infinite geometry)

An analytical expression for the solution of the Stefan problem can be derived in a semi-infinite one-dimensional geometry. In this particular case, the liquid melt forms a semi-infinitely large matrix phase. The Al concentration infinitely far away from the front must remain constant at the initial concentration C_{Al}^{0}.

$$Z = \infty : C_{Al} = C_{Al}^{0} \tag{7.19}$$

With such particular initial and boundary conditions, the diffusion equations (7.13) and (7.14) are known to have solutions with general form [252]:

$$\frac{C_O}{C_O^{sat.}} = c_1 + c_2 erf\left(\frac{Z}{\sqrt{4D_O t}}\right) \qquad 0 \le Z \le Z_r(t) \tag{7.20}$$

$$\frac{C_{Al}}{C_{Al}^{0}} = c_3 + c_4 erf\left(\frac{Z}{\sqrt{4D_{Al} t}}\right) \qquad Z_r(t) \le Z \le \infty \tag{7.21}$$

Application of the initial conditions (Eq. (7.15)) and the boundary conditions given by Eqs. (7.16), (7.17) and (7.19) allows the evaluation of the integration constants c_i. The concentration profiles are then expressed as a function of the front position $Z_r(t)$:

$$\frac{C_O}{C_O^{sat.}} = 1 - \frac{erf\left(\frac{Z}{\sqrt{4D_O t}}\right)}{erf\left(\frac{Z_r}{\sqrt{4D_O t}}\right)} \qquad 0 \le Z \le Z_r(t) \tag{7.22}$$

$$\frac{C_{Al}}{C_{Al}^{0}} = 1 - \frac{1 - erf\left(\frac{Z}{\sqrt{4D_{Al}t}}\right)}{1 - erf\left(\frac{Z_r}{\sqrt{4D_{Al}t}}\right)} \qquad Z_r(t) \le Z \le \infty \tag{7.23}$$

The position of the front position $Z_r(t)$ is calculated thanks to the boundary condition Eq. (7.18), which gives the following relation:

$$1 - erf\left(\sqrt{\frac{\lambda}{D_{Al}}}\right) = \frac{3}{2}\sqrt{\frac{D_{Al}}{D_O}}\frac{C_{Al}^{0}}{C_O^{sat.}} erf\left(\sqrt{\frac{\lambda}{D_O}}\right)\exp\left(\frac{\lambda}{D_O} - \frac{\lambda}{D_{Al}}\right) \tag{7.24}$$

where $\lambda = \frac{Z_r(t)^2}{4t}$. The concentration profiles at each time step can be calculated by first evaluating the position of the front with Eq. (7.24), and inserting this value in Eqs. (7.22) and (7.23).

7.2.2. Numerical solutions (finite geometry)

In modelling counter current diffusion problems, the main difficulty arises in tracking the motion of the reaction front. In the ideal case described before, an analytical solution can be found. However, for a system of finite dimension, no analytical solutions are available and numerical methods are required to solve the partial differential equations. Several methods are available in the literature, mostly differing on the way the front motion is described. Section 7.2.2.1 introduces a numerical model to solve diffusion-controlled moving boundary problem, later referred as model A. In section 7.2.2.2, the diffusion problem is solved using a simplified model decoupling the diffusion and the reaction processes, referred as model B.

7.2.2.1. Model for diffusion-controlled moving boundary system with solute conservation (model A)

The approach used in the present work follows that described by Illingworth *et al.* [253]. Essentially, they developed the model to study transient liquid phase (TLP) bonding and to describe isothermal phase changes controlled by the diffusion of matter. The problem considers the diffusion of one solute in a liquid and a solid phase, which are separated by a moving interface

controlled by diffusion. In that case, the moving interface separates the solid and liquid phases, in which the solute has different diffusivities. In the present problem description, two solutes are involved, i.e. Al and O, in a single liquid phase, i.e. Fe. The moving interface described by Illingworth becomes a moving reaction front in this particular case. The idea proposed by Illingworth [253] is to impose a transformation that fixes the interface instead of using a constant spatial discretisation. The interface is then able to move without constraints, while ensuring that its position coincides always with a discretisation point. With such a description, they ensure the conservation of solute at each time step.

Two new positional variables are introduced in order to divide the melt into two regions. With this coordinate system, the region A defined between 0 and $Z_r(t)$ (diffusion region of oxygen) corresponds to $0 < u < 1$ and region B defined between $Z_r(t)$ and L (diffusion domain of aluminium) corresponds to $0 < v < 1$. At each time steps, the reaction front position is fixed at $u = 1$ and $v = 0$. A fully implicit, conservative finite difference method was used. The problem was decoupled in a set of linear equations that are solved iteratively. The detailed calculations are provided in section A.1 of the Appendix. The numerical scheme has a first order accuracy in space and time, and allows the use of irregular meshes. The implicit algorithm was written in computer code and tested for convergence and accuracy by comparing the results with the analytical solution given in Eqs. (7.22) to (7.24).

7.2.2.2. Simplified model decoupling diffusion and reaction processes (model B)

In the previous approach, a reaction front was imposed where the reaction between Al and O to form Al_2O_3 takes place. This reaction front divides the domain in two sub-domains, in which only one species is allowed to be transported. One of the strong assumptions made in this scheme was to impose that the Al and O concentrations at equilibrium were zero, implying that Al and O cannot be present in the same sub-domain. These assumptions imply that the reaction front has no physical thickness and that further nucleation or growth is not possible elsewhere than at the reaction front. In this approach, the diffusion equations for Al and O are written on the entire domain (from 0 to L), so that Al and O concentration profiles can be calculated over the entire domain. Al and O diffuse over one time step without constraints on the presence of the other species.

The diffusion equations for Al and O were solved using the finite difference approximations for the derivatives using an explicit scheme. Details of the calculation procedure are provided in section A.2 of the Appendix.

Equations (7.25) and (7.26) describe the evolution of the concentration profiles as a function of time and position in the whole domain.

$$C_{Al}(i,j+1) = C_{Al}(i,j) + \frac{D_{Al}\delta t}{(L\cdot\delta u)^2}\left(C_{Al}(i+1,j) - 2C_{Al}(i,j) + C_{Al}(i-1,j)\right) \quad (7.25)$$

$$C_{O}(i,j+1) = C_{O}(i,j) + \frac{D_{O}\delta t}{(L\cdot\delta u)^2}\left(C_{O}(i+1,j) - 2C_{O}(i,j) + C_{O}(i-1,j)\right) \quad (7.26)$$

where δt and δu correspond to, respectively the time and space steps, and symbols i and j denote discretisations of, respectively, space and time.

Up to now, the Al and O concentrations are not coupled. For each time step, the diffusion and the Al_2O_3 formation processes are solved in two separated steps. The diffusion equations described in Eqs. (7.25) and (7.26) are first solved over the time step dt to calculate the temporary Al and O concentrations at time t_2 (= t_1 + dt), given the concentration profiles at time t_1. This is illustrated in Figure 7-2 (a), where the temporary Al and O concentration profiles at time t_2 (indicated by dashed lines) are calculated from the corresponding profiles at time t_1.

Once the Al and O concentration profiles are determined over the whole domain at time t_2, the temporary Al and O concentrations are evaluated at each grid point for possible reaction. The reaction constant $K' = a_O^3 \cdot a_{Al}^2$ is evaluated at every grid point and time step, and compared with the equilibrium reaction constant K. Two cases are then possible. If $K' > K$, the melt is locally supersaturated and reaction is allowed. Al and O are then consumed until the local equilibrium composition of the melt. This case is exemplified by point A in Figure 7-2 (b), of which the melt composition is located in the Al_2O_3 stability domain. The melt composition will move from point A to point B situated on the equilibrium line, by consuming a certain amount of Al and O. The ratio of Al to O used up to reach point B is fixed by the stoichiometry of the reaction, as illustrated in Eq. (7.27).

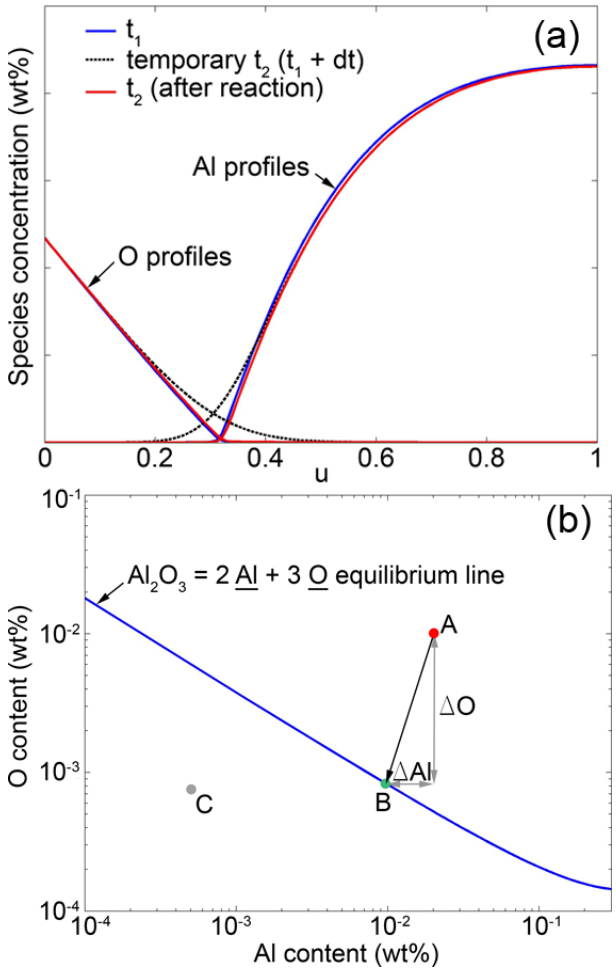

Figure 7-2: (a) Approach used to decouple the diffusion and the reaction processes to calculate the Al and O concentration profiles over a time step dt, starting from the corresponding profiles at time t_1. The profiles are exaggerated for clarity. (b) Al and O contents in liquid Fe in equilibrium with solid Al_2O_3 at 1600 °C. Point A represents the case the melt composition is initially in the Al_2O_3 stable region. The melt composition moves then to point B on the equilibrium line, following the stoichiometry of the reaction. Point C corresponds to the case the equilibrium constant is not reached.

$$\frac{\Delta \mathrm{Al}}{\Delta \mathrm{O}} = \frac{2M_{\mathrm{Al}}}{3M_{\mathrm{O}}} \tag{7.27}$$

where Δi is the difference in concentration of element i (in wt%) due to Al_2O_3 formation, and M_i the molecular weight of element i. The slope of the

line connecting point A to point B is fixed by relation (7.27). The corresponding equilibrium composition is therefore easily accessible from any melt composition situated in the Al_2O_3 stability domain. If $K' \leq K$, the melt is or locally unsaturated, or already in equilibrium with solid Al_2O_3. The Al and O concentrations are unchanged (point C in Figure 7-2 (b)). After that the Al and O concentration profiles are corrected to consider the reaction (Figure 7-2 (a), red line), the latter are employed to calculate the future concentration profiles at time $t_2 + dt$ and the whole procedure is repeated.

In this approach, the diffusion and the reaction are decoupled to solve the sets of equations easily. To obtain a solution which is closer to the actual physical process occurring during the experiments, the diffusion equations should be solved with additional constraints provided by the equilibrium activity product (Eq. (2.6) in Chapter 2) and by mass balance equations. However, the latter generates a complex system of equations. Though the relation between Al and O at equilibrium is known, the position of the local melt composition on the equilibrium line is a priori unknown. The present approach provides therefore only estimations on the concentration profiles and supersaturation degrees of the melt at different location and as a function of initial conditions and time.

Separate calculation of the diffusion and the formation of Al_2O_3 may overestimate the transport of species because the elements are first distributed and then removed if reaction is taking place. Because the phenomenon is handled in two successive steps instead of simultaneously, transport of elements by diffusion is calculated over the time step assuming that the total mass of dissolved element is available for transport, which is not always the case. Part of it might have been consumed through the reaction and should not be transported over the time step. With a simultaneous solution of the diffusion and the reaction processes, the excess concentration regarding the solubility product would be removed concurrently and would not be taken into account in the diffusion process over that time step. Intuitively, the choice of the time step should have a significant impact on the calculation results. This will be discussed in section 7.3.1.4.

In this particular case, the error made by decoupling the two processes is limited due to several reasons. First, the Al and O diffusion coefficients in liquid Fe are small. In that case, the transport of species is limited, given that sufficiently small time steps are used. Secondly, the level of concentrations investigated is high compared to the equilibrium values. Combined with small transport ability, the modification brought to the concentration profiles by only mass transport is small compared to the actual concentrations. The

shape of the equilibrium curve and the evolution of the melt composition during the diffusion process might have an impact on the correction to be made on the concentration profiles.

7.3. Results

7.3.1. Comparison analytical versus numerical solution

The values of the parameter used in the analytical solution and numerical estimation are listed in Table 7-1. The calculations were performed on the case of a Fe-Al alloy containing initially 0.22 mass% Al and held in an atmosphere with a p_{O_2} of 2.0 10^{-9} atm. According to Eq. (7.8), the value of the p_{O_2} fixes the oxygen saturation in liquid Fe at 0.1171 mass%. The height of the liquid bath, L, is approximately 1.3 cm. Numerical calculations using model A were conducted by discretising regions A and B with 250 points using irregular meshes. The latter enables a fine resolution where large concentration gradients are created, such as near the reaction front. In the case of model B, the melt bath was discretised with 200 points using regular spacing.

Table 7-1: Definition of the variables used for the analytical and numerical results

Parameter	value	unit
Time step – δt	100	s
Number of time step	90	-
Melt temperature – T	1600	°C
Initial reaction front position – $Z_r(0)$	0	cm
Height of the liquid melt bath – L	1.3	cm
Reaction area – A	7.068	cm^2
Number of discretisation point (model A) – N	250	-
Molar fraction of <u>O</u> at saturation – $C_O^{sat.}$	4.076 10^{-3}	-
Initial molar fraction of <u>Al</u> – C_{Al}^0	4.54 10^{-3}	-
Density liquid Fe - ρ_{Fe}	7.1	g cm^{-3}
Density pure Al_2O_3(s) - $\rho_{Al_2O_3}$	4.0	g cm^{-3}
Diffusion coefficient of <u>O</u> – D_O	1.4 10^{-4} [244]	cm^2 s^{-1}
Diffusion coefficient of <u>Al</u> – D_{Al}	5.33 10^{-5} [204]	cm^2 s^{-1}

7.3.1.1. Motion of the reaction front Z_r

The accuracy of the numerical solution can be assessed by comparing the numerical results performed using model A with a large value of L with the analytical solution using a semi-infinite geometry. Figure 7-3 shows the evolution of the position of the reaction front for the analytical solution and numerical solutions with L = 50 cm and 1.3 cm. According to the analytical solution, the front position varies with the square root of time. For a large value of L (50 cm), the numerical results are in close agreement with analytical predictions. For L = 1.3 cm, which is the experimental value of the melt height at 1600 °C, the numerical predictions are close to the analytical solution when time is less than 4000 sec. This means that the diffusion length is small compared to L and that the finite geometry does not affect diffusion for such values of time. Deviation from the analytical solution becomes significant for time larger than 4000 s. The motion of the front is accelerated compared to the semi-infinite geometry. At t = 8100 s (2 h 15 min), the front position reached the bottom of the crucible and, therefore, all Al is consumed.

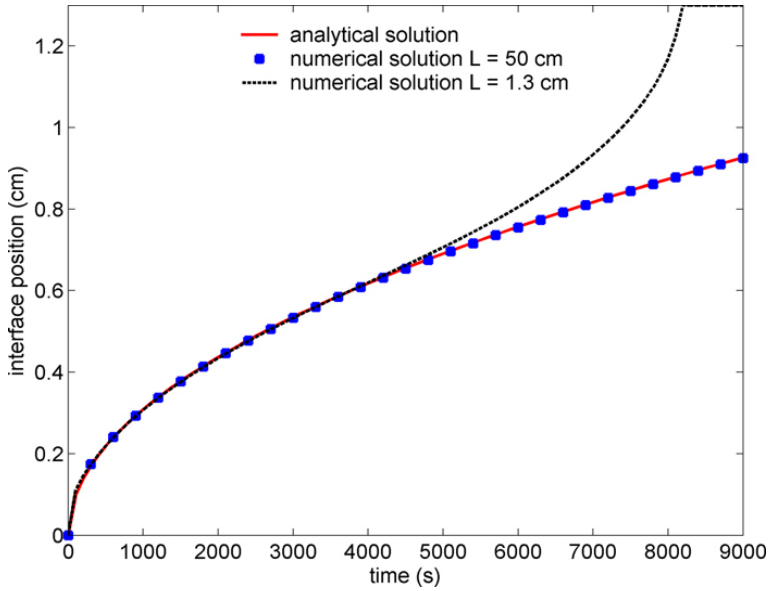

Figure 7-3: Evolution of the reaction front position Z_r (cm) with time (C_{Al}^{0} = 0.22 wt%, $C_{O}^{sat.}$ = 0.1171 wt%).

7.3.1.2. Concentration profiles

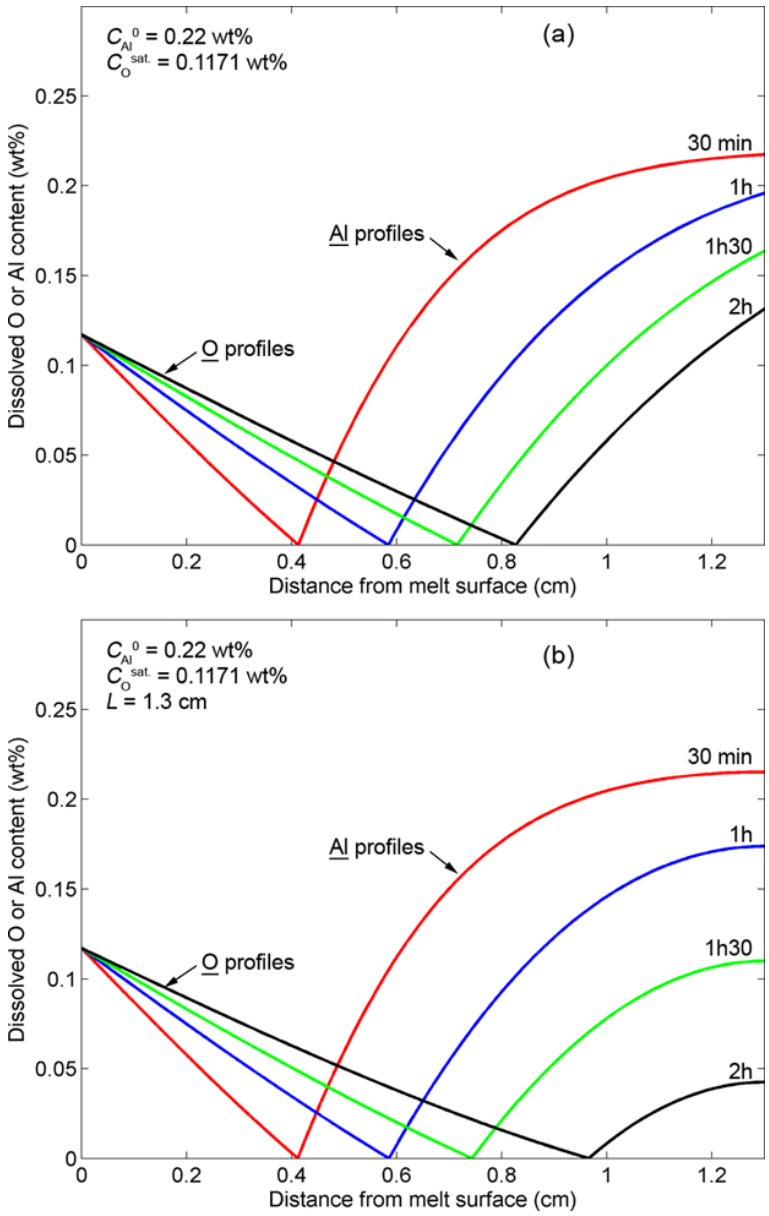

Figure 7-4: Evolution of the concentration profiles of O and Al in the melt for different time (30 min, 1 h, 1 h 30 min and 2 h): concentration profiles calculated (a) analytically (semi-infinite system) and (b) with the numerical solution (model A) using L = 1.3 cm, corresponding to the typical liquid bath height.

For the particular case described in Table 7-1, the concentration profiles through the melt were calculated and plotted in Figure 7-4 (a) for the analytical (semi-infinite geometry) solution and in Figure 7-4 (b) for the model A using a finite geometry system. The concentration profiles obtained after 30 min, 1 h, 1 h 30 min and 2 h are shown. The vertical axis Z is plotted horizontally, the value "0" representing the melt surface ($Z = 0$). The left side of the curves corresponds to the O profile, and the right side, to that of Al.

The calculations show that the slope of the curves of the O and Al profiles are initially steep and become flatter with time. The comparison between Figure 7-4 (a) and (b) shows that the profiles calculated analytically and those calculated numerically are identical for a diffusion time of 30 min, indicating that the fixed boundary at $Z = L$ has limited influence on the diffusion of both species for such durations.

For longer time, the profiles differ significantly. The Al profile is vanishing faster as a result of the additional boundary condition (zero flux). Consequently, O can diffuse deeper in the melt, pushing the reaction front further. Moreover, the slope of the concentration profile curves near the reaction front is lower compared to the analytical solution. This may have an influence on the characteristics of the inclusions formed at the reaction front (because of different supersaturation degree). It is therefore important to have access to this information in order to study the influence of the melt conditions on the characteristics (number, size distribution, shape) of the inclusions.

Figure 7-5 shows the Al and O concentration profiles obtained with model B, using a time step of 0.1 s instead of 100 s (model A). A smaller time step is required to ensure a numerically stable solution of the explicit scheme. As mentioned in section 7.2.2.2, the Al and O profiles overlap when non-zero Al and O equilibrium contents are involved in the calculations. As seen in Figure 7-5, the overlapping is very limited given the low Al and O equilibrium values. From this observation, the assumption that Al and O equilibrium values are negligible is reasonable and would not introduce too large errors on the estimated profiles. The concentration profiles in Figure 7-5 are almost identical to those in Figure 7-4 (b) obtained with numerical model A. The reaction fronts and the intersection of the Al and O profiles are approximately located at the same position. This suggests that the error brought by the simplification on the Al and O equilibrium values has negligible influence on later concentration profiles.

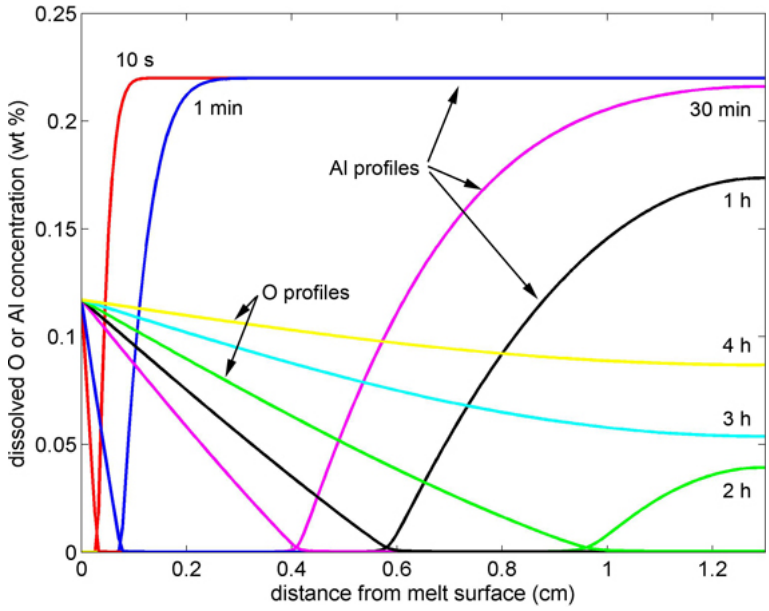

Figure 7-5: O and Al concentration profiles calculated with the decoupled model (model B) for different diffusion time (10 s, 1 min, 30 min, 1 h, 2 h, 3 h and 4 h). Conditions: C_{Al}^{0} = 0.22 wt%, $C_{O}^{sat.}$ = 0.1171 wt%, dt = 0.1 s, L = 1.3 cm.

7.3.1.3. Prediction of inclusion formation

The rate of inclusion formation at the reaction front can be evaluated at each time step by the rate of mass transfer, $N_{O,reaction}$ (mole s^{-1}), through the reaction front:

$$N_{O,reaction} = -\frac{\rho_{Fe} A}{M_{Fe}} D_O \left.\frac{\partial C_O}{\partial Z}\right|_{Z=Z_r} \tag{7.28}$$

where ρ_{Fe} and M_{Fe} are, respectively, the density (g cm^{-3}) and the molar weight (g $mole^{-1}$) of liquid Fe, and A the reaction area (cm^2). The values of these parameters are listed in Table 7-1. Considering the stoichiometry of the Al_2O_3 formation reaction, the rate of Al_2O_3 formation, $N_{Al_2O_3}$, is:

$$N_{Al_2O_3} = \frac{1}{3} N_{O,reaction} . \tag{7.29}$$

The spatial derivative of C_O at the reaction front position Z_r is calculated from Eq. (7.22) for the semi-infinite geometry, which gives the following analytical expression for $N_{Al_2O_3}$:

$$N_{Al_2O_3,anal} = \frac{2}{3}\frac{\rho_{Fe}A}{M_{Fe}}\frac{C_O^{sat.}}{erf\left(\sqrt{\frac{\lambda}{D_O}}\right)}\sqrt{\frac{D_O}{4\pi t}}\exp\left(-\frac{\lambda}{D_O}\right). \tag{7.30}$$

In the case of a finite dimension medium (model A), the spatial derivative of C_O is estimated following the same discretisation and integration procedures described in section A.1 of the Appendix. $N_{Al_2O_3}$ is estimated thanks to the relation:

$$N_{Al_2O_3,num} = \frac{1}{3}\frac{\rho_{Fe}A}{M_{Fe}}\frac{D_O}{Z_r^{j+\sigma}}\frac{p_{N-2}^{j+1}}{1-u_{N-2}}. \tag{7.31}$$

Similar to the discussion on the reaction front position, $N_{Al_2O_3}$ estimated from the numerical model A with a high value of L is consistent with that derived from the analytical solution. Figure 7-6 (a) depicts the evolution of $N_{Al_2O_3}$ with the position of the reaction front obtained with the analytical and numerical solutions. $N_{Al_2O_3}$ given by the analytical solution (semi-infinite geometry) is high when the reaction front is located near the melt surface and decreases exponentially with the reaction front position (i.e. time). The evolution of $N_{Al_2O_3}$ calculated numerically with L = 1.3 cm is close to the analytical solution until the reaction front position is 0.6 cm below the melt surface (t = 4000 s). Above this value, $N_{Al_2O_3}$ given by the numerical calculation decreases faster compared to the analytical solution. At t = 8100 s, $N_{Al_2O_3}$ is zero, corresponding to the moment the reaction front reaches the fixed boundary of the system (Z = L, Figure 7-3). $N_{Al_2O_3}$ gives an indication of the supersaturation degree of the melt for the Al_2O_3 formation. It will have a significant influence on the number, size distribution and morphology of the inclusions. As shown in Figure 7-6, the latter decreases exponentially with time.

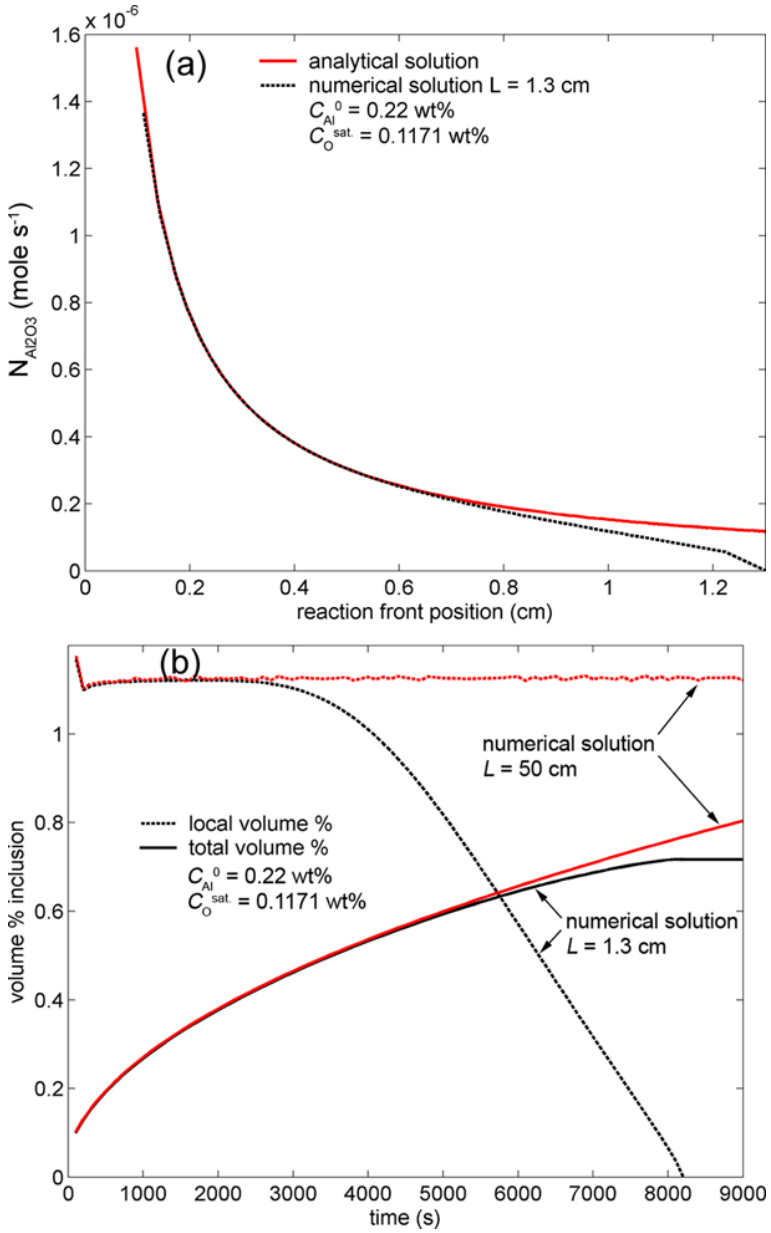

Figure 7-6: (a) Evolution of $N_{Al_2O_3}$ at the reaction front Z_r as a function of the reaction front position, calculated with the analytical solution (solid line) and numerical solution (model A) with L = 1.3 cm (dashed line). (b) Evolution of the local (dashed lines) and total (solid lines) volume percentages of inclusion as calculated numerically (model A) with two different values of L. L = 50 cm is employed to reproduce the analytical solution.

By performing a mass balance on the number of moles of Al at each time step, the local and total volume percentage of Al_2O_3 inclusions can be evaluated. The local volume percentage is the volume percentage of inclusions formed in a volume dV, which is defined by motion of the reaction front during a time dt:

$$\text{local vol.\%} = 100 \frac{\left(\text{mole Al}_2\text{O}_3\left(t_2\right) - \text{mole Al}_2\text{O}_3\left(t_1\right)\right)}{\left(Z_r\left(t_2\right) - Z_r\left(t_1\right)\right) A} \frac{M_{Al_2O_3}}{\rho_{Al_2O_3}} \tag{7.32}$$

where $M_{Al_2O_3}$ and $\rho_{Al_2O_3}$ are, respectively, the molecular weight (g mol^{-1}) and the density (g cm^{-3}) of Al_2O_3. The total volume percentage of Al_2O_3 inclusions corresponds to the total volume of inclusions existing at time t divided by the melt volume.

With the analytical solution (Figure 7-6 (b)), the local volume percentage of inclusions is constant with time, while the total volume percentage of inclusion increases and tends to an infinite value (given that the melt height is infinite). The local volume percentage obtained with the finite geometry (numerical solution) is initially constant and matches the value given by the analytical solution. From $t \sim 2000$ s, it decreases rapidly and becomes zero at $t = 8100$ s, corresponding to the time the reaction front reaches the fixed boundary. The evolution of the total volume fraction of inclusion with time is identical to the semi-infinite case until $t \sim 4000$ s. For longer times, the total volume fraction increases slower and, at $t = 8100$ s, levels off at 0.72 vol. %. This value corresponds to the consumption of all available Al in the melt through the reaction with O, thereby fixing the maximum amount of Al_2O_3.

7.3.1.4. Accumulated supersaturation

Due to non-zero equilibrium concentrations, the Al and O concentration profiles overlap, as highlighted by the calculation results of model B (Figure 7-5). During the diffusion of the species, a build-up in Al and O concentration might appear in that region of the melt. To estimate the Al and O supply to the reaction, the term *accumulated supersaturation* S_{acc} is used and defined by the activity product before (i.e. after calculating the new profile with the diffusion equations) and after the Al_2O_3 formation reaction. It indicates how the diffusion process drives the local concentrations away from the equilibrium values. It can be used to estimate the oversupply of O and Al to the formation and the growth of inclusions located in the melt area where $\log(S) > 0$.

It should be mentioned that term accumulated supersaturation does not represent the true supersaturation of the melt. The accumulated supersaturation is affected by the choice of the model parameters (time and space steps) due to the decoupling procedure (section 7.2.2.2). It should be considered as a comparative value between calculations performed with the same time step rather than an absolute value. This aspect will be discussed further in this section. The idea of S_{acc} is to provide an indication of the accumulation rate, with which a balance between accumulation, nucleation and growth rate would be derived. However, this requires further development of the present model.

The evolution of the accumulated supersaturation as a function of time and position relative to the melt surface is shown in Figure 7-7. Compared to the previous models, the reaction is not limited to one specific position, but is taking place over an area, due to the overlapping of the concentration profiles (Figure 7-5). The accumulated supersaturation is not an infinitely sharp peak as predicted by previous models, but shows a finite distribution around a maximum value. The accumulated supersaturation is high at the beginning of the diffusion process, due to the large difference between the actual and the equilibrium concentration values. The maximum value is high and the distribution around the maximum is narrow. With longer holding times, the maximum peak value of the accumulated supersaturation decreases significantly and the distribution around the peak broadens.

The position of the maximum peak coincides with the intersection of the Al and O concentration profiles and with the reaction front position calculated with previous models. However, if we assume that Al_2O_3 formation occurs as soon as $\log(S_{acc}) > 0$, the position of the reaction front would be located at the right end of the $\log(S_{acc})$ distribution and not at the position of the maximum. The reaction front position would be shifted deeper in the melt compared to other model results, the extent of the shift increasing with time. As seen in Figure 7-7, the $\log(S_{acc})$ curves are not zero only on a small portion of the melt depth, in which $K' > K$ and Al and O concentrations are determined by the equilibrium line (Figure 7-2 (b)). The reaction is not taking place significantly elsewhere in the melt. With this approach to solve the diffusion and reaction equations, inclusion nucleation and growth is allowed over an area, which gives a more realistic and physical interpretation of the calculation results.

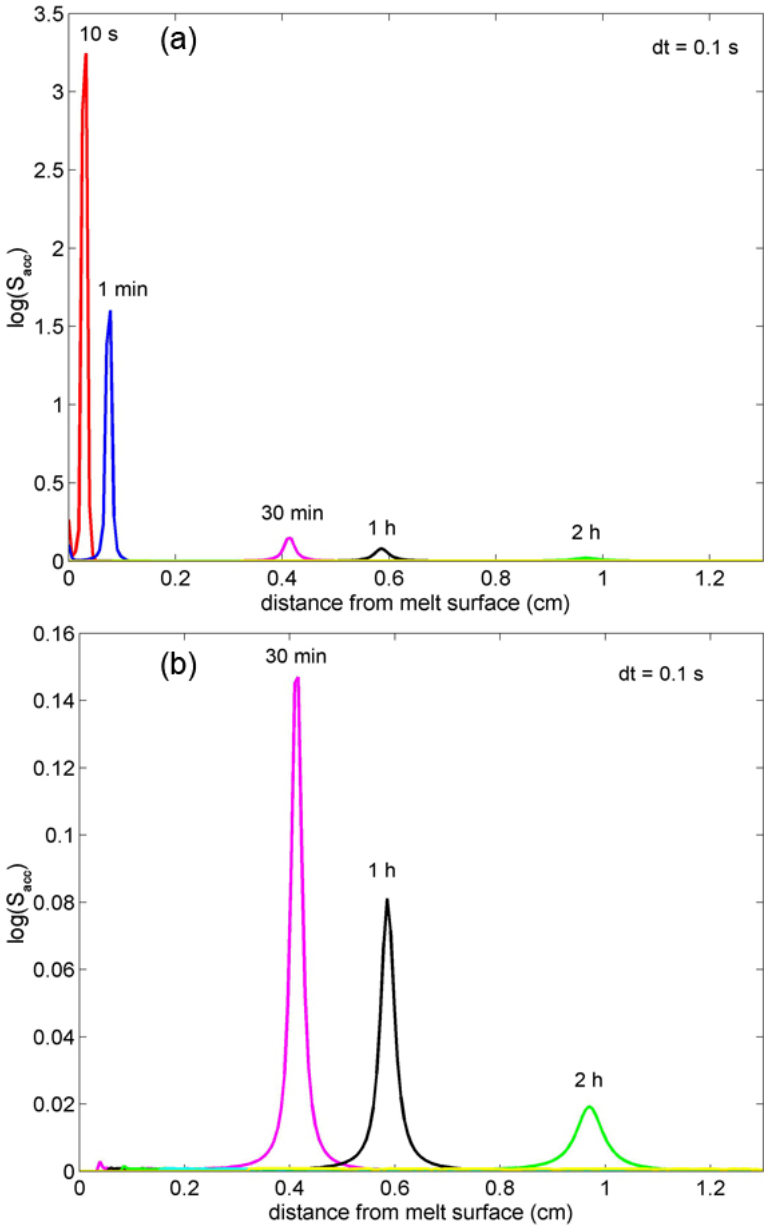

Figure 7-7: Evolution of the logarithm of the accumulated supersaturation S_{acc}, calculated with model B, as a function of time and the position relative to the melt surface with identical condition as in Figure 7-5. ((b) is an enlargement of (a) for diffusion times of 30 min, 1 h and 2 h). The time step used in the calculation is 0.1 s.

The influence of the time step on the concentration profiles and on the accumulated supersaturation should be investigated by comparing the results with an analytical solution of the problem. Since such analytical solution is not available, the influence of the time step was determined by performing the calculations with the same initial concentrations (C_{Al}^{0} = 0.22 wt% and $C_{O}^{sat.}$ = 0.072 wt%) and the same grid size, but different time steps. Due to the large driving force for mass transport at the beginning of the reoxidation process, the error due to a too large time step is more important for short diffusion time. The difference in the results become very small for longer holding time because the driving force for diffusion decreases as the concentration profiles become flatter. Table 7-2 gives the difference in the Al and O concentrations as a function of the time step and the diffusion time compared to the results obtained with a time step of 10^{-4} s. Because of the limited diffusion ability of Al and O, the difference in the Al and O concentration profiles obtained with different time steps is only a couple of ppm and have therefore a very limited influence on the concentration profiles.

Table 7-2: Maximum difference in the Al and O concentration profiles (respectively ΔAl and ΔO) as a function of the time step dt and the diffusion time. The reference is the Al and O concentration profiles calculated with dt = 10^{-4} s.

Diffusion time	ΔAl (wt%)		ΔO (wt%)	
(s)	dt = 0.02 s	dt = 0.01 s	dt = 0.02 s	dt = 0.01 s
1	$1.12\ 10^{-3}$	$5.34\ 10^{-4}$	$8.78\ 10^{-5}$	$3.61\ 10^{-5}$
10	$1.10\ 10^{-4}$	$5.30\ 10^{-5}$	$9.09\ 10^{-6}$	$3.72\ 10^{-6}$
30	$3.70\ 10^{-5}$	$1.80\ 10^{-5}$	$1.86\ 10^{-6}$	$2.00\ 10^{-7}$
60	$1.80\ 10^{-5}$	$9.00\ 10^{-6}$	$7.60\ 10^{-7}$	$9.00\ 10^{-7}$
120	$9.00\ 10^{-6}$	$9.00\ 10^{-6}$	$3.10\ 10^{-6}$	$3.50\ 10^{-6}$

Because the accumulated supersaturation is evaluated from the Al and O contents calculated after diffusion, it will also be significantly affected by the choice of the time step. If the time step is small, the changes in the Al and O concentration profiles due to diffusion process over one time step is small and the accumulated supersaturation will be much less compared to the use of a larger small step. This influence of the time step on the log(S_{acc}) for diffusion times of 1, 10 and 30 s is illustrated in Figure 7-8. The influence of the time step is to decrease the log(S_{acc}) by a certain factor. The other characteristics of the log(S_{acc}) curves are unchanged. For this reason, the accumulated supersaturation should be used as a comparative value between calculations performed with the same time step. It is meant to calculate the

oversupply to inclusion growth predicted by the numerical model instead of a true supersaturation.

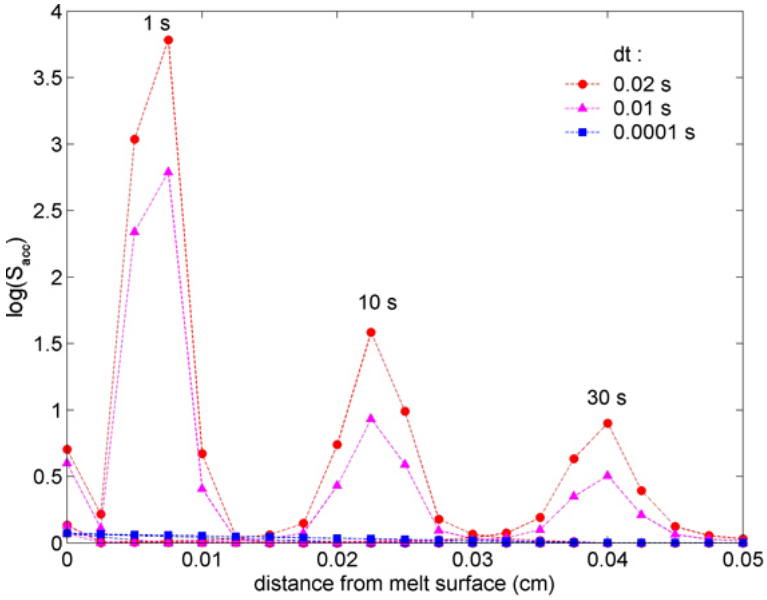

Figure 7-8: Influence of the time step on the value of S_{acc} at each node after a diffusion time of 1, 10 and 30 s (calculation conditions of model B: C_{Al}^{0} = 0.22 wt%, $C_{O}^{sat.}$ = 0.0720 wt%, L = 0.5 cm).

An application of the dependence of the time step on the value of $\log(S_{acc})$, as shown in Figure 7-8, is to estimate the time necessary for the melt in order to reach locally a certain level of accumulated surpersaturation for the reaction to take place.

7.3.2. Influence of initial Al and O contents on diffusion

In the previous section, the influence of using a finite or a semi-infinite geometry on the moving boundary diffusion problem was examined. In this section, the influence of a modification in the initial Al and O contents on the motion of the reaction front, the concentration profiles, the formation of inclusions at the moving reaction front and on the supersaturation will be discussed for the finite geometry case, using both numerical models with L = 1.3 cm. Two values (high and low) are assigned to the initial Al content C_{Al}^{0} and to the p_{O_2}, which is converted to an O content at saturation in liquid Fe ($C_{O}^{sat.}$). The input values for the numerical model are listed in Table 7-3.

Table 7-3: Input parameters for the numerical model.

Input parameters		Value	
		high	low
C_{Al}^{0}	(wt%)	0.22	0.1
	(molar fraction)	0.00454	0.00207
p_{O_2}	(atm)	$2.0\ 10^{-9}$	$4.3\ 10^{-10}$
$C_{O}^{sat.}$	(wt%)	0.1171	0.0543
	(molar fraction)	0.00408	0.00189

7.3.2.1. Motion of the reaction front

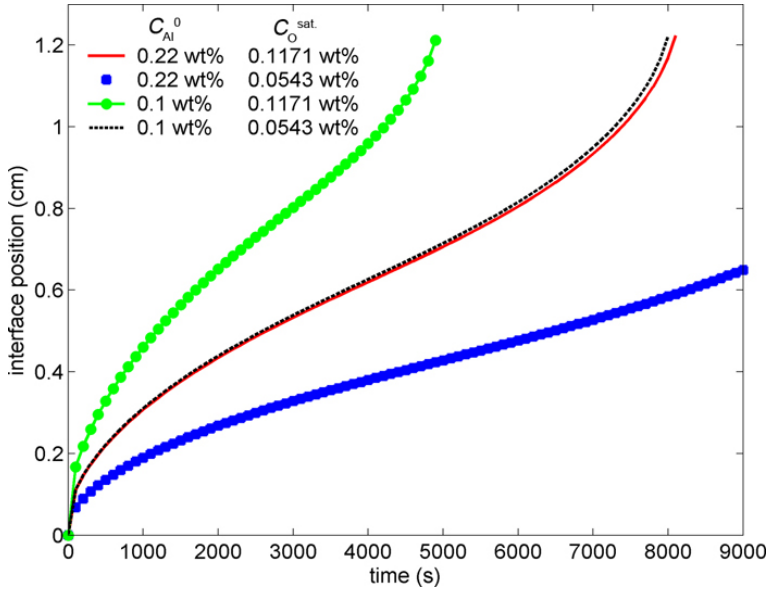

Figure 7-9: Evolution of the reaction front position as a function of time for different combinations of initial Al contents C_{Al}^{0} and O saturation levels $C_{O}^{sat.}$ in liquid Fe. The results are obtained with the numerical model A, using L = 1.3 cm.

The influence of different values of C_{Al}^{0} and $C_{O}^{sat.}$ on the reaction front position as a function of time, calculated with model A, is shown in Figure 7-9. The combination low C_{Al}^{0} with high $C_{O}^{sat.}$ results in a high reaction front velocity. The reaction front reaches the fixed boundary at t = 5000 s (1

h 23 min). The opposite combination (high C_{Al}^{0} with low $C_{O}^{sat.}$) has a slow reaction front velocity. After 9000 s (2 h 30 min), the front position covers only half of the available distance. The front velocities of the combination high C_{Al}^{0} and high $C_{O}^{sat.}$ and that of low C_{Al}^{0} and low $C_{O}^{sat.}$ lie in between and are almost identical due to similar ratio employed between low and high values of C_{Al}^{0} and $C_{O}^{sat.}$.

7.3.2.2. Concentration profiles

As can be seen in Figure 7-10, the concentration profiles for Al and O, which are calculated with model A, are very dependent on the initial conditions. With similar position of the reaction front (Figure 7-9), the combination of low C_{Al}^{0} with low $C_{O}^{sat.}$ gives O and Al concentration profiles less steep compared to the combination high C_{Al}^{0} and high $C_{O}^{sat.}$. As observed in Figure 7-9, the reaction front moves slowly in the case high C_{Al}^{0} and low $C_{O}^{sat.}$. The slopes of the Al and O concentration profile curves are steep even after 2 h (Figure 7-10 (b)). With a high reaction front velocity, the curve of the O profile after 1 h for the combination low C_{Al}^{0} and high $C_{O}^{sat.}$ is high and Al is almost completely consumed (Figure 7-10 (a)). After 2 h, Al is used up and only O diffuses in the melt (the corresponding profile is therefore not shown in Figure 7-10 (b)).

7.3.2.3. Predictions of inclusion formation

The influence of different combinations of input variables on $N_{Al_2O_3}$ at the reaction front as a function of time is depicted in Figure 7-11, using model A. For time less than 3600 s, the highest $N_{Al_2O_3}$ values are observed with high initial Al concentrations, even if the O saturation level is decreased. Consistently, the combination high C_{Al}^{0} with high $C_{O}^{sat.}$ gives the highest $N_{Al_2O_3}$ value, while the lowest one is met by combining low C_{Al}^{0} with low $C_{O}^{sat.}$. Concerning the mixed combinations, increasing C_{Al}^{0} results in higher $N_{Al_2O_3}$ than increasing $C_{O}^{sat.}$. For time longer than 3600 s, the curves describing $N_{Al_2O_3}$ decrease abruptly when the reaction front approaches the fixed boundary.

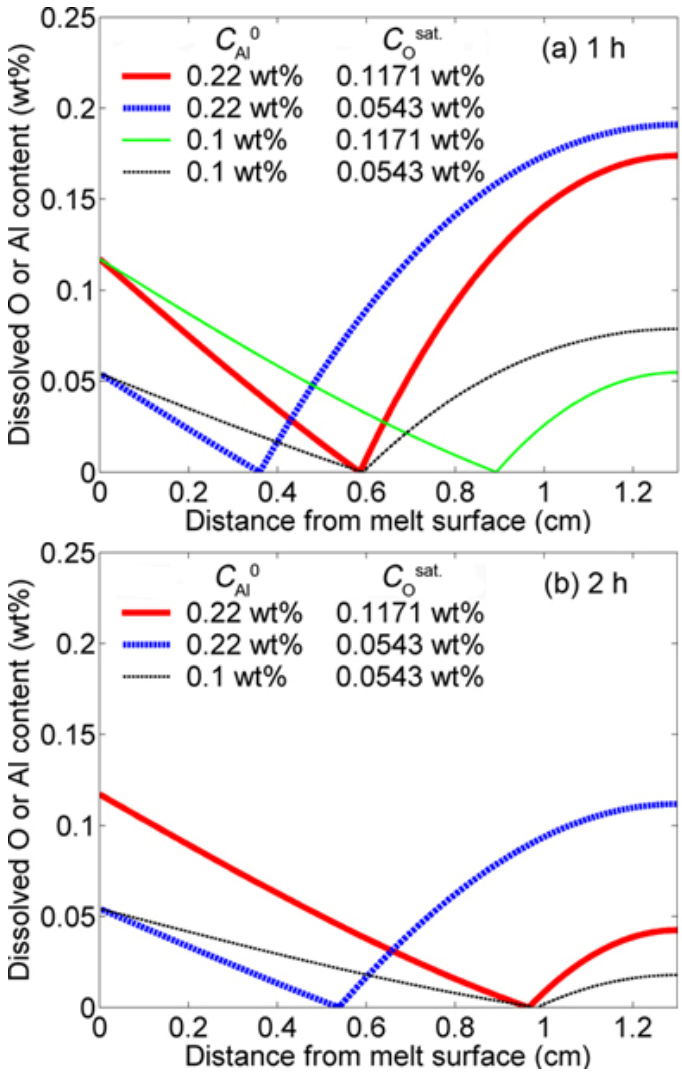

Figure 7-10: Calculated O (left side curves) and Al profiles (right side curves) for various initial Al concentrations and O saturation levels. The calculations are performed with model A with melt height of 1.3 cm and diffusion time of (a) 1 h and (b) 2 h.

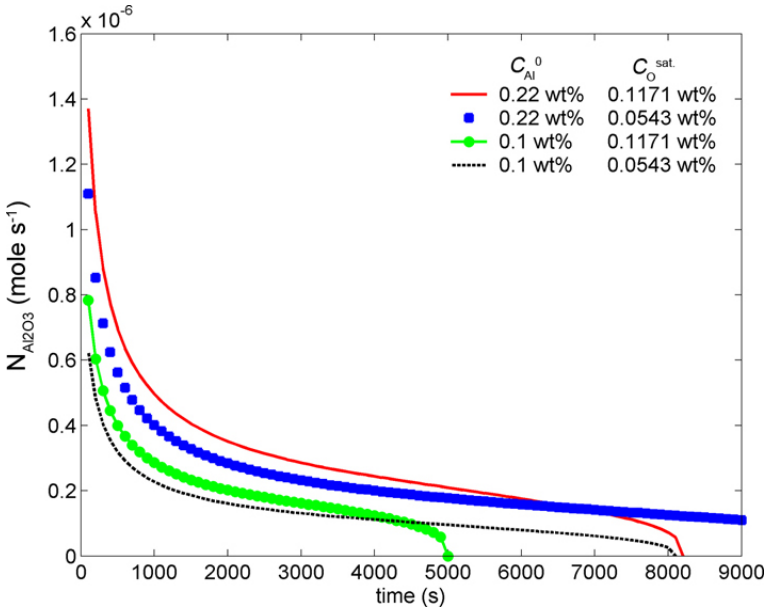

Figure 7-11: Evolution of $N_{Al_2O_3}$ at the reaction front Z_r as function of time, for various initial Al concentrations and O saturation levels. These calculations are performed with model A and L = 1.3 cm.

The local volume percentage, as mentioned in Figure 7-6 (b), is constant until a certain diffusion time (Figure 7-12 (a)). Because of a high $N_{Al_2O_3}$ (Figure 7-11) and a slow reaction front velocity (Figure 7-9), the local volume percentage obtained with high C_{Al}^0 and low $C_O^{sat.}$ is, with a value of 1.48 vol. %, higher than the three other cases. The combination high C_{Al}^0-high $C_O^{sat.}$ lies in second place with 1.12 vol. %, followed by the combination low C_{Al}^0-low $C_O^{sat.}$ (0.51 vol. %) and finally the combination low C_{Al}^0-high $C_O^{sat.}$ (0.43 vol. %). High initial Al concentration in the melt would result in high local volume percentage. On the other hand, increasing the O saturation level would decrease the local volume percentage. The influence of this parameter on the local volume % is, however, less than C_{Al}^0.

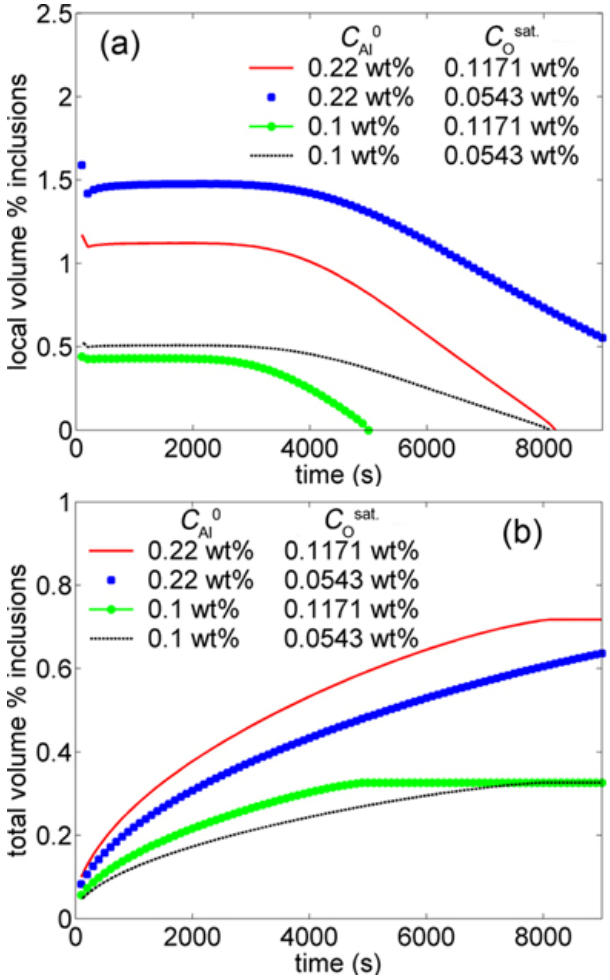

Figure 7-12: Evolution of (a) the local volume percentage and (b) the total volume percentage of inclusion as a function of time, for various initial Al concentrations and O saturation levels. These calculations are performed with model A and L = 1.3 cm.

After a certain time, the local volume percentage decreases as a result of the bounded domain. The slope seems to be related with the O saturation level. The decrease tends to be more rapid (steep slope) when the O saturation level is high.

The evolution of the total volume percentage with time is shown in Figure 7-12 (b). The four curves follow the same scheme. The total volume percentage increases fast during the first hundreds seconds, then levelled off at a constant volume percentage once the reaction front reaches the end of the bounded domain. This maximum volume percentage is determined and

fixed by the value of C_{Al}^{0}, because the amount of Al in the system is finite. The maximum total volume percentage when C_{Al}^{0} is 0.1 wt% is 0.33 vol. % and 0.72 vol. % when C_{Al}^{0} is 0.22 wt%. Increasing the O saturation level in liquid Fe brings the curves up and decreases the time needed to reach the maximum total volume percentage.

7.3.2.4. Accumulated supersaturation

The influence of the initial conditions on the evolution of the accumulated supersaturation was studied using the calculation results of model B and initial Al and O content listed in Table 7-3. The results are shown in Figure 7-13 (a) and (b) for a diffusion time of 1 h and 2 h, respectively. For a diffusion time of 1 h (Figure 7-13 (a)), the highest accumulated supersaturation is obtained with the combination high C_{Al}^{0} and high $C_{O}^{sat.}$, and the lowest accumulated supersaturation value is reached with the opposite combination. With a diffusion time of 2 h (Figure 7-13 (b)), the accumulated supersaturation curves have significantly decreased compared to the 1 h case. Due to lower reoxidation rate with the combination C_{Al}^{0} = 0.22 wt% and $C_{O}^{sat.}$ = 0.0543 wt%, the accumulated supersaturation moves slower through the melt bath. Also the maximum peak decreases slower and becomes the highest compared to the three other combinations of initial values. The combination C_{Al}^{0} = 0.1 wt% and $C_{O}^{sat.}$ = 0.1171 wt% provides the highest reoxidation rate. Al is completely consumed within 2 h and the accumulated supersaturation is approximately zero over the melt depth.

The evolution of the total amount of Al_2O_3 is depicted in Figure 7-13 (c) and (d) for various initial conditions and diffusion time of 1 h and 2 h. It is defined as the total amount of Al_2O_3 (in mol) which has formed during the reoxidation process at a grid point (considering all previous time steps). For diffusion time of 1 h, the curve shape is similar for all combinations of initial conditions, since the influence of the fixed boundary condition is not significant for this diffusion time. The total amount of Al_2O_3 is constant at a certain level and over a certain distance in the melt, which are both determined by the initial conditions. In general, high C_{Al}^{0} in the melt generates more Al_2O_3. However, with a lower $C_{O}^{sat.}$ imposed at the melt surface and identical C_{Al}^{0}, the reoxidation rate of the melt is decreased (Figure 7-10 (a) and (b)). In that case, the level of constant value of the total amount of Al_2O_3 is higher, but the penetration depth is smaller.

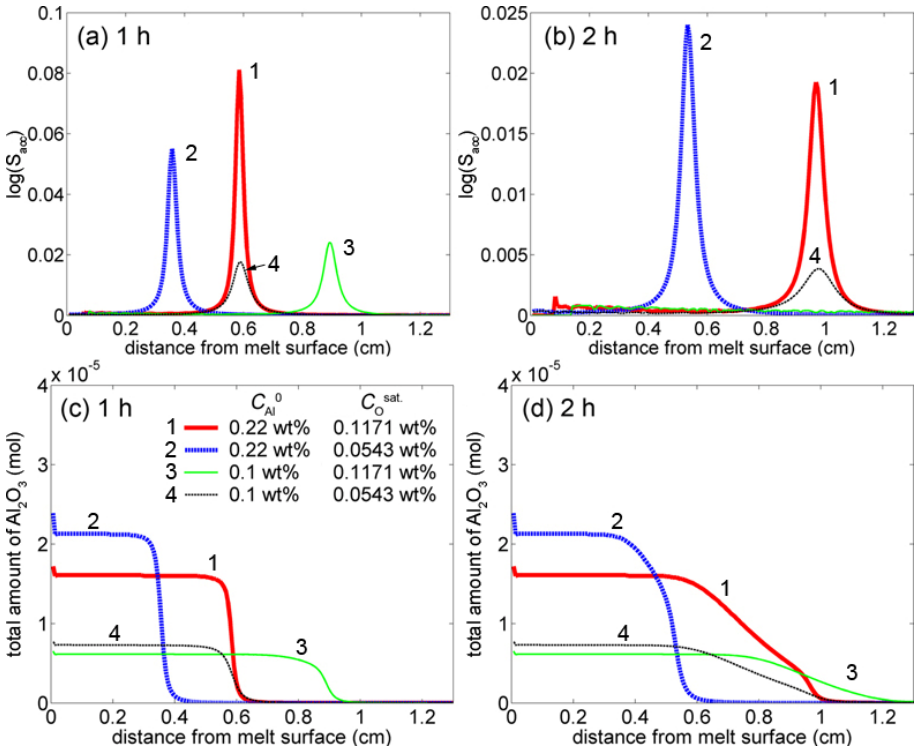

Figure 7-13: Influence of changing the initial conditions on (a) and (b) the accumulated supersaturation S_{acc}; (c) and (d) the total amount of Al_2O_3 formed during the reoxidation process. The diffusion time is fixed at 1 h for the left-hand side figures and 2 h for the right-hand side. The bath height L is 1.3 cm and the time step 0.1 s.

7.4. Some perspectives to improve the diffusion-reaction model

7.4.1. Integrating the nucleation theory

According to the classical theory of nucleation, there is a free energy barrier for nucleation, which is due to two opposed free energy contributions during the nucleation of a new phase in a supersaturated solution. The formation of a given volume of more stable phase provides a negative contribution to the free energy, whereas the creation of a new interface between the nuclei and the parent phase gives a positive contribution. As nuclei are very small, the surface free energy to the interface is dominant. This implies that the parent

phase must have a certain energy state before the size of the nucleus reaches the critical value determined by the maximum in the free energy. The condition given by $S > 1$ is not always sufficient to get nucleation in the parent phase and the energy barrier for nucleation might require that the critical supersaturation of the melt, S^*, is much higher than 1. The condition to form Al_2O_3 inclusions is not necessarily given by $S = 1$ (i.e. when the melt composition enters the Al_2O_3 stability domain (Figure 7-2 (b)), but when the local supersaturation is greater than S^*.

Imposing a critical supersaturation S^* for the reaction to take place may have a significant influence on the formation of Al_2O_3 inclusions and on the diffusion of species. The experimental value of $\log(S^*) = 3.5$ measured by Li and Suito [36] can be integrated in the calculations. However, S^* is not a constant and depends on the surface free energy σ, which is strongly dependent on the <u>O</u> content. In Li's study [36], the influence of <u>O</u> on S^* is not explicitly described and the value of $\log(S^*) = 3.5$ is the only reported value. To consider the influence of σ on nucleation, the full description of the classical homogeneous nucleation theory, which was summarized in section 2.2.2.1 in Chapter 2, should be applied. It was shown that the critical supersaturation is strongly dependent on the interfacial free energy σ and on the frequency factor for nucleation, which is again a function of σ and the critical nuclei size. An algorithm can be developed in order to integrate the nucleation theory in the numerical model and evaluate the actual S^* at each time and space steps. Since the value of σ has a significant influence on the parameters for nucleation, the dependency of σ with the <u>O</u> content in liquid Fe and with the particle size (σ_0, see section 2.2.2.1 in Chapter 2) should be carefully formulated.

7.4.2. Coupling the diffusion process and the Al_2O_3 formation reaction

The procedure used in the numerical model A showed many advantages to approach the solution of the diffusion process. The model is fully implicit, conservative and uses a variable space discretisation scheme. In order to improve the precision and accuracy of the decoupled model, the diffusion and inclusion formation should be calculated simultaneously. Ideally, we would like to use similar approach to solve the coupled problem, by using additional equations to take into account the Al_2O_3 formation reaction and fulfil the equilibrium conditions.

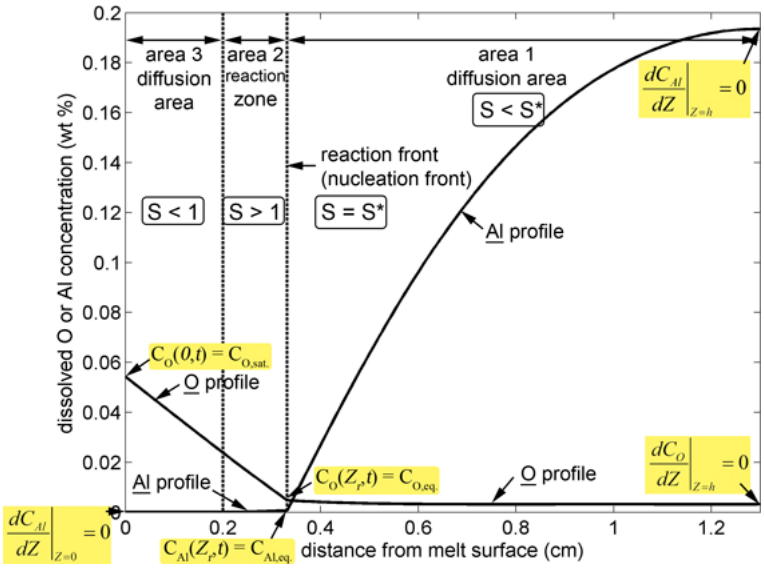

Figure 7-14: Schematic diagram showing the Al and O concentration profiles across the melt at time t > 0. The melt is imaginary divided in three areas depending on the local S value. The boundary conditions for each area are highlighted in yellow.

In this new approach, the melt height would be divided in three areas, as represented in Figure 7-14. Each area would be descritised using its own space variable varying between 0 and 1. Area 1 is located between the reaction front position Z_r and the bottom of the crucible. This area is characterised by $S < S^*$, i.e. the nucleation of Al_2O_3 cannot take place. The Al and O profile are therefore calculated directly from the diffusion equations, using appropriate boundary conditions (zero flux at the crucible bottom and equilibrium compositions at Z_r). In a similar way, area 3 is located just under the melt surface and is characterized by $S < 1$, i.e. mass transport of one of the species is too small to have enough driving force for the reaction. In that case, the Al and O concentration profiles are determined only by the diffusion equations, using appropriate boundary conditions. Area 2, the reaction zone, is located between areas 1 and 3 and is defined by S > 1, implying that both Al and O mass transport and the reaction must be taken in consideration. In the reaction zone, the diffusion equations (7.13) and (7.14) must be solved with additional constraints on the reaction stoichiometry, on the global mass balance and on the equilibrium melt composition given by Eq. (2.6) in Chapter 2. More investigation on similar subject in the literature is necessary to develop the model or to find a more appropriate approach to the problem.

7.4.3. Inclusion population balance

The purpose of the modelling work is to provide an estimate of the melt conditions as a function of time and initial conditions. The predictions are then used to link the reoxidation conditions with the inclusion characteristics. The inclusion behaviour, i.e. nucleation, growth and removal from the melt, is not treated in the description and formulation of the models developed in this chapter. To extend the diffusion model, existing models for inclusion nucleation, growth and removal could be coupled to the diffusion model to produce time- and space-dependent inclusion size distributions as a function of the reoxidation conditions. The diffusion model would provide the melt composition at each iterations, which would be used to compute the nucleation events, the various growth mechanisms, inclusion transport and removal by the nucleation-growth-removal model.

7.5. Conclusions

The present chapter was dedicated to the prediction of the evolution of the Al and O concentration profiles in liquid Fe containing initially Al during a reoxidation process. The problem was treated as a one-dimensional diffusion problem with moving boundary at the reaction front between liquid Fe containing O and liquid Fe containing Al. Fick's second law was used to predict the concentration profiles. The governing equations were solved analytically in a semi-infinite geometry and numerically for a finite geometry. For the numerical scheme, two different approaches were used.

First, a fully implicit, conservative finite difference method was used (model A). The problem was decoupled in a set of linear equations that are solved iteratively. The numerical scheme has a first order accuracy in space and time, and allows the use of irregular meshes. The numerical model was validated by comparing the results obtained with a large melt depth with those obtained analytically in semi-infinite geometry. The results of the models enable to predict the motion of the reaction front, the Al and O concentration profiles, the rate of Al_2O_3 inclusion formation, the inclusion volume percentage, etc. as a function of C_{Al}^0, p_{O_2} and time.

The second numerical model for the reoxidation of Fe-Al alloy (model B) involves the mass transport of Al and O by pure diffusion and the thermodynamics of inclusion formation. In the model, the diffusion process and the Al_2O_3 formation reaction were solved in two successive steps using an explicit scheme. The predicted concentration profiles are very similar to those obtained with the previous model, which did not consider the

equilibrium values after the reaction. An overlap between the Al and O profiles in the vicinity of the reaction area is noticed when non-zero equilibrium melt composition are involved in the calculations. The overlap is however very limited in size and magnitude given the low value of the equilibrium composition compared to the initial concentration. Moreover, it was found that, in the case of Al_2O_3 formation, decoupling the diffusion and the reaction did not lead to a large error, given that sufficiently small time step and relatively high Al concentration are chosen.

The accumulated supersaturation S_{acc} of the melt was estimated after each time step. It was shown that S_{acc} is very high and located near the melt surface shortly after the beginning of the reoxidation process. The motion and the intensity of S_{acc} decrease significantly with time.

Modelling the reoxidation process helps to understand the trends and to estimate the conditions at which formation and growth of inclusion takes place in the melt. The results of the calculations showed that the initial Al content in the melt and the p_{O_2} applied in the gas phase have a significant influence on the formation and growth conditions during the diffusion process, which consequently will influence the inclusion characteristics. In the next chapter, the predictions are compared with experimental observations.

Chapter 8
Formation and morphology of Al_2O_3 inclusions by reoxidation of Fe-Al alloys

In Chapter 7, the reoxidation process of Fe-Al alloys was investigated theoretically. It was shown that the initial conditions, i.e. the initial Al content of the Fe-Al alloy and the p_{O_2} in the gas phase, will influence the diffusion process, which controls the local conditions for the formation and growth of Al_2O_3 inclusions. As a result, different characteristics might be observed among the Al_2O_3 inclusions formed at the reaction front.

In the present Chapter, the results of reoxidation experiments are presented. The latter consisted in exposing liquid Fe containing about 0.2 wt% Al to an atmosphere maintained at a fixed p_{O_2}. The evolution of the Al content and the formation and morphology of Al_2O_3 inclusions in the samples taken at specific time are investigated under different oxidizing conditions and compared with the predictions. Specific attention is given on the modification in inclusion morphologies, which are linked to the local conditions using the predictions of the diffusion model. Finally, the inclusion morphologies obtained after reoxidation are compared with those obtained by the deoxidation process.

8.1. Experimental procedure

Fe-Al alloys of desired composition were prepared by melting pure electrolytic iron and pure aluminium in a vacuum arc furnace, as described in Chapter 4. After the melting, the surface of the alloys was cleaned to remove contaminations.

In the reoxidation experiments, about 70 g of Fe-Al alloy was melted in an alumina crucible in deoxidized Ar ($p_{O_2} < 10^{-20}$ atm). The oxygen content in the off-gas was measured at less than 10^{-14} ppm with the solid state ceramic oxygen sensor. After the temperature was adjusted to 1600 °C, a sample was taken to determine the initial Al content, C_{Al}^0, of the Fe-Al alloy. The sampling was performed by dipping an Al_2O_3 tube to the bottom of the crucible, followed by suction of a small volume of melt and withdrawal of the tube to the top part of the furnace. After the sampling, an oxidizing atmosphere was brought in the furnace chamber by applying a CO/CO_2 gas mixture, of which the ratio fixes the equilibrium p_{O_2} at a given temperature. Two different experimental approaches were examined.

- During test 1, the p_{O_2} was increased every 30 min, after having taken a sample from the bottom of the crucible. The purpose was to study the evolution of the Al content, inclusion number and morphology as a function of the p_{O_2}.
- During tests 2 and 3, the p_{O_2} was fixed at 4.3 10^{-10} atm and 2.0 10^{-9} atm, respectively. This p_{O_2} was maintained during the whole test, while samples were taken each hour from the bottom of the crucible. The aim was to consider the evolution of the Al concentration and inclusion characteristics with time at a fixed p_{O_2}. After the desired reaction time, the atmosphere was changed to deoxidized Ar and the crucible was quenched in water.

The conditions for each test are listed in Table 8-1.

Table 8-1: Experimental conditions for the reoxidation tests, including the initial Al content (C_{Al}^0), the sampling time and the applied p_{O_2}.

test	C_{Al}^0 (wt%)	time (min)	p_{O_2} (atm)
1	0.32	30	4.3 10^{-10}
	0.28	30	2.0 10^{-9}
	0.25	30	1.7 10^{-7}
2	0.28	60	4.3 10^{-10}
		120	
		132	
3	0.22	60	2.0 10^{-9}
		120	
		180	
		240	

The samples were prepared for analysis, using the analysis techniques described in Chapter 4. The soluble and insoluble Al fractions of each sample were measured using ICP-AES. Most of the samples were also subjected to inclusion extraction, by dissolution of the metal matrix in HCl (1:1). The inclusions were collected on a filtration membrane and investigated with SEM for size and morphology assessment. The cross sectional area of the quenched crucible of test 3 was measured using AIA operating on an automated SEM.

8.2. Results and discussion

8.2.1. Evolution of the Fe-Al alloy composition with p_{O_2}

Prior to the investigation of the influence of various oxygen partial pressures in the gas phase on the reoxidation process, a blank test was conducted to estimate the consumption of Al under argon atmosphere. During the blank test, a Fe-Al alloy containing initially about 0.37 wt% Al was melted at 1600 °C under deoxidized Ar atmosphere. Afterwards, a sample was taken every 30 min without modification of p_{O_2} in the gas phase. The evolution of the Al content as a function of the holding time is given in Figure 8-1.

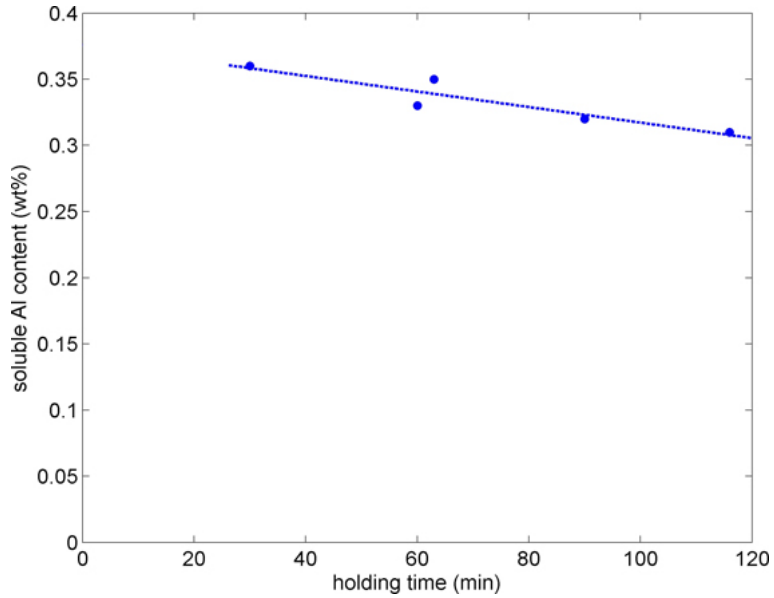

Figure 8-1: Evolution of the Al content as a function of holding time under deoxidized Ar (blank test).

Figure 8-1 indicates that part of the Al is inevitably consumed during the experiments without modifying intentionally the p_{O_2} in the gas phase. The vapour pressure of pure Al at 1600 °C is 1.76 10^{-3} atm [254]. Given the low Al activity in liquid Fe (~ 4.5 10^{-4} calculated with FactSage software [255] using the liquid Fe database [31]), the evaporation of Al from the melt cannot explain the loss of soluble Al in Figure 8-1. As Al is most probably consumed through reoxidation, the O pickup may originate from the sampling procedure, and/or from small leaks, and/or from imperfect Ar flushing failing to remove air from the furnace completely. From the linear regression between the experimental values plotted in Figure 8-1, about 0.0177 wt% Al is oxidized for a holding time of 30 min when the Al content is initially 0.37 wt%.

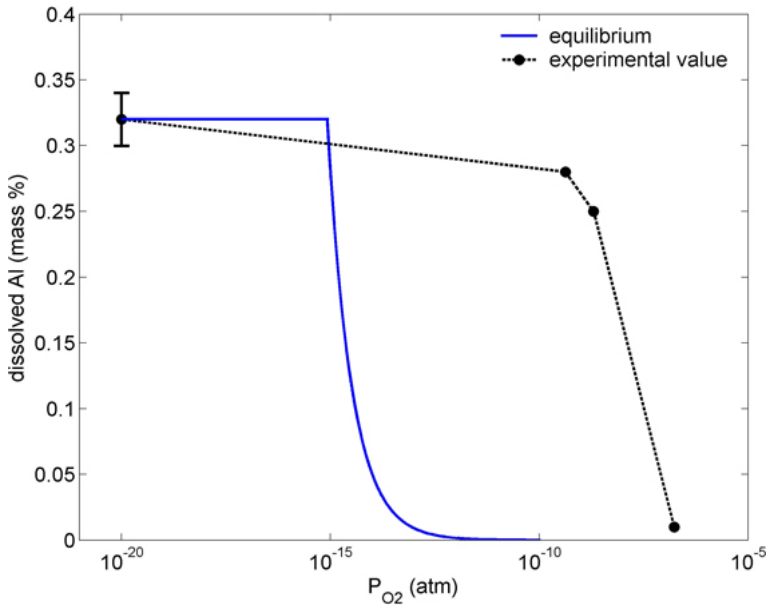

Figure 8-2: Evolution of the Al content in the melt as function of p_{O_2} applied during 30 min. The experimental values (test 1, plain markers) are compared with thermodynamic predictions (continuous line).

The evolution of the Al content as a function of p_{O_2} during test 1 is shown in Figure 8-2. The experimental values, measured from samples taken from the bottom of the crucible ($Z = L$), are compared with thermodynamic predictions [31]. The inherent oxidation by the furnace setup during the complete experiment, which was revealed in Figure 8-1, is indicated by the error bar at the p_{O_2} of 10^{-20} atm. Both experimental and calculated results revealed an increasing consumption of Al content with p_{O_2}. The

experimental data are clearly deviating from the error bar with changing the p_{O_2}. The latter confirms the reaction between Al and O, which was intensified with the oxygen potential in the atmosphere. The equilibrium calculations indicate that the Al consumption through oxidation is initiated at p_{O_2} values higher than 10^{-16} atm, and is followed by a sharp decrease of the Al content between 10^{-15} and 10^{-12} atm.

As seen in Figure 8-2, the experimental values are deviating from the equilibrium calculations. Although experimental and calculated data are following the same tendency, the experimental values seem to be shifted to higher p_{O_2} values. Whereas the equilibrium calculations predict that Al is entirely consumed at a p_{O_2} of 2.0 10^{-9} atm, Al was still measured experimentally. Equilibrium between liquid Fe and the gas phase was not reached due to diffusional limitations resulting from the absence of natural convection and external stirring. In order to assess the actual oxygen activity in the melt, the O and Al concentration profiles in the melt need to be evaluated.

8.2.2. Evolution of inclusion morphology with p_{O_2}

After extraction, the evolution of the morphological characteristics of Al_2O_3 inclusions as a function of p_{O_2} during test 1 was examined. The following observations were made:

- The dominant shape with low p_{O_2} (4.3 10^{-10} atm) is the angular form (Figure 8-3 (a)). These inclusions were mainly individual with a size ranging between 1 and 4 μm.
- With an intermediate p_{O_2} (2.0 10^{-9} atm), spherical and angular inclusions were present in the samples. Their size ranged between 2 and 5 μm. Clusters and dendrites, whose size was less than 10 μm, were also observed, but remained rare. The primary arm of the dendrites was generally broad, while secondary arms were very short, sometimes non-existent.
- Aggregates of spherical inclusions (Figure 8-3 (b)) were more numerous in the samples subjected to a higher p_{O_2} (1.7 10^{-7} atm). Dendrites and clusters were more frequently observed, as seen in Figure 8-3 (c). However, individual angular and spherical inclusions were always present, the latter being dominant compared to faceted inclusions.

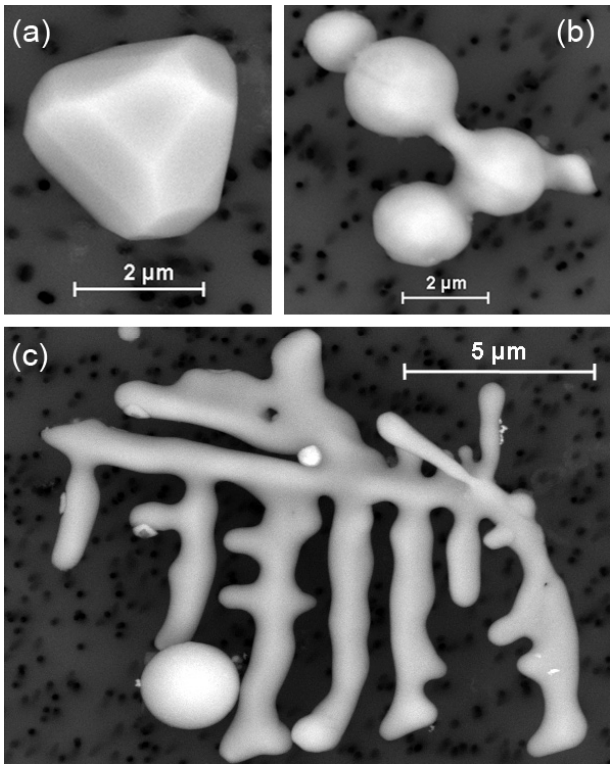

Figure 8-3: Evolution of inclusion morphologies (after extraction) as a function of p_{O_2} during test 1: (a) faceted inclusion at p_{O_2} = 4.3 10^{-10} atm; (b) aggregate and (c) dendrite and large spherical inclusion observed at p_{O_2} of 2.0 10^{-9} atm and 1.7 10^{-7} atm.

8.2.3. Comparison experimental results with predictions for diffusion of Al and O in liquid Fe and Al_2O_3 formation

Due to the absence of natural convection and external stirring during the reoxidation experiments, the mass transport of O and Al through the melt was mainly controlled by diffusion processes. Because detection and precise measurements of low Al and O concentrations are difficult, the diffusion process was approached theoretically in order to assess the actual oxygen activity in the melt. Mathematical modelling of the counter diffusion of Al and O with formation of Al_2O_3 inclusions at the reaction front was the subject of Chapter 7. An analytical solution was derived in a semi-infinite one-dimensional geometry and a numerical solution, using two distinct approaches, was developed for the finite geometry. The Al and O concentration profiles, the motion of the reaction front and the rate of

inclusion formation and the accumulated supersaturation of the melts were predicted as a function of C_{Al}^0, p_{O_2} and time.

The diffusion problem was described as follows. At time $t < 0$, the liquid Fe-Al alloy of known composition C_{Al}^0 and height L is held at a temperature of 1600 °C with $p_{O_2} < 10^{-20}$ atm. From $t > 0$, a specific p_{O_2} is applied in the gas phase. The O content at the melt surface is determined by the equilibrium between liquid Fe and O_2(g) at 1600 °C and assumed constant throughout the oxidation process. Diffusion of O_2(g) in the gas phase and the presence of an oxide layer on the melt surface were not considered in the model.

O diffuses from the surface into the melt and reacts with Al in an instantaneous irreversible reaction 2 Al + 3 O = $Al_2O_{3(s)}$. It is further assumed that the equilibrium Al and O concentrations are negligibly small. The reaction front, i.e. the location where O and Al meet and react to form solid Al_2O_3, is therefore created parallel to the melt surface at a distance Z_r from it. The reaction front divides the melt into two regions: an upper region A ($0 < Z < Z_r$) characterized by an O gradient and containing Al_2O_3 inclusions and a lower region B ($Z_r < Z < L$) with an Al gradient. The position of the reaction front evolves with time because region A grows over region B as Al is consumed in the chemical reaction.

The calculations were performed with the experimental conditions listed in Table 8-1 as initial conditions for the analytical and numerical solutions described in Chapter 7. The numerical calculations were performed with model A (section 7.2.2.1 in Chapter 7). The O content at the melt surface was calculated as 1173 ppm for $p_{O_2} = 2.0\ 10^{-9}$ atm and 543 ppm for $p_{O_2} = 4.3\ 10^{-10}$ atm (see section 7.1.2 of Chapter 7). The diffusion coefficients of O and Al in liquid Fe at 1600 °C were taken as, respectively, $1.4\ 10^{-8}$ $m^2\ s^{-1}$ [244] and $5.33\ 10^{-9}$ $m^2\ s^{-1}$ [204]. The melt height was calculated from the charge weight corrected by the mass of samples taken during the experiments.

The predictions using the analytical solution (solid lines) were compared with the Al content measured at the melt bottom during tests 2 and 3, as depicted in Figure 8-4. For a holding time of 1 h, the predicted evolution of the calculated Al content agrees fairly well with the experimental data. However, the difference between the experimental data and the predictions increases for longer holding time, especially with a p_{O_2} of $2.0\ 10^{-9}$ atm. The calculated results predict less Al than experimentally observed. After 4 h reoxidation, the calculations using the analytical model predict that the Al content is zero. According to the calculations, the reaction front reached the bottom of the crucible ($Z = L$) after 3.5 h.

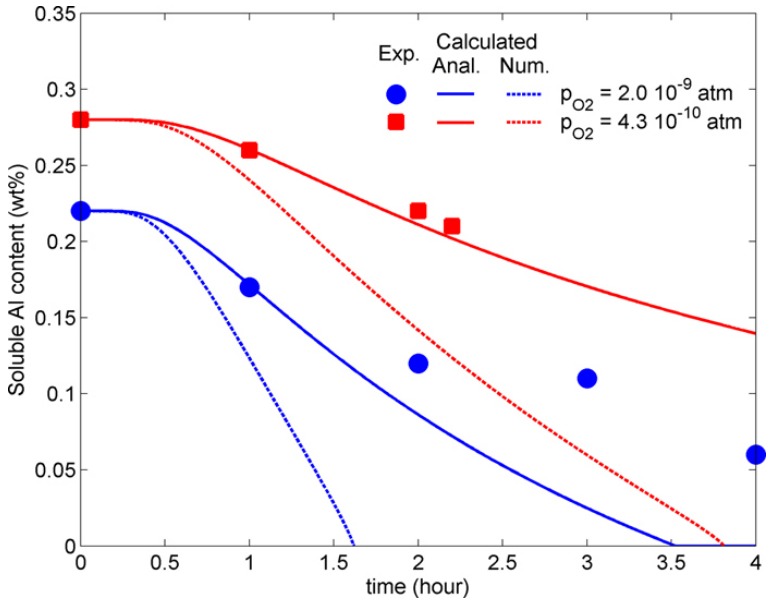

Figure 8-4: Evolution of the Al content in the Fe-Al alloy at the melt bottom ($Z = L$) as a function of holding time for tests 2 (p_{O_2} = 4.3 10^{-10} atm) and 3 (p_{O_2} = 2.0 10^{-9} atm). The experimental data (square markers for test 2 and round markers for test 3) are compared with the predictions using the analytical solution (solid lines) and the numerical solution (dashed lines).

As seen in Figure 8-4, the solutions of the numerical models (dashed lines) are deviating even more from the experimental points. In a finite geometry, the motion of the reaction front is accelerated when the latter approaches the crucible bottom ($Z = L$, Figure 7-3 in Chapter 7). Once the position of the diffusion front reaches about half of the melt height, the Al content is consumed faster. For that reason, the Al content at the melt bottom calculated by the numerical model is decreasing faster compared to the analytical solution. For a p_{O_2} of 2.0 10^{-9} atm, the numerical models predict that the Al is completely consumed within 2 h.

The difference between experimental observations and predictions probably originate from other reactions not taken into consideration in the model and/or a change in the rate limiting step during the oxidation process.

One of the possible reasons is the transformation of Al_2O_3 inclusions into $FeAl_2O_4$ taking place near the melt surface. This transformation was observed among the inclusions gathered at the melt surface of sample 3. As seen in Figure 8-5, these inclusions consist of an Al_2O_3 core surrounded by

an Fe-rich aluminate phase, which appears brighter. Due to a higher O content near the melt surface, Al_2O_3 inclusions moving to the surface undergo a reaction with Fe(l) and O to form $FeO.Al_2O_3$. This compound is more stable compared to Al_2O_3 in liquid Fe containing more than approximately 0.072 wt% O [35]. Some O is consumed through the formation of this compound at the surface and is, therefore, not available for diffusion and reaction with Al. The results of the calculations shown in Figure 8-4 do not consider this reaction near the surface, which may explain why the predictions underestimate the Al content at the melt bottom.

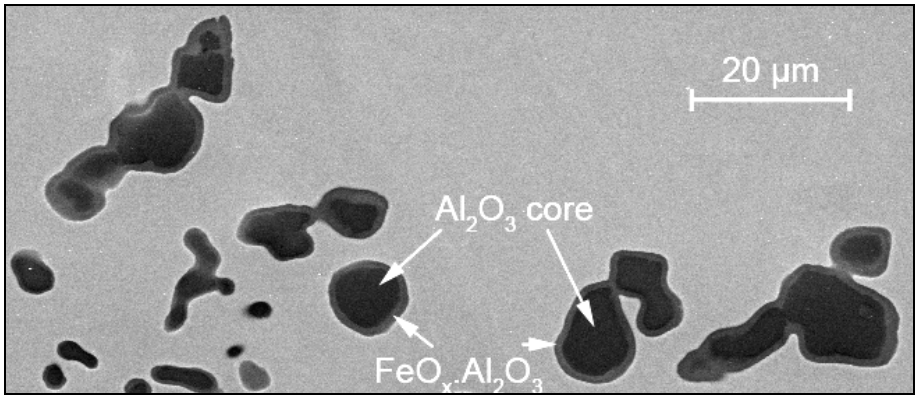

Figure 8-5: Transformation of Al_2O_3 inclusions into $FeO.Al_2O_3$ taking place near the melt surface of sample 3 (4 h, p_{O_2} = 2.0 10^{-9} atm). The inclusions consist of an Al_2O_3 core surrounded by a $FeO_x.Al_2O_3$ phase which appears brighter.

With higher p_{O_2} value in the gas phase, the proportion of Al_2O_3 inclusion transformed into $FeO.Al_2O_3$ is expected to be larger compared to lower p_{O_2} value. The formation of an Fe aluminate phase around the Al_2O_3 inclusions was not observed in the final sample of test 2 since the O content fixed at the surface was lower than 0.072 wt%. Meanwhile, the deviation between the experimental data and the predictions becomes more pronounced with test 3 compared to 2 (Figure 8-4), which indicate the effect of a higher p_{O_2} value on the extent of $FeO.Al_2O_3$ formation and, consequently, on the O and Al diffusion process.

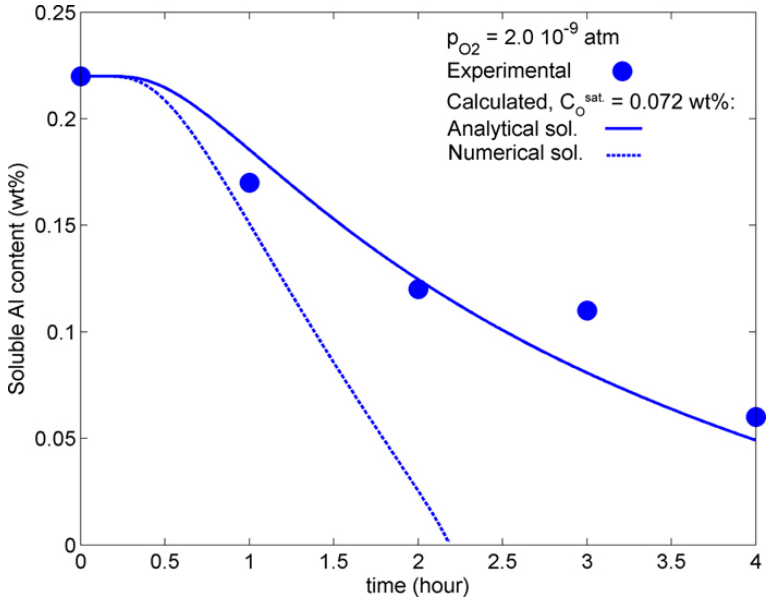

Figure 8-6: Evolution of the Al content in the Fe-Al alloy at the melt bottom ($Z = L$) as a function of holding time for test 3 (p_{O_2} = 2.0 10^{-9} atm). The experimental data (solid markers) are compared with the predictions using the analytical (solid line) and the numerical solutions (dashed line). The calculations are performed with $C_O^{sat.}$ = 0.072 wt% to take into account the transformation reaction of Al_2O_3 into $FeAl_2O_4$ at the melt surface.

As Al_2O_3 inclusions, which were formed during the reoxidation process, move towards the melt surface, the excess O compared to the $FeAl_2O_4$ stability point is used to produce the Fe aluminate phase. The diffusion problem can be simplified by using this value as new boundary condition for the O content at the melt surface. The new predictions for test 3 are compared with the experimental results in Figure 8-6. When using the analytical model (solid line in Figure 8-6), a better fit of the experimental results is obtained when the boundary condition at the melt surface is set at 0.072 wt% O. Under these conditions, the predicted position of the reaction front for test 3 after 4 h reoxidation time is approximately 8.7 mm below the melt surface (7.9 mm after solidification, Table 8-2). In the case of test 2, the predicted position of the reaction front after 2 h reoxidation time is approximately 4.3 mm below the melt surface (3.9 mm after solidification, Table 8-2).

Table 8-2: Position of the reaction front (mm) under the melt surface (after solidification) for tests 2 (2 h, $p_{O_2} = 4.3\ 10^{-10}$ atm) and 3 (4 h, $p_{O_2} = 2.0\ 10^{-9}$ atm) according to the calculations and the experimental results. L indicates that the reaction front has reached the melt bottom ($Z = L$) within the test duration. $D_O = 1.4\ 10^{-8}$ m^2 s^{-1} [244] and $D_O^* = 10^{-9}$ m^2 s^{-1}.

	Reaction front position (mm)	
	Test 2	Test 3
Analytical solution (D_O)	3.9	7.9
Numerical solution (D_O)	L	L
Numerical solution (D_O^*)	0.41	1.4
Measured	~1.1	~4-4.5

On the other hand, the results using the numerical solutions are still deviating significantly from the experimental values (dashed line in Figure 8-6). The numerical predictions overestimate the Al consumption during the reoxidation process. This disagreement may originate from several reasons, of which the most important are listed below.

- Diffusion of gaseous O_2 in the gas phase might become rate limiting. In that case, the diffusion of O_2 through the boundary layer to the melt surface must be included in the diffusion model. The flux of O_2(g) diffusing through the gas boundary layer is given by Eq. (8.1) [110].

$$J = \frac{k_m}{RT}\left(p_{O_2} - p_{O_{2,G\text{-}M}}\right) \tag{8.1}$$

  where k_m is the mass transfer coefficient, p_{O_2} and $p_{O_2,G\text{-}M}$ are the O_2 partial pressure in the bulk gas and at the gas-metal interface (in Pa). The mass transfer coefficient is strongly dependent on the geometry of the system and can be derived from dimensional relations. If diffusion of O_2 in the gas boundary layer is rate limiting, the constant O concentration fixed at the melt surface should be modified accordingly.

- The equilibrium between O_2(g) and the melt surface was not attained immediately. The boundary condition for the O content at the melt surface was lower than the fixed value and changed with time. However, the reaction at the interface is usually not considered as rate limiting [109].

- The formation of an oxide film on the melt surface may have decreased the diffusion rate as O must dissolve and diffuse through

the oxide layer. An additional equilibrium might be installed between the gas phase and the oxide layer as well as between the oxide layer and the melt. The oxidation rate of the melt would decrease once a continuous oxide film covers completely the melt surface and becomes relatively thick. The nature of the oxide film (solid or liquid) might also play a significant role on the diffusion of O through the film since diffusivities are usually several orders of magnitude lower in the solid state than in the liquid state. Under the present conditions, only solid Al_2O_3 produced by the reaction with Al is expected to form on the melt surface as FeO is unstable at so low O content. Assuming that all Al is oxidised and all Al_2O_3 products covered homogeneously the melt surface, the thickness of the oxide film would attain approximately 100 µm. After the experiments, no continuous Al_2O_3 layer was observd at the melt surface. The slower observed reoxidation rate is not believed to be caused by this mechanism.

- The choice of the diffusion coefficient of O and Al (D_O and D_{Al}) in liquid Fe may provide sources of inaccuracy in the predictions. As the diffusion process calculated by the numerical model seemed too fast compared to the experimental observations, D_O and/or D_{Al} used in the calculations might be too large. The influence of a lower value of one of the diffusion coefficient on the evolution of the Al content at the melt bottom is shown in Figure 8-7. The calculations are performed with D_{Al}^* (D_O^*) = 10^{-9} m^2 s^{-1} instead of D_{Al} (D_O) and keeping D_O (D_{Al}) unchanged. With using D_{Al}^* and original D_O value in the numerical model (dashed lines in Figure 8-7), the Al content at the melt bottom remains nearly constant for a quite long period and suddenly decreases when the reaction front approaches the fixed boundary $Z = L$. This behaviour is not in agreement with the experimental data, suggesting that D_{Al} should not be decreased. When using the original D_{Al} value and $D_O^* = 10^{-9}$ m^2 s^{-1} (solid lines in Figure 8-7), which is one order of magnitude lower than D_O and lower than D_{Al}, the predictions of the numerical model on the Al content at the bottom of the melt are in better agreement with the experimental values. Using D_O^*, the position of the reaction front is approximately 1.6 mm below the melt surface after 4 h reoxidation under the conditions of test 3 (1.4 mm after solidification) and 0.45 mm below the melt surface after 2 h reoxidation under the conditions of test 2 (0.41 mm after solidification).

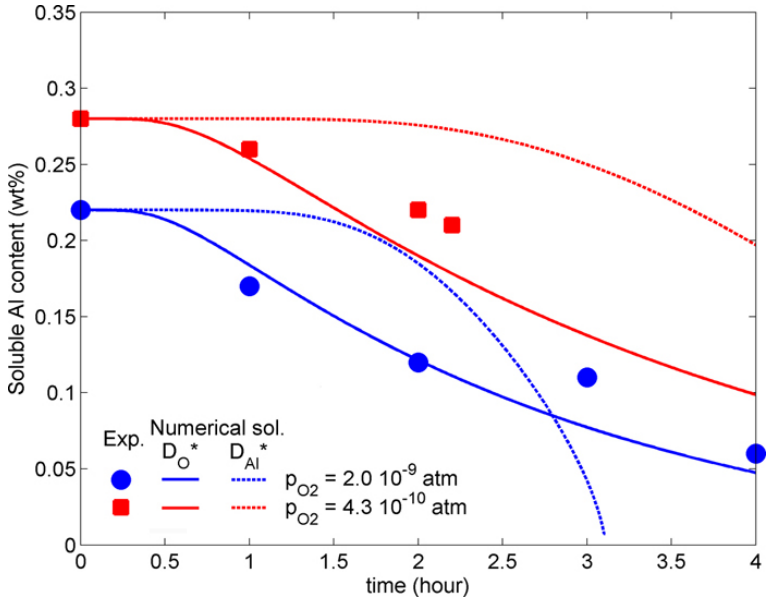

Figure 8-7: Evolution of the Al content at the melt bottom (Z = L) with time for tests 2 (p_{O_2} = 4.3 10^{-10} atm) and 3 (p_{O_2} = 2.0 10^{-9} atm). The experimental values are compared with the numerical calculations using D_O* (solid lines) or D_{Al}* (dashed lines) and the conditions of tests 2 and 3 (D_O* = D_{Al}* = 10^{-9} m^2 s^{-1}).

- Reoxidation of molten steel surface may take place after a significant time delay between the introduction of O_2(g) in the gas phase and the observation of the first inclusions on the melt surface, as reported by Wang [110, 186, 256] using the CSLM technique. The time delay results from the necessity to reach a certain level of supersaturation inside the melt volume near the surface prior to the nucleation of inclusions. The latter required that enough O_2 has been dissolved in that melt volume. The mass transfer of O_2 through the gas boundary layer controlled the formation of inclusions at the surface. Under the present conditions, the time delay should be less than 30 min as the experimental results in Figure 8-2 and Figure 8-4 showed that the Al content measured at the melt bottom was decreasing upon a modification of the p_{O_2}.

- The melt must be supersaturated in order to have nucleation and/or growth of non-metallic inclusions (section 7.4.1 in Chapter 7). The existence of a critical supersaturation for the formation of inclusions may modify the Al and O concentration profiles in the melt to some extent. The Al consumption would be slowed down compared to the case without imposed critical supersaturation. As a result, the Al

content measured at the melt bottom would be higher than that given in Figure 8-6.

The reactions involved during the overall reoxidation process are clearly very complex. Most of the mechanisms were simplified or not considered in the mathematical models due to the complexity of the reactions to be solved mathematically and/or unknown physical data to describe the kinetic processes properly. The improvement of the model would require a more systematic study of the diffusion to identify the rate limiting steps and to assess quantitatively kinetic parameters, such as diffusion and mass transfer coefficients, under the present conditions. From the above considerations, diffusion of O_2 in the gas boundary layer and the creation of supersaturated conditions at the melt surface and in the bulk seemed to have played an important role on the reoxidation rate of the melt.

8.2.4. Inclusion mapping for test 3

SEM-AIA measurements were conducted on the final sample cross-section of test 3 (reoxidation time = 4 h, C_{Al}^{0} = 0.22 wt%, p_{O_2} = 2.0 10^{-9} atm). A mapping of the sample cross-section was built based on the results from the AIA measurements and is presented in Figure 8-8. The cross-section shows only a representative part of the sample. The position of the markers indicates the inclusion location relative to the sample surface, while the marker shape and colour corresponds to the size class. The size is determined by the cross section area of the inclusion.

The mapping reveals that inclusions are mainly located in two regions. Most of them are found near the surface (area I in Figure 8-8), as a result of flotation. They consist of large inclusions with an average size of 5.8 μm and contributing to 600 vol. ppm (corresponding to ~150 ppm O). The inclusion layer near the melt surface is sometimes disrupted due to the motion of the large inclusions during quenching. The other area is located more in-depth in the sample, 4 to 4.5 mm below the surface (area III in Figure 8-8) and contains numerous small inclusions with an average size of 1.3 μm and contributing to 30 vol. ppm (~8 ppm O). This zone was not limited to the sample width represented in Figure 8-8, but was also observed throughout the cross section.

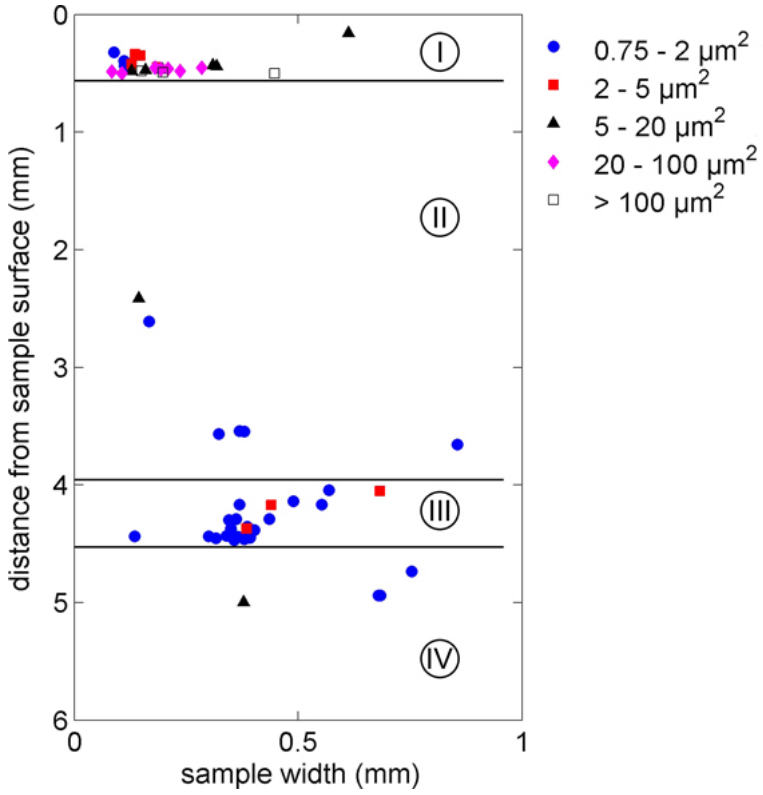

Figure 8-8: Mapping of inclusion size, as determined by SEM-AIA measurements on the final sample cross-section of test 3 (4 h, p_{O_2} = 2.0 10^{-9} atm). The markers indicate the position of the inclusion relative to the sample surface, while the marker shape and colour correspond to the size class. The horizontal lines show the separation between areas in the sample according to inclusion frequency.

Apart from these two zones, very few inclusions are detected. Area II (Figure 8-8) is a large area with very few inclusions, corresponding to the region above the reaction front according to the mathematical description (region A in Figure 7-1 (b) in Chapter 7). Area IV (Figure 8-8), the furthest from the sample surface, contains Al and almost no inclusions, which is analogous to region B in Figure 7-1 (b) (Chapter 7). Area III (Figure 8-8) located in between would correspond to the reaction front, where formation of Al_2O_3 takes place. According to the results of the analytical model depicted in Figure 8-6 for test 3, the reaction front is located approximately 7.9 mm below the melt surface (after solidification, Table 8-2). This value is too large compared to the observed position of the reaction front (Figure 8-8 and Table 8-2). When using the numerical model with D_O* which gives a

satisfying agreement between the calculated and measured Al content at the melt bottom (Figure 8-7), the calculated position of the reaction front is approximately 1.4 mm below the melt surface (after solidification, Table 8-2). This value is much smaller than the observed value of 4~4.5 mm. The predicted motion of the reaction front is too slow when using D_O*, suggesting that another or additional process should be considered in the mathematical description of the reoxidation process.

8.2.5. Evolution of inclusion morphology at fixed p_{O_2}

8.2.5.1. Test 3

In the final sample of test 3, the Al_2O_3 inclusion morphology near the surface (area I) is significantly different from those observed in the bulk (area III). Aggregates, dendrites, clusters and bars are abundant near the sample surface (Figure 8-9 (a) and (b)). The majority of the clusters observed near the melt surface have a plate-like structure, as seen in Figure 8-10 (a) after extraction of the inclusions from the metal matrix. The aggregates have irregular shapes, mostly angular. The dendritic and cluster structure of the aggregates suggests that they were formerly dendrites or clusters, which underwent collisions with other inclusion and/or sintering process with holding time.

Cavities are often observed in the aggregates (Figure 8-9 and Figure 8-10 (b)), as a result of surface reorganisation and densification of these high surface-area inclusions. As seen in Figure 8-9, the cavities in the inclusions are originally filled with Fe. Note that the Fe aluminate phase surrounding the inclusions near the sample surface, as depicted in Figure 8-9, cannot be found after extraction of the inclusions, as Fe aluminate is dissolved by the acid during the extraction procedure. The Fe aluminate phase is not observed inside the cavity (Figure 8-9), suggesting that the transformation of Al_2O_3 into Fe aluminate takes place mainly at the outer surface of the inclusion, as the O transport to the outer surface is easier than that to the cavity. It is unclear what the influence of the Fe aluminate transformation would have on the morphology of the original inclusion. The latter may have enhanced the formation of facets on the Al_2O_3 inclusion forming the core. Moreover, reoxidation conditions were reported to promote the adhesion and coalescence of Al_2O_3 inclusions [24]. In that case, FeO and $FeAl_2O_4$ were observed in the bond between the Al_2O_3 particles.

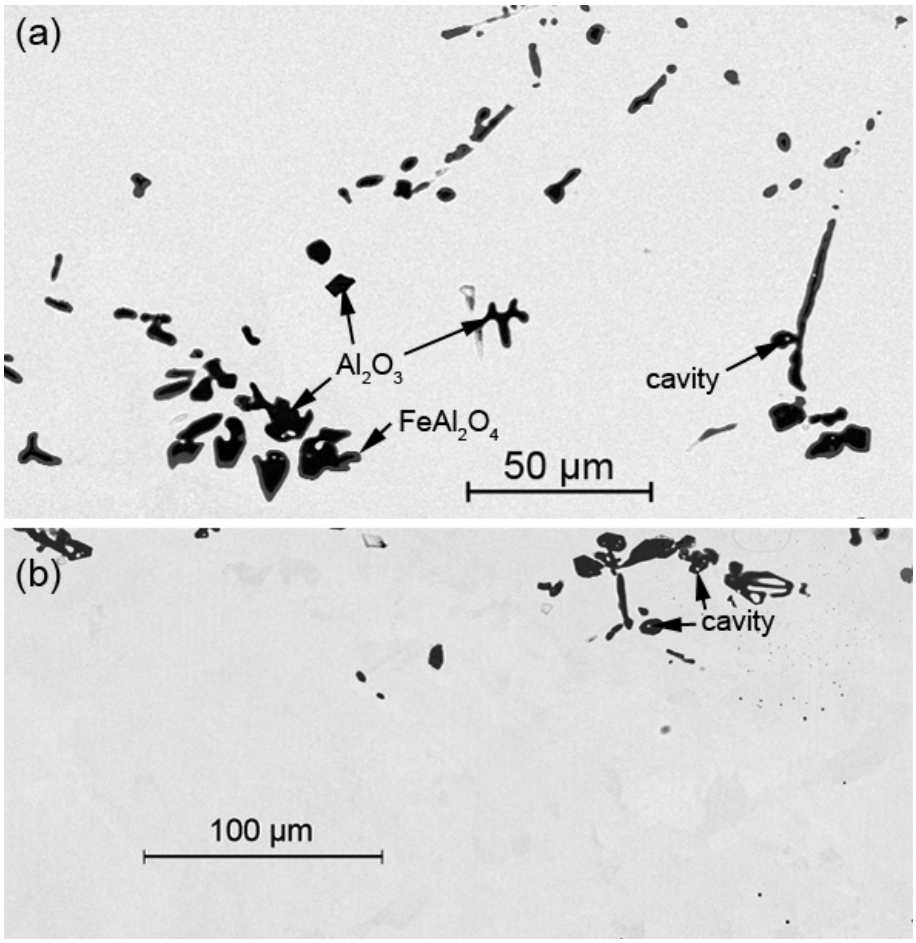

Figure 8-9: (a) and (b) Aggregates, dendritic and plate-like clusters near the surface of the final sample of test 3 (4 h, p_{O_2} = 2.0 10^{-9} atm). Most of them consist of an Al_2O_3 core surrounded by an Fe-rich aluminate phase.

The results of the mathematical models for the counter diffusion of Al and O and the formation of Al_2O_3 inclusions (Chapter 7) can be used to link the inclusion morphologies with the local nucleation and growth conditions. The predictions revealed that the conditions at the beginning of the diffusion process generate high availability of O and Al at the reaction front. The latter is due to the proximity of the gas phase, generating steep Al and O profiles at the beginning of the reoxidation process (Figure 7-4 and Figure 7-5). High supersaturation conditions and high Al_2O_3 formation rate are thus created locally (Figure 7-6 and Figure 7-7). These conditions promoted the formation of dendrites, clusters and bars among Al_2O_3 inclusion morphologies near the sample surface. According to Tiekink [175], diffusion

of O and Al would determine the occurrence of dendrites and bars. Sufficient supersaturation and mass transport rate of O and Al must be maintained long enough to obtain these shapes. It seems that such conditions are provided near the sample surface.

The aggregates have irregular shapes (Figure 8-10 (b)), and are believed to be formed by collision and coagulation of inclusions originating from deeper in the melt, which are moving to the surface during the oxidation process. As reported by Braun [70], clusters and other large surface inclusions have a high collision efficiency compared to more compact inclusions. Therefore, aggregates are most likely formed from a dendrite or cluster. With high holding time, aggregates are becoming more complex as the number of collisions increases, but more compact as sintering and densification processes occur. In test 3, high reoxidation conditions were met near the melt surface, which might have promoted coalescence between Al_2O_3 particles and, consequently, promoted growth of the aggregates.

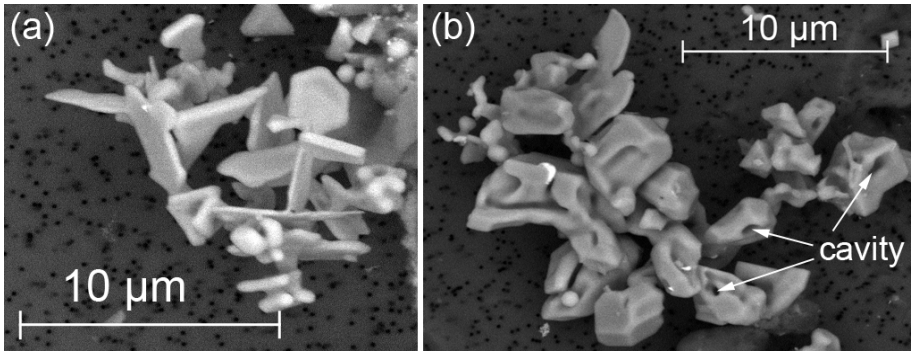

Figure 8-10: Inclusion morphologies observed in area I (melt surface in Figure 8-8) of the final sample of test 3 (4 h, p_{O_2} = 2.0 10^{-9} atm), after extraction: (a) Al_2O_3 cluster with plate-like structure; (b) aggregates of Al_2O_3 inclusions forming large angular structure. Cavities in the aggregates were often observed.

In contrast with the numerous clusters and aggregates found near the sample surface, the inclusions, which are located in area III, consist of individual and compact inclusions, mostly spherical ones (Figure 8-11 and Figure 8-12). Neither the formation of an Fe aluminate phase surrounding them nor the presence of cavities in the inclusion were observed.

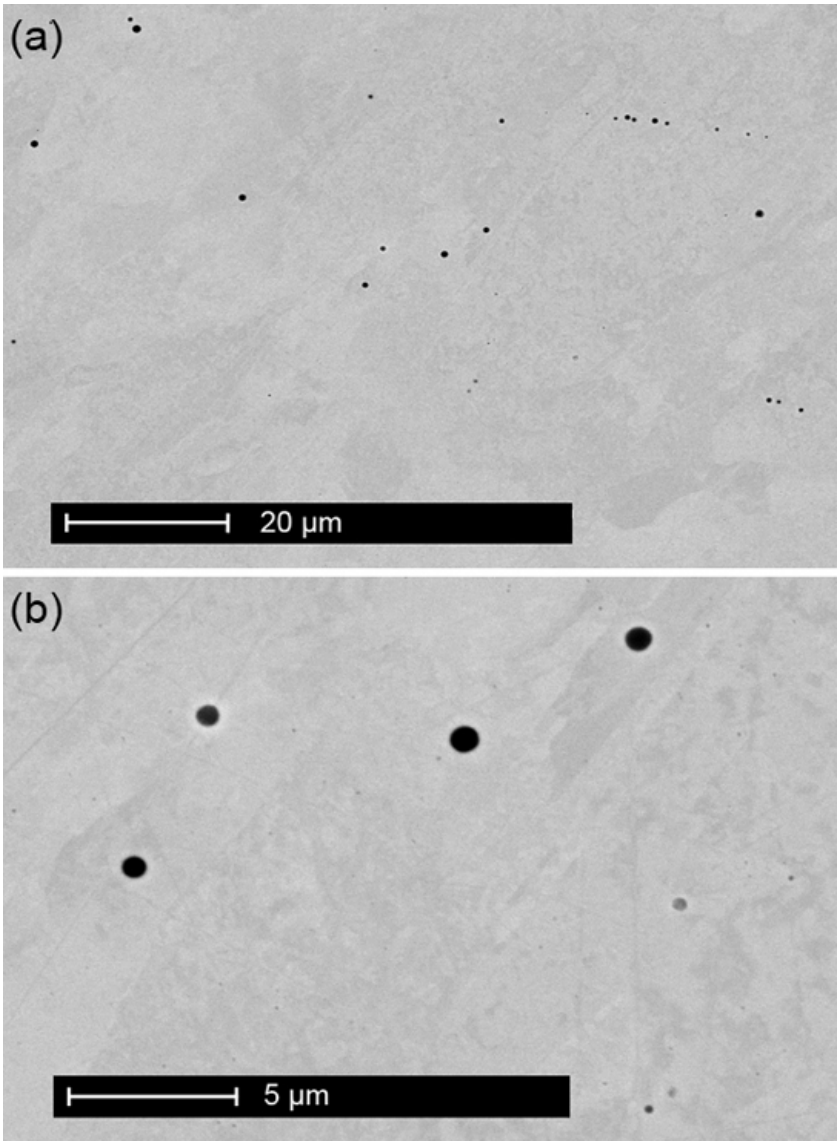

Figure 8-11: (a) Overview of the numerous small spherical Al_2O_3 inclusions located in zone III (Figure 8-8) in the final sample of test 3 (4 h, $p_{O_2} = 2.0\ 10^{-9}$ atm). (b) enlargement of (a).

According to the predictions, as time progresses, the reaction front is more and more distant from the sample surface, and the concentration profiles are progressively flatter (Figure 7-4 and Figure 7-5). Al and O become less available at the reaction front compared to the initial stage, causing a decrease in the local supersaturation with respect to Al and O and a decrease of the formation rate (Figure 7-6 and Figure 7-7). As a result, inclusion

shapes should theoretically evolve to compact and more faceted ones. The observed inclusions in the bulk are compact but spherical (Figure 8-11 and Figure 8-12), which are usually obtained under high local supersaturation conditions during nucleation.

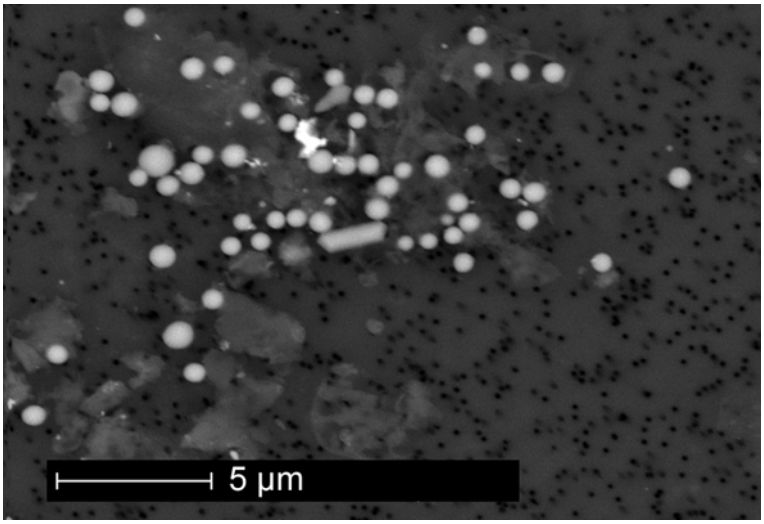

Figure 8-12: Small spherical Al_2O_3 inclusions originating from Zone III (Figure 8-8) in the final sample of test 3 (4 h, p_{O_2} = 2.0 10^{-9} atm), after extraction.

As highlighted in section 3.2.1.1 in Chapter 3, the mechanism for the formation of spherical Al_2O_3 inclusions is still unclear. Several mechanisms are reported. As evidence of the presence of clusters or dendrites cannot be found in this area, spherical inclusions cannot possibly be formed through the dismembering of dendrites arms [166, 177, 178]. Two different possibilities for the formation of spherical inclusions in the zone III of the sample are proposed, based on the way high supersaturation conditions can be obtained at this specific location.

According to the nucleation theory, a critical supersaturation level must be reached before nucleation can take place. Such a condition for nucleation implies that the formation of inclusions is not continuous, but takes place after a specific time interval. This time delay between two successive nucleation events is required to build up the local critical supersaturation for nucleation through the counter-diffusion of Al and O. Also, the entire melt becomes gradually supersaturated (with $S < S^*$) as O and Al can diffuse in both directions without being consumed by the reaction. Once the critical supersaturation is reached at a specific location, nucleation occurs and the supersaturation decreases rapidly. Spherical inclusions might form if the

value of the critical supersaturation required for nucleation is high. The mass transport rate of Al and O seemed however too low to maintain the supersaturation at a high enough level close to the inclusion to obtain bars and dendrites, as observed at the melt surface. Facets can form on the spherical inclusions to decrease the surface energy while they move upwards to the melt surface.

The other possibility, as concluded by Wasai [179] and Dekkers [171, 172], is that these spherical inclusions are secondary inclusions. They would form upon cooling of the melt, which provided high supersaturation and uniform growth conditions for the formation of spherical inclusions. As both Al and O must be available in that specific area, the area III still indicates the position of the highest supersaturation conditions, i.e. where the O and Al profiles would overlap.

8.2.5.2. Test 2

The majority of the inclusions observed near the surface of the final sample of test 2 are individual and mostly angular (Figure 8-13). Aggregates are much less abundant compared to test 3. High surface-area inclusions, which are less abundant than those in test 3, consist mainly of dendrites and plate-like clusters. The transformation of Al_2O_3 into Fe aluminate did not take place due to the lower O content compared to the equilibrium value (720 ppm). The position of the reaction front was approximately 1.1 mm below the melt surface (Table 8-2) and was too close to the sample surface to observe notable differences in inclusion morphologies, i.e. area II depicted in Figure 8-8 was too small to reveal clearly the reaction front. No area containing mostly spherical inclusions were noticed in the final sample of test 2. The discrepancy between the measured and calculated position of the reaction front was also noticed with test 2 (Table 8-2). The results obtained with the numerical solution underestimated the reoxidation rate, whereas the results of the analytical solution overestimated it. As mentioned above, this disagreement between predictions and observations highlights that the reoxidation process is complex and controlled by (an)other process.

As seen in Figure 8-13, the surface of the sample after quenching is covered by a thin slag layer of about 10 to 20 μm thick, consisting of mainly FeO. A thin film of Al_2O_3 inclusions (darker phase at the slag layer bottom in Figure 8-13) was found between the metal and the slag. The formation of the FeO layer most probably took place during the quenching of the sample (upon short exposure to air, upon contact with water or during cooling of CO(g) when the crucible is lifted to the colder part of the furnace). As the oxide

layer is relatively thin, its influence on the reoxidation rate during the experiment is believed to be limited.

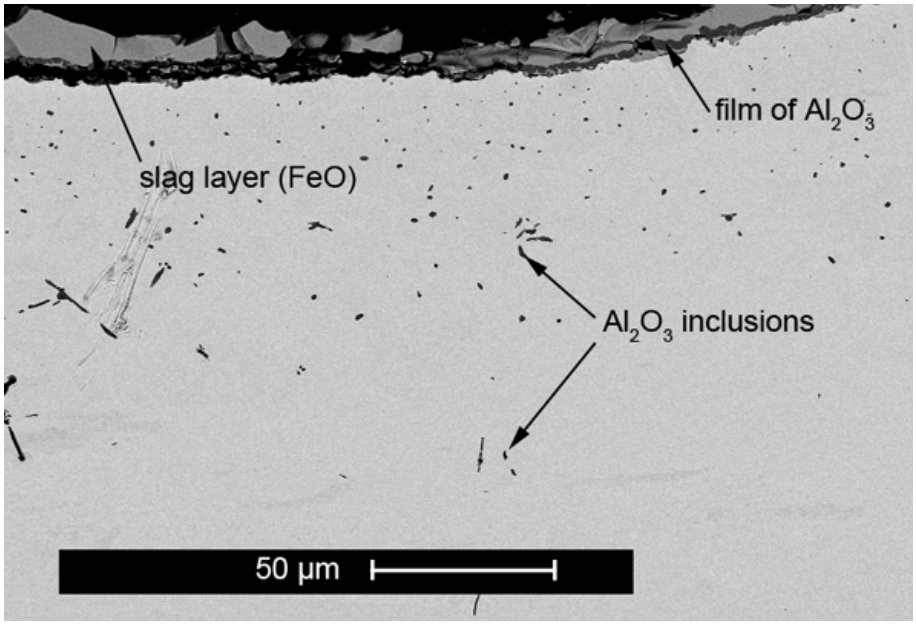

Figure 8-13: Overview of the inclusions found near the surface of the final sample of test 2 (2 h, $p_{O_2} = 4.3\ 10^{-10}$ atm).

The dominance of angular inclusions observed in test 2 is consistent with the observations made with test 1. This evolution may be attributed to a difference of supersaturation degree with respect to Al and O. As highlighted in section 7.3.2 in Chapter 7, decreasing the p_{O_2} resulted in a change of the Al and O concentration profiles (Figure 7-10), a decrease of the reaction front velocity (Figure 7-9), the rate of Al_2O_3 formation (Figure 7-11) and supersaturation values (Figure 7-13 (a) and (b)). These conditions promoted the formation of angular and more compact inclusions, as shown in Figure 8-14, compared to test 3 with higher p_{O_2} value.

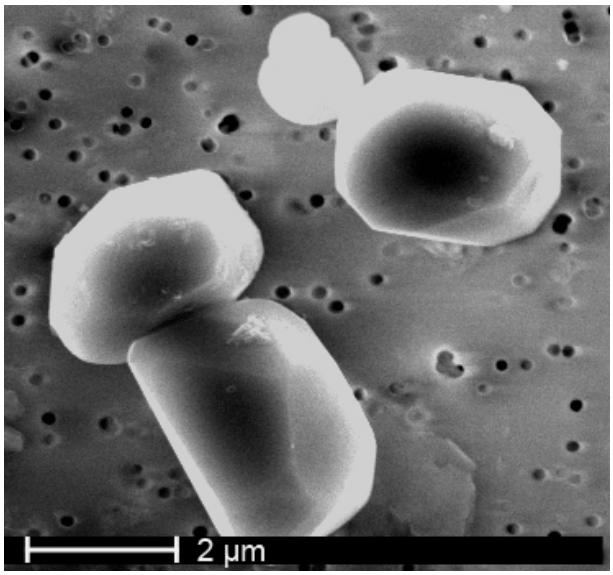

Figure 8-14: Angular inclusions located near the sample surface of the final sample of test 2 (2 h, $p_{O_2} = 4.3\ 10^{-10}$ atm), after extraction.

The presence of fewer aggregates compared to the test 3 may be attributed to several factors. The number of collisions was lower than under the conditions provided in test 3 due to the shorter holding time and the fewer high surface-area inclusions. Also the Fe aluminate phase surrounding the inclusions near the sample surface, which might have played a role in promoting the coalescence of inclusions in test 3, was absent in the case of test 2. Also, the few aggregates and angular inclusions originating from the final sample of test 2 did not show any cavity formation.

8.2.6. Comparison of the morphology under deoxidation and reoxidation conditions

As highlighted in section 6.3.4 of Chapter 6 discussing the evolution of inclusion morphology at the onset of deoxidation, clusters, bars and dendrites of Al_2O_3 inclusions were not observed in the reaction zone. The absence of these typical high supersaturation morphologies was attributed to a limited mass transport of $\underline{O}$ to the growing crystal, resulting from the high velocity of the diffusion front. Furthermore, once the diffusion front moved away from the newly formed Al_2O_3 inclusions, the latter are surrounded by an Fe-Al melt containing a small amount of $\underline{O}$. Assuming that the evolution of the interfacial energy of an Fe-Al melt with $\underline{O}$ content is similar to that of liquid Fe, decreasing the $\underline{O}$ content creates less favourable conditions for

nucleation and growth of inclusions due to the increase of the interfacial energy.

In contrast, the nucleation and growth conditions created during the reoxidation experiments allowed the formation of dendrites and clusters, suggesting that high supersaturation conditions were maintained long enough near the inclusions. In contrast with the deoxidation conditions, the newly formed Al_2O_3 inclusions are surrounded by an O rich melt containing a small amount of Al as the diffusion front moves downwards and the inclusions move upwards. Taking into consideration surface energy, the interfacial tension of liquid Fe decreases with increasing O content. The latter may promote the formation of new inclusions and/or growth into dendrite or cluster shapes as the surface energy is less. In addition, local variations in the Al and O concentration profiles are more likely to occur as the sample volume and the holding time are much larger compared to those involved in the deoxidation experiments. Local variations in the supersaturation conditions might have promoted specific growth conditions, leading to specific inclusion shapes.

8.3. Conclusions

Reoxidation experiments were conducted at 1600 °C and consisted in bringing liquid Fe containing about 0.2 wt% Al in contact with an atmosphere maintained at a fixed p_{O_2}. The purpose was to study the formation and the morphology of Al_2O_3 inclusions under different oxidizing conditions. The following conclusions were derived:

- Mass transport of Al and/or O to the reaction front was confirmed to be the rate limiting step during the oxidation of the Fe-Al melt, resulting in a higher measured Al content compared to the equilibrium values.
- The evolution of the Al content in the sample taken at specific time during the reoxidation process was compared with the calculation results given by the diffusion models developed in Chapter 7.
    a. When using the analytical solution for the diffusion-controlled moving boundary problem (semi-infinite geometry), good agreement between predictions and experimental data was obtained for holding times less than 1 h. For longer times, the calculations predicted less Al than experimentally observed when the p_{O_2} was 2.0 10^{-9} atm. This divergence is believed to originate from the transformation of Al_2O_3 into $FeO.Al_2O_3$ observed near the

sample surface. A better agreement was obtained when the value of the boundary condition for the O content at the melt surface is fixed at 720 ppm, the value from which $FeO.Al_2O_3$ is reported to become more stable than Al_2O_3.

b. In the case of the numerical model solving the diffusion-controlled moving boundary problem with a finite geometry, the O diffusion coefficient in the melt must be decreased to $1.0\ 10^{-9}\ m^2\ s^{-1}$ in order to obtain a good fit between the experimental values and the calculations with the numerical models (finite geometry).

- A reaction front, at which Al_2O_3 inclusions are formed, was observed during the investigation of the cross section of the final samples of tests 2 and 3. The comparison between the measured position of the reaction front and that predicted by the numerical diffusion model showed that the predictions underestimated the motion of the reaction front. This is likely due to the occurrence of (an)other rate limiting process(es), such as diffusion of $O_2(g)$ through the gas boundary layer and/or the creation of supersaturated conditions at the melt surface and in the bulk.
- Distinct morphologies were noticed among the inclusions formed during reoxidation. Dendrites, clusters, aggregates and bars were observed near the sample surface and at high p_{O_2}, while compact and faceted shapes were found at lower p_{O_2}, where lower supersaturation conditions are generated. These differences were attributed to the evolution of the local supersaturation with respect to Al and O near the reaction front, as the availability of Al and O decreases as diffusion progresses.

Chapter 9
General conclusions

The objective of this work was to study the influence of the main process parameters during secondary steelmaking, namely the dissolved aluminium and oxygen contents in liquid steel, on the formation, growth and the morphology of inclusions.

Experiments have been designed at the lab scale to study the formation of inclusions during deoxidation as well as during reoxidation of liquid melt under controlled conditions. The formation and growth conditions were evaluated in order to determine the relationship between the process parameters and the inclusion size distribution and morphology. The comprehension of the mechanisms that determine the characteristics of inclusions will enhance clean steel production through the control of the non-metallic inclusions.

9.1. Summary of the results

During the steelmaking process, non-metallic inclusions have two distinct origins. The first inclusion source is the deoxidation process, by which a deoxidant is added to molten steel to decrease the dissolved oxygen content. The second inclusion source involves all mechanical and chemical reactions between the deoxidized steel and its environment. Chapter 2 showed that many factors contribute to the formation of inclusions during the steelmaking process. The origin and the comprehension of the formation mechanisms of the inclusions are, therefore, rendered complex.

Non-metallic inclusions are usually considered to be detrimental to the quality of the final product. The task of the steelmaker is therefore to improve inclusion removal and to avoid steel contamination by unintended reactions. Another approach is to beneficially utilise non-metallic inclusions, by controlling the characteristics of the remaining inclusions in order to nullify their detrimental effect and even improve the performance of the final

steel product. This approach has been coined as inclusion engineering. In both cases, the production of clean, high quality steels requires, besides the decrease of the number of inclusions, the control of their morphology, composition and size distribution during steel processing. The importance of inclusion engineering was outlined in Chapter 2, with some industrial application examples.

In Chapter 3, the relation between the growth conditions and the inclusion morphologies was reviewed. Various Al_2O_3 inclusion morphologies have been reported in steel: clusters and dendrites, aggregates, faceted inclusions, platelets and spherical inclusions. Inclusion morphology is largely controlled by the degree of supersaturation of the melt. Therefore, the process conditions are key parameters for the control of inclusion characteristics. High supersaturation conditions promote the formation of dendritic, cluster and spherical inclusions, while faceted inclusions and the development of facets on existing inclusions arise from low supersaturation conditions. However, the mechanism leading to Al_2O_3 inclusion morphologies are still unclear and quantitative data describing the relationship between inclusion morphology and process parameters are rare.

The literature review highlighted the importance of the process parameters on the control of non-metallic inclusions. The first task of this research was to build an appropriate experimental setup in order to control the conditions during the experiments (temperature, atmosphere and sampling). Analytical methods were also developed in order to quantify the composition of the metal, to draw the inclusion size distribution based on thousands of inclusion size measurements and to assess the inclusion morphologies after their extraction from the metal matrix.

Chapters 5 and 6 were dedicated to the study of the formation of Al_2O_3 inclusions under deoxidation conditions. In Chapter 5, deoxidation was performed by adding a large amount of Al into molten Fe in order to create high supersaturation conditions for the formation of Al_2O_3 inclusions. The evolution of the $\underline{Al}$ content in the melt indicated that the Al mixing is slow under the present experimental conditions. However, the addition of a large amount of cold Al created a temperature gradient, along with $\underline{Al}$ and $\underline{O}$ concentration gradients through the melt. These complex conditions were reflected in the shape of the inclusion size distributions and in the occurrence or absence of specific inclusion morphologies. The differences observed in the shapes of the inclusion size distributions and in the inclusion morphologies were attributed to different growth mechanisms prevailing during the deoxidation process.

An innovative experimental approach, aiming to observe the formation and morphology of inclusions shortly after their formation, was presented in

Chapter 6. The formation of inclusions during the early stages of deoxidation was simulated by bringing, inside a quartz tube, a piece of Al in contact for a short time (1 to 60 s) with liquid Fe containing different dissolved oxygen levels. During the short contact between Fe and Al, a reaction zone was created by the interdiffusion of Fe and Al. The reaction zone consisted of several layers of intermetallic compounds of the Fe-Al binary system. Due to the temperature difference between liquid Fe and cold Al during the contact, liquid Fe solidified at the interface, forming a shell, while part of the Al melted. The microstructures of the samples after quenching were interpreted to determine whether the reaction zone was fully liquid during the experiments. Based on the microstructure, the concentration profiles, diffusion processes in solid and liquid phases, estimations on the growth rate of Fe-Al intermetallic layers, and on the behaviour of Al_2O_3 inclusions in the reaction zone, it was shown that the reaction zone was completely liquid and that the solid Fe shell melted for the samples with holding time of 30 and 60 s.

In the second part of Chapter 6, the formation and characteristics of the inclusions formed shortly after the deoxidation stage were examined. These inclusions were located in the area between the initial Fe-Al boundary and the final diffusion front. In the samples with high $\underline{O}$ content, small spherical and angular inclusions were found near the diffusion front, while aggregates of small inclusions resulting from collisions were numerous further away from the diffusion front. Larger inclusions, likely resulting from heterogeneous nucleation of Al_2O_3 on FeO_x and/or SiO_2 inclusions were found. With lower $\underline{O}$ content, the amount of inclusions decreased and faceted inclusions were dominant among the morphologies, owing to lower supersaturation conditions.

Fe shell formation and melting, and inclusion formation in the reaction zone are relevant phenomena for the secondary steelmaking industry as they take place during the addition and dissolution of Al in the ladle. These results could be combined with a model on the dissolution behaviour of the deoxidiser, for instance, to enhance inclusion removal by predicting the location and the morphology of inclusions depending on the addition practice and melt conditions.

In Chapters 7 and 8, the formation and morphology of Al_2O_3 inclusions were investigated under different oxidizing conditions as differences in kinetics and thermodynamic driving forces can lead to important changes in the inclusion characteristics compared to the deoxidation process. The reoxidation experiments consisted in bringing liquid Fe containing about 0.2 wt% Al in contact with an atmosphere maintained at a fixed p_{O_2}. As mass transport of $\underline{Al}$ and/or $\underline{O}$ are the main limiting step under the present

experimental conditions, the governing equations of Al and O diffusion in liquid Fe were solved in Chapter 7, using three approaches. The Al and O concentration profiles through the melt, the motion of the reaction front, the inclusion formation rate and the accumulated supersaturation were calculated as a function of time and initial conditions in order to provide a relation between the local conditions and the inclusion characteristics observed during the experiments.

The predictions were used to assist with the interpretation of the experimental results in Chapter 8. Mass transport of Al and/or O to the reaction front was confirmed to be the rate limiting step during the oxidation of the Fe-Al melt. When using the analytical solution for the diffusion-controlled moving boundary problem (semi-infinite geometry), good agreement between predictions and experimental data was obtained when the transformation reaction of Al_2O_3 into $FeAl_2O_4$ was considered near the melt surface for O content $\geq$ 720 ppm. Dendrites and bars were observed near the sample surface and at high p_{O_2}, while compact and faceted shapes were found at lower p_{O_2}, where lower supersaturation conditions were generated. These differences were attributed to the evolution of the local supersaturation with respect to Al and O near the reaction front, as the availability of Al and O decreases as diffusion progresses.

A possible application of the results on Fe-Al melt reoxidation is the selection of appropriate slag and refractory composition to avoid the formation of detrimental inclusions, based on the oxygen potential difference created between the atmosphere, slag, refractory or other component and liquid steel.

This research highlighted the significant influence of the supersaturation condition on the inclusion morphologies. The comparison between the morphologies obtained after deoxidation and reoxidation suggested that the supersaturation and the availability or mass transport of O to the new inclusions determine the size and morphology of the inclusion. Based on the present investigations, Figure 9-1 shows the evolution of the Al_2O_3 inclusion morphology as a function of the supersaturation and the O availability to the inclusion during its growth.

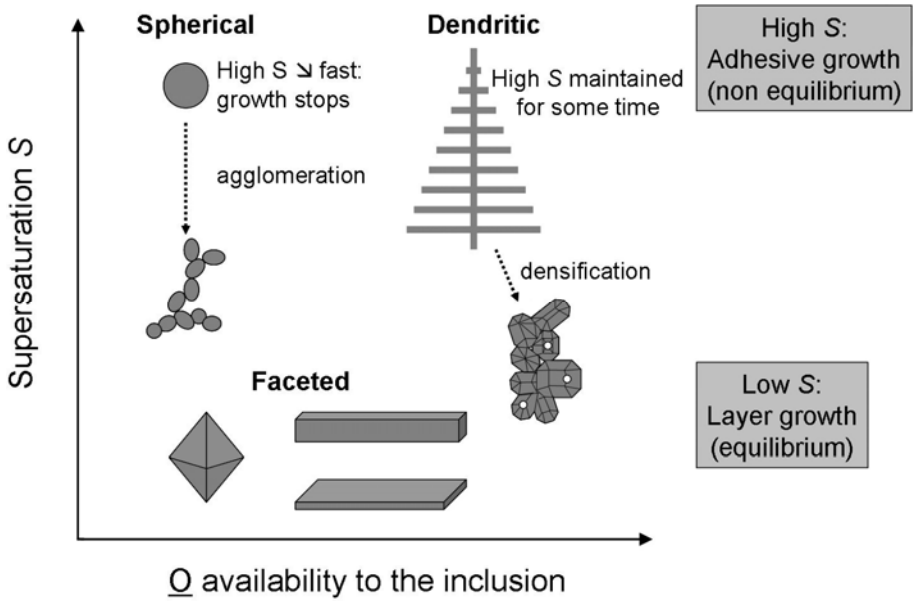

Figure 9-1: Evolution of the growth shapes of Al_2O_3 inclusions observed in this study as a function of the O availability (transport of O to the inclusion) and the supersaturation degree of the melt.

Faceted inclusions resulting from layer growth (reaction controlled) were found under low supersaturation conditions (Figure 9-1). With increasing supersaturation, the system is driven away from equilibrium into a regime where kinetics control the inclusion shape. Spherical inclusions were found numerously in the reaction zone during the contact between Al and Fe with high O content owing to the high local supersaturation conditions. The fast motion of the Fe/Fe-Al diffusion front prevented O diffusion into the reaction zone (top left corner of Figure 9-1). As a result, the local supersaturation level dropped very fast after nucleation, decreasing drastically the inclusion growth rate. The inclusions evolving in an Al-rich Fe melt were subjected to agglomeration with time. Conversely, high supersaturation conditions provided during reoxidation of Fe-Al melts induced the formation of dendritic inclusions at the melt surface. Counter-diffusion of Al and O near the melt surface and high supersaturation conditions were maintained long enough to obtain dendritic shaped inclusions (top right corner of Figure 9-1). With time, they underwent a densification process to form more compact and faceted inclusions.

9.2. Suggestions for future work

A number of experiments and improvements of the experimental method would enable to gain more data on the influence of deoxidation and reoxidation conditions on the inclusion characteristics. Some suggestions are listed below.

- *Inclusion formation at the early stage of deoxidation:*

The experimental technique presented in Chapter 6 could be changed in order to suppress the temperature difference between Fe and Al prior to the contact. The latter would require designing another experimental setup in order to melt and maintain separately Fe and Al at the same temperature. The device would then enable the two liquids to be brought into contact without creating strong turbulences. Also, the large density difference between liquid Fe and liquid Al should be carefully considered. As the temperature gradient between Fe and Al would then be reduced, a fully liquid and isothermal reaction zone would be provided. It should be noted that such isothermal conditions would help to investigate the fundamental relation between supersaturation and inclusion morphology, but would not simulate the industrial situation, where a temperature gradient is present during the addition of Al into liquid steel.

The influence of lower supersaturation conditions can be investigated by replacing pure Al by Fe-Al alloys in which the Al content is varied. In that case, the Fe-Al alloy should be homogeneous and free of inclusions, which would require a careful preparation. Moreover, Al could be replaced by other deoxidizers or alloying elements, such as Mn, Si, Mg, Ti, to investigate their influence on the formation and characteristics of inclusions.

Ideally, an experimental technique that provides in-situ observation of the deoxidation process would help to study the interactions between Al and Fe and the formation of inclusions just after the Al addition. The CSLM technique, which has already been successfully used to study the behaviour of inclusions on the surface of molten steel, could be modified to perform such experiments. The modification of the CSLM equipment consists of a specifically designed device that enables performing additions at high temperature in the CSLM gold image furnace chamber. Though the modified lid of the CSLM furnace chamber has been designed and built, preliminary tests showed that the oxygen content in the gas phase should be as low as possible. Otherwise, the melt surface is rapidly covered by an Al_2O_3 layer that prevents a good observation. With an adequate gas atmosphere, further experiments using the new device could provide interesting data on the early stage of deoxidation.

- *Reoxidation conditions and formation of Al_2O_3 inclusions:*

Further reoxidation experiments could be performed using the same technique described in Chapter 8 with other Al contents for the Fe-Al alloy. For example, the Al content can be decreased to 0.1 wt% and 500 ppm to provide lower supersaturation conditions. Another experimental approach, similar to that used for the observation of the early stage of deoxidation, could be employed for the observation of the reoxidation process. Other oxygen sources for the reoxidation of the melt, such as slag or refractory, could be investigated.

Further modelling work would be required to improve the model that was presented in Chapter 7. Ideally, the advantages provided by each of the three approaches could be combined in one model to provide a better representation of the real situation. More efforts could be provided to incorporate the nucleation theory, which takes into account the existence of a critical supersaturation for the formation of inclusion, and to couple the diffusion process and the Al_2O_3 formation reaction. Moreover, the motion of the inclusions was not considered in the present model. Including a population balance in the model would provide predictions of the evolution of the inclusion population in the melt as a function of time, initial conditions and position in the melt. The predictions could be compared with the experimental results to help to understand the conditions under which the inclusions were formed and grew during the reoxidation experiments. Also, the model could be used to predict the evolution of steel reoxidation and the formation of inclusions resulting from reactions with the gas phase, the slag, the refractories and any other possible oxygen sources in contact with molten steel.

- *Nature of Al_2O_3 inclusions:*

The morphology of Al_2O_3 inclusions can be easily assessed after their extraction from the metal matrix. Diffraction analyses using the Focused Ion Beam combined with Electron Backscattered Diffraction (FIB-EBSD) were initiated on the extracted inclusions to obtain a relation between the crystal structure of the Al_2O_3 inclusion and its morphology. Without any further preparation (i.e. no FIB milling), the diffraction patterns of several inclusion morphologies revealed that dendrites and "flower-like" inclusions are one single crystal and that spherical inclusions, even less than 1 µm size, are crystalline. However, the phases could not be clearly identified as the diffraction patterns could not be unambiguously indexed. The main difficulties arise from a non-flat crystal surface and not properly oriented facets, which cause distortions and shadows in the diffraction pattern. Several attempts of FIB milling of extracted inclusions were conducted to

produce a high quality surface amenable for EBSD measurements. The trials were not successful due to carbon contamination of the ion milled surface during milling. Another preparation method of the extracted inclusions could eliminate this problem by providing a flat surface for the diffraction analysis and ensuring that the morphology of the inclusion can be identified.

- *Size distribution of inclusions during secondary steelmaking*

Inclusion size distributions are important tools for the evaluation of the steel cleanliness. Nowadays, automated analysis and imaging techniques are more and more frequently used to measure, in a limited time, size, composition and other characteristics of a large amount of inclusions on sample cross sections. These techniques offer a great opportunity to collect a large amount of information on the evolution of inclusion size distributions during secondary steelmaking.

Interpretation of these inclusion size distributions is important as it can provide information on the inclusion growth history, such as the efficiency of the deoxidation reaction and the occurrence of accidental reoxidation events. As inclusion morphology is the result of growth, a relation between inclusion size distribution and morphology is expected. Combining inclusions size distribution measurement using AIA techniques with systematic investigations of inclusion morphologies conducted on the same sample (taken from industrial runs or lab experiments) would provide two viewpoints reflecting the growth conditions. The shape of the inclusions can help to understand and interpret the size distribution and vice-versa. Also, automated analysis techniques could be used or developed to characterize the three-dimension shape of the inclusions in a more statistical approach.

As outlined in the text, retrieving quantitative information from a size distribution requires appropriate statistical description of the observed size distribution combined with modelling population balance equations. Stereological methods need to be carefully employed for non-metallic inclusions in steels as their shapes can be quite different compared to crystals from geological systems. This would provide an interesting association of industrial runs, lab experiments and modelling work.

Bibliography

[1] I. Sunagawa: Morphology of minerals, in: Morphology of crystals, Part B, I. Sunagawa (ed.), Terra Science Publishing, Tokyo, (1987), 509-587.

[2] Steeluniversity.org: http://www.steeluniversity.org (accessed July 2009).

[3] SteelMATTER (MATTER, University of Liverpool): http://www.matter.org.uk/steelmatter/ (accessed July 2009).

[4] The Visible Hand of Steel Industry: http://schabrun.com/ (accessed July 2009).

[5] E. T. Turkdogan: Fundamentals of Steelmaking, Institute of Materials (ed.), Cambridge University Press, London, UK, (1996), 209-244.

[6] E. T. Turkdogan: Fundamentals of Steelmaking, Institute of Materials (ed.), Cambridge University Press, London, UK, (1996), 245-296.

[7] R. Fandrich, H. B. Lüngen and C. D. Wuppermann: Secondary metallurgy - Status 2007. *Proc. 7th Int. Conf. on Clean Steel*, Balatonfured, Hungary, June 4-6, (2007), Hungarian Mining and Metall. Soc., 28-37.

[8] E. T. Turkdogan: Fundamentals of Steelmaking, Institute of Materials (ed.), Cambridge University Press, London, UK, (1996), 112-113.

[9] Introduction to continuous casting (The Continuous Casting Consortium, University of Illinois): http://ccc.illinois.edu/introduction/overview.html (accessed July 2009).

[10] Y. Sahai and T. Emi: Tundish technology for clean steel production, World Scientific, Singapore, (2008), 1-15.

[11] R. Kiessling: Non-metallic inclusions in steel - Part III, 2nd Ed., The Institute of Materials, London, UK, (1978).

[12] L. F. Zhang and B. G. Thomas: State of the art in the control of inclusions during steel ingot casting. *Metallurgical and Materials Transactions B* **37** (5) (2006) 733-761.

[13] M. Nadif, J. Lehmann, M. Burty and J. F. Domgin: Control of steel reoxidation and CC nozzle clogging: an overview. *Proc. 7th Int. Conf. on Clean Steel*, Balatonfured, Hungary, June 4-6, (2007), Hungarian Mining and Metall. Soc., 38-47.

[14] A. Ghosh: Secondary steelmaking: principles and applications, CRC Press, Boka Raton, FL, (2000), 255-270, 274.

[15] A. Nicholson and T. Gladman: Non-metallic inclusions and developments in secondary steelmaking. *Ironmaking & Steelmaking* **13** (2) (1986) 53-69.

[16] H. V. Atkinson and G. Shi: Characterization of inclusions in clean steels: a review including the statistics of extremes methods. *Progress in Materials Science* **48** (5) (2003) 457-520.

[17] T. A. Engh: Principles of Metal Refining, Oxford University Press, Oxford, (1992), 19-38.

[18] D. Brooksbank and K. W. Andrews: Stress field around inclusions and their relations to mechanical properties. *Journal of the Iron and Steel Institute* **210** (1972) 246-255.

[19] T. Emi: Improving steelmaking and steel properties, in: Fundamentals of Metallurgy, S. Seetharaman (ed.), Woodhead Publishing, Cambridge, UK, (2005), 503-554.

[20] L. F. Zhang and B. G. Thomas: State of the art in evaluation and control of steel cleanliness. *ISIJ International* **43** (3) (2003) 271-291.

[21] Y. Sahai and T. Emi: Tundish technology for clean steel production, World Scientific, Singapore, (2008), 43-46.

[22] R. Dekkers, B. Blanpain, P. Wollants, F. Haers, B. Gommers and C. Vercruyssen: A morphological comparison between inclusions in aluminium killed steels and deposits in submerged entry nozzle. *Steel Research International* **74** (6) (2003) 351-355.

[23] S. Basu, S. K. Choudhary and N. U. Girase: Nozzle clogging behaviour of Ti-bearing Al-killed ultra low carbon steel. *ISIJ International* **44** (10) (2004) 1653-1660.

[24] K. Sasai and Y. Mizukami: Mechanism of alumina adhesion to continuous caster nozzle with reoxidation of molten steel. *ISIJ International* **41** (11) (2001) 1331-1339.

[25] C. Van Der Eijk, Ø. Grong and J. Walmsley: Effects of deoxidation practice on the inclusion formation in low alloy structural steels. *Proc. 6th International Conference on Molten Slags, Fluxes and Salts*, Stockholm, Sweden-Helsinki, Finland, 12-17 June, (2000), KTH, Stockholm.

[26] K. Yamamoto, S. Matsuda, T. Haze, R. Chijiiwa and H. Mimura: A Newly Developed Ti-Oxide Bearing Steel Having High HAZ Toughness. *Proc. Int. Symp. Residual and Unspecified Elements in Steel*, Bal Harbour F1, USA, 11-13 November, (1987), ASTM International, 266.

[27] O. Grong, L. Kolbeinsen, C. Van Der Eijk and G. Tranell: Microstructure control of steels through dispersoid metallurgy using novel grain refining alloys. *ISIJ International* **46** (6) (2006) 824-831.

[28] G. K. Sigworth and J. F. Elliott: Thermodynamics of liquid dilute iron alloys. *Metal Science Journal* **8** (9) (1974) 298-310.

[29] M. W. Chase, J. L. Curnutt, R. A. Mcdonald and A. N. Syverud: JANAF thermochemical tables. *Journal of Physical and Chemical Reference Data* **7** (3) (1978) 793-940.

[30] Steelmaking Data Sourcebook, The Japan Society for the Promotion of Science - 19th Committee on Steelmaking (ed.), Gordon and Breach Science Publishers, Montreux, Switzerland, (1988), 45.

[31] I. H. Jung, S. A. Decterov and A. D. Pelton: A thermodynamic model for deoxidation equilibria in steel. *Metallurgical and Materials Transactions B* **35** (3) (2004) 493-507.

[32] J. W. Christian: The theory of transformations in metals and alloys - Part I Equilibrium and general kinetic theory, 2nd Ed., Pergamon, Oxford, UK, (1975), 418-448.

[33] D. Turnbull and J. C. Fisher: Rate of nucleation in condensed systems. *The Journal of Chemical Physics* **17** (1) (1949) 71-73.

[34] M. L. Turpin and J. F. Elliott: Nucleation of oxide inclusions in iron melts. *Journal of the Iron and Steel Institute* **204** (1966) 217-225.

[35] K. Wasai, K. Mukai, H. Fuchiwaki and A. Yoshida: Determination of aluminum and oxygen contents in liquid iron in equilibrium with alpha-alumina and hercynite. *ISIJ International* **39** (8) (1999) 760-766.

[36] G. Q. Li and H. Suito: Electrochemical measurement of critical supersaturation in Fe-O-M (M=Al, Si, and Zr) and Fe-O-Al-M (M=C, Mn, Cr, Si, and Ti) melts by solid electrolyte galvanic cell. *ISIJ International* **37** (8) (1997) 762-769.

[37] J. Lee and K. Morita: Interfacial reaction of nitrogen with molten iron: a theoretical study. *Scandinavian Journal of Metallurgy* **34** (2) (2005) 131-136.

[38] H. Ono, H. Fukagawa, K. Morita and N. Sano: Effects of O, Se, and Te on the rate of nitrogen dissolution in molten iron. *Metallurgical and Materials Transactions B* **27** (5) (1996) 848-853.

[39] R. J. Fruehan and L. J. Martonik: The rate of absorption of nitrogen into liquid-iron containing oxygen and sulfur. *Metallurgical Transactions B* **11** (4) (1980) 615-621.

[40] S. Banya, F. Ishii, Y. Iguchi and T. Nagasaka: Rate of nitrogen desorption from liquid iron-carbon and iron-chromium alloys with argon. *Metallurgical Transactions B* **19** (2) (1988) 233-242.

[41] M. Byrne and G. R. Belton: Studies of the interfacial kinetics of the reaction of nitrogen with liquid-iron by the N-15-N-14 isotope exchange-reaction. *Metallurgical Transactions B* **14** (3) (1983) 441-449.

[42] P. C. Glaws and R. J. Fruehan: The kinetics of the nitrogen reaction with liquid iron-sulfur alloys. *Metallurgical Transactions B* **16** (3) (1985) 551-559.

[43] G. R. Belton: The interplay between strong adsorption of solutes and interfacial kinetics at the liquid-metal surface. *Canadian Metallurgical Quarterly* **21** (2) (1982) 137-143.

[44] G. R. Belton and R. W. H. Medalist: How fast can we go - The status of our knowledge of the rates of gas-liquid metal reactions. *Metallurgical Transactions B* **24** (2) (1993) 241-258.

[45] H. Ohta and H. Suito: Effect of sulfur and oxygen on engulfment and pushing of deoxidation particles of ZrO_2 and Al_2O_3 during solidification of Fe-10mass%Ni alloy. *ISIJ International* **46** (4) (2006) 472-479.

[46] K. Nakashima and K. Mori: Interfacial properties of liquid iron alloys and liquid slags relating to iron- and steel-making processes. *ISIJ International* **32** (1) (1992) 11-18.

[47] J. Tanabe and H. Suito: Effect of sulfur on supersaturation in aluminum deoxidized liquid-iron. *Steel Research* **66** (4) (1995) 146-153.

[48] Q. Jiang, D. S. Zhao and M. Zhao: Size-dependent interface energy and related interface stress. *Acta Materialia* **49** (16) (2001) 3143-3147.

[49] H. Suito and H. Ohta: Characteristics of particle size distribution in early stage of deoxidation. *ISIJ International* **46** (1) (2006) 33-41.

[50] C. Wert and C. Zener: Interference of growing spherical precipitate particles. *Journal of Applied Physics* **21** (1) (1950) 5-8.

[51] U. Lindborg and K. Torssell: A collision model for growth and separation of deoxidation products. *Transactions of the Metallurgical Society of Aime* **242** (1) (1968) 94-102.

[52] T. Hong, T. Debroy, S. S. Babu and S. A. David: Modeling of Inclusion Growth and Dissolution in the Weld Pool. *Metallurgical and Materials Transactions B* **31** (1) (2000) 161-169.

[53] H. Ohta and H. Suito: Effects of dissolved oxygen and size distribution on particle coarsening of deoxidation product. *ISIJ International* **46** (1) (2006) 42-49.

[54] A. Einstein: Investigations on the Theory of Brownian Movement, R. Fürth (ed.), Dover Publication, New York, NY, (1956), 1-18.

[55] Du Sichen: Improving process design in steelmaking, in: Fundamentals of Metallurgy, S. Seetharaman (ed.), Woodhead Publishing, Cambridge, UK, (2005), 392-393.

[56] D. Y. Sheng, M. Söder, P. Jonsson and L. Jonsson: Modeling micro-inclusion growth and separation in gas-stirred ladles. *Scandinavian Journal of Metallurgy* **31** (2) (2002) 134-147.

[57] M. Söder, P. Jonsson and L. Jonsson: Inclusion growth and removal in gas-stirred ladies. *Steel Research International* **75** (2) (2004) 128-138.

[58] H. Shibata, H. Yin and T. Emi: The capillary effect promoting collision and agglomeration of inclusion particles at the inert gas-steel interface. *Philosophical Transactions of the Royal Society of London - Series A* **356** (1998) 957-966.

[59] H. Yin, H. Shibata, T. Emi and M. Suzuki: "In-situ" observation of collision, agglomeration and cluster formation of alumina inclusion particles on steel melts. *ISIJ International* **37** (10) (1997) 936-945.

[60] H. Yin, H. Shibata, T. Emi and M. Suzuki: Characteristics of agglomeration of various inclusion particles on molten steel surface. *ISIJ International* **37** (10) (1997) 946-955.

[61] D. D. Eberl, V. A. Drits and J. Srodon: Deducing growth mechanisms for minerals from the shapes of crystal size distributions. *American Journal of Science* **298** (6) (1998) 499-533.

[62] Z. Kozisek and P. Demo: Size distribution of nuclei formed by homogeneous nucleation in closed systems. *Journal of Aerosol Science* **40** (1) (2009) 44-54.

[63] J. Zhang and H. G. Lee: Numerical modeling of nucleation and growth of inclusions in molten steel based on mean processing parameters. *ISIJ International* **44** (10) (2004) 1629-1638.

[64] L. F. Zhang and W. Pluschkell: Nucleation and growth kinetics of inclusions during liquid steel deoxidation. *Ironmaking & Steelmaking* **30** (2) (2003) 106-110.

[65] H. Ohta and H. Suito: Characteristics of particle size distribution of deoxidation products with Mg, Zr, Al, Ca, Si/Mn and Mg/Al in Fe-10mass%Ni alloy. *ISIJ International* **46** (1) (2006) 14-21.

[66] K. Beskow and Du Sichen: Experimental study of the nucleation of alumina inclusions in liquid steel. *Scandinavian Journal of Metallurgy* **32** (6) (2003) 320-328.

[67] M. Wakoh and N. Sano: Behavior of alumina inclusions just after deoxidation. *ISIJ International* **47** (5) (2007) 627-632.

[68] M. Söder, P. Jonsson and J. Alexis: Most relevant mechanisms of inclusion growth in an induction-stirred ladle. *Scandinavian Journal of Metallurgy* **31** (3) (2002) 210-220.

[69] A. Karasev and H. Suito: Quantitative evaluation of inclusion in deoxidation of Fe-10 mass pct Ni alloy with Si, Ti, Al, Zr, and Ce. *Metallurgical and Materials Transactions B* **30** (2) (1999) 249-257.

[70] T. B. Braun, J. F. Elliott and M. C. Flemings: Clustering of alumina inclusions. *Metallurgical Transactions B* **10** (2) (1979) 171-184.

[71] M. Söder: Growth and removal of inclusions during ladle refining, Ph. D. Thesis, KTH Royal Institute of Technology, Stockholm, (2004).

[72] A. Karasev and H. Suito: Analysis of size distributions of primary oxide inclusions in Fe-10 mass pct Ni-*M* (*M* = Si, Ti, Al, Zr, and Ce) alloy. *Metallurgical and Materials Transactions B* **30** (2) (1999) 259-270.

[73] Y. Miki and B. G. Thomas: Modeling of inclusion removal in a tundish. *Metallurgical and Materials Transactions B* **30** (4) (1999) 639-654.

[74] Y. J. Kwon, J. Zhang and H. G. Lee: A CFD-based nucleation-growth-removal model for inclusion behavior in a gas-agitated ladle during molten steel deoxidation. *ISIJ International* **48** (7) (2008) 891-900.

[75] A. D. Randolph and M. A. Larson: Theory of particulate processes, Academic Press, New York, NY, (1971).

[76] B. D. Marsh: Crystal size distribution (CSD) in rocks and the kinetics and dynamics of crystallization. 1. Theory. *Contributions to Mineralogy and Petrology* **99** (3) (1988) 277-291.

[77] B. D. Marsh: On the interpretation of crystal size distributions in magmatic systems. *Journal of Petrology* **39** (4) (1998) 553-599.

[78] K. V. Cashman and B. D. Marsh: Crystal size distribution (CSD) in rocks and the kinetics and dynamics of crystallization. 2. Makaopuhi lava lake. *Contributions to Mineralogy and Petrology* **99** (3) (1988) 292-305.

[79] J. D. Blower, J. P. Keating, H. M. Mader and J. C. Philips: The evolution of bubble size distributions in volcanic eruptions. *Journal of Volcanology and Geothermal Research* **120** (1-2) (2003) 1-23.

[80] M. D. Higgins: Origin of anorthosite by textural coarsening: Quantitative measurements of a natural sequence of textural development. *Journal of Petrology* **39** (7) (1998) 1307-1323.

[81] B. J. Mccoy: A new population balance model for crystal size distributions: Reversible, size-dependent growth and dissolution. *Journal of Colloid and Interface Science* **240** (1) (2001) 139-149.

[82] D. D. Eberl, D. E. Kile and V. A. Drits: On geological interpretations of crystal size distributions: constant vs. proportionate growth. *American Mineralogist* **87** (8-9) (2002) 1235-1241.

[83] D. E. Kile and D. D. Eberl: On the origin of size-dependent and size-independent crystal growth: Influence of advection and diffusion. *American Mineralogist* **88** (10) (2003) 1514-1521.

[84] H. Cabane, D. Laporte and A. Provost: Experimental investigation of the kinetics of Ostwald ripening of quartz in silicic melts. *Contributions to Mineralogy and Petrology* **142** (3) (2001) 361-373.

[85] I. N. Bindeman: Fragmentation phenomena in populations of magmatic crystals. *American Mineralogist* **90** (11-12) (2005) 1801-1815.

[86] A. G. Simakin and I. N. Bindeman: Evolution of crystal sizes in the series of dissolution and precipitation events in open magma systems. *Journal of Volcanology and Geothermal Research* **177** (4) (2008) 997-1010.

[87] H. S. Kim, H. G. Lee and K. S. Oh: Evolution of size, composition, and morphology of primary and secondary inclusions in Si/Mn and Si/Mn/Ti deoxidized steels. *ISIJ International* **42** (12) (2002) 1404-1411.

[88] M. Suzuki, R. Yamaguchi, K. Murakami and M. Nakada: Inclusion particle growth during solidification of stainless steel. *ISIJ International* **41** (3) (2001) 247-256.

[89] H. Goto, K. Miyazawa and K. Tanaka: Effect of oxygen-content on size distribution of oxides in steel. *ISIJ International* **35** (3) (1995) 286-291.

[90] H. Goto, K. I. Miyazawa, W. Yamada and K. Tanaka: Effect of cooling rate on composition of oxides precipitated during solidification of steels. *ISIJ International* **35** (6) (1995) 708-714.

[91] M. Guo and H. Suito: Influence of dissolved cerium and primary inclusion particles of Ce_2O_3 and CeS on solidification behavior of Fe-0.20mass%C-0.02mass%P Alloy. *ISIJ International* **39** (7) (1999) 722-729.

[92] H. Ohta and H. Suito: Dispersion Behavior of MgO, ZrO_2, Al_2O_3,CaO-Al_2O_3 and MnO-SiO_2 deoxidation particles during solidification of Fe-10mass%Ni alloy. *ISIJ International* **46** (1) (2006) 22-28.

[93] H. Ohta and H. Suito: Precipitation and dispersion control of MnS by deoxidation products of ZrO_2, Al_2O_3, MgO and MnO-SiO_2 particles in Fe-10mass%Ni alloy. *ISIJ International* **46** (4) (2006) 480-489.

[94] S. C. Park, I. H. Jung, K. S. Oh and H. G. Lee: Effect of Al on the evolution of non-metallic inclusions in the Mn-Si-Ti-Mg deoxidized steel during solidification: experiments and thermodynamic calculations. *ISIJ International* **44** (6) (2004) 1016-1023.

[95] H. Goto, K. Miyazawa and T. Kadoya: Effect of the composition of oxide on the reaction between oxide and sulfur during solidification of steels. *ISIJ International* **35** (12) (1995) 1477-1482.

[96] H. Gaye, P. Rocabois, J. Lehmann and M. Bobadilla: Kinetics of inclusion precipitation during steel solidification. *Steel Research* **70** (8-9) (1999) 356-361.

[97] J. Lehmann, P. Rocabois and H. Gaye: Kinetic model of non-metallic inclusions' precipitation during steel solidification. *Journal of Non-Crystalline Solids* **282** (1) (2001) 61-71.

[98] P. Rocabois, J. Lehmann, H. Gaye and M. Wintz: Kinetics of precipitation of non-metallic inclusions during solidification of steel. *Journal of Crystal Growth* **198/199** (1999) 838-843.

[99] M. Wintz, M. Bobadilla, J. Lehmann and H. Gaye: Experimental study and modeling of the precipitation of non-metallic inclusions during solidification of steel. *ISIJ International* **35** (6) (1995) 715-722.

[100] Z. Z. Liu, J. Wei and K. K. Cai: A coupled mathematical model of microsegregation and inclusion precipitation during solidification of silicon steel. *ISIJ International* **42** (9) (2002) 958-963.

[101] Z. T. Ma and D. Janke: Characteristics of oxide precipitation and growth during solidification of deoxidized steel. *ISIJ International* **38** (1) (1998) 46-52.

[102] S. S. Babu, S. A. David, J. M. Vitek, K. Mundra and T. Debroy: Development of macrostructure and microstructure of carbon-manganese low-alloy steel welds - inclusion formation. *Materials Science and Technology* **11** (2) (1995) 186-199.

[103] S. S. Babu, S. A. David, J. M. Vitek, K. Mundra and T. Debroy: Model for inclusion formation in low alloy steel welds. *Science and Technology of Welding and Joining* **4** (5) (1999) 276-284.

[104] D. J. Dyson, A. J. Rose, M. M. Whitwood and D. P. Wilcox: Studies in development of clean steels - Part 2 Use of chemical analyses. *Ironmaking & Steelmaking* **25** (4) (1997) 279-286.

[105] K. Sasai and Y. Mizukami: Reoxidation behavior of molten steel in tundish. *ISIJ International* **40** (1) (2000) 40-47.

[106] T. Emi, W. M. Boorstein and R. D. Pehlke: Absorption of gaseous oxygen by liquid iron. *Metallurgical Transactions* **5** (9) (1974) 1959-1966.

[107] T. Emi and R. D. Pehlke: The kinetics of oxidation of iron-silicon and iron-aluminum alloy melts by pure oxygen and oxygen-bearing gases. *Metallurgical Transactions B* **6** (1) (1975) 95-101.

[108] K. Sasai and Y. Mizukami: Effects of tundish cover powder and teeming stream on oxidation rate of molten steel in tundish. *ISIJ International* **38** (4) (1998) 332-338.

[109] K. Sasai and Y. Mizukami: Effect of stirring on oxidation rate of molten steel. *ISIJ International* **36** (4) (1996) 388-394.

[110] Y. Wang and S. Sridhar: Reoxidation on the surface of molten low-carbon aluminum-killed steel. *Steel Research International* **76** (5) (2005) 355-361.

[111] H. Sun and R. D. Pehlke: Kinetics of oxidation of carbon in liquid iron-carbon-silicon-manganese-sulfur alloys by carbon dioxide in nitrogen. *Metallurgical and Materials Transactions B* **26** (2) (1995) 335-344.

[112] H. Sun and R. D. Pehlke: Modeling and experimental study of gaseous oxidation of liquid iron alloys. *Metallurgical and Materials Transactions B* **27** (5) (1996) 854-864.

[113] L. Wang and C. Beckermann: Prediction of reoxidation inclusion composition in casting of steel. *Metallurgical and Materials Transactions B* **37** (4) (2006) 571-588.

[114] M. A. T. Andersson, L. T. I. Jonsson and P. G. Jönsson: A thermodynamic and kinetic model of reoxidation and desulphurisation in the ladle furnace. *ISIJ International* **40** (11) (2000) 1080-1088.

[115] B. Coletti, B. Gommers, C. Vercruyssen, B. Blanpain, P. Wollants and F. Haers: Reoxidation during ladle treatment. *Ironmaking & Steelmaking* **30** (2) (2003) 101-105.

[116] W. W. Huh and W. G. Jung: Effect of slag composition on reoxidation of aluminum killed steel. *ISIJ International* **36** (suppl) (1996) s136-s139.

[117] S. H. Kim and B. Song: Thermodynamic aspects of steel reoxidation behavior by the ladle slag system of CaO-MgO-SiO_2-Al_2O_3-Fe_tO-MnO-P_2O_5. *Metallurgical and Materials Transactions B* **30** (3) (1999) 435-442.

[118] H. Sun and K. Mori: Oxidation rate of aluminum in molten iron by CaO-SiO_2-Al_2O_3-FeO-MnO slag. *ISIJ International* **36** (suppl) (1996) s34-s37.

[119] H. Suito: Supersaturation and steel reoxidation by the slag. *Proc. The Ethem T. Turkdogan Symposium on Fundamentals and Analysis*

of New and Emerging Steelmaking Technologies, Pittsburgh, PA, May 15-17, (1994), The Iron and Steel Society, 141-152.

[120] D. C. Park, I. H. Jung, P. C. H. Rhee and H. G. Lee: Reoxidation of Al-Ti containing steels by $CaO-Al_2O_3-MgO-SiO_2$ slag. *ISIJ International* **44** (10) (2004) 1669-1678.

[121] H. Goto and K. Miyazawa: Reoxidation behavior of molten steel in non-killed and Al-killed steels. *ISIJ International* **38** (3) (1998) 256-259.

[122] J. Poirier, M. A. Guiban, P. Blumenfeld, M. Boher and P. Bourrier: Contribution of refractories to the steel quality and cleanliness. *La Revue de Métallurgie - Cahiers d'Informations Techniques* **97** (10) (2000) 1145-1159.

[123] M. A. Guibain, J. Poirier, J. De Lorgeril, V. Guyot, C. Diot, E. Hanse and P. Dumas: Development of new continuous casting refractories to reduce alumina clogging. *Proc. 26th McMaster Symposium on Iron and Steelmaking*, Hamilton, Canada, June 2-4, (1998).

[124] A. F. Dick, X. Yu, R. J. Pomfret and K. S. Coley: Attack of submerged entry nozzles by mould flux and dissolution of refractory oxides in the flux. *ISIJ International* **37** (2) (1997) 102-108.

[125] S. Riaz, K. C. Mills and K. Bain: Experimental examination of slag/refractory interface. *Ironmaking & Steelmaking* **29** (2) (2002) 107-113.

[126] G. J. Hassall, K. G. Bain, N. Jones and M. O. Warman: Modelling of ladle glaze interactions. *Ironmaking & Steelmaking* **29** (5) (2002) 383-389.

[127] K. Beskow, J. Jia, C. H. P. Lupis and Du Sichen: Chemical characteristics of inclusions formed at various stages during the ladle treatment of steel. *Ironmaking & Steelmaking* **29** (6) (2002) 427-435.

[128] K. Beskow, N. N. Tripathi, M. Nzotta, A. Sandberg and Du Sichen: Impact of slag-refractory lining reactions on the formation of inclusions in steel. *Ironmaking & Steelmaking* **31** (6) (2004) 514-518.

[129] K. Beskow and Du Sichen: Ladle glaze: major source of oxide inclusions during ladle treatment of steel. *Ironmaking & Steelmaking* **31** (5) (2004) 393-400.

[130] N. N. Tripathi, M. Nzotta, A. Sandberg and Du Sichen: Effect of ladle age on formation of non-metallic inclusions in ladle treatment. *Ironmaking & Steelmaking* **31** (3) (2004) 235-240.

[131] I. H. Jung, J. H. Son, S. M. Jung, H. Gaye and H. G. Lee: Formation of non-metallic inclusions by ladle glaze. *Proc. The 4th International Congress on the Science and Technology of Steelmaking*, Gifu, Japan, October 6-8, (2008), The Iron and Steel Institute of Japan, 395-398.

[132] J. H. Son, I. H. Jung, S. M. Jung, H. Gaye and H. G. Lee: Chemical reaction of glazed refractory with Al-deoxidized molten steel. *ISIJ International* **48** (11) (2008) 1542-1551.

[133] M. Thunman, J. Gran and Du Sichen: Impact of slag-refractory reaction on the formation of non-metallic inclusions. *Proc. The 4th International Congress on the Science and Technology of Steelmaking*, Gifu, Japan, October 6-8, (2008), The Iron and Steel Institute of Japan, 391-394.

[134] F. Fuhr, G. Torga, F. Medina and C. Cicutti: Application of slag tracers to investigate source of non-metallic inclusions. *Ironmaking & Steelmaking* **34** (6) (2007) 463-470.

[135] I. H. Jung, J. H. Son, S. M. Jung, H. Gaye and H. G. Lee: Influence of ladle glaze on steel cleanliness during ladle treatments. (in preparation).

[136] Y. B. Kang, H. S. Kim, J. Zhang and H. G. Lee: Practical application of thermodynamics to inclusions engineering in steel. *Journal of Physics and Chemistry of Solids* **66** (2-4) (2005) 219-225.

[137] S. Mizoguchi and J. I. Takamura: Control of oxides as inoculants. *Proc. Sixth International Iron and Steel Congress*, Nagoya, Japan, October 21-26, (1990), Iron and Steel Institute of Japan, 598-604.

[138] J. I. Takamura and S. Mizoguchi: Roles of oxides in steels performance. *Proc. Sixth International Iron and Steel Congress*, Nagoya, Japan, October 21-26, (1990), Iron and Steel Institute of Japan, 591-597.

[139] D. S. Sarma, A. V. Karasev and P. G. Jönsson: On the role of non-metallic inclusions in the nucleation of acicular ferrite in steels. *ISIJ International* **49** (7) (2009) 1063-1074.

[140] I. Sunagawa: Crystals: growth, morphology, and perfection, Cambridge University Press, Cambridge, UK, (2005), 10-19.

[141] X. Y. Liu, E. S. Boek, W. J. Briels and P. Bennema: Prediction of crystal growth morphology based on structural analysis of the solid-fluid interface. *Nature* **374** (1995) 342-345.

[142] Z. Berkovitch-Yellin, I. Weissbuch and L. Leiserowitz: Ab initio derivation of crystal morphology, in: Morphology and growth unit of crystals, I. Sunagawa (ed.), Terra Scientific Publishing, Tokyo, (1989), 247-278.

[143] Encyclopedia of Surface and Colloid Science, P. Somasundaran (ed.) 2nd Ed., CRC Press, Boca Raton, FL, (2006), 1075-1076.

[144] I. Sunagawa: Growth histories of mineral crystals as seen from their morphological features, in: Crystal growth technology, K. Byrappa and T. Ohachi (eds.), William Andrew Inc., Norwich, NY, (2002), 1-23.

[145] M. Giulietti, M. M. Seckler, S. Derenzo, M. I. Ré and E. Cekinski: Industrial crystallization and precipitation from solutions: state of the technique. *Brazilian Journal of Chemical Engineering* **18** (4) (2001) 423-440.

[146] M. Kitamura and I. Sunagawa: Role of a spiral with negative curvature in growth of a polyhedral crystal, in: Morphology and growth unit of crystals, I. Sunagawa (ed.), Terra Scientific Publishing, Tokyo, (1989), 279-286.

[147] W. Kossel: Zur theorie des kristallwachstums. *Nachrichten von der Gesellschaft der Wissenschaften zu Göttingen* **2** (1927) 135-143.

[148] I. N. Stranski: Zur theorie des kristallwachstums. *Zeitschrift fur Physikalische Chemie* **136** (1928) 259-278.

[149] W. K. Burton, N. Cabrera and F. C. Frank: The growth of crystals and the equilibrium structure of their surfaces. *Philosophical Transactions of the Royal Society of London - Series A* **243** (866) (1951) 299-358.

[150] T. Ohachi and I. Taniguchi: Thermal evolution of crystal shapes on alpha-Ag_2S, in: Morphology and growth unit of crystals, I. Sunagawa (ed.), Terra Scientific Publishing, Tokyo, (1989), 203-217.

[151] M. C. Desjonquères and D. Spanjaard: Concepts in surface physics, 2nd Ed., Springer, Berlin, (1996), 15-16, 41.

[152] C. Borchert, N. Nere and D. Ramkrishna: Modeling of the Evolution of Crystal Morphologies in Crystallizers. Presentation at ERC seminar series, School of Chemical Engineering, Purdue University, April 6, 2007.

[153] C. Borchert, N. Nere, D. Ramkrishna, A. Voigt and K. Sundmacher: On the prediction of crystal shape distributions in a steady-state continuous crystallizer. *Chemical Engineering Science* **64** (4) (2009) 686-696.

[154] R. Docherty and P. Meenan: The study of Molecular Materials using computational chemistry, in: Molecular modeling applications in crystallization, A. M. Myerson (ed.), Cambridge University Press, Cambridge, UK, (1999), 125-127.

[155] P. Bennema, H. Meekes and W. J. P. Van Enckevort: Crystal growth and morphology: a multi-faceted approach, in: Growth, dissolution, and pattern formation in geosystems, B. Jamtveit and P. Meakin (eds.), Kluwer Academic Publishers, Dordrecht, The Netherlands, (1999), 21-64.

[156] P. Bennema: On the crystallographic and statistical mechanical foundations of the forty-year old Hartman-Perdok theory. *Journal of Crystal Growth* **166** (1-4) (1996) 17-28.

[157] P. Hartman: Sur la morphologie des cristaux. *Bulletin de Minéralogie* **101** (1978) 195-201.

[158] Z. Berkovitch-Yellin: Toward an ab initio derivation of crystal morphology. *Journal of the American Chemical Society* **107** (26) (1985) 8239-8253.

[159] P. Di Martino, R. Censi, L. Malaj, D. Capsoni, V. Massarotti and S. Martelli: Influence of solvent and crystallization method on the crystal habit of metronidazole. *Crystal Research and Technology* **42** (8) (2007) 800-806.

[160] N. Blagden: Crystal growth: from the classical to molecular description, in: Crystal engineering: the design and application of functional solids, K. R. Seddon and M. Zaworotko (eds.), Kluwer Academic Publishers, Dordrecht, The Netherlands, (1999), 138-145.

[161] K. Okohira, N. Sato and H. Mori: Observation of three-dimensional shapes of inclusions in low-carbon aluminum-killed steel by scanning electron microscope. *Transactions ISIJ* **14** (1974) 102-109.

[162] E. Steinmetz and H. U. Lindenberg: Morphology of inclusions at aluminum deoxidation. *Archiv Fur Das Eisenhuttenwesen* **47** (4) (1976) 199-204.

[163] E. Steinmetz and H. U. Lindenberg: Oxide morphology at manganese and manganese-silicon deoxidation. *Archiv Fur Das Eisenhuttenwesen* **47** (2) (1976) 71-76.

[164] E. Steinmetz, H. U. Lindenberg, W. Morsdorf and P. Hammerschmid: Growth shapes of aluminum-oxides in steels. *Archiv Fur Das Eisenhuttenwesen* **48** (11) (1977) 569-574.

[165] E. Steinmetz, H. U. Lindenberg, W. Morsdorf and P. Hammerschmid: Shapes and formation of aluminum-oxides in raw ingots and continuously cast slabs. *Stahl Und Eisen* **97** (23) (1977) 1154-1159.

[166] S. W. Robinson, I. W. Martin and F. B. Pickering: Formation of alumina in steel and its dissemination during mechanical working. *Metals Technology* **6** (May) (1979) 157-169.

[167] E. Steinmetz, H. U. Lindenberg, P. Hammerschmid and W. Glitscher: Formation of oxides in aluminum deoxidized steel melts with re-oxidation processes. *Stahl Und Eisen* **103** (11) (1983) 539-545.

[168] E. Steinmetz and C. Andreae: Influence of oxygen on the formation of aluminum-oxides in iron heats. *Steel Research* **62** (2) (1991) 54-59.

[169] W. Tiekink, J. Brockhoff and J. Van Der Stel: Morphology of alumina during deoxidation and slab casting of IF and DDQ steel grades. *Proc. 4th International Conference on Clean Steel*, Balatonszeplak, Hungary, June 8-10, (1992), 704-717.

[170] W. Tiekink, A. Pieters and J. Hekkema: Al_2O_3 in steel - Morphology dependent on treatment. *Proc. 77th Steelmaking Conference/123rd AIME Annual Meeting*, Chicago, Il, Mar 20-23, (1994), Iron & Steel Soc Aime, 423-427.

[171] R. Dekkers: Non-metallic inclusions in liquid steel, Ph. D. Thesis, Katholieke Universiteit Leuven, Leuven, (2002).

[172] R. Dekkers, B. Blanpain, P. Wollants, F. Haers, C. Vercruyssen and B. Gommers: Non-metallic inclusions in aluminium killed steels. *Ironmaking & Steelmaking* **29** (6) (2002) 437-444.

[173] R. Dekkers, B. Blanpain and P. Wollants: Crystal growth in liquid steel during secondary metallurgy. *Metallurgical and Materials Transactions B* **34** (2) (2003) 161-171.

[174] H. M. Pielet, H. T. Tsai and R. T. Gass: Characterization of inclusions in TiSULC steels from degasser to mold. *Proc. ISSTech Conference*, Indianapolis, USA, April 27-30, (2003), The Iron and Steel Society, 241-255.

[175] W. Tiekink, R. Boom, A. Overbosch, J. Landskroon and B. Deo: Initial stages of alumina formation. *Proc. 7th Int. Conf. on Clean Steel*, Balatonfured, Hungary, June 4-6, (2007), Hungarian Mining and Metall. Soc., 48-57.

[176] P. Patnaik: Handbook of inorganic chemicals, McGraw-Hill, New York, NY, (2002), 11.

[177] M. C. Flemings: Solidification processing. *Metallurgical Transactions* **5** (10) (1974) 2121-2134.

[178] T. Z. Kattamis, J. C. Coughlin and M. C. Flemings: Influence of coarsening on dendrite arm spacing of aluminum-copper alloys. *Transactions of The Metallurgical Society of AIME* **239** (10) (1967) 1504-1511.

[179] K. Wasai, K. Mukai and A. Miyanaga: Observation of inclusion in aluminum deoxidized iron. *ISIJ International* **42** (5) (2002) 459-466.

[180] W. Ostwald: Studies upon forming and changing solid bodies. *Zeitschrift für Physikalische Chemie* **22** (1897) 289-330.

[181] I. N. Stranski and D. Totomanow: Rate of formation of (crystal) nuclei and the Ostwald step rule. *Zeitschrift für Physikalische Chemie* **163** (1933) 399-408.

[182] K. Wasai and K. Mukai: Thermodynamic analysis on metastable alumina formation in aluminum deoxidized iron based on Ostwald's step rule and classical homogeneous nucleation theories. *ISIJ International* **42** (5) (2002) 467-473.

[183] J. H. Adair, S. B. Cho, N. S. Bell and A. J. Perrotta: Recent developments in morphological control of α-Al_2O_3 particles synthesized in 1,4-butanediol solution. *Journal of Dispersion Science and Technology* **22** (2&3) (2001) 143-165.

[184] D. M. Stefanescu: Science and engineering of casting solidification, 2nd Ed., Springer, New York, NY, (2009), 177-183.

[185] J. S. Langer: Instabilities and pattern formation in crystal growth. *Reviews of Modern Physics* **52** (1) (1980) 1-28.

[186] Y. Wang, S. Sridhar, A. W. Cramb, A. Gomez and C. Cicutti: Reoxidation of low-carbon, aluminum-killed steel. *Iron & steel technology* **1** (2) (2004) 87-96.

[187] P. Kaushik, D. Kruse and M. Ozgu: Assessment of castability issues in interstitial-free (IF) steels. *La Revue de Métallurgie - Cahiers d'Informations Techniques* **105** (2) (2008) 92-101.

[188] M. Burty, L. Peeters, E. Perrin, S. Münzer, P. Colucci, D. Salvadori, F. Schadow, J. M. Valcarcel and J. Claes: Some keys to reach long-sequence casting. *La Revue de Métallurgie - Cahiers d'Informations Techniques* **192** (11) (2005) s119-s127.

[189] E. T. Turkdogan: Physical chemistry of high temperature technology, Academic Press, New York, NY, (1980), 7.

[190] F. E. Huggins, G. P. Huffman and R. J. Lee: Scanning electron microscope based automated image analysis (SEM-AIA) and Mossbauer-spectroscopy - quantitative characterization of coal minerals. *ACS Symposium series* **205** (1982) 239-258.

[191] K. H. Friedrichs: Electron microscopic analyses of dust from the lungs and the lymph nodes of talc-mine employees. *American Industrial Hygiene Association Journal* **48** (7) (1987) 626-633.

[192] C. Q. Yin and D. L. Johnson: An individual particle analysis and budget study of Onondaga lake-sediments. *Limnology and Oceanography* **29** (6) (1984) 1193-1201.

[193] A. Schwoeble, A. Dalley, B. Henderson and G. Casucco: Computer-controlled SEM and microimaging of fine particles. *Journal of Metals* **40** (8) (1988) 11-14.

[194] M. D. Higgins: Measurement of crystal size distributions. *American Mineralogist* **85** (9) (2000) 1105-1116.

[195] CSD Corrections 1.3 (Les Sciences de la Terre à l'UQAC): http://geologie.uqac.ca/~mhiggins/csdcorrections.html (accessed October 2009).

[196] M. D. Higgins: Closure in crystal size distributions (CSD), verification of CSD calculations, and the significance of CSD fans. *American Mineralogist* **87** (1) (2002) 171-175.

[197] Lognormal distributions: Theory and applications, E. L. Crow and K. Shimizu (eds.), Marcel Dekker Inc., New York, NY, (1988), 9.

[198] E. L. Limpert, W. A. Stahel and M. Abbt: Log-normal distributions across the sciences: keys and clues. *BioScience* **51** (5) (2001) 341-352.

[199] D. L. Turcotte: Fractals and chaos in geology and geophysics, 2nd Ed., Cambridge University Press, Cambridge, (1997), 35-40.

[200] J. J. Pak, J. O. Jo, S. I. Kim, W. Y. Kim, T. I. Chung, S. M. Seo, J. H. Park and D. S. Kim: Thermodynamics of titanium and oxygen dissolved in liquid iron equilibrated with titanium oxides. *ISIJ International* **47** (1) (2007) 16-24.

[201] W. Y. Cha, D. S. Kim, Y. D. Lee and J. J. Pak: A thermodynamic study on the inclusion formation in ferritic stainless steel melt. *ISIJ International* **44** (7) (2004) 1134-1139.

[202] G. Auclair, R. Meilland and F. Meyer: Methods for assessment of cleanliness in superclean steels. Application to bearing steels. *La Revue de Métallurgie - Cahiers d'Informations Techniques* **93** (1) (1996) 119-130.

[203] R. Inoue, T. Ariyama and H. Suito: Extraction and evaluation of inclusion particles in steel. *Proc. Asia Steel International Conference 2009*, Busan, Korea, 24-27 May, (2009), s11-16.

[204] M. Kawakami, S. Yokoyama, K. Takagi, M. Nishimura and J. S. Kim: Effect of aluminum and oxygen content on diffusivity of aluminum in molten iron. *ISIJ International* **37** (5) (1997) 425-431.

[205] B. Deo and R. Boom: Fundamentals of steelmaking metallurgy, Prentice Hall International, New York, NY, (1993), 124-127.

[206] T. A. Engh: Principles of Metal Refining, Oxford University Press, Oxford, (1992), 223-228.

[207] S. Sanyal, S. Chandra, S. Kumar and G. G. Roy: An improved model of cored wire injection in steel melts. *ISIJ International* **44** (7) (2004) 1157-1166.

[208] R. B. Bird, W. E. Stewart and E. N. Lightfoot: Transport Phenomena, 2nd Ed., John Wiley & Sons, New York, NY, (2002), 349.

[209] R. B. Bird, W. E. Stewart and E. N. Lightfoot: Transport Phenomena, 2nd Ed., John Wiley & Sons, New York, NY, (2002), 376-378.

[210] H. S. Carslaw and J. C. Jaeger: Conduction of heat in solids, 2nd Ed., Oxford University Press, Oxford, UK, (1959), 200.

[211] L. Pandelaers, F. Verhaeghe, B. Blanpain and P. Wollants: Interfacial reactions during the dissolution of titanium in liquid iron. *Proc. Defect and Diffusion Forum*, (2008), Trans Tech Publications, 467-473.

[212] L. Pandelaers, F. Verhaeghe, P. Gardin, D. Barrier, B. Blanpain and P. Wollants: The dissolution behavior of titanium in liquid steel under varying convection conditions and analysis of the reaction zone development between titanium and the solidified steel shell. *Proc. AISTech*, St. Louis, MO, USA, 4-7 May, (2009), 937-947.

[213] L. Pandelaers, F. Verhaeghe, B. Blanpain, P. Wollants and P. Gardin: Interfacial reactions during titanium dissolution in liquid iron: a combined experimental and modeling approach. *Metallurgical and Materials Transactions B* **40** (5) (2009) 676-684.

[214] S. Sanyal, J. K. Saha, S. Chandra and C. Bhanu: Model based optimisation of aluminium wire injection in steel melts. *ISIJ International* **46** (5) (2006) 779-781.

[215] U. R. Kettner: Binary alloy phase diagrams, T. B. Massalski (ed.) 2nd Ed., ASM International, Materials Park, OH, (1990), 147.

[216] M. Palm: Concepts derived from phase diagram studies for the strengthening of Fe-Al-based alloys. *Intermetallics* **13** (12) (2005) 1286-1295.

[217] M. Hansen: Constitution of Binary Alloys, 2nd Ed., MacGraw-Hill, New York, NY, (1958), 90-95.

[218] H. R. Shahverdi, M. R. Ghomashchi, S. Shabestari and J. Hejazi: Microstructural analysis of interfacial reaction between molten aluminium and solid iron. *Journal of Materials Processing Technology* **124** (3) (2002) 345-352.

[219] O. Kubaschewski: Iron-binary phase diagrams, Springer, Berlin, (1982), 5-9.

[220] A. Bouayad, C. Gerometta, A. Belkebir and A. Ambari: Kinetic interactions between solid iron and molten aluminium. *Materials Science and Engineering A* **363** (1-2) (2003) 53-61.

[221] K. Bouché, F. Barbier and A. Coulet: Intermetallic compound layer growth between solid iron and molten aluminium. *Materials Science and Engineering A* **249** (1-2) (1998) 167-175.

[222] H. R. Shahverdi, M. R. Ghomashchi, S. Shabestari and J. Hejazi: Kinetics of interfacial reaction between solid iron and molten aluminium. *Journal of Materials Science* **37** (5) (2002) 1061-1066.

[223] V. I. Dybkov: Interaction of 18Cr-10Ni Stainless-Steel with Liquid Aluminum. *Journal of Materials Science* **25** (8) (1990) 3615-3633.

[224] T. Sasaki and T. Yakou: Features of intermetallic compounds in aluminized steels formed using aluminum foil. *Surface & Coatings Technology* **201** (6) (2006) 2131-2139.

[225] Y. J. Li, Y. L. Zhang and Y. X. Liou: Characteristics of phase constitution in the Fe-Al alloy layer of calorized steel pipe. *Journal of Materials Science* **30** (10) (1995) 2635-2639.

[226] S. Kobayashi and T. Yakou: Control of intermetallic compound layers at interface between steel and aluminum by diffusion-treatment. *Materials Science and Engineering A* **338** (1-2) (2002) 44-53.

[227] Y. J. Li, J. Wang and X. Holly: X-ray diffraction and TEM analysis of Fe-Al alloy layer in coating of new hot dip aluminised steel. *Materials Science and Technology* **19** (5) (2003) 657-660.

[228] T. Sasaki and T. Yakou: Effects of heat treatment conditions on formation of Fe-Al alloy layer during high temperature aluminizing. *ISIJ International* **47** (7) (2007) 1016-1022.

[229] T. Sasaki and T. Yakou: Tool wear and surface roughness during machining of high-temperature aluminized steel. *Journal of Materials Processing Technology* **197** (1-3) (2008) 89-95.

[230] F. A. Elrefaie and W. W. Smeltzer: Thermodynamics of the system iron-aluminum-oxygen between 1073 K and 1573 K. *Metallurgical Transactions B* **14** (1983) 85-93.

[231] H. Itoh, M. Hino and S. Ban-Ya: Assessment of Al deoxidation equilibrium in liquid iron. *Tetsu-to-Hagané* **83** (12) (1997) 773-778.

[232] H. Yin: Inclusion characterization and thermodynamics for high-Al advanced high-strength steels. *Iron & Steel Technology* **3** (6) (2006) 64-73.

[233] Y. Kang, M. Thunman, Du Sichen, T. Morohoshi, K. Mizukami and K. Morita: Aluminum deoxidation equilibrium of molten iron-aluminum alloy with wide aluminum composition range at 1873 K. *ISIJ International* **49** (10) (2009) 1483-1489.

[234] A. A. Kodentsov, G. F. Bastin and F. J. J. Van Loo: The diffusion couple technique in phase diagram determination. *Journal of Alloys and Compounds* **320** (2) (2001) 207-217.

[235] F. P. Incropera and D. P. Dewitt: Fundamentals of Heat and Mass Transfer, 4th Ed., John Wiley, New York, (1996), 510.

[236] A. Lemembre and J.-P. Petit: Laminar natural convection in a laterally heated and upper cooled vertical cylindrical enclosure. *Journal of Heat and Mass Transfer* **41** (16) (1998) 2437-2454.

[237] D. M. Stefanescu: Science and engineering of casting solidification, 2nd Ed., Springer, New York, NY, (2009), 273-274.

[238] Y. Plevachuk, I. Egry, J. Brillo, D. Holland-Moritz and I. Kaban: Density and atomic volume in liquid Al-Fe and Al-Ni binary alloys. *International Journal of Materials Research* **98** (2) (2007) 107-111.

[239] J. Zollinger, J. Lapin, D. Daloz and H. Combeau: Influence of oxygen on solidification behaviour of cast TiAl-based alloys. *Intermetallics* **15** (10) (2007) 1343-1350.

[240] V. I. Dybkov: Interaction of iron-nickel alloys with liquid aluminium - Part II - Formation of intermetallics. *Journal of Materials Science* **35** (7) (2000) 1729-1736.

[241] J. W. Christian: The theory of transformations in metals and alloys - Part I Equilibrium and general kinetic theory, 2nd Ed., Pergamon, Oxford, UK, (1975), 448-457.

[242] E. Schroer, S. Hopfe, P. Werner, U. Gösele, G. Duscher, M. Rühle and T. Y. Tan: Oxide precipitation at silicon grain boundaries. *Applied Physics Letters* **70** (3) (1997) 327-329.

[243] E. T. Turkdogan: Fundamentals of Steelmaking, Institute of Materials (ed.), Cambridge University Press, London, UK, (1996), 134.

[244] T. Iida and R. I. L. Guthrie: The physical properties of liquid metals, Clarendon Press, Oxford, UK, (1993), 221.

[245] K. Mukai: Wetting and Marangoni effect in iron and steelmaking processes. *ISIJ International* **32** (1) (1992) 19-25.

[246] G. Kaptay: Classification and general derivation of interfacial forces, acting on phases, situated in the bulk, or at the interface of other phases. *Journal of Materials Science* **40** (9-10) (2005) 2125-2131.

[247] S. Kimura, Y. Nabeshima, K. Nakajima and S. Mizoguchi: Behavior of nonmetallic inclusions in front of the solid-liquid interface in low-carbon steels. *Metallurgical and Materials Transactions B* **31** (5) (2000) 1013-1021.

[248] H. B. Yin and T. Emi: Marangoni flow at the gas/melt interface of steel. *Metallurgical and Materials Transactions B* **34** (5) (2003) 483-493.

[249] Z. F. Yuan, W. L. Huang and K. Mukai: Local corrosion of magnesia-chrome refractories driven by Marangoni convection at the slag-metal interface. *Journal of Colloid and Interface Science* **253** (1) (2002) 211-216.

[250] T. A. Engh: Principles of Metal Refining, Oxford University Press, Oxford, (1992), 51 and 362.

[251] T. A. Engh: Principles of Metal Refining, Oxford University Press, Oxford, (1992), 362.

[252] R. B. Bird, W. E. Stewart and E. N. Lightfoot: Transport Phenomena, 2nd Ed., John Wiley & Sons, New York, NY, (2002), 617.

[253] T. C. Illingworth and I. O. Golosnoy: Numerical solutions of diffusion-controlled moving boundary problems which conserve solute. *Journal of Computational Physics* **209** (1) (2005) 207-225.

[254] S. Panda and S. E. Pratsinis: Modeling the synthesis of aluminum particles by evaporation-condensation in an aerosol flow reactor. *Nanostructured Materials* **5** (7-8) (1995) 755-767.

[255] C. W. Bale, E. Bélisle, P. Chartrand, S. A. Decterov, G. Eriksson, K. Hack, I. H. Jung, Y. B. Kang, J. Melançon, A. D. Pelton, C. Robelin and S. Petersen: FactSage thermochemical software and databases -- recent developments. *Calphad-Computer Coupling of Phase Diagrams and Thermochemistry* **33** (2) (2009) 295-311.

[256] Y. Wang and S. Sridhar: The effect of gas flow rate on the evolution of the surface oxide on a molten low carbon Al killed steel. *Journal of Materials Science* **40** (9-10) (2005) 2179-2184.

Appendix

A.1. Solution of the counter diffusion problem using Illingworth's approach

The governing equations, which were described in section 7.1.3 of Chapter 7, are:

$$\frac{\partial C_O}{\partial t} = D_O \frac{\partial^2 C_O}{\partial Z^2} \qquad 0 \le Z \le Z_r(t) \tag{A.1}$$

$$\frac{\partial C_{Al}}{\partial t} = D_{Al} \frac{\partial^2 C_{Al}}{\partial Z^2} \qquad Z_r(t) \le Z \le L \tag{A.2}$$

With appropriate initial and boundary conditions:
Initial conditions: $t = 0$, $Z > 0$:

$$\begin{cases} C_{Al}(Z,0) = C_{Al}^0 \\ C_O(Z,0) = 0 \\ Z_r(0) = 0 \end{cases} \tag{A.3}$$

Boundary conditions: $t > 0$:

$$Z = 0 : C_O(0,t) = C_O^{sat.} \tag{A.4}$$

$$Z = Z_r(t) : C_O = C_{Al} = 0 \tag{A.5}$$

$$Z = Z_r(t) : -\frac{1}{3} D_O \frac{\partial C_O}{\partial Z} = \frac{1}{2} D_{Al} \frac{\partial C_{Al}}{\partial Z} \tag{A.6}$$

Following Illingworth's approach [253], two new positional variables are introduced:

$$u(t)=\frac{Z}{Z_r(t)} \text{ and } v(t)=\frac{Z-Z_r(t)}{L-Z_r(t)}.$$

With this coordinate system, the region A defined between 0 and $Z_r(t)$ (diffusion region of oxygen) corresponds to $0 < u < 1$ and region B defined between $Z_r(t)$ and L (diffusion domain of aluminium) corresponds to $0 < v < 1$. At each time steps, the reaction front position is fixed at $u = 1$ and $v = 0$. Writing $p(u,t)$ as the O concentration in domain A (corresponding to $C_O(Z,t)$ in $0 < Z < Z_r(t)$) and $q(v,t)$ as the Al concentration in domain B (corresponding to $C_{Al}(Z,t)$ in $Z_r(t) < Z < L$), Eqs. (A.1) and (A.2) becomes:

$$Z_r(t)^2\frac{\partial p(u,t)}{\partial t}-uZ_r(t)\frac{dZ_r(t)}{dt}\frac{\partial p(u,t)}{\partial u}=D_O\frac{\partial^2 p(u,t)}{\partial u^2} \qquad 0<u<1 \qquad \text{(A.7)}$$

$$-(1-v)\left(L-Z_r(t)\right)\frac{dZ_r(t)}{dt}\frac{\partial q(v,t)}{\partial v}+\left(L-Z_r(t)\right)^2\frac{\partial q(v,t)}{\partial t}=D_{Al}\frac{\partial^2 q(v,t)}{\partial v^2} \qquad 0<v<1 \qquad \text{(A.8)}$$

Equation (A.7) becomes, using the identities $\frac{\partial(pu)}{\partial u}=p+u\frac{\partial p}{\partial u}$ and $\frac{\partial(pZ_r)}{\partial t}=p\frac{dZ_r}{dt}+Z_r\frac{\partial p}{\partial t}$:

$$\frac{\partial(pZ_r)}{\partial t}=\frac{dZ_r}{dt}\frac{\partial(pu)}{\partial u}+\frac{D_O}{Z_r}\frac{\partial^2(pu)}{\partial u^2} \qquad 0<u<1 \qquad \text{(A.9)}$$

Similarly, Eq. (A.8) becomes:

$$\frac{\partial\left(q(L-Z_r)\right)}{\partial t}=\frac{dZ_r}{dt}\frac{\partial\left(q(1-v)\right)}{\partial v}+\frac{D_{Al}}{L-Z_r}\frac{\partial^2(qv)}{\partial v^2} \qquad 0<v<1 \qquad \text{(A.10)}$$

The space coordinate u is discretised at N points. Equation (A.9) is integrated by the finite volume technique over one space step and one time step δt ($= t^{j+1} - t^{j}$), $u_{i\pm½}$ being the position midway between u_i and $u_{i\text{-}1}$.

$$\int_{u_{i-½}}^{u_{i+½}} \int_{t^j}^{t^{j+1}} \frac{\partial(pZ_r)}{\partial t} dt du = \int_{t^j}^{t^{j+1}} \int_{u_{i-½}}^{u_{i+½}} \left(\frac{dZ_r}{dt} \frac{\partial(pu)}{\partial u} + \frac{D_O}{Z_r} \frac{\partial^2(pu)}{\partial u^2} \right) du dt \qquad 0 < u < 1 \qquad \text{(A.11)}$$

The concentration and the reaction front position at u_i after a proportion σ of the time step has elapsed are written $p_i^{j+\sigma}$ and $Z_r^{j+\sigma}$, respectively. It follows:

$$\left(p_i^{j+1} Z_r^{j+1} - p_i^j Z_r^j\right)\left(\frac{u_{i+1} - u_{i-1}}{2}\right) = \frac{\delta t D_O}{Z_r^{j+\sigma}} \left(\frac{p_{i+1}^{j+\sigma} - p_i^{j+\sigma}}{u_{i+1} - u_i} - \frac{p_i^{j+\sigma} - p_{i-1}^{j+\sigma}}{u_i - u_{i-1}} \right) + \left(Z_r^{j+1} - Z_r^j\right)\left(p_{i+½}^{j+\sigma} u_{i+½} - p_{i-½}^{j+\sigma} u_{i-½}\right) \qquad \text{(A.12)}$$

Similarly, after integration and discretisation, Eq. (A.10) becomes:

$$\left(q_i^{j+1}\left(L - Z_r^{j+1}\right) - q_i^j\left(L - Z_r^j\right)\right)\left(\frac{v_{i+1} - v_{i-1}}{2}\right) = \frac{\delta t D_{Al}}{L - Z_r^{j+\sigma}} \left(\frac{q_{i+1}^{j+\sigma} - q_i^{j+\sigma}}{v_{i+1} - v_i} - \frac{q_i^{j+\sigma} - q_{i-1}^{j+\sigma}}{v_i - v_{i-1}} \right) + \left(Z_r^{j+1} - Z_r^j\right)\left(q_{i+½}^{j+\sigma}\left(1 - v_{i+½}\right) - q_{i-½}^{j+\sigma}\left(1 - v_{i-½}\right)\right) \qquad \text{(A.13)}$$

Equations (A.12) and (A.13) can be used to generate a set of finite difference approximations for the future compositions in regions A and B, for i = 1 to N - 2. For i = 0 and N - 1, the finite volume technique must be applied to the relevant boundary conditions. In the present problem definition, we impose that $C_{Al} = C_O = 0$ at the moving reaction front and $C_O = C_O^{sat.}$ at the melt surface (Z = 0), which turns into, respectively:

$$\begin{cases} u = 1 : p_{N-1}^{j+1} = 0 \\ v = 0 : q_0^{j+1} = 0 \\ u = 0 : p_0^{j+1} = C_O^{sat.} \end{cases} \tag{A.14}$$

At the fixed boundary $Z = L$, a zero flux is ensured by imposing that $\left.\frac{\partial q}{\partial v}\right|_{v=1} = 0$. Eq. (A.10) is integrated between $v_{N-½}$ and v_{N-1}. Doing so gives the following expression for $v = 1$ ($i = N - 1$):

$$\begin{aligned} &\left(q_{N-1}^{j+1}\left(L - Z_r^{j+1}\right) - q_{N-1}^{j}\left(L - Z_r^{j}\right)\right)\left(\frac{1 - v_{N-2}}{2}\right) = \\ &\qquad -\frac{\delta t D_{Al}}{L - Z_r^{j+1}}\left(\frac{q_{N-1}^{j+\sigma} - q_{N-2}^{j+\sigma}}{1 - v_{N-2}}\right) \\ &\qquad -\left(Z_r^{j+1} - Z_r^{j}\right) q_{(N-1)-½}^{j+\sigma}\left(1 - \frac{1 + v_{N-2}}{2}\right) \end{aligned} \tag{A.15}$$

Finally, Eq. (A.6) needs to be discretised to obtain the position of the moving reaction front at each time step:

$$-2\frac{D_O}{Z_r(t)}\left.\frac{\partial p}{\partial u}\right|_{u=1} = 3\frac{D_{Al}}{L - Z_r(t)}\left.\frac{\partial q}{\partial v}\right|_{v=0} \tag{A.16}$$

After integration, the latter gives the following relation:

$$2\frac{D_O}{Z_r^{j+\sigma}}\frac{p_{N-2}^{j+1}}{1 - u_{N-2}} = 3\frac{D_{Al}}{L - Z_r^{j+\sigma}}\frac{q_1^{j+1}}{v_1} \tag{A.17}$$

Or,

$$\frac{Z_r^{j+\sigma}}{L - Z_r^{j+\sigma}} - K\frac{p_{N-2}^{j+1}}{q_1^{j+1}} = 0 \tag{A.18}$$

where K is a constant given by $\frac{2}{3}\frac{D_O}{D_{Al}}\frac{v_1}{1 - u_{N-2}}$.

Equations (A.12), (A.13) and (A.17) form thus the set of equations for the diffusion problem described earlier, taking into account the finite dimension of the system. To solve these equations, one has to find adequate values at intermediate time ($j + \sigma$) and position ($i \pm ½$).

According to Illingworth, a fully implicit scheme ($\sigma = 1$) predict monotonic concentration profiles and gives an error proportional to δt. Concerns about non-monotonic (oscillating) solutions, a fully implicit up/down-wind approximation scheme was used for the intermediate concentrations $p_{i\pm½}^{j+\sigma}$ and $q_{i\pm½}^{j+\sigma}$. Such first order approximation schemes for space and time variations can generate smooth and non-oscillating concentration profiles.

If $Z_r^{j+1} > Z_r^j$ (positive interface velocity), $p_{i+½}^{j+\sigma} = p_{i+1}^{j+1}$, $q_{i+½}^{j+\sigma} = q_{i+1}^{j+1}$ and $p_{i-½}^{j+\sigma} = p_i^{j+1}$, $q_{i-½}^{j+\sigma} = q_i^{j+1}$. In case of negative interface velocity, i.e. $Z_r^{j+1} < Z_r^j$, the intermediate concentrations become $p_{i+½}^{j+\sigma} = p_i^{j+1}$, $q_{i+½}^{j+\sigma} = q_i^{j+1}$ and $p_{i-½}^{j+\sigma} = p_{i-1}^{j+1}$, $q_{i-½}^{j+\sigma} = q_{i-1}^{j+1}$.

As seen in the sets of equations and the previous analytical solution, the concentration profiles and the motion of the interface (or reaction front) are strongly coupled, inducing that the non-linear equations have to be solved simultaneously. An iterative method has to be developed, ensuring the convergence to the solution in an efficient way.

If estimates of Z_r^{j+1} are available, the diffusion equations (A.12) and (A.13) become linear and the values of the concentrations p_i^{j+1} and q_i^{j+1} can be calculated. The equation can be written in a tri-diagonal matrix, which can be inverted cheaply. The system of linear equations to solve is represented as follows:

$$A\begin{pmatrix} c_0^{j+1} \\ c_1^{j+1} \\ c_2^{j+1} \\ \dots \\ c_{N-1}^{j+1} \end{pmatrix} = \begin{pmatrix} d_0 \\ d_1 \\ d_2 \\ \dots \\ d_{N-1} \end{pmatrix},$$

$$A = \begin{pmatrix} dg(0) & up(0) & 0 & 0 & 0 & \dots & 0 \\ lw(1) & dg(1) & up(1) & 0 & 0 & \dots & 0 \\ 0 & lw(2) & dg(2) & up(2) & 0 & \dots & 0 \\ \dots & \dots & \dots & \dots & \dots & \dots & \dots \\ 0 & 0 & 0 & 0 & \dots & lw(N-1) & dg(N-1) \end{pmatrix} \quad \text{(A.19)}$$

where c_i^{j+1} represents the solute concentration p_i^{j+1} or q_i^{j+1} depending on the diffusion zone and where the values for $dg(i)$, $lw(i)$, $up(i)$ and d_i are derived from Eqs. (A.12), (A.13) and from the boundary condition equations.

For instance, the system of linear equations becomes, in the diffusion zone delimited by $0 < u < 1$ ($c_i^{j+1} = p_i^{j+1}$) and in case of a positive velocity:

- For $i = 0$: $dg(0) = 1;\ up(0) = 0;\ d_0 = C_O^{sat.}$
- For $i = N$ - 1: $dg(N-1) = 1;\ up(N-1) = 0;\ d_{N-1} = 0$
- For $1 \le i \le N-2$:

$$\begin{cases} lw(i) = -\dfrac{\delta t D_O}{Z_r^{j+1}(u_i - u_{i-1})} \\ dg(i) = Z_r^{j+1}\left(\dfrac{u_{i+1} - u_{i-1}}{2}\right) + \dfrac{\delta t D_O}{Z_r^{j+1}}\left(\dfrac{1}{u_{i+1} - u_i} + \dfrac{1}{u_i - u_{i-1}}\right) \\ \qquad + \left(Z_r^{j+1} - Z_r^j\right)u_i \\ up(i) = -\dfrac{\delta t D_O}{Z_r^{j+1}}\left(\dfrac{1}{u_{i+1} - u_i}\right) - \left(Z_r^{j+1} - Z_r^j\right)u_{i+1} \\ d_i = p_i^j Z_r^j\left(\dfrac{u_{i+1} - u_{i-1}}{2}\right) \end{cases}$$

An algorithm was elaborated to decouple and linearise the problem at each time step:

1) Take Z_r^j, p_i^j and q_i^j as initial values for Z_r^{j+1}, p_i^{j+1} and q_i^{j+1}.
2) Calculate the error on the difference given by the left hand side of Eq. (A.18).
3) If the absolute value of the error is larger than a given tolerance, the estimate of the interface position Z_r^{j+1} does not satisfy the boundary condition described by Eq. (A.17). A new estimate of the interface position has to be found according to the sign of the error. If the latter is positive (negative), the interface position has to be decremented (incremented) of a space step.
4) If the error has changed of sign, the space step applied to the interface position has to be decreased in order to refine the solution. In the present case, the space step was divided by two.
5) With the new estimate of the interface position, calculate future concentrations p_i^{j+1} and q_i^{j+1} with Eqs. (A.12), (A.13), and boundary conditions (A.14) and (A.15).
6) Repeat steps 2) to 5) until the error falls under a given tolerance. In the successive case, the values of the interface position and concentrations correspond to a solution of the implicit set of discretised equations.

A.2. Solution of the diffusion problem using a decoupling approach

The diffusion equations for Al and O in liquid Fe are given by Fick's second law:

$$\frac{\partial C_O(Z,t)}{\partial t} = D_O \frac{\partial^2 C_O(Z,t)}{\partial Z^2} \tag{A.20}$$

$$\frac{\partial C_{Al}(Z,t)}{\partial t} = D_{Al} \frac{\partial^2 C_{Al}(Z,t)}{\partial Z^2} \tag{A.21}$$

These equations have to be solved over the melt bath limited between $Z = 0$ (the melt surface) and $Z = L$. The liquid Fe-Al alloy is initially at temperature of 1600 °C and has a homogeneous composition C_{Al}^0. At time $t > 0$, a

constant and fixed O concentration, $C_O^{sat.}$, is applied at the melt surface (Z = 0).

The diffusion of both Al and O is restrained in the domain $0 \le Z \le L$. A new variable $u = \frac{Z}{L}$ is defined. Then,

$$\frac{\partial}{\partial Z} = \frac{1}{L}\frac{\partial}{\partial u} \tag{A.22}$$

and the diffusion equations for Al and O in liquid Fe (Eqs. (A.20) and (A.21)) become:

$$\frac{\partial C_O(u,t)}{\partial t} = \frac{D_O}{L^2}\frac{\partial^2 C_O(u,t)}{\partial u^2} \tag{A.23}$$

$$\frac{\partial C_{Al}(u,t)}{\partial t} = \frac{D_{Al}}{L^2}\frac{\partial^2 C_{Al}(u,t)}{\partial u^2} \tag{A.24}$$

on the domain $0 \le u \le 1$. The following boundary conditions are imposed:

- Fixed O concentration at the melt surface from $t > 0$: $u = 0$, $C_O(0,t) = C_O^{sat.}$;
- Zero flux of O at the fixed boundary $Z = L$ ($u = 1$): $\left.\frac{\partial C_O}{\partial u}\right|_{u=1} = 0$;
- Zero flux of Al at the fixed boundaries $Z = 0$ ($u = 0$) and $Z = L$ ($u = 1$): $\left.\frac{\partial C_{Al}}{\partial u}\right|_{u=0} = \left.\frac{\partial C_{Al}}{\partial u}\right|_{u=1} = 0$.

The finite difference method was used to solve the partial derivative equations by replacing spatial and time derivatives by suitable approximations, and solving numerically the resulting difference equations. The space coordinate u is discretised at N points equally distant u_i, with $i = 0$ to N - 1 and δu the grid size. The derivatives of the Al and O concentrations are approximated in terms of the values of, respectively, C_{Al} and C_O at the grid points using a second order central difference approximation. The first spatial derivative of the concentration C becomes

$$\left.\frac{\partial C}{\partial u}\right|_{u_i,t^j} = \lim_{\Delta u\to 0}\frac{\Delta C}{\Delta u} \approx \frac{C(i+1,j)-C(i-1,j)}{u_{i+1}-u_{i-1}} = \frac{C(i+1,j)-C(i-1,j)}{2\delta u}. \tag{A.25}$$

where $C(i\ ,j)$ denotes the concentration at the grid point i and time j. The second spatial derivative is approximated using a second order central difference approximation at $u_{i\pm 1/2}$, the position midway between two grid points.

$$\left.\frac{\partial^2 C}{\partial u^2}\right|_{u_i} = \lim_{\Delta u\to 0}\frac{\Delta\left(\frac{\partial C}{\partial u}\right)}{\Delta u} \approx \frac{\left.\frac{\partial C}{\partial u}\right|_{u_{i+1/2}} - \left.\frac{\partial C}{\partial u}\right|_{u_{i-1/2}}}{u_{i+1/2}-u_{i-1/2}} = \frac{C(i+1,j)-2C(i,j)+C(i-1,j)}{(\delta u)^2} \tag{A.26}$$

The derivatives with respect to time are integrated over a time step δt $(=t^{j+1}-t^j)$ using a first order forward approximation:

$$\left.\frac{\partial C}{\partial t}\right|_{u_i,t^j} \approx \frac{C(i,j+1)-C(i,j)}{t^{j+1}-t^j} = \frac{C(i,j+1)-C(i,j)}{\delta t}. \tag{A.27}$$

Substituting the approximation equations (A.26) and (A.27) for the derivatives in the diffusion equations (A.23) and (A.24) and rearranging, the finite difference approximation for the future Al and O concentrations are, for $i = 1$ to $N-2$:

$$C_{Al}(i,j+1) = C_{Al}(i,j) + \frac{D_{Al}\delta t}{(L\cdot\delta u)^2}\left(C_{Al}(i+1,j)-2C_{Al}(i,j)+C_{Al}(i-1,j)\right) \tag{A.28}$$

$$C_{O}(i,j+1) = C_{O}(i,j) + \frac{D_{O}\delta t}{(L\cdot\delta u)^2}\left(C_{O}(i+1,j)-2C_{O}(i,j)+C_{O}(i-1,j)\right). \tag{A.29}$$

The equations for $i = 0$ and $i = N - 1$ are obtained by introducing the boundary conditions into the numerical solution scheme. The implementation of the no flux boundary conditions at $Z = 0$ and $Z = L$ for C_{Al}, and at $Z = L$ for C_O is performed by integrating the differential equations over the "half" control volume adjacent to the boundary. The approximation equations for the future Al concentrations at $Z = 0$ ($i = 0$) and $Z = L$ ($i = N - 1$) are, respectively,

$$C_{Al}(0, j+1) = C_{Al}(0, j) + \frac{2D_{Al}\delta t}{(L \cdot \delta u)^2}\left(C_{Al}(1, j) - C_{Al}(0, j)\right) \tag{A.30}$$

and

$$C_{Al}(N-1, j+1) = C_{Al}(N-1, j) + \frac{2D_{Al}\delta t}{(L \cdot \delta u)^2}\left(C_{Al}(N-2, j) - C_{Al}(N-1, j)\right). \tag{A.31}$$

Similarly, the approximation equations for the future O concentrations at $Z = 0$ ($i = 0$) and $Z = L$ ($i = N - 1$) are obtained by applying the fixed O concentration condition at $Z = 0$ and no flux boundary condition at $Z = L$. It gives, respectively,

$$C_O(0, j+1) = C_O^{sat.} \tag{A.32}$$

and

$$C_O(N-1, j+1) = C_O(N-1, j) + \frac{2D_O\delta t}{(L \cdot \delta u)^2}\left(C_O(N-2, j) - C_O(N-1, j)\right). \tag{A.33}$$

Given a distribution of the Al and O concentrations at an initial time j, the concentration profiles at time $j + 1$ can be found by applying Eqs. (A.28) to (A.33) sequentially for i = 0 through N – 1.

It should be noted that the discretisation of the diffusion equations used in this section is explicit. For that reason, the finite difference approximations are only valid to some order of δu and δt. Although the method is consistent

(truncation error → 0 in the limit that $\delta u \to 0$, $\delta t \to 0$), the numerical scheme is only stable and convergent when

$$\frac{\max\left(D_{Al}, D_O\right)\delta t}{\left(L \cdot \delta u\right)^2} \leq \frac{1}{2}. \tag{A.34}$$

With an adequate choice of the grid size, the convergence criteria can be used to obtain the maximum value of δt to guarantee convergence to a solution of the discretized equations.

List of publications

Publications in international reviewed journals

Published:

- M. A. Van Ende, M. Guo, P. T. Jones, B. Blanpain and P. Wollants: Manganese and chromium distribution between $CaO\text{-}SiO_2\text{-}MgO_{sat.}\text{-}Cr_2O_3\text{-}MnO$ slags and Fe-Cr-Mn stainless steel. *ISIJ International* **48** (10) (2008) 1331-1338.

- M. A. Van Ende, M. Guo, E. Zinngrebe, R. Dekkers, J. Proost, B. Blanpain and P. Wollants: Morphology and growth of alumina inclusions in Fe-Al alloys at low oxygen partial pressure. *Ironmaking and Steelmaking* **36** (3) (2009) 201-208.

- M. A. Van Ende, M. Guo, P. T. Jones, B. Blanpain and P. Wollants: Degradation of MgO-C refractories by MnO-rich stainless steel slags. *Ceramics International* **35** (6) (2009) 2203-2212.

- M. A. Van Ende, M. Guo, R. Dekkers, M. Burty, J. Van Dyck, P. T. Jones, B. Blanpain and P. Wollants: Formation and evolution of Al-Ti oxide inclusions during secondary steel refining. *ISIJ International* **49** (8) (2009) 1133-1140.

Submitted:

- M. A. Van Ende, M. Guo, J. Proost, B. Blanpain and P. Wollants: A laboratory study on the onset of liquid Fe deoxidation by Al addition – Part 1: Interfacial reactions between oxygen containing Fe and Al. *Metallurgical and Materials Transactions B* (submitted).

- M. A. Van Ende, M. Guo, J. Proost, B. Blanpain and P. Wollants: A laboratory study on the onset of liquid Fe deoxidation by Al addition – Part 2: Formation and morphology of Al_2O_3 inclusions. *Metallurgical and Materials Transactions B* (submitted).

Contributions to proceedings of international conferences

- M. A. Van Ende, M. Guo, E. Zinngrebe, R. Dekkers, J. Proost and B. Blanpain: Morphology and growth of alumina inclusions in Fe-Al alloys at low oxygen partial pressure. Proc. 7th International Conference on Clean Steel, 4-6 June 2007, Balatonfüred, Hungary, 103-114.

- M. A. Van Ende, M. Guo, P. T. Jones, N. De Wispelaere, N. Akdut, B. Blanpain and P. Wollants: Wear mechanisms of MgO-C refractories in contact with MnO-rich stainless steel slags. Proc. 10th Unified International Technical Conference on Refractories (UNITECR), 18-21 September 2007, Dresden, Germany, 222-225.

- M. A. Van Ende, M. Guo, R. Dekkers, M. Burty, J. Van Dyck, P. T. Jones, B. Blanpain and P. Wollants: Pilot-scale study of Al–Ti deoxidation behavior in liquid steel during Al killing and Ti alloying. Proc. 3rd Baosteel Biennial Academic Conference, 26-28 September 2008, Shanghai, China, B-47-B-51.

- M. A. Van Ende, M. Guo, J. Proost, B. Blanpain and P. Wollants: Formation of inclusions at the Fe/Al interface by capillary tube tests. Proc. 4th International Congress on the Science and Technology of Steelmaking, 6-8 October 2008, Gifu, Japan, 445-448.

- M. A. Van Ende, M. Guo, P. T. Jones, B. Blanpain and P. Wollants: Thermodynamics of manganese oxide in CaO-SiO_2-$MgO_{sat.}$-Cr_2O_3-MnO slags for the production of high Mn stainless steel. Proc. VIII International Conference on Molten Slags, Fluxes and Salts, 18-21 January 2009, Santiago, Chile, 257-266.

- M. Guo, M. A. Van Ende, P. T. Jones, B. Blanpain, P. Wollants, E. Zinngrebe, S. van der Laan, C. Van Hoek, A. Westendorp: Interaction between steel and distinct gunning materials in the tundish. Proc. the Iron and Steel Technology Conference and Exposition (AISTech 2009), 4-7 May 2009, St. Louis, MO, USA, Vol. II, 621-630.

- M. A. Van Ende, M. Guo, Z. Sun, J. Proost, B. Blanpain and P. Wollants: Formation of Al_2O_3 inclusions by reoxidation of Fe-Al alloys. Proc. Asia Steel International Conference 2009, 24-27 May 2009, Busan, Korea, Proc. No. S3-12.

- M. Guo, P. T. Jones, M. A. Van Ende, B. Blanpain and P. Wollants: Interaction between alumina runner bricks and carbon steel. Proc. Asia Steel International Conference 2009, 24-27 May 2009, Busan, Korea, Proc. No. S3-03.

- M. A. Van Ende, M. Guo, B. Blanpain and P. Wollants: Laboratory study on the formation of inclusions at the on-set of deoxidation and during reoxidation. Proc. International Conference on the Advances in Theory of Ironmaking and Steelmaking (ATIS 2009), 9-11 December 2009, Bangalore, India.

Presentations at international conferences

Oral presentations:

- M. A. Van Ende*, M. Guo, E. Zinngrebe, R. Dekkers, J. Proost and B. Blanpain: Morphology and growth of alumina inclusions in Fe-Al alloys at low oxygen partial pressure. The 7th International Conference on Clean Steel, 4-6 June 2007, Balatonfüred, Hungary.

- M. A. Van Ende*, J. Lehmann, J. Proost, B. Blanpain: Morphology and growth of Al_2O_3 inclusions in Al-killed steels. ArcelorMittal PhD Day, 12 September 2007, Maizières-lès-Metz, France.

- M. A. Van Ende*, M. Guo, J. Proost, B. Blanpain and P. Wollants: Formation of inclusions at the Fe/Al interface by capillary tube tests. The 4th International Congress on the Science and Technology of Steelmaking, 6-8 October 2008, Gifu, Japan.

- M. Guo, M. A. Van Ende*, P. T. Jones, B. Blanpain, P. Wollants, E. Zinngrebe, S. van der Laan, C. Van Hoek, A. Westendorp: Interaction between steel and distinct gunning materials in the tundish. The Iron and Steel Technology Conference and Exposition (AISTech 2009), 4-7 May 2009, St. Louis, MO, USA.

- M. A. Van Ende*, M. Guo, Z. Sun, J. Proost, B. Blanpain and P. Wollants: Formation of Al_2O_3 inclusions by reoxidation of Fe-Al alloys. Asia Steel International Conference 2009, 24-27 May 2009, Busan, Korea.

- M. A. Van Ende*, M. Guo, J. Proost, B. Blanpain and P. Wollants: Morphology of Al_2O_3 inclusions formed at the Fe/Fe-Al alloy interface. Euromat 2009, 7-10 September 2009, Glasgow, UK.

Poster presentations:

- M. A. Van Ende, B. Blanpain and J. Proost: Morphology and behaviour of Al_2O_3 inclusions in Al-killed steels. The Gordon Research Conference (GRC) on High Temperature Materials, Processes and Diagnostics, 16-21 July 2006, Waterville, Maine, USA.

- M. A. Van Ende, M. Guo, P. T. Jones, N. De Wispelaere, N. Akdut, B. Blanpain and P. Wollants: Experimental determination of Mn and Cr distribution between CaO-SiO2-MgO-Cr2O3-MnO slag and Fe-18Cr-12Mn stainless steel. Euromat 2007, 10-13 September 2007, Nürnberg, Germany.

Curriculum Vitae

Personal data

Marie-Aline Van Ende
Date and place of birth: 2 September 1981, Marche-en-Famenne, Belgium
Nationality: Belgium
Home address: Route de Méan 6, B-5374 Maffe (Havelange), Belgium
e-mail address: vanende@gmail.com

Education

September 2004-Present: PhD student at the Department of Metallurgy and Materials Engineering (MTM), KULeuven, Belgium, and at the département Sciences des Matériaux et des Procédés (MAPR), Université Catholique de Louvain, Belgium.

- Fellowship from F.N.R.S.-F.R.I.A.
- Internship at Corus
- Thirteen publications in peer-reviewed international scientific journals and in conference proceedings (see 'List of publications')

2001-2004: Ingénieur civil chimiste (degree equivalent to Master of Chemical Engineering), Université Catholique de Louvain, Belgium.

- Master thesis: Production of high purity MnO from manganese carbonate (written in French)
- Internship at Hydrométal: Development of a new process to remove Hg from Pb residues

1999-2001: Candidat ingénieur civil (degree equivalent to Bachelor of Engineering), Université Catholique de Louvain, Belgium.